THESIS TITLE

THERAPEUTIC EFFECT OF MICROBIAL PROTEASES IN PROTEASE-ACTIVATED RECEPTOR (PARs) INDUCED APOPTOSIS IN OVARIAN CANCER CELLS

The thesis submitted for the degree of Doctor of Philosophy (Science)

in Life Science and Biotechnology

By

NIRAJ NAG

(Index No.: 104/19/Life Sc./26)

ICMR- National Institute of Cholera and Enteric Diseases, Kolkata

(Renamed as ICMR- National Institute for Research in Bacterial Infections)

Department of Life Science and Biotechnology

Jadavpur University

Kolkata, India

(2024)

आई. सी. एम. आर. – राष्ट्रीय कॉलरा और आंत्र रोग संस्थान
ICMR - NATIONAL INSTITUTE OF CHOLERA AND ENTERIC DISEASES
स्वास्थ्य अनुसंधान विभाग, स्वास्थ्य और परिवार कल्याण मंत्रालय, भारत सरकार
Department of Health Research, Ministry of Health and Family Welfare, Govt. of India
WHO COLLABORATING CENTRE FOR RESEARCH AND TRAINING ON DIARRHOEAL DISEASES

CERTIFICATE FROM THE SUPERVISOR

This is to certify that the thesis entitled "**Therapeutic effect of microbial proteases in Protease-activated receptor (PARs) induced apoptosis in ovarian cancer cells**" was submitted by **Shri. Niraj Nag** who got his name registered on **September 23, 2019**, for the award of **Ph.D. (Science)** degree of **Jadavpur University**, is absolutely based upon his own work under my supervision and that neither this thesis nor any part of it has been submitted for either any degree / diploma or any other academic award anywhere before.

.....

Date: 31.07.2024 (Signature of the Supervisor date with official seal)

Amit Pal, PhD
Scientist – 'G' & Head
Division of Molecular Pathophysiology
ICMR- National Institute of Cholera & Enteric Diseases
P-33, CIT Road, Scheme – XM, Beliaghata
Kolkata, West Bengal – 700010, India
Email: palamit.app@gmail.com / pala.niced@gov.in

डॉ अमित पाल / DR. AMIT PAL
वैज्ञानिक 'जी' / Scientist 'G'
आई.सी.एम.आर.-राष्ट्रीय कॉलरा और आंत्र रोग संस्थान
ICMR-National Institute of Cholera and Enteric Diseases
पी-33, सी. आई. टी. रोड, स्कीम-XM, बेलियाघाटा
P-33, C.I.T. Road, Scheme-XM, Beliaghata
कोलकाता-700010 / Kolkata - 700010

Dedicated to
My Lovely Parents,
and
To the Fond Memories
of My Grandparents

This Thesis is a Fruit
of their Blessings

THIS BELONGS TO
MY FAMILY

ACKNOWLEDGEMENTS

I would like to express heartfelt gratitude to all those who have contributed in countless ways to the success of this thesis work and made this journey a memorable one for me. In this thesis, every step, from inception to completion, stands as a testament to the collaborative spirit and collective effort of all involved. I deeply appreciate the invaluable contributions made by each member of the team, without which this work would not have been possible. Each individual's dedication, expertise, and commitment to excellence played an integral role in the successful completion of this journey. Together, we have achieved a significant milestone in advancing knowledge and understanding in our field.

First and foremost, I would like to express my enormous gratitude to **Dr. Amit Pal**, Scientist- '**G**' and Head, Division of Molecular Pathophysiology, ICMR-NICED, Kolkata, India for his invaluable advice over the past five years. As my mentor, his relentless enthusiasm, patience and support have made it possible for me to achieve my goals. I have been fortunate to have a practical, judicious, efficient, supportive and inspiring supervisor like him. His countless advice and constant criticism were instrumental in shaping the overall direction of my research work. I believe to have become a better person under his guidance and wish to reinstate his qualities within myself. I thank him for everything I have and for all that I will achieve in the future as a researcher.

I also take this opportunity to offer my sincerest thanks to the **University Grants Commission (UGC), India** for providing financial assistance in the form of a research fellowship and contingency that enabled me to be financially independent during my PhD tenure.

Next up, I am deeply grateful to **Dr. Shanta Dutta**, Director of ICMR-NICED, for providing me with the opportunity to work at this esteemed institute and for ensuring the availability of all necessary instrumentation facilities. The work in my thesis work would not have been possible without close collaboration with a few laboratories. My sincere thanks go to **Dr. SantaSabuj Das** (NICED), **Dr. Nabendu Sekhar Chatterjee**

(NICED), **Dr. Sulagna Basu** (NICED), **Dr. Asish Mukhopadhyay** (NICED), **Dr. Moumita Bhoumick** (NICED), **Dr. Sandipan Ganguly** (NICED), **Dr. Hemanta Koley** (NICED), **Dr. Manoj Kumar Chakrabarti** (NICED), **Dr. Sib Sankar Roy** (CSIR-IICB) and **Dr. Shruti Chatterjee** (Nirma University), **Dr. Sutapa Mukherjee** (CNCI) for providing resources, reagents and helpful suggestions that were immensely helpful in completion of the thesis work.

I am compelled to extend my heartfelt gratitude to my seniors, **Dr. Tanusree Ray** and **Dr. Rima Tapader**, affectionately referred to as **Tanusree di** and **Rima di**, for their invaluable guidance and support across all facets of my journey. I would also take the privilege to thanking my lab mates **Dr. Dwiprohi Kar** and **Dr. Nanda Singh** for their cooperation.

The routine nature of PhD life finds its reprieve in the companionship shared with exceptional colleagues turned friends like **Mr. Saibal Saha**, **Mr. Avik Mukherjee**, and **Dr. Mainak Chakraborty**. From engaging in morning discussions at the local teashop near NICED to embarking on exhilarating road trips to amazing destinations, our experiences have been filled with joy and adventure. I am so lucky to have such amazing coworkers cum friends.

I would also like to extend my sincere gratitude to **Mr. Ananda Pal (Andy)** and **Mr. Animesh Gope** who have helped me overcome many difficulties I faced during my PhD. I thank them for their patience and incredible assistance with my flow cytometry and imaging experiments.

My special thanks go to **Mr. Biplab Roy** for his help with animal experiments and microbial screening. I also thank **Mr. Rishikesh Kumar** for helping me with administrative work.

I acknowledge the unwavering support received from **Suparna, Oishika, Vipul Da, Amrita, Prolay, Sangeeta, Sohini, Swarnali, Pritam and Parash Prasad** for making the journey an absolute memorable one for me. They have been gracious in welcoming me with widely opened arms despite being from different laboratories.

I am grateful to the **scholars** and **staffs** of NICED for making this place seem like home. I thank NICED canteen staffs, security staffs, animal house staffs, electrical section, cleaning and maintenance staffs for their continuous support.

I would like to thank all the intern students whom I had the opportunity to mentor. Some of these young refreshing minds like **Ms. Anuprerna P. Gangadhar** and **Mr. Palash Paul** left an impact on me.

I would like to dedicate a special acknowledgment to **Dr. Rajdeep Das**, my dear friend from our college days, whose collaboration and unwavering support have been instrumental throughout my PhD journey. I have felt truly fortunate to have him by my side. Rajdeep's constant encouragement, insightful advice, constructive criticism, and heartfelt camaraderie have been a continuous source of strength and inspiration. His belief in my abilities and his readiness to help, regardless of the challenges, have profoundly impacted my academic and personal growth. I shall continue to be the loudest cheerleader for him always and forever. Thank you, Rajdeep, for being a faithful friend and an invaluable part of this journey.

I must also specially mention **Dr. Elizabeth Mahapatra**, who has impressed me with her undying spirit, vision, and writing skills. Although she is my junior at CNCI, she has guided me wholeheartedly like an experienced professional. I cannot thank her enough for always being there when I needed her. Working with Elizabeth as a collaborator has renewed my focus, and her motivation and relentless quest to achieve the best in life has rejuvenated my spirit.

I am forever indebted to my steadfast friends, **Mr. Arup Dutta Roy** and **Mr. Anik Das**, for their constant support and company. Our weekend gossip sessions, bike rides, and vacation trips refresh and motivate me, helping me focus on my work throughout the week. I consider myself incredibly fortunate to have them as friends by my side.

Next, I would also like to extend my gratitude to **Dr. Atish Barua (Atish Da)** whose valuable advice and unconditional support like an elder brother have helped me overcome many hurdles I faced during my PhD.

I would like to express my heartfelt gratitude to my former mentors, **Dr. Manas Ranjan Ray** from CNCI, Kolkata, and **Prof. Samir Kumar Patra** from NIT-Rourkela, for instilling in me a deep passion for learning during my training days. Their guidance and support have been instrumental in shaping my academic journey and inspiring me to pursue a doctorate. I am immensely proud to have been their student and forever grateful for their invaluable mentorship.

I seize this opportunity to extend my gratitude to **Ms. Priyanka Chakraborty Sarkar** from NIT-Rourkela, affectionately known as our **Priyanka Di**, for her invaluable guidance in introducing me to cell culture techniques firsthand. Her charming personality and support have been akin to that of a real elder sister, constantly motivating and inspiring me throughout. I also thank my colleagues and friends from NIT-Rourkela **Mr. Joy Khag**, **Dr. Abtar Mishra** and **Mr. Sougata Ghosh** for their cooperation.

Since childhood, the principle of "*mens sana in corpore sano*" (a sound mind in a sound body) has been instilled in me. In this light, I extend my gratitude to my gym coaches, **Mr. Soumya Dasgupta** and **Mr. Abhishek Mukherjee**, for their tremendous dedication to maintaining my physical and mental fitness. Their consistent efforts have been instrumental in ensuring my holistic well-being.

As someone deeply rooted in Bengali culture, I feel compelled to acknowledge the profound impact of **Mr. Sunil Gangyopadhyay**'s (fondly called **Sunil da**) poetry and writings, which have served as a source of solace and inspiration during moments of leisure. His words have felt like a divine gift, enriching my free time with their depth and beauty. Additionally, the timeless melodies of **Rabindrasangeet** have been a constant source of motivation for me. **Ms. Srabani Sen**, a renowned singer, silently conveys the essence of Rabindrasangeet through her sweet voice, whether I am exhausted or engrossed in work on my laptop throughout the day. I hold these stalwarts in the highest regard and express my profound respect for their contributions in this journey.

I rely on **Ms. Ritoja Shee (Bhumisuta)** for moving ahead. In addition to being my constant companion, she has been my best friend for the last seven years. Despite our quarrels, she has stood by my side through every high and low, providing perpetual support and encouragement. She is one of the driving forces behind my progress, lifting me up during times of adversity. She taught me to never settle for mediocrity despite challenges. With her composed, pragmatic, responsible and thoughtful approach to obstacles, she has imparted invaluable life lessons. She is always there for me, a friend for a lifetime. I pledge to remain her strongest supporter, cheering her on endlessly, now and forever.

I cannot end without acknowledging my parents **Mr. Mridulendu Nag** and **Mrs. Dipika Nag** who are the ultimate superheroes of my life. They have been instilling the importance of pursuing higher education within me right from childhood. They have always championed me for manifesting my education in becoming a better human being. I am indebted to them for teaching me the core humane values in life which have fuelled my journey this far. With researchers, life is not always hunky dory when it comes to finances. Yet, my parents have chosen to put up with all the odds because they wanted to facilitate me in my aspirations. I hope, someday I manage to give them the comfort they deserve and fulfill all their wishes. Therefore, simply writing a single paragraph fails to capture the depth of their contributions, sacrifices, and support in every facet of my life. Their presence definitely has been transformative, shaping my journey of life in profound ways that extend far beyond mere words.

I will have to thank my little sister **Mrs**. **Nisha (Buli)**. Despite being the youngest in my family, she has always been my greatest support. Moreover, I would like to thank my elder brothers **Mr. Tamal Nag** and **Mr. Prolay Nag** for inspiring me not only during my PhD but also in life. They have been patiently shouldering all my responsibilities at home. I express my love to my trusty **bike**, affectionately named **Kremlin**, for being a reliable companion and saving me precious time during the congested rush hours of Kolkata, our bustling metropolis. With my family being the wind beneath my wings, I dare to soar higher fearlessly. My family is not an important thing but it's everything to me. **Without them**, it would have been impossible for me to have come this far in life.

I express my deepest respect to **those who lost their lives to cancer**. Their struggle inspires researchers like us to continue the battle against this devastating disease.

Lastly, but certainly not least, I extend my deepest gratitude to the **Almighty God** for the blessings bestowed upon me, serving as a guiding light throughout my journey. I am thankful for the unwavering confidence instilled in me by the divine presence, which has been instrumental in navigating through challenges, including surviving the COVID-19 pandemic.

I extend my sincerest apologies to **those whose contributions I am unable to mention** here due to constraints of space and time. I am grateful to each one of them.

As **Swami Vivekananda** wisely said, "Put your heart, mind, and soul into even your smallest acts. This is the secret of success." I earnestly believe that I have strived to adhere to this principle to the best of my ability, and I am committed to continuing to embody it in all my endeavours in the future.

I conclude this section with the classic words of **Robert Frost**:

“The woods are lovely, dark and deep,
But I have promises to keep,
And miles to go before I sleep,
And miles to go before I sleep."

Thank you all !!!

……. *Niraj Nag*

Contents

Page no.

Abbreviations

Ab - Antibody

AP - Alkaline phosphatase

Bax - Bcl-2-associated protein x

Bcl 2 - B cell lymphoma-2

C57BL/6 - C57 black 6 laboratory mice

DMEM - Dulbecco's modified Eagle's medium

DMSO - Dimethyl sulfoxide

EDTA - Ethylenediaminetetraacetic acid

EGFR - Epidermal growth factor receptor

EMT - Epithelial to mesenchymal transition

EOC - Epithelial ovarian cancer

ERK - Extracellular signal-regulated kinase

FACS - fluorescence-activated cell sorter

FBS - Foetal bovine serum

FITC - Fluorescein isothiocyanate

GAPDH or **G3PDH** - Glyceraldehyde-3-phosphate dehydrogenase

gm - Gram (only with numbers)

GPCR - G protein coupled receptor

h – Hours (only with numbers)

H_2DCFDA - 2',7'-dichlorodihydrofluorescein diacetate

HGSOC - High-grade serous ovarian cancer

HRP - Horseradish peroxidase

IACR - Indian Association of Cancer Research

IC_{50} - Half-maximal inhibitory concentration

JC1 - 5,5,6,6'-tetrachloro- 1,1',3,3'-tetraethylbenzimi-dazoylcarbocyanine iodide

LGSOC - Low grade serous ovarian cancer

MAPK - Mitogen-activated protein kinase

MEMα - Minimum essential Eagle's medium with alpha modification

MFI – Mean fluorescence intensity

min - Minute (only with numbers)

ml - Milliliter (only with numbers)

mRNA - messenger RNA

MTT - 3-(4,5-dimethylthiazol-2-yl)-2,5-dimethyltetrazolium bromide

NFκB - Nuclear factor kappa-light-chain-enhancer of activated B cells

NS - Not significant

OC - Ovarian cancer

OD - Optical density

OVCa - Ovarian carcinoma

p - Probability

PAGE - Polyacrylamide gel electrophoresis

PAR – Protease activated receptor

PAR-1– Protease activated receptor 1

PARP - Poly (ADP-ribose) polymerase

PBS - Phosphate buffered saline

PBST - Phosphate Buffered Saline with 0.1% Tween 20

PCR - Polymerase chain reaction

PEMΦ - Peritoneal macrophage

PI - Propidium iodide

PMSF- Phenylmethylsulphonyl fluoride

qRT-PCR - Quantitative reverse transcriptase polymerase chain reaction

ROS - Reactive oxygen species

RPMI 1640 - Roswell Park Memorial Institute medium 1640

SD - Standard deviation

SDS - Sodium dodecyl-sulphate

SE - Standard error

SEM - Standard error of the mean

WB - Western Blot

µg - Microgram (only with numbers)

µl - Microliter (only with numbers)

Zn/Zn^{2+} - Zinc

Preface

In this study, we focus on the search for a novel microbial extracellular protease that induces apoptosis in cancer cells. This involves employing a robust screening approach to environmental microbial isolates, followed by the identification and characterisation of the protease. Several pieces of evidence suggest that microbial proteases possess anticancer effects. Hence, the protease activity could potentially enhance anti-carcinogenesis by disrupting the balance of pro and antiapoptotic proteins. However, the mechanisms underlying such effects and whether they entail any potential signalling pathways remain poorly understood. Based on this, we purified Peptidase M84 from the culture supernatant of *Bacillus altitudinis* strain GDL-186, which exhibited cytotoxicity against ovarian cancer cells. This finding has significant implications for cancer therapy.

Highlights of the study

- Peptidase M84, derived from an environmental isolate of *Bacillus altitudinis*, exhibits anti-cancer properties.
- This metalloprotease triggers ROS-dependent apoptosis in PAR-1-positive ovarian cancer cells.
- PAR-1-negative healthy cells remain unaffected by Peptidase M84 treatment.
- Peptidase M84 enhances the efficacy of PAR-1 targeted therapy for ovarian cancer.

CHAPTER 1

Introduction

Despite significant advancements in chemotherapy regimens for ovarian cancer, it remains one of the most lethal gynaecological malignancies, characterised by high recurrence and mortality rates. While cytoreductive surgery combined with platinum-based chemotherapy is the standard treatment for epithelial ovarian cancer (EOC), mortality rates have not seen a significant decrease (Kurnit et al., 2021). For example, according to Globocan 2018, ovarian cancer ranks eighth among the most common malignancies affecting Indian females. Consequently, there is an urgent need for new therapies and alternative targets to combat ovarian cancer. In this context, the anticancer potential of natural microbial enzymes has been extensively explored. Microorganisms abundantly provide structurally diverse natural products, making them valuable resources for drug discovery (Huang et al., 2021). Compared to chemically synthesised drugs, the extraction and purification of natural bacterial products are relatively cost-effective (Sahayasheela et al., 2022). Bacterial toxins and enzymes have been recognised for their anti-cancer effects, modulating various cellular processes such as apoptosis, differentiation, and proliferation. When used alone or in combination with other anticancer drugs or irradiation, bacterial products can enhance the efficacy of cancer therapy (Trivanović et al., 2021).

Extracellular or secreted proteases are crucial for the survival of protease-secreting bacteria and are found ubiquitously in nature, originating from plants, animals, and microbes. These degradative enzymes hydrolyse the peptide bonds in polypeptide chains of amino acids, selectively modifying proteins (Tapader et al., 2019). Bacillus species are extensively studied and recognised as dynamic, active, and industrially significant producers of extracellular alkaline proteases (EC.3.4.21-24.99). The global market for these enzymes is rapidly expanding, with proteases accounting for 20% of the 60% of all marketed enzymes. Proteases are fundamental to nearly all forms of life on Earth and can be isolated and purified through various fermentation processes in a relatively short time, exhibiting high substrate specificity and catalytic activity. These producers thrive in diverse environments, including water, soil, and highly alkaline conditions. Alkaline proteases have been segregated from sources like detergent contamination, dried fish, sand soil, and slaughterhouses (Razzaq et al., 2019; Song et al., 2023). Research has shown that alkaline fibrinolytic proteases can degrade fibrin, indicating potential applications as anticancer drugs and in future thrombolytic therapy. Proteases play roles in normal and pathological processes, potentially serving as

therapeutic agents against diseases such as cancer and AIDS (Rawlings et al., 2004). Our study involved extensive screening of various environmental microbial isolates to identify a naturally occurring microbial extracellular protease capable of inducing apoptosis in ovarian cancer cells, with the aim of elucidating its anticancer mechanism.

The purification of these enzymes is a complex process involving various methods to recover value-added products. The choice of purification technique depends on whether the enzyme is extracellular or intracellular. The primary goal during enzyme production and purification is to produce cost-effective, high-value end products using economical techniques. Typically, protein recovery from a crude biological mixture involves precipitation methods, using reagents such as salts and organic solvents. Ammonium sulphate is commonly used for protein precipitation in aqueous solutions with acidic, neutral, or alkaline pH, enhancing salt solubility under alkaline conditions, unlike sodium sulphate which has limited solubility at low temperatures. For the purification of proteases, ion exchange (e.g., CM-Sephadex, DEAE-Sephadex) and gel filtration chromatography are effective techniques, particularly for alkaline, acidic, and neutral proteases from bacterial sources like *Bacillus cereus* AT and *Bacillus circulans*. Dialysis membranes are preferred for enzyme recovery, while ultrafiltration, a pressure-driven separation process, is cost-effective and results in minimal enzyme activity loss. Additionally, gel filtration is used to determine the molecular mass of proteins, employing reference standards of proteins with known molecular weights (Razzaq et al., 2019; Song et al., 2023; Tapader et al., 2019).

Proteases can induce bio-signalling pathways and control cellular functions through the cleavage of protease-activated receptors (PARs), a notable G-protein coupled receptors (GPCRs). The subtypes of PARs, ranging from PAR 1–4, have been found to be overexpressed in cancer cells with respect to healthy normal cells. PARs play important roles in the apoptosis of cancer cells and carcinogenesis depending on the stimuli (Flynn & Buret, 2004). Studies demonstrated the differential expression pattern of PAR-1 in both transcriptional and translational levels in ovarian carcinoma tissue samples, while, negligible or none in the normal ovarian surface epithelium (Grisaru-Granovsky et al., 2005). Moreover, PAR-1 agonists also showed apoptosis in intestinal epithelial cells (Chin et al., 2003). Nevertheless, the molecular mechanism by which overexpression of PAR-1 can perturb the viability of cancer cells remains a less examined area of cancer research. PAR-1 activation can trigger ROS generation in cancer cells (Mußbach et al.,

2015; Ray & Pal, 2016). Depending on their concentration, reactive oxygen species (ROS) can have contrasting effects on cancer development. Oxidative stress, characterised by an imbalance between reactive oxygen species (ROS) and antioxidants, has been associated with various health conditions They may either trigger or promote tumorigenesis by facilitating the transformation and proliferation of cancer cells, or induce cell death (Hayes et al., 2020). The realignment of redox balance is crucial for how tumour cells tolerate high ROS levels. Both PAR-1 and ROS are also reported to be associated with the activation of NF-kB and MAP kinases imparting apoptosis of cancer cells (Ray & Pal, 2016; Sheng et al., 2020). Abundant evidence suggests that p38 and NF-κB are involved in enhancing cellular ROS levels and the intrinsic pathway of cell apoptosis (Ray & Pal, 2016; Tapader et al., 2018). When there's an excessive production of reactive oxygen species (ROS) surpassing the cellular antioxidant capacity, it results in oxidative stress, which ultimately affects a wide range of signalling pathways. Excessive ROS generation can lead to oxidative damage and cell death (Ray & Pal, 2016; Tapader et al., 2018). Therefore, PAR-1 mediated ROS targeting therapy using proteases may be proven to be advantageous to selectively kill cancer cells.

Our study presents a novel approach to selectively kill ovarian cancer cells of both human and murine origin using Peptidase M84, a major secretory protein from *Bacillus altitudinis*. We purified Peptidase M84 from an environmental isolate of *Bacillus altitudinis* and identified it as a potent anticancer agent for the first time. Peptidase M84 induces apoptosis in ovarian cancer cells with high selective toxicity, while showing no significant apoptotic effects on normal human ovarian epithelial cells or mouse peritoneal macrophage cells. More than 90% of all ovarian malignancies are classified as epithelial ovarian cancer (EOC), including aggressive high-grade serous carcinoma, we believed that initially testing Peptidase M84 for its apoptosis-inducing capabilities in an *in vitro* setup could help design a more effective treatment strategy. Our findings broaden the prospects for apoptosis-inducing proteases from environmental isolates in cancer treatment. In the present study, we have gone through various experimental approaches to show that Peptidase M84 secreted by *Bacillus altitudinis* has anticancer properties. Our current study depicts a deeper understanding of the mechanism by which Peptidase M84 induces apoptosis in ovarian cancer cells, specifically through a PAR-1/ROS-dependent pathway, which was previously unexplored. Thus, Peptidase M84 holds potential for future chemotherapeutic use in treating ovarian cancer.

CHAPTER 2

Review of Literature

2.1. Cancer Therapy and Natural Compounds

Cancer persists as a formidable challenge of the 21st century, posing a fatal threat to humanity. It stands as the second leading cause of global mortality, claiming approximately 9.6 million lives in 2018 alone. Roughly one in six deaths worldwide is attributed to this devastating disease (Patra, 2008; Siegel et al., 2020). The array of treatments and therapies available varies according to cancer type. Nevertheless, researchers persistently strive to refine anticancer compounds for therapeutic application. A wealth of cytotoxic compounds, sourced from nature, demonstrate promising antitumor and anticarcinogenic properties. Through meticulous isolation, purification, and development processes, numerous anticancer compounds have emerged from diverse natural reservoirs such as plants and microbes (Huang et al., 2021; Trivanović et al., 2021) . A concerted effort, driven by focused objectives and collaborative endeavours, holds the potential to expedite the discovery of novel anticancer drugs boasting enhanced efficacy. The bounty of nature offers humanity a rich trove of resources ripe for drug discovery. Nearly half of the pharmaceuticals in use today, designed to combat human ailments, are sourced from natural products found on land. While conventional chemotherapy has proven its efficacy, its utility is hampered by significant side effects. Thus, in the realm of cancer research, emphasis is placed on prevention, early detection, and the exploration of innovative alternative therapies.

2.2. Ovarian Cancer

Exploring the gravity of ovarian cancer in women, it ranks as the seventh most prevalent cancer and the second highest contributor to gynaecological malignancy-related deaths. On a global scale, it stands as the eighth most common cause of cancer-induced mortality. Alarmingly, the five-year survival rate hovers at a mere 47%. Epithelial Ovarian Cancer (EOC) constitutes the lion's share, representing 85-90% of all cases (Z. Liu et al., 2024). This variant can be further classified into five subtypes, distinguished by their origin, pathogenesis, risk factors, prognosis, and molecular characteristics (Torre et al., 2018). In 2020, the global incidence of ovarian carcinoma (OvCa) saw an estimated 313,959 new cases, resulting in 207,252 deaths. Among malignant ovarian

tumours, approximately 90% originate from epithelial cells, while 5-6% are attributed to sex cord-stromal tumours (such as granulosa cell tumours and thecomas), and 2-3% are germ cell tumours (including teratomas and dysgerminomas) (Brett M. et al., 2017). Most epidemiological research, including our study, predominantly focuses on epithelial ovarian carcinoma. Ovarian cancer has the worst prognosis among gynaecologic cancers, with approximately 314,000 new cases and 207,000 deaths annually (Cabasag et al., 2022). This disease is characterised by heterogeneity and distinct histotypes, each with unique molecular features, clinical presentations, and prognoses (Soslow, 2008; Peres et al., 2018). According to the WHO classification, 90% of ovarian tumours originate from the epithelium, 3% from germ cells, and 2% from sex-cord stromal cells (Hanby and Walker, 2004; Herrington and Herrington, 2020). The 5-year survival of OVCa patients in India is about 45% (Mhatre et al., 2023).

2.3. Classification and histological subtypes

Epithelial ovarian carcinoma (EOC) encompasses a diverse range of histologic subtypes (histotypes) characterised by variations in cellular origin, pathogenesis, molecular profiles, gene expression patterns, and prognosis. The main malignant histotypes include high-grade serous (HGSOC; 70%), endometrioid (ENOC; 10%), clear cell (CCOC; 10%), mucinous (MOC; 3%), and low-grade serous (LGSOC; <5%). Additionally, within these categories, particularly among serous and mucinous tumours, there exist borderline or low malignant potential (LMP) tumours, which exhibit microscopic features of malignancy without evident invasion into surrounding stromal tissues (Ciucci et al., 2022a; G. Li et al., 2023).

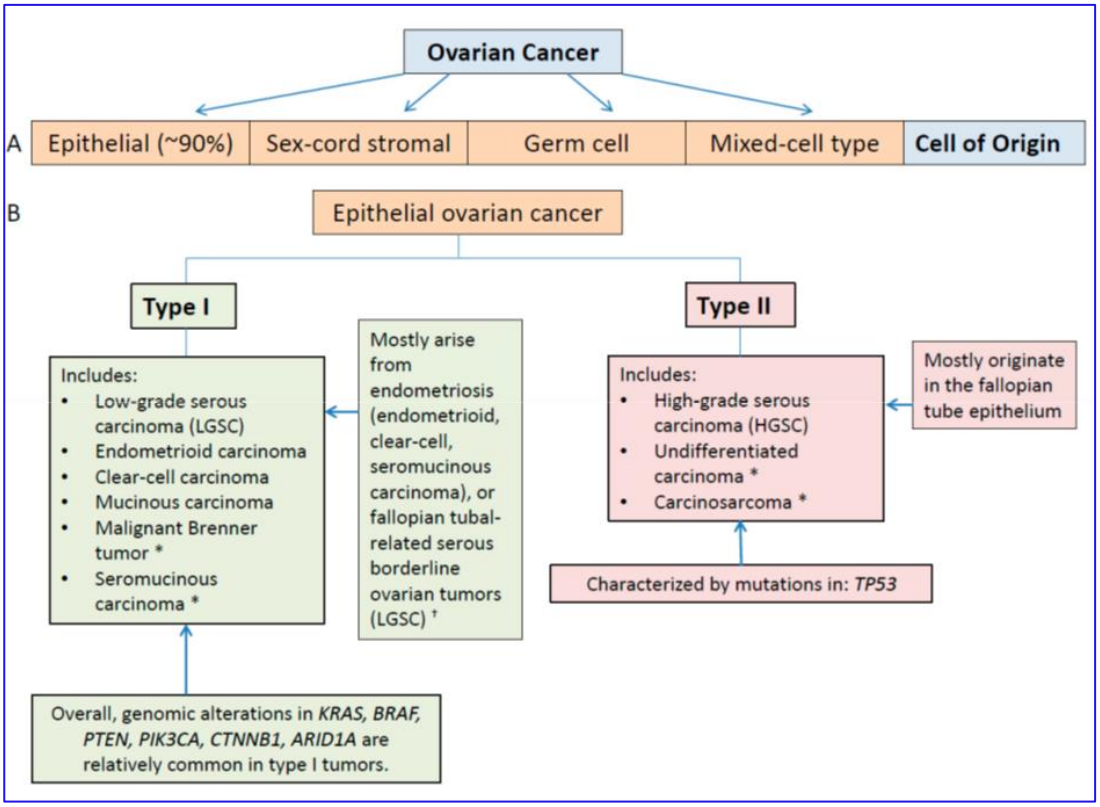

Figure 2.1. Classification of ovarian cancer based on histological subtypes

(A) Histological subtypes of ovarian cancer; and (B) Epithelial ovarian cancer classification paradigm based on molecular and clinicopathologic evidence that type I and type II tumours develop through different pathways (Kurman et al., 2015). * Rare tumour; † Mucinous and malignant Brenner tumours are considered to be possible exceptions that may arise from transitional cells at or close to the junction of the fallopian tube and the peritoneum; Sourced from (Rojas et al., 2016).

The majority of patients with epithelial ovarian cancer are diagnosed at an advanced stage. Despite significant advances in treatment over the past several decades, recurrent ovarian cancer remains almost uniformly fatal. More than 70% of those diagnosed with International Federation of Gynaecology and Obstetrics (FIGO) stage III or IV ovarian cancer (2014) will experience a recurrence within the first five years. Given the critical clinical needs of these patients, our focus here is on the treatment of advanced disease (Kurnit et al., 2021).

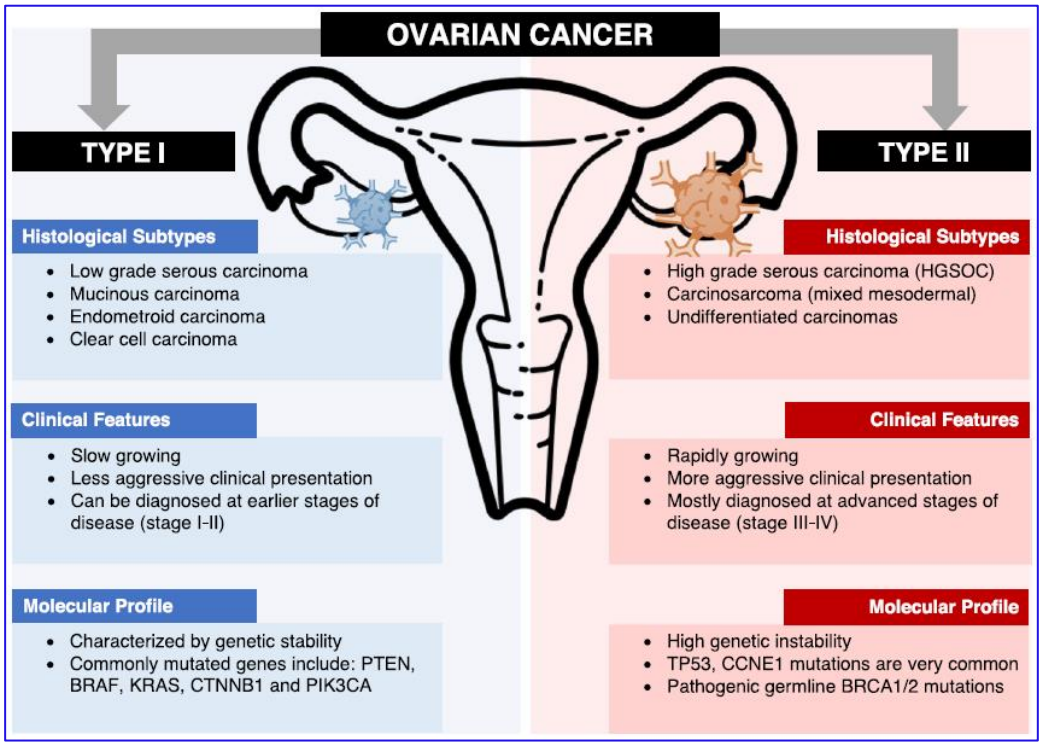

Figure 2.2. Schematic representation of ovarian cancer classification into Type I and Type II tumours depending on histology, clinical features, and molecular profile with commonly associated mutations. Type I tumours tend to be slow growing, less aggressive, and more likely to be diagnosed at earlier stages of disease associated with genetic stability. Type II tumours usually present with more aggressive, rapid growing disease that is diagnosed in more advanced stages, and are associated with a higher degree of genetic instability; Sourced from (Zhu et al., 2022)

2.4. Worldwide scenario

Ovarian cancer (OC) incidence exhibits significant geographic variation. The highest age-adjusted incidence rates are observed in developed regions such as North America and Central and Eastern Europe, where rates generally exceed 8 per 100,000. In contrast, rates are intermediate in South America (5.8 per 100,000) and lowest in Asia and Africa (≤3 per 100,000). Migration from low-incidence to high-incidence countries increases risk, emphasising the importance of non-genetic risk factors. Within the United States, racial differences in incidence and mortality reflect international patterns: rates are

highest among Whites, intermediate among Hispanics, and lowest among Blacks and Asians. Similarly, in large countries like China, incidence and mortality are higher in developed, urban regions compared to less developed, rural areas. In most developed countries, including North America and Europe, OC incidence and mortality have gradually declined since the 1990s. Conversely, historically less developed countries experiencing recent economic growth and lifestyle changes have seen increases in OC incidence and mortality rates (Brett M. et al., 2017).

In India, the estimated incidence of ovarian cancer is the second highest globally, following China. Among South Central Asian countries, India accounts for 76.5% of ovarian cancer cases and 77.5% of the mortality associated with the disease (Globocan 2020, gco/iarc.fr).

High-grade serous ovarian cancer (HGSOC) is the most common histologic type of epithelial ovarian cancer (EOC). It typically presents at an advanced stage (III–IV). Despite an initial response to surgical debulking and first-line therapy with carboplatin and paclitaxel (with or without bevacizumab), most tumours eventually develop drug resistance. As a result, the 5-year survival rate generally remains below 30% (Y. Zhang et al., 2019).

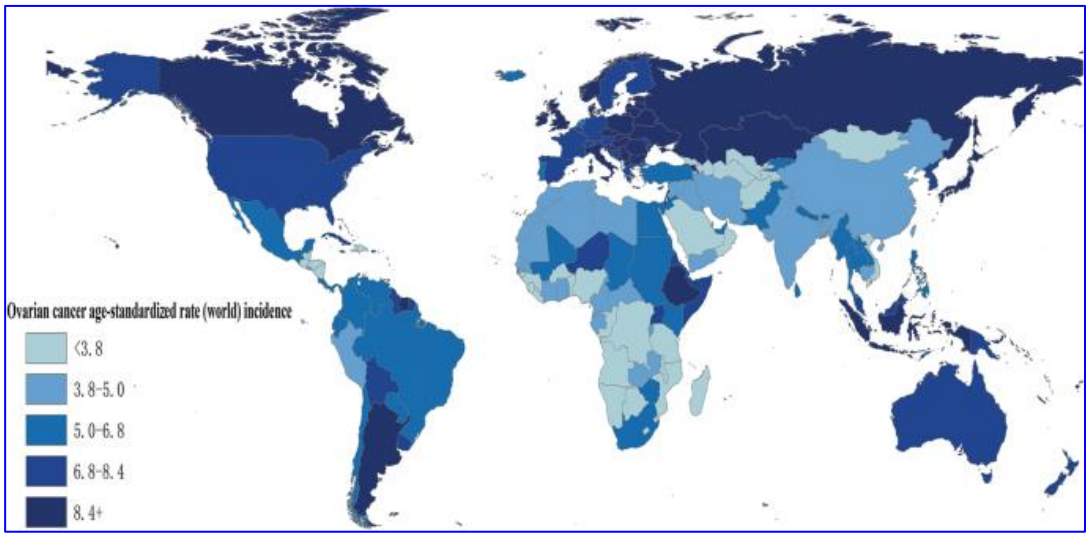

Figure 2.3. Estimated international variation in age-standardized (world) ovarian cancer incidence rates for all ages. National OC incidence estimates in 2012 for 184 countries were extracted from the GLOBOCAN 2012 database (http://globocan.iarc.fr) (Y. Zhang et al., 2019).

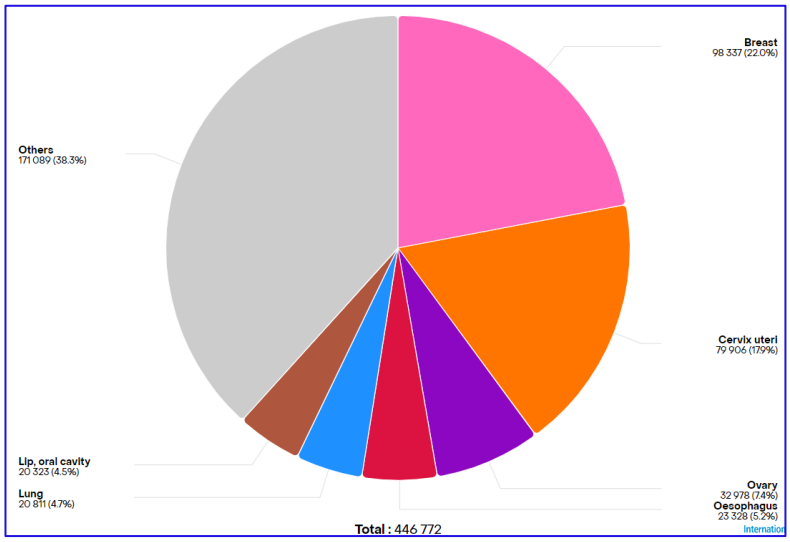

Figure 2.4. Ovarian cancer mortality in India, Data version: Globocan 2022 (version 1.1)-08.02.2024. Cancer TODAY; IACR – https://gco.iacr.who.int

2.5. Current treatment strategy, challenges and limitations

Currently, the main treatment modalities for ovarian cancer (OC) include surgical debulking, radiotherapy, and chemotherapy. However, these treatments often result in unwanted side effects and drug resistance due to the lack of targeted therapies. This highlights the urgent need to decipher complex disease biology and identify potential biomarkers that could significantly enhance early diagnosis and predict responses to specific therapies. Chemotherapy for OC, in particular, adversely affects patients' quality of life with severe side effects such as fatigue, arthralgia, and neurotoxicity. Understanding the biology of heterogeneous OCs is crucial for accurately exploring the disease's mechanisms. Researchers are investigating potential therapeutic targets for OC management, including intrinsic signalling pathways, angiogenesis, hormone receptors, and immunologic factors (Kurnit et al., 2021).

Newly diagnosed high-grade serous epithelial ovarian cancer (EOC) patients typically undergo radical surgery followed by adjuvant platinum and taxane combination chemotherapy. However, for patients where upfront surgery is contraindicated due to medical reasons such as comorbidities or poor performance status, or where complete cytoreduction is unachievable, neoadjuvant chemotherapy (NACT) followed by interval debulking surgery (IDS) and adjuvant chemotherapy is an alternative option. Currently,

there is a lack of consensus on the best candidates for NACT, with some authors suggesting that this approach may be harmful for certain patients by promoting early chemoresistance (Moschetta et al., 2020).

The majority of newly diagnosed epithelial ovarian cancer (EOC) patients undergo radical surgery, a treatment approach initially proposed by Meigs et al. in 1934 and later refined by Griffiths et al. in 1975. This surgery is typically followed by six to eight cycles of adjuvant platinum and taxane combination chemotherapy. Despite aggressive treatment at diagnosis, most patients experience disease relapse within the first five years, and only about a quarter of cases are ultimately cured (Moschetta et al., 2020).

2.6. Need for new anticancer agents

Recent treatments for ovarian cancer primarily include surgery and chemotherapy, with the standard regimen involving a combination of platinum-based drugs and taxanes. While these treatments can be effective, they often come with significant disadvantages. Chemotherapy is associated with severe side effects, such as nausea, fatigue, and neuropathy, and many patients eventually develop resistance to these drugs, leading to relapse. Additionally, current treatments are generally not tailored to individual patients, resulting in variable effectiveness. These limitations underscore the need for alternative precision medicine approaches, which aim to develop targeted therapies based on the specific genetic and molecular profiles of each patient's cancer. Precision medicine holds the promise of improving efficacy, reducing side effects, and overcoming drug resistance by offering more personalized and targeted treatment options (Cristea et al., 2010) .

Ultimately, the goal is to create more effective methods for detecting and treating this lethal disease. Achieving these ambitious objectives requires the careful selection of preclinical models and meticulous study design to ensure that preclinical data can be successfully translated to clinical settings.

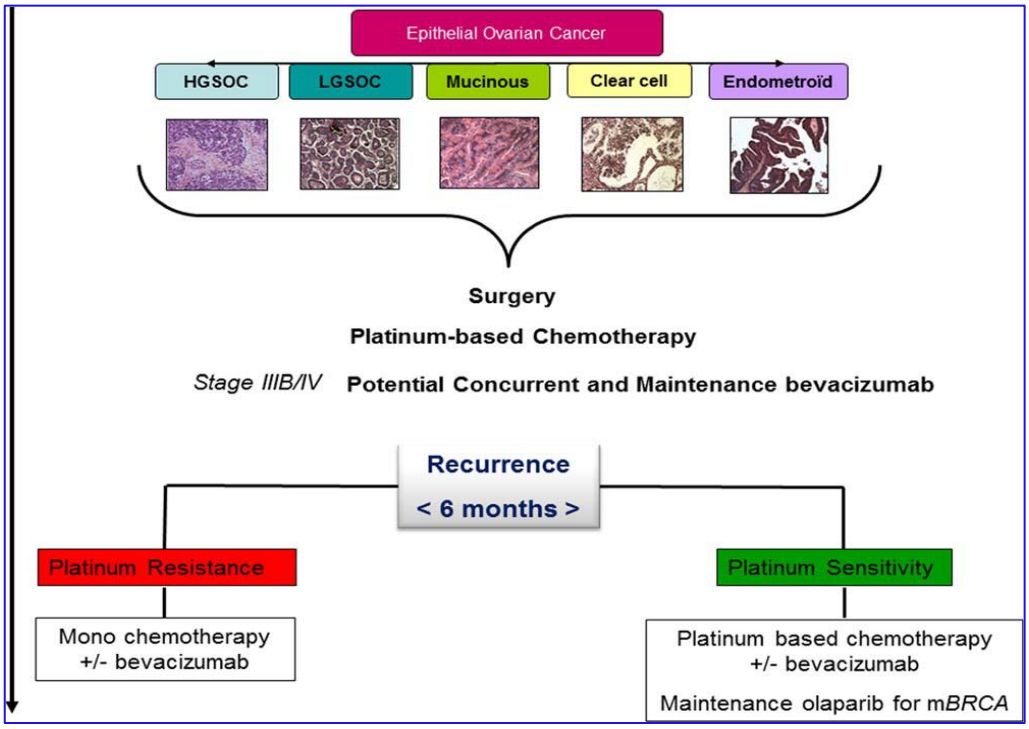

Figure 2.5. Current treatment strategy in ovarian cancer is illustrated. HGSOC, high-grade serous ovarian cancer; LGSOC, low-grade serous ovarian cancer; mBRCA, breast cancer gene mutation; Source (Lheureux et al., 2015).

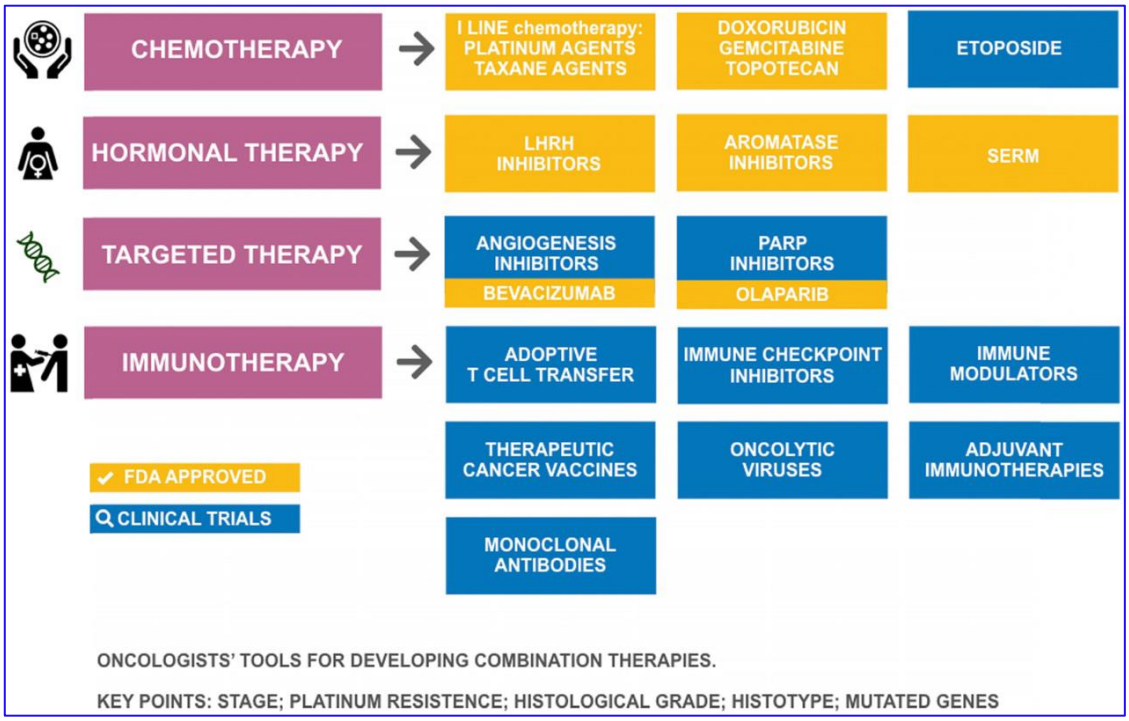

Figure 2.6. Tools in the pharmacologic arsenal for treatment of ovarian cancer. SERM: selective oestrogen receptor modulator; LHRH: Luteinizing-hormone-releasing hormone; PARP: poly (ADP-ribose) polymerase; Source (Di Lorenzo et al., 2018).

2.7. Currently available drugs, targeted pathways and their limitations

Bevacizumab, the most-studied anti-VEGF therapy that inhibits angiogenesis in the tumour microenvironment, holds great promise for ovarian cancer (OC) treatment. However, its efficacy is only modest due to redundant angiogenic pathways. Concurrently, there has been a surge in clinical trials with several drug candidates that precisely target signal enzymes to induce apoptosis and autophagy, focusing on inhibiting angiogenesis in site-specific OC cells.

Surgery and chemoradiotherapy are the most frequently used treatment options for ovarian cancer (OC). However, chemoradiotherapy is associated with severe side effects, and radiotherapy (RT) provides only minor therapeutic benefits, often resulting in poor survival outcomes. Therefore, targeting specific signalling pathways presents a promising molecular approach for OC therapy. This strategy aims to inhibit tumour growth, cell invasion, migration, and metastasis, offering a potentially more effective treatment with fewer side effects (Akter et al., 2022)

Enzastaurin (LY317615.HCl) is a radiosensitising, ATP-competitive, selective inhibitor of protein kinase C beta (PKC-beta). It inhibits tumour cell growth by upregulating the proapoptotic activity of caspase-9 and caspase-3. (I. Vergote, 2014; I. B. Vergote et al., 2013).

Resveratrol, a small polyphenol compound, increases apoptosis induction in ovarian cancer cells by activating it in an AMPK-dependent manner. It also activates caspase 3, leading to the inhibition of mTOR expression and activation, a downstream signalling target of AMPK. (Akter et al., 2022; Y. Liu et al., 2018).

Better prognosis in ovarian cancer (OC) has been associated with the identification of novel therapeutic targets. Recent advancements in understanding OC biology have led to the discovery of numerous molecular targets, such as growth factor receptors, cell cycle regulators, signal transduction pathways, and angiogenic mechanisms. These molecular targets offer promising avenues for therapy. Unlike conventional chemotherapy, molecularly targeted agents exhibit higher selectivity and lower toxicity, providing new hope for more effective and tolerable treatments for OC (Akter et al., 2022).

Trastuzumab (Herceptin), a targeted monoclonal antibody for ErbB2, is approved for treating ErbB2-positive breast cancer. However, according to the GOC study, trastuzumab has limited efficacy in ovarian cancer. Nonetheless, a partial but long-lasting response was observed when combination therapy with trastuzumab. Other receptor-binding inhibitors, such as cetuximab, have different mechanisms of action compared to tyrosine kinase inhibitors (TKIs) like gefitinib and erlotinib. (Akter et al., 2022; Wilken et al., 2010, J. Zhang et al., 2015).

The proteasome's activity presents a promising therapeutic avenue for cancer treatment. PS341 (bortezomib), a dipeptide boronic acid derivative, achieves this by reversibly inhibiting the 20S proteasome, thereby preventing protein degradation. Cyclins (CDKs) and IkB proteins, which act as corepressors of nuclear factor-kappa B (NF-κB) activation, emerge as potential targets. Inhibiting IkB degradation leads to reduced NF-κB transcription factor activity. Despite NF-kB's prominent antiapoptotic role, the use of PS-341 and NF-κB blockers tends to enhance chemotherapy-induced apoptosis (Akter et al., 2022).

Anticancer drugs targeting microtubules, such as taxanes and vinca alkaloids, have been longstanding first-line treatments for breast cancer and various other cancers, including ovarian, prostate, head and neck, and lung cancers. In phase III clinical trials, polyglutamated paclitaxel (CT2103), a cytotoxic agent, demonstrated superior treatment responses and fewer side effects compared to traditional paclitaxel. (Akter et al., 2022).

CA125 antigen has been utilized for over two decades in the US for screening high-risk women for ovarian cancer (OC). Initially used as a predictive marker in preinvasive OC, CA125, despite its limited sensitivity and specificity, is strongly associated with epithelial OC. Consequently, combining non-invasive immunotherapy with chemotherapy may represent a promising therapeutic strategy for improving survival outcomes in OC (Akter et al., 2022; Kurnit et al., 2021).

More than half (58%) of ovarian cancer (OC) patients are diagnosed at an advanced stage (III or IV), resulting in poor prognosis due to the lack of early detection. The standard treatment for advanced OC typically involves cytoreductive tumour surgery followed by chemotherapy and/or radiotherapy, regardless of tumour heterogeneity or hormone therapy options. However, chemotherapy resistance remains a significant

challenge in achieving a cure and favourable prognosis. The choice of treatment depends on various factors, including the cancer's molecular subtype, stemness, clinical stage, disease dynamics, and the patient's age and overall health. A range of chemotherapeutic agents is available for treating ovarian cancer, either alone or in combination. Platinum-based drugs (cisplatin and carboplatin). Unfortunately, these agents are associated with severe side effects, including sustained nausea and vomiting, hair loss, mouth sores, acute renal injury, ototoxicity, infertility, anaemia, leukopenia, thrombocytopenia, and long-term peripheral neuropathy. Additionally, chemotherapeutic agents suffer from poor bioavailability, high dose requirements, low therapeutic indices, and nonspecific targeting, leading to elevated toxicity in normal cells and drug resistance in cancer cells (Akter et al., 2022). Currently, only two targeted agents have received approval for the treatment of ovarian cancer from both the U.S. Food and Drug Administration and the European Medicines Agency (EMA). These are the polyadenosine diphosphate (ADP)-ribose polymerase (PARP) inhibitor, olaparib, and the antiangiogenic agent, bevacizumab, both approved for patients with advanced disease previously treated with chemotherapy. Additionally, first-line bevacizumab has been approved by the EMA for the treatment of ovarian cancer. In Europe, trabectedin, which inhibits DNA replication and transcription and induces DNA double-strand breaks and loss of homologous recombination repair, is also available for the treatment of patients with advanced ovarian cancer (Akter et al., 2022).

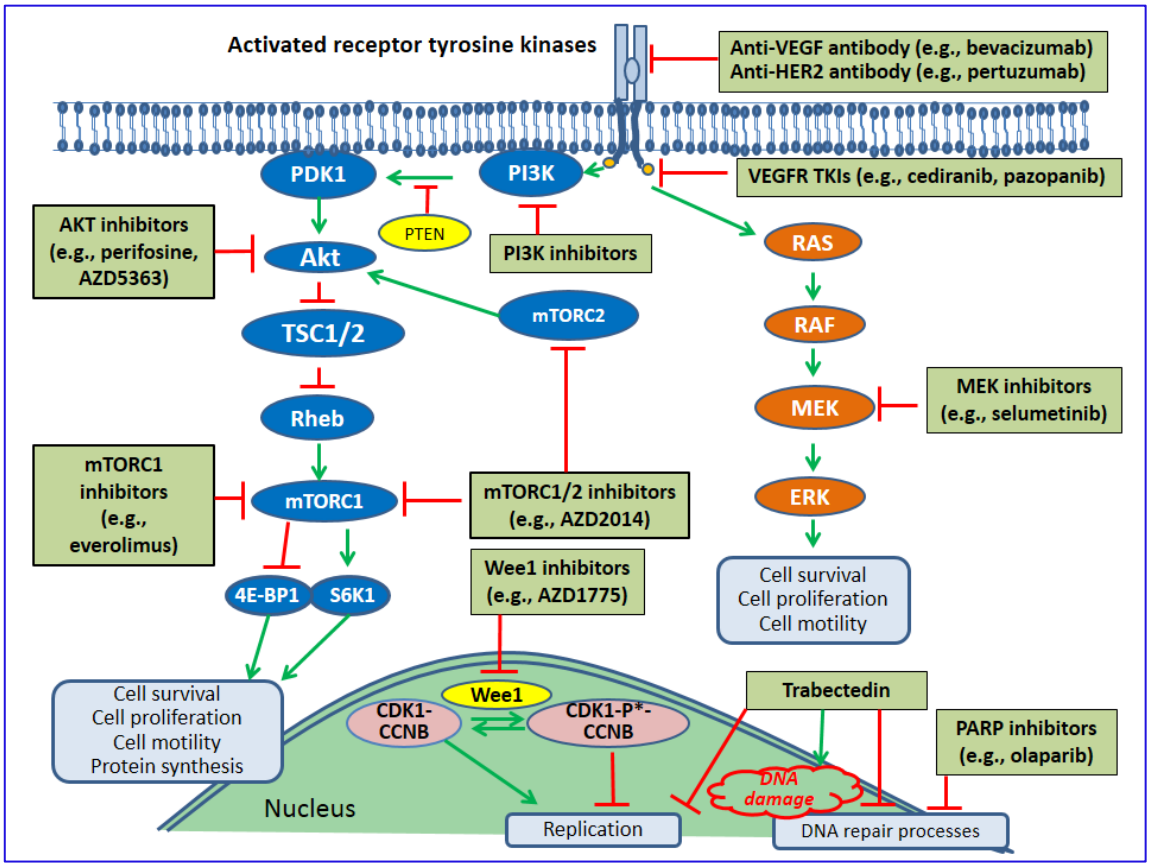

Figure 2.7. Multiple potential therapies targeting specific molecular alterations are currently under investigation for the treatment of ovarian cancer. Source: (Rojas et al., 2016)

2.8. Microbes and microbial products in cancer therapy

Microorganisms, ubiquitous in nature, wield remarkable therapeutic potential in the realm of anticancer therapies. The historical utilisation of bacteria in cancer treatment traces back centuries, with the observation of tumour regression in patients with gas gangrene after infection by *C. Perfringens* in 1813 marking a significant milestone. This paved the way for subsequent exploration, wherein wild-type *Clostridium perfringens* was detected in cancer patients in the early 19th century. Subsequent experiments injected live anaerobic bacteria into animal models, probing their oncolytic effects. A pivotal figure in this narrative is Dr. William Coley (1862-1936), a bone sarcoma surgeon at New York Cancer Hospital. Dr. Coley's systematic experimental therapy, initiated nearly a century ago, showcased the remarkable potential of bacterial infection

in tumour regression. He meticulously documented nearly 47 cases wherein bacterial infection exhibited beneficial effects in tumorigenesis. Notably, the administration of *Streptococcus pyogenes* led to significant tumour regression in a patient with inoperable bone sarcoma (McCarthy, n.d.; Trivanović et al., 2021). Over the following four decades, Dr. Coley explored various microbial mixtures, such as heat-killed streptococcal organisms combined with *Serratia marsceacens*, each demonstrating varying effectiveness. These mixtures functioned akin to vaccines, stimulating patient immunity by leveraging bacterial components as antigens, collectively termed Coley's toxin. The widespread application of Coley's toxin in cancer treatment during this period yielded promising outcomes, with over a quarter of patients experiencing cure. These limitations often curtail the application of such approaches in cancer treatment due to the unpredictable efficacy, heightened immune response, and associated side effects and toxicities. Despite these challenges, the relentless pursuit of new alternative anticancer therapies with enhanced selective toxicity persists, aiming to transcend conventional chemotherapies and propel the frontier of cancer research and therapeutics forward for the betterment of patient outcomes (Chakrabarty et al., 2014; Zahaf & Schmidt, 2017).

Bacterial toxins have emerged as potent agents in the fight against cancer, demonstrating significant success in various studies (Nag et al., 2024). These toxins possess the ability to modulate fundamental cellular processes crucial to cancer progression, including the regulation of cell proliferation, apoptosis, and differentiation, ultimately culminating in cell death. Notably, these cellular alterations are intricately linked with the intricate pathways of carcinogenesis. In the contemporary landscape of cancer treatment, while conventional therapies abound, their efficacy is often overshadowed by the burden of side effects. Consequently, there is a concerted effort to explore alternative targets for cancer therapy. In this pursuit, bacterial enzymes have emerged as promising candidates, offering novel avenues for combating cancer with potentially fewer adverse effects (Craik et al., 2011; Nag et al., 2024). In the context of cancer therapy, it is imperative to delve into the realm of microbial enzymes and their pivotal roles, elucidating the major molecular mechanisms that render them valuable in cancer biology. Understanding the collective knowledge surrounding the use of various microbial enzymes in anticancer therapy can pave the way for the development of effective strategies for prevention, treatment, and management (Chakrabarty et al., 2014; Zahaf & Schmidt, 2017).

2.9. Microbial enzymes as cancer therapeutics

Microbial enzymes have diverse applications as anti-cancer agents. The hallmark of cancer cells is their uncontrolled proliferation and rapid growth, which necessitates metabolic reprogramming to meet their increased nutrient demands (Vachher et al., 2021). Consequently, cancer cells often depend on normal cells for certain nutrients, primarily amino acids, making them auxotrophic. In contrast, normal cells have lower amino acid requirements (Cantor et al., 2012). This difference in amino acid needs creates a metabolic vulnerability in cancer cells, providing a rationale for amino acid depletion therapy (AADT) (Tabe et al., 2019). Microbial enzymes that degrade amino acids are particularly useful in AADT due to their ready availability, high productivity, and ease of manipulation. However, being foreign proteins, these enzymes can be unstable and may elicit an immune response. To improve the pharmacokinetic properties of these anticancer enzymes, various strategies such as genetic manipulation, encapsulation, and the creation of fusion proteins need to be developed before their administration to cancer patients. Therefore, a deep understanding of cancer cell metabolism can help define novel therapeutic approaches to inhibit tumour growth (Vachher et al., 2021).

Microbial enzymes with anti-cancerous potential.

Enzyme	Class	Producer microorganism	Mechanism of action	Targeted cancers
Asparaginase	Hydrolase	*Escherichia coli*, *Erwinia chrysanthemi*	Hydrolysis of L-asparagine into ammonia and aspartate	Acute Lymphoblastic Leukemia, T cell lymphoma, ovarian carcinoma, lymphosarcoma
Arginine deiminase	Hydrolase	*Mycoplasma arginini*, *Mycoplasma homininis*	Hydrolysis of L-arginine into ammonia and citrulline	Hepatocellular carcinoma, melanoma, plural mesothelioma, Hodgkin's lymphoma, prostrate, renal, breast cancer
Methioninase	Lyase	*Clostridium sporogenes*, *Pseudomonas putida*	The α,γ elimination reaction of L-methionine to α-ketobutyrate, ammonia and methanethiol	Melanoma, Walker 256 carcinoma, glioma, kidney, prostate, bladder, colon cancer
Lysine oxidase	Oxido-reductase	*Trichoderma viride*	Oxidative deamination of L-lysine into α –keto-E-amnocaproic acid, hydrogen peroxide and ammonia	Intracranial gliomas, colorectal cancer, Human tumor xenografts
Glutaminase	Hydrolase	*Bacillus cereus*, *Achromobacter* sp, *Aeromonas veroni*	Hydrolysis of L-glutamine to glutamate and ammonia	Hela cells, Hepatocellular carcinoma cells (HepG2), Acute lymphocytic leukemia
Phenylalanine ammonia lyase	Lyase	*Rhodosporidium toruloides*	Transformation of L-phenylalanine to ammonia and *trans*-cinnamic acid	Leukemia, colorectal cancer

Table 2.1. Microbial enzymes with anti-cancer properties; Source (Vachher et al., 2021)

As biopharmaceuticals, enzymes offer several advantages, including high substrate specificity and affinity, efficient catalysis with reduced toxicity, and minimal side effects. Enzymatic catalysis allows the simultaneous conversion of multiple targets, including prodrugs, into the desired products, enabling the administration of smaller quantities of therapeutics (Yari et al., 2017). Microorganisms produce a vast array of enzymes due to their physiological, geographic, and genomic diversity. These microbial enzymes are increasingly utilised in the healthcare sector both as therapeutic and diagnostic agents. In 2019, the market size for microbial enzymes was estimated to be approximately 9.9 billion USD and is projected to grow at a compound annual growth rate (CAGR) of 7.1% from 2020 to 2027 (Enzymes Market Size, Share & Trends Analysis Report by Application, 2020). Microbial enzymes are highly valuable as therapeutic agents because they are economical, consistent, and easy to isolate. The primary advantage of microbial enzyme production is the ability to achieve high yields on inexpensive media in a short time. Additionally, techniques such as fusion proteins, PEGylation, point mutations, nanocarrier encapsulation, and other genetic manipulation methods can be employed to enhance the efficiency and ensure a standardized supply of enzymes through microbial fermentation (Taipa et al., 2019). Globally, scientists are increasingly recognising the broad potential of various microbial enzymes in therapeutics and biopharmaceuticals, leading to a rapid rise in the application of these enzymes as curative agents (Taipa et al., 2019; UmaMaheswari et al., 2016).

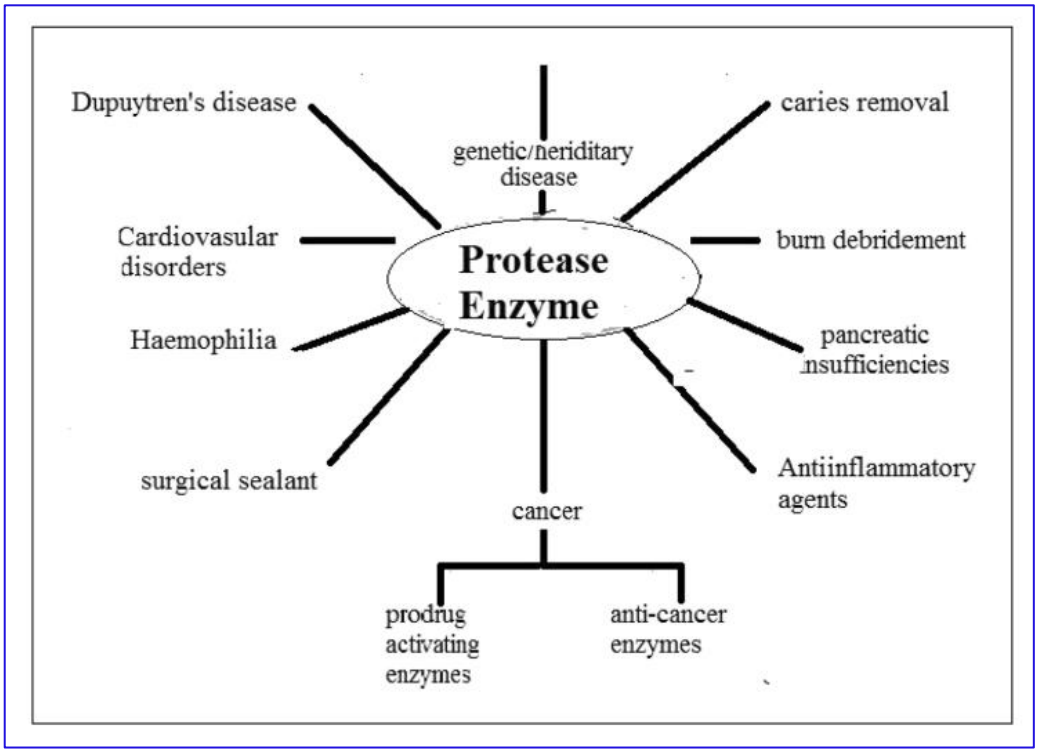

Figure 2.8. Major therapeutic aspect of proteases; Source (Shankar et al., 2021)

2.10. Microbial protease; the star player

One such key player is the protease, a ubiquitous enzyme known for its ability to catalyse the hydrolysis of peptide bonds in proteins. Proteases are widely distributed in nature, spanning microorganisms, animals, plants, and even viruses. This ubiquity underscores their significance as potential candidates for therapeutic intervention in cancer. Proteases, enzymes renowned for their ability to break down proteins, hold a paramount position due to their widespread applications in both physiological and commercial realms. Their significant industrial relevance is evidenced by their involvement in nearly 25% of the total global enzyme sales, with approximately two-thirds of commercially synthesized proteases originating from microbial sources. Protease production is a common trait across all living organisms, but it is primarily exploited commercially in microorganisms that produce one or more extracellular proteases. These versatile enzymes demonstrate the capability to degrade various biomolecules such as proteins, lipids, chitin, pectin, and starch. Operating at the forefront of physiological processes in both prokaryotes and eukaryotes, proteases present a formidable challenge for precise classification due to their immense diversity. Their classification defies simple categorization based on traditional enzyme

nomenclature rules or evolutionary relatedness grounded in amino acid sequences (Razzaq et al., 2019; Shankar et al., 2021).

Delving deeper into their classification reveals six distinct types, delineated by the nature of the functional group involved in catalytic reactions. These types include metalloproteases, serine proteases, aspartic proteases, cysteine proteases, threonine proteases, and glutamic proteases. However, among these, the first three types undergo extensive study, reflecting their prominence and significance in various biological processes. Further classification of proteases is based on their site of action on the substrate, dividing them into endo and exopeptidases. These enzymes catalyse the cleavage of polypeptides at distinct sites. Endopeptidases target peptide bonds located internally within the peptide, proximal to both the amino and carboxyl terminal ends. Conversely, exopeptidases cleave peptide bonds close to the amino and carboxyl termini of polypeptide chains. Among exopeptidases, those acting on the amino termini are termed aminopeptidases, while those targeting the carboxyl termini are referred to as carboxypeptidases. Another classification criterion, rooted in amino acid sequence, enables the categorization of proteases into different families and subsequently into distinct "clans," grouping proteases that have evolved divergently from a common ancestor. Additionally, enzymes exhibit variations in their pH optima, a significant determinant of enzyme activity. This discrepancy in pH optima serves as another basis for classification, with proteases classified as acidic, alkaline, or neutral based on their optimal pH conditions (Rao et al., 1998; Tapader et al., 2018, 2019).

Microbial extracellular secreted proteases serve as potent virulence factors (VFs) implicated in the pathogenesis of various pathogenic microorganisms, contributing significantly to disease progression. Their roles in aiding pathogens to infiltrate host tissues, target a plethora of extracellular and intracellular host molecules, and circumvent host defence mechanisms are well-documented. Proteases represent a rapidly growing class of drugs with significant potential. The U.S. Food and Drug Administration has already approved 12 protease-based therapies, and numerous next-generation or entirely novel proteases are currently in clinical development. Consequently, proteases have a promising future as a distinct therapeutic category with a wide range of clinical applications (Rao et al., 1998; Tapader et al., 2019).

2.11. Microbial proteases can be classified into several categories

i. Proteases that hydrolyse specific proteins, such as collagenase, elastase, and keratinase.

ii. Proteases similar to well-known proteolytic enzymes, including chymotrypsin, trypsin, and pepsin.

iii. Proteases active across different pH ranges, such as alkaline, acid, or neutral proteases.

iv. Proteases are categorised by their catalytic mechanisms, involving specific amino acid residues at their active sites, such as aspartic proteases, cysteine proteases, metalloproteases, and serine proteases (Rao et al., 1998).

v. Proteases classified by their hydrolysis site specificity: endopeptidases, which act internally within polypeptide chains, and exopeptidases, which act near the termini of polypeptide chains. Various subtypes of endopeptidases and exopeptidases have been identified by the Enzyme Commission (EC).

According to the Nomenclature Committee of the International Union of Biochemistry and Molecular Biology (1992), proteases are categorized under subgroup 4 of group 3 (hydrolase).

Researchers have successfully produced proteases from various microbial sources, accounting for two-thirds of the global commercial protease market (Beg and Gupta, 2003). Since the advent of enzymology, microbial proteolytic proteases have been the most widely studied enzymes due to their vital role in metabolic activities and their extensive industrial applications (Rao et al., 1998; Sandhya et al., 2005; Younes and Rinaudo, 2015). Microbial proteases are preferred in the market because of their high yield, low time and space requirements, ease of genetic manipulation, and cost-effectiveness (Razzaq et al., 2019). These characteristics make them more suitable for biotechnological applications compared to plant and animal proteases (Razzaq et al., 2019).

Proteolytic enzymes from microbes and mammalian systems are typically small, dense, and structurally spherical (Oberoi et al., 2001). Microbial proteases are extensively utilized across various industrial sectors. These extracellular alkaline proteases are secreted into the liquid broth from which they are extracted and purified through

downstream processes to produce the final product. Microbial proteases are less labour-intensive to produce than plant and animal proteases.

Bacillus subtilis, being non-pathogenic and capable of producing extracellular proteins, is a promising host for the production of recombinant protease enzymes. *B.subtilis* secretes industrially important proteases, such as subtilisin (apr) and metalloproteases (npr). Bacillus spp. are among the most widely utilized microbes for protease production, making them a key player in the commercial exploitation of proteases. Proteases are increasingly recognised as eco-friendly alternatives to chemicals, serving as valuable indicators for environmental health and sustainability (Razzaq et al., 2019). The study of the biochemical and molecular aspects of proteolytic systems, such as proteases, is increasingly attracting researchers' attention for several reasons. The commercial value of robust and novel bacterial enzymes is becoming more evident, driving researchers and engineers to seek out these enzymes. In the future, protein engineering will be crucial in developing proteases with new properties. Among these, alkaline bacterial proteases are particularly important for various industries, and their use is expected to grow. Therefore, researchers are adopting advanced strategies like protein/genetic engineering, molecular biology, and computational biology to create improved protease-producing strains. By inducing *in vitro* evolutionary changes in protein primary structures, bacterial strains with desirable traits can be developed. A major goal for scientists is to achieve bacterial proteases with enhanced characteristics such as improved yield, altered substrate specificity, increased thermal stability, adjusted optimal pH, and prevention of auto-proteolytic inactivation (Razzaq et al., 2019; Tapader et al., 2019; Vachher et al., 2021).

2.12. Metalloprotease

Metalloproteases are categorized based on their specificity and action into four groups: neutral, alkaline, Myxobacter I, and Myxobacter II. Neutral proteases exhibit specificity for hydrophobic acids and are inhibited by chelating agents like EDTA. Among protease types, metalloproteases show the greatest diversity. For instance, thermolysin, a well-studied neutral protease produced by *B. stearothermophilus*, lacks disulfide bridges in its single peptide structure. With a molecular weight of 34 kDa, thermolysin contains an essential Zn atom and four Ca atoms embedded between its two folded lobes, which

impart thermotolerance. This neutral protease is highly stable, with a half-life of 1 hour at 80ºC (Razzaq et al., 2019; Song et al., 2023; Vachher et al., 2021). Metalloproteases (classified as 3.4.17) active sites contain metal ions.

2.13. Therapeutic applications of microbial proteases

Over recent decades, the therapeutic application of proteases has yielded promising clinical outcomes, indicating a promising trajectory for their expanded utilization. When administered in their active state, proteases typically exhibit a biological half-life measured in minutes, which can be extended by several hours through various methods. Protease engineering has proven successful in modifying their properties and will continue to be utilised for this purpose. Moreover, the therapeutic advantages of protease drugs need not be limited to their primary proteolytic functions; they can be employed in contexts where their involvement is unconventional. Notably, proteases can be co-administered with conventional small molecule therapies and formulated alongside other proteins without compromising their integrity prior to patient administration. Given the pivotal roles of proteases in both normal physiology and disease processes, there exists a wide array of opportunities to harness their potential for therapeutic applications.

Didemnin B from *Tridemnum solidum*, one of the earliest anti-cancer drugs of marine origin, entered clinical studies (Xu et al., 2012). Similarly, Azurin from *Pseudomonas aeruginosa* and MakA from *Vibrio cholerae* have shown promising anticancer effects (Punj et al., 2004; Toh et al., 2022, Nadeem et al., 2021). Microbial proteases contribute to cancer therapy through various mechanisms, including the inactivation of antimicrobial peptides, disruption of the defensive mucosal barrier, and induction of apoptosis in target cells (Nag et al., 2024). For example, a protease obtained from *Serratia mercescens kums* 3958 induced significant tumour regression when injected into solid tumours in BALB/c mice (Maeda et al., n.d.). Previously, bacterial subtilisin, a serine protease, was reported to potentiate apoptosis via the ubiquitin-mediated tubulin degradation pathway in breast cancer cells (Singh et al., 2022).

Some important therapeutic enzymes and their applications	
Enzyme	Application
L-Asparaginase	Anti-tumour
L-glutaminase	Anti-tumour
Serratiopeptidase	Anti-inflammatory
Collagenase	Skin ulcers
Lipases	Digest lipids
Streptokinase	Anticoagulant
Urokinase	Anti-coagulant
Laccase	Detoxifier
L-Arginase	Anti-tumour
L-Tyrosinase	Anti-tumour
Ribonuclease	Anti-viral

Table 2.2. Some important therapeutic enzymes and their application; Source (Shankar et al., 2021)

L-asparaginase (ASNase), a clinically important microbial enzyme isolated from various environmental sources, has shown promising outcomes in cancer therapy (Alrumman et al., 2019; Vimal & Kumar, 2017). Studies on extracellular metalloprotease arazyme from *Serratia proteamaculans* suggested its effectiveness in inhibiting metastatic murine melanoma via MMP-8 cross-reactive antibody stimulation (Pereira et al., 2014). These findings provide insights into the cytotoxic mechanisms of action of microbial proteases on cancer cells. While the use of microbial proteases in cancer therapy remains relatively underexplored, noteworthy observations date back over 30 years. A protease isolated from *Serratia marcescens* kums 3958, exhibited remarkable tumour regression potential *in vivo*. This protease demonstrated potent antitumor activity upon injection into tumours in BALB/c mice (Maeda et al., 1987). Similar *in vivo* tumour regression outcomes were observed with subtilisin from *Bacillus subtilis* and thermolysin from *Bacillus stearothermophilus*. These studies shed light on a potential mechanism underlying the cytotoxic action of proteases: α2M receptor-mediated endocytosis of the protease complex, followed by the destruction of cellular integrity post-regeneration of proteolytic activity (Maeda et al., n.d.). Moreover, investigations into the purified hemagglutinin protease (HAP) from *Vibrio cholerae*, lacking the cholera toxin gene, revealed a noteworthy cell-distending effect on cervical cancer cell lines. Treatment with the 35 kDa purified protease and active 45 kDa form

of HAP induced cellular morphological changes, including cell distention and rounding, in Hela cells in a time- and dose-dependent manner. Notably, these effects were effectively inhibited by EDTA, a metal ion chelator and inhibitor of metalloproteases like HAP (A. Ghosh et al., 2006). Compelling evidence supporting the efficacy of bacterial protease in cancer cell eradication stems from the analysis of the effects of HAP purified from the culture supernatant of *Vibrio cholerae* C6709 in Swiss albino mice. Notably, a mere one microgram of purified HAP has been shown to exert a potent antitumor effect when administered via injection into Ehrlich ascites carcinoma (EAC) tumours in an *in vivo* model (Ray et al., 2016; Ray & Pal, 2016). Further evidence of protease-induced apoptosis comes from a subtilisin-like putative serine protease, F5, derived from the Tiger Milk mushroom *(Lignosus rhinocerus)* sclerotium. This protease exhibited apoptotic effects against MCF7 breast cancer cells *in vitro*, with activation of both caspase 8 and 9 (Yap et al., 2018). Similarly, a serine protease CMP with anti-cell proliferating activity was purified from the *Cordyceps militaris*. CMP displayed strong cytotoxic effects against MCF7, 5637, and A549 cells (Park et al., 2009). Studies conducted with secreted proteases from Actinomycetes spp. Isolated from natural environmental soil samples revealed their potent cytotoxic effects on human lung adenocarcinoma cells (Balachandran et al., 2012).

2.14. Apoptosis

Apoptosis is a crucial physiological process of cell death that occurs without releasing intracellular contents, thereby avoiding the activation of an inflammatory response. This process is vital for embryonic development, immune system regulation, and response to DNA damage. However, dysregulation of apoptosis can have significant consequences, including carcinogenesis. An imbalance between cell proliferation and cell death is a hallmark of malignant tumours. Thus, maintaining cellular homeostasis between proliferation and cell death is essential for normal physiological processes. Apoptosis has been extensively studied over the last two decades and is now recognized as a critical process of controlled cell death activated in response to cell injury and during normal development and morphogenesis. For example, the apoptotic death of nearly half of newly produced peripheral neurons during formation helps regulate their quantity to match the needs of target organs in the periphery. The induction of apoptosis

is essential for embryonic development and differentiation in complex organisms. It occurs in a controlled manner, characterized by morphological markers such as cell shrinkage, chromatin condensation, and blebbing of the cytoplasmic membrane. Dysregulation of apoptosis is linked to various pathologies, including tumour growth and the development of chemoresistance in cancer cells (Gorski and Marra, 2002). In mammals, apoptosis is triggered by two well-known pathways. Extrinsic signals, such as tumour necrosis factor (TNF), Fas (CD95/APO1), and TNF-related apoptosis-inducing ligand receptors (TRAIL), can induce apoptosis. Internal stimuli, including mitochondrial transduction, can also trigger apoptosis. For example, the activation of cysteine aspartyl proteases (caspases) leads to the permeabilization of mitochondrial membranes, chromatin condensation, and DNA fragmentation, resulting in cell death (Chaudhry et al., 2022; Zo, n.d.).

2.15. Chemotherapeutic drugs target apoptosis

The signalling molecules involved in the apoptotic pathway play a key role in regulating apoptosis. These molecular proteins are potential biomarkers for advanced cancer treatment and therapeutics. The development of these biomarkers has led to the emergence of targeted therapy as a more effective cancer treatment compared to conventional methods. Standard chemotherapies affect both normal and cancerous rapidly dividing cells, whereas targeted therapies act on specific molecular targets related to particular cancers. Many targeted apoptotic biomarkers are currently in clinical trials. Targeted therapies are designed to interact specifically with their targets, while many standard chemotherapies were identified for their ability to kill cells. Targeted therapies are often cytostatic, blocking tumour cell proliferation, whereas standard chemotherapy agents are cytotoxic, killing tumour cells. Therefore, combining apoptotic biomarkers with chemotherapy could enhance the efficacy of cancer treatment. Further complicating the analysis of cell death is the fact that apoptosis is a common response to cell stress. Not only can drugs induce an apoptotic response, but so can disturbances in cell physiology caused by the loss of gene expression, overexpression of genes, or expression of mutant genes. For example, the oncogene c-myc can stimulate apoptosis when it is overexpressed or when its expression is suddenly

reduced. Although the regulation of apoptosis is not an intrinsic function of most drugs and genes, if the goal of a drug is to cause cancer cell death, its ability to induce cell suicide indirectly might be just as important as its direct cytotoxic activity. Anti-cancer treatments primarily aim to kill cancer cells and may or may not cause side effects to healthy cells. Currently accepted cancer therapies include a combination of medications, surgery, radiation, or a combination of these methods. Chemotherapeutic drugs can relieve symptoms, extend life, and even cure cancer in some cases. The best cancer drugs have a low risk of harming healthy cells during treatment. Apoptosis significantly impacts the lifespan of healthy cells and the prognosis of malignant cells. Therefore, regulating apoptosis could benefit cancer treatment and prevention. The aberrant response of malignant cells to apoptosis induction is often caused by excessive cellular proliferation, which can involve the overexpression of inhibitors or members of the IAP family. Cancer cells also have inactivated cell cycle-regulating genes, and Bcl-2 expression is adjusted in tumours. Various malignancies, inflammatory diseases, viral infections, and autoimmune diseases are linked to inhibited or suppressed apoptosis (Chaudhry et al., 2022).

Interestingly, inducing apoptosis has emerged as a target for novel mechanism-based drug discovery. Previously, increased cellular proliferation was thought to be solely due to an accumulation of cells, but it is now understood that decreased cell death also contributes to cell proliferation. Therefore, it is crucial to screen apoptotic inducers from natural products, whether as crude extracts (from plants or marine organisms) or as isolated components. Various studies have shown that compounds derived from natural sources can effectively treat and prevent cancer. Isolated secondary metabolites from multiple natural sources and mechanistic in-vitro studies provide better molecular understanding for future therapeutic agents. Different plant extracts, fractions, synthetic palladium, and other complexes are used to screen for cytotoxicity and modes of cell death, reducing the cost of isolating phytochemicals and synthetic compounds while providing insights into potential therapeutic agents. The ability to trigger apoptosis may serve as a unifying principle for various chemopreventive drugs, each with a unique mode of action. Understanding these mechanisms could lead to new strategies for cancer prevention and treatment (Carneiro & El-Deiry, 2020; Chaudhry et al., 2022; Zo, n.d.).

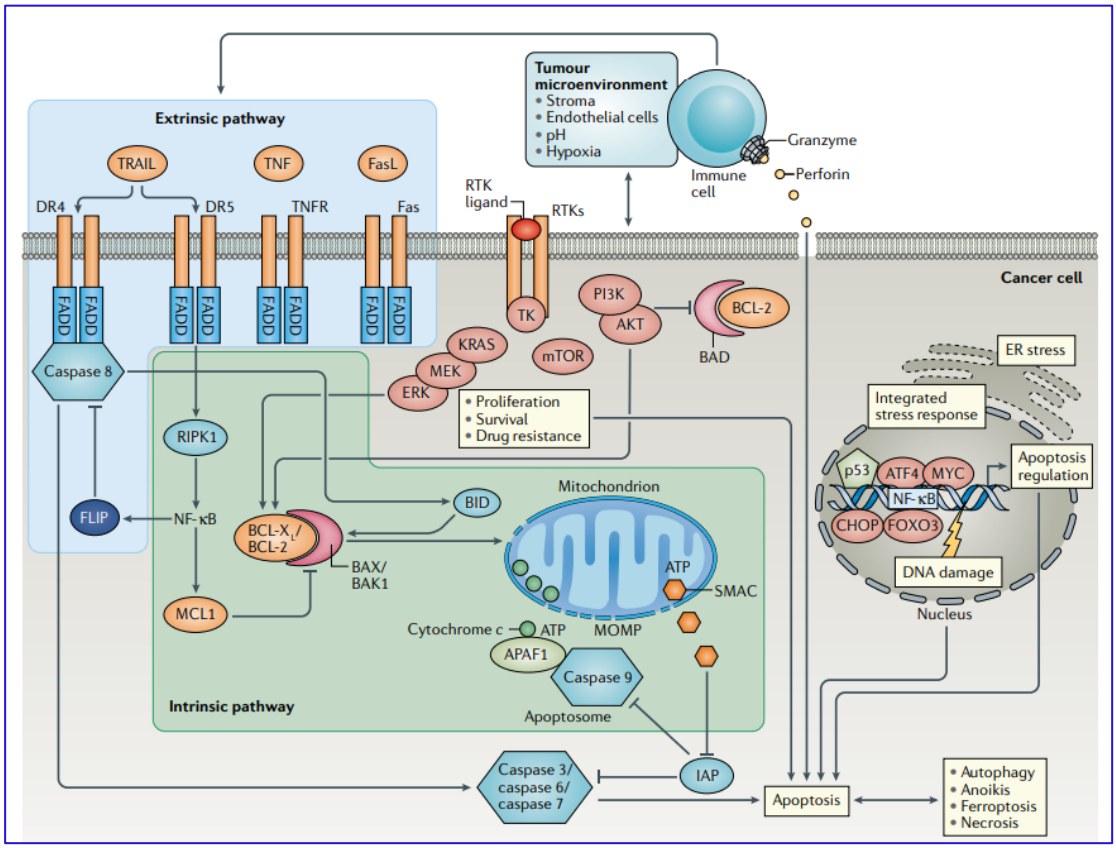

Figure 2.9. Overview of apoptosis signalling pathways and the effects of pro-survival signalling, immune cells and the tumour microenvironment. Source (Carneiro & El-Deiry, 2020)**.**

2.16. Protease Activated Receptor (PAR)

A subset of proteases functions as signalling molecules, orchestrating cell functions through specific G-Protein Coupled Receptors (GPCRs) known as protease-activated receptors (PARs). These PARs serve as major signalling hubs, with their activation associated with the cleavage by proteases.

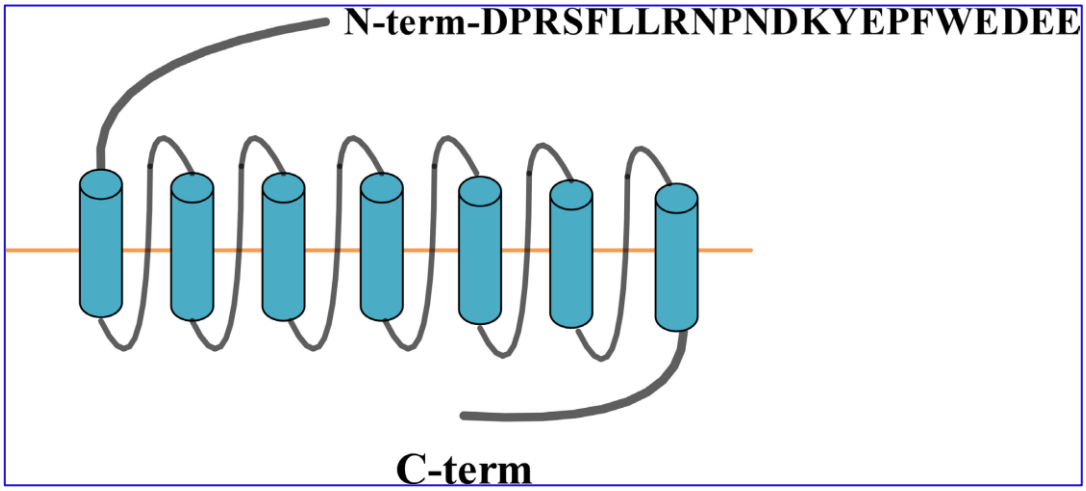

Figure 2.10. Diagrammatic representation of PAR-1; Source (X. Liu et al., 2017)

Comprising four distinct subtypes (PAR 1, PAR 2, PAR 3, and PAR 4), PARs are implicated in various cellular processes, including carcinogenesis and apoptosis, depending on the stimuli. Studies have indicated that the expression of PARs is generally higher in malignant cells compared to normal healthy cells (X. Liu et al., 2017).

2.17. Physiological activity of PAR-1 and its role in cancer

PAR-1, in particular, demonstrates a nuanced role in apoptosis induction, with its effects contingent upon the dosage of thrombin or other physiological agonists. PAR-1-mediated effects encompass apoptosis induction in neuronal, endothelial, and epithelial cells, fibroblasts, as well as tumour cells. Histological and biochemical analyses have unveiled a differential expression pattern of PAR-1 in ovarian carcinoma tissue samples. Malignant ovarian tissues exhibit elevated levels of PAR-1 at both transcriptional and translational levels, whereas negligible to absent expression is observed in normal

ovarian surface epithelium. Similarly, increased PAR-1 protein expression has been reported in breast carcinoma biopsies. Notably, inhibition of PAR-1 via antisense cDNA has been shown to impede the invasion of metastatic breast cancer cells in culture through the basement membrane (Boire et al., 2005; Kamath et al., n.d.). PAR-1 has garnered attention as a promising oncogenic target due to its involvement in the invasive and metastatic processes of various cancers, including those of the ovaries, breast, colon, lung, prostate, and melanoma. Typically activated by serine proteases such as thrombin, factor Xa, and activated protein C, PAR-1 exerts its effects on apoptosis primarily in epithelial, endothelial, fibroblasts, and neuronal tumour cells. PARs, members of the G-protein coupled receptors family, are activated through irreversible proteolytic cleavage by various proteases. Upon activation, the activating protease binds to and cleaves the N-terminus of PAR-1, generating a new N-terminal domain known as the 'tethered ligand', which intramolecularly binds to initiate transmembrane signalling. Notably, a specific N-terminal peptide sequence of PAR-1 itself serves as the activation signal. Following protease cleavage, the N-terminal 41-amino-acid domain of PAR1 is released into the extracellular environment, with potential biological activity, although this remains contentious. Recent studies suggest that this released N-terminal region of PAR1, termed 'Parstatin', inhibits vascular endothelial cell growth factor (VEGF) and fibroblast growth factor-induced angiogenesis both in vitro and in vivo, regulating intracellular signalling events (Zania et al., 2009). Previous research has also indicated the effects of the released N-terminus of PAR1 at the platelet cell surface, influencing platelet function (Furman, Krueger, et al., 2000; Furman, Nurden, et al., 2000).

Interestingly, PAR-1's role in apoptosis modulation is context-dependent, with its activation either inducing or inhibiting apoptosis based on the dosage of its physiological agonist thrombin or synthetic receptor activators. Despite its classification as a proto-oncogene, PAR-1 expression levels are significantly elevated in cancer cells compared to normal healthy epithelial cells. The intriguing behaviour of PAR-1 in ovarian cancer, where it functions as a tumour suppressor gene, presents a paradox. While PAR-1 is typically implicated in promoting tumour metastasis, its activation with Peptidase M84 induces apoptotic signalling, facilitating tumour regression. This paradoxical phenomenon is not unique to PAR-1 and has been observed in other molecules implicated in tumorigenesis, including GM-CSF, RAR-β2, E-cadherin,

CD44, α/β-catenin, and CAV1. Despite these complexities, PAR-1 has emerged as a promising target for chemotherapeutic drugs, with compounds like vorapaxar and atopaxar advancing into clinical trials, marking it as a focal point of recent research endeavours (Soh et al., 2010)

Thrombin-mediated activation of PAR-1 regulates various signalling pathways, including the phosphatidylinositol 3-kinase (PI3K), protein kinase C, c-Jun N-terminal kinase (JNK), p38 MAPK, RhoGTPase, and NFκB. PARs play pivotal roles in haemostasis, thrombosis, and inflammation, and have been implicated in cancer progression, rendering them significant drug targets. Recent studies indicate that different agonists, including proteases and synthetic peptide ligands, induce distinct signalling responses through the activation of the same PAR. This phenomenon, known as 'functional selectivity' or 'biased agonism', is well-documented for GPCRs. Ligand activation of PARs likely induces conformational changes within the transmembrane helices, exposing receptor cytoplasmic surfaces crucial for interaction with the α subunits of heterotrimeric G proteins at the inner leaflet of the plasma membrane (Oldham and Hamm, 2007; 2008). Unlike most classic GPCRs, where ligand binding occurs in a pocket formed by the transmembrane helices, the activation of PARs is thought to occur through peptide ligand interactions with residues in the second extracellular loop (Gerszten et al., 1994). Recent high-resolution structures of various GPCRs reveal significant diversity in the second extracellular loops, ligand-binding pockets, and intracellular loops, indicating distinct mechanisms of GPCR activation and signal transduction (Oldham & Hamm, 2008).

Upon activation, GPCRs act as guanine nucleotide exchange factors, facilitating the exchange of GDP for GTP on the α subunit, leading to dissociation of the βγ subunit. Both the GTP-bound α subunit and βγ subunits signal to various effectors, promoting diverse cellular responses (Oldham and Hamm, 2007; 2008). PAR1 and PAR2, when activated, couple to multiple heterotrimeric G-protein subtypes, including Gi, Gq, and G12/13 (Coughlin, 2005; Russo et al., 2009b). PAR4 activates Gq and G12/13, while PAR3 was previously believed not to signal autonomously. However, recent studies indicate that thrombin activation of natively expressed PAR3 can elicit Rho- and Ca^{2+}-dependent release of ATP from lung epithelial A549 cells, a cell type seemingly devoid of PAR1 or PAR4 expression (Seminario-Vidal et al., 2009, Agarwal et al., 2008)).

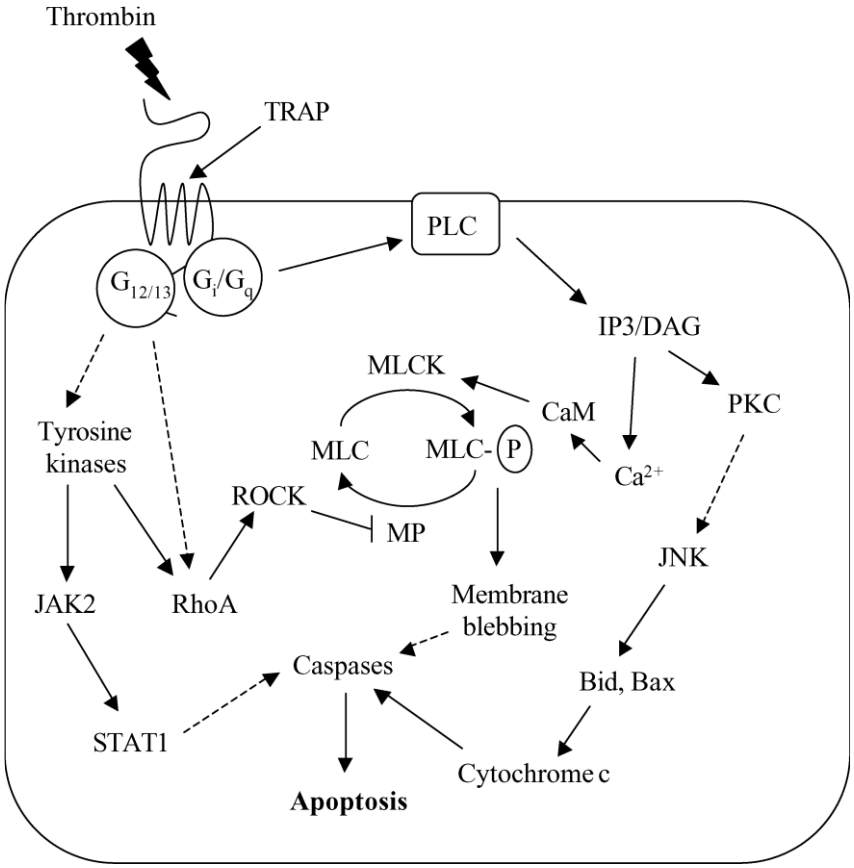

Figure 2.11. Putative signalling pathways involved in the pro-apoptotic response to PAR-1 activation. Sourced from (Flynn & Buret, 2004)

Dashed lines represent pathways for which the intermediates have not yet been identified. TRAP, thrombin receptor activating peptide; PLC, phospholipase C; IP3, inositol triphosphate; DAG, diacylglycerol; PKC, protein kinase C; CaM, calmodulin; MLCK, myosin light chain kinase; MLC, myosin light chain; MP; myosin light chain phosphatase; ROCK, Rho kinase; JAK2, Janus kinase 2; STAT1, signal transducer and activator of transcription 1.

2.18. Canonical Activation of PAR-1

When a protease acts on the receptor activator ligand, it irreversibly cleaves it within the canonical N-terminal domain site (Figure 2A). Subsequently, this cleaved ligand binds to the second extracellular loop of the receptor, triggering a conformational change that initiates signalling cascades. PAR1 is cleaved at its canonical site, LDPR41 # S42FLLRN, by thrombin. PAR2 is activated at its canonical cleavage site, SKGR34 # S35LIGKV, by trypsin (Song et al., 2023).

2.19. Non-canonical or Biased Activation

The concept of biased activation emerged, characterized by receptor stimulation at sites other than the canonical cleavage site, termed "non-canonical sites." Such biased activation leads to incomplete or different signalling compared to canonical activation, as proteases can activate PARs in this manner. The first instance of biased activation was described in PAR1 signalling. Researchers demonstrated that MMP1 activates PAR1 via an activator ligand located two amino acids upstream of the one generated by thrombin (PRSFLLR ligand), resulting in the same signalling as thrombin-induced activation. Conversely, another study showed biased PAR1 activation by activated protein C through a non-canonical site, yielding effects opposite to those induced by thrombin, such as anti-inflammatory effects and endothelial barrier protection. PAR1 can also undergo biased activation by various proteases and coagulation cascade components, including plasmin, factor X, granzymes A, trypsins, kallikreins, and cathepsin G (Song et al., 2023).

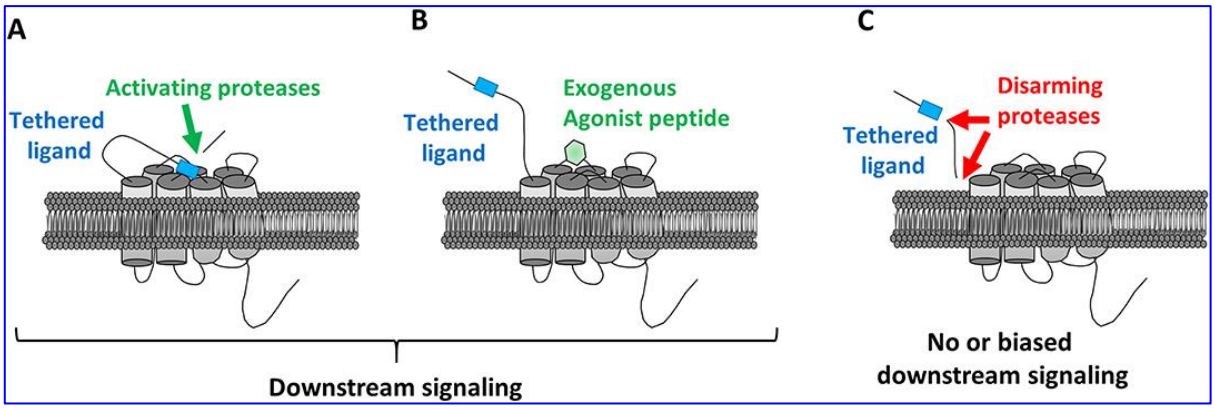

Figure 2.12. Mechanisms regulating PARs activation. Source (Song et al., 2023)

(A) Proteolytic cleavage by an activating protease resulting in the binding of the tethered ligand to the ECL2, and downstream signalling activation. (B) Binding of an exogenous synthetic agonist peptide on ECL2 without proteolytic cleavage inducing downstream signalling activation. (C) No or Biased activation by disarming proteases cleaving the N-terminal domain after the tethered ligand either inhibiting the signal transduction or inducing biased downstream signalling compared to the one induced par the activating

2.20. PAR-1; a hotspot target for cancer therapy

PAR-1, the pioneer member of the Protease-Activated Receptors (PARs) family, was simultaneously discovered by two independent laboratories in 1991. Its identification occurred during the quest to pinpoint GPCRs responsible for mediating the thrombin signalling pathway in both human and hamster cells. Thrombin-activated PAR-1 exhibits expression not only across various blood cell types but also in epithelial cells, neurons, astrocytes, and immune cells. Moreover, PAR-1 expression extends to cancer-associated fibroblasts, epithelial cells, blood vessel myocytes, mast cells, and macrophages within the tumour microenvironment. In macrophages, PAR-1 upregulates levels of numerous growth factors, including thrombin. Subsequent studies have increasingly delved into the role of PAR-1 in the biological functions of tumour cells, along with the exploration of PAR-1 agonists and inhibitors. PAR-1 has emerged as a prominent target for drug development, with compounds like vorapaxar and atopaxar advancing to phase 3 and phase 2 clinical trials, respectively. The evaluation of clinical efficacy in recent years has become a focal point of research, offering promising avenues for novel clinical treatment approaches (X. Liu et al., 2017).

In contrast to the tightly regulated and rapid control of PAR-1 activation in normal tissues, PAR-1 is constitutively activated in cancer cells. Thrombin initiates signalling pathways in tumour cells by engaging with PAR-1. The persistent stimulation of the second messenger ERK1/2 underlies most cellular responses to this activation. In a rat model of benign tumours, PAR-1-mediated suppression of pro-apoptotic genes resulted in tumour growth and invasion. Inhibition of PAR-1 activity effectively curtailed *in vivo* tumour growth, highlighting PAR-1's anti-apoptotic effects. This sustained activation of second messenger signalling enables PAR-1 to collaborate with growth factor receptors like EGFR and ErbB/Her2, or with MMP-1 derived from fibroblasts, to mediate the Ca^{2+} pathway in cancer. Additionally, both PAR-1 and MMP-1 independently upregulate Galectin-3. Furthermore, PAR-1 signalling interacts with the Hippo-YAP pathway to foster tumorigenesis (Flynn & Buret, 2004; Grisaru-Granovsky et al., 2005).

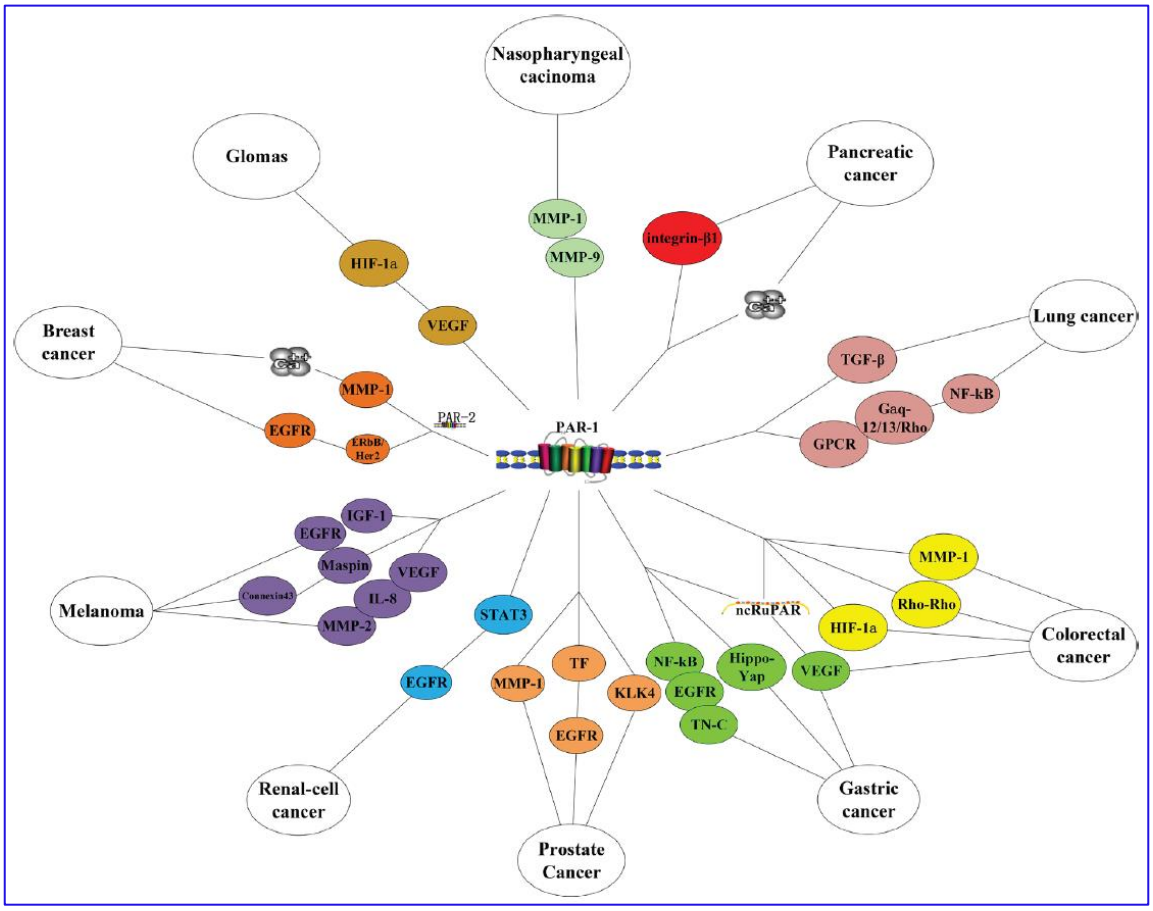

Figure 2.13. Involvement of PAR-1 in cancers; Source (X. Liu et al., 2017)**.**

PAR-1's involvement in cancer cell invasion and metastasis is notable. High PAR-1 expression is closely associated with an invasive phenotype and distant metastasis across multiple tumour cell lines. PAR-1 enhances cancer cell invasiveness by augmenting adhesion to the extracellular matrix. Upon thrombin/PAR-1 stimulation, various cancer cell lines exhibit increased adhesion to platelets, aorta, and capillaries. Prothrombin-induced HIF-1α upregulates torsion mRNA expression, with protein levels mediated by activated PAR-1, thereby EMT and tumour metastasis. Overexpression of NF-κB and EGFR can activate PAR-1 signalling, promoting tumour cell growth and invasion. Notably, in contrast to normal tissue, STAT3-dependent transactivation of EGFR and PAR-1 is significantly increased in endothelial cells of clear cell renal cell carcinoma. PAR-1 stimulates the Akt/PKB signalling pathway, leading to decreased expression of pro-apoptotic factors Bim and Bax, as well as lower cleavage levels of caspase-3 and caspase-9, thereby inducing less apoptosis. In summary, the findings outlined above demonstrate that PAR-1's promotion of tumour growth and metastasis is mediated through its regulation of adhesion and pro-angiogenic factors. This highlights

PAR-1 as a potential therapeutic target in cancer treatment. Experimental research suggests that PAR-1 inhibitors may effectively suppress tumour cell proliferation, diminish invasion and metastasis, and inhibit tumour angiogenesis. The development of drugs targeting PAR-1 has garnered considerable attention. Currently, vorapaxar (SCH530348) and atopaxar (E5555) represent two clinical formulations of PAR-1 inhibitors that have undergone extensive clinical development. Recent studies indicate that vorapaxar exhibits the potential to inhibit epithelial ovarian cancer (EOC) progression in ovarian cancer (Boire et al., 2005; X. Liu et al., 2017).

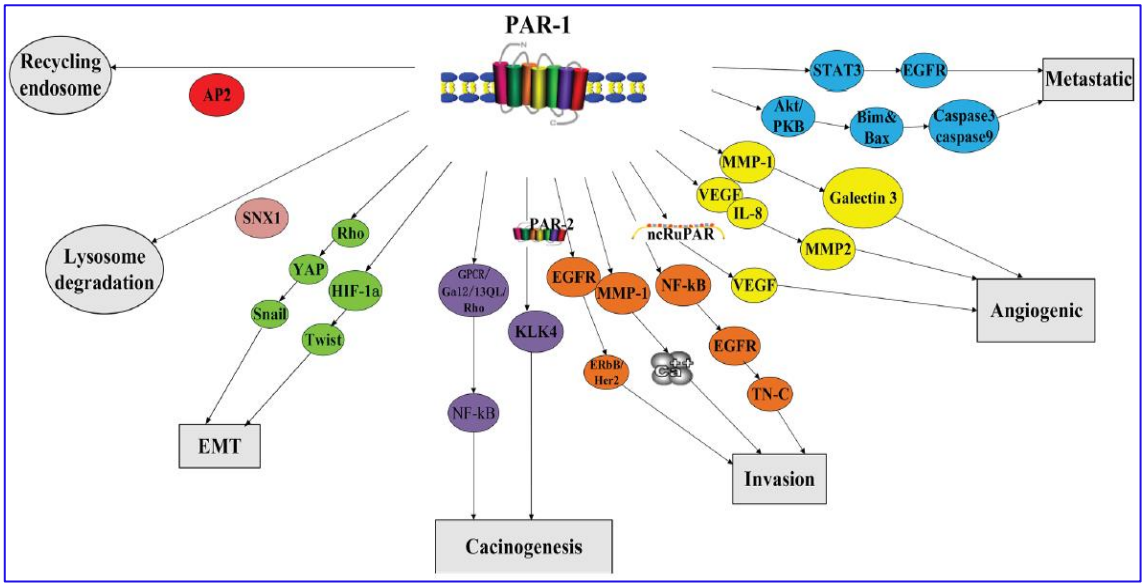

Figure 2.14. Major physiological functions of PAR-1; Source (X. Liu et al., 2017)**.**

2.21. Oxidative stress

Oxidative stress, characterized by an imbalance between reactive oxygen species (ROS) and antioxidants, has been associated with various health conditions such as neurodegenerative diseases, cardiovascular disorders, and diabetes mellitus (Sies, 2015). These connections underscore the importance of maintaining a delicate equilibrium between ROS and antioxidants. Cells have intricate biochemical and genetic mechanisms to uphold this balance, and any disruption to these mechanisms can lead to significant pathophysiological effects.

2.22. Redox balance in Cancer

While reactive oxygen species (ROS) and reactive nitrogen species (RNS) can initiate carcinogenesis, they also promote the proliferation of initiated cells during the promotion and progression stages of tumourigenesis. However, oxidative stress can induce senescence or cell death in neoplastic cells at all stages of tumorigenesis, including anchorage-independent growth and metastasis. It is well recognized that cancer cells commonly exhibit increased levels of glutathione (GSH) and thioredoxin (TXN) or thioredoxin reductase (TXNRD), presumably to counteract the high ROS burden, and this is often associated with poor prognosis (Benhar et al., 2016).

Compared to normal cells, cancer cells maintain higher levels of ROS, which sustains their phenotype. One could argue that all cytotoxic cancer drugs, whether directly or indirectly, induce oxidative stress. Nonetheless, a variety of drugs have been developed utilizing redox platforms to target various pathways. Depending on their concentration, reactive oxygen species (ROS) can have contrasting effects on cancer development. They may either trigger or promote tumorigenesis by facilitating the transformation and proliferation of cancer cells, or induce cell death. To cope with elevated ROS levels, tumour cells undergo alterations in sulphur-based metabolism, NADPH generation, and the activity of antioxidant transcription factors (Hayes et al., 2020).

During the initiation stage, genetic alterations enable cells to survive in the presence of high ROS levels by activating antioxidant transcription factors or increasing NADPH production through the pentose phosphate pathway (PPP). As cancer progresses and metastasises, tumour cells adapt to oxidative stress by enhancing NADPH production through various mechanisms, including the activation of AMPK, the PPP, and reductive glutamine and folate metabolism.

Cancer cells often experience disrupted redox balance, where reactive oxygen species (ROS) play a role in promoting tumour growth. However, high levels of ROS can also be toxic to cells. Tumour cells, despite producing elevated ROS during hyperproliferation, have adapted mechanisms to thrive under conditions where redox balance is shifted away from a reduced state. They achieve this by increasing their antioxidant defences to support ROS-driven proliferation while avoiding ROS levels that would trigger cellular senescence, apoptosis, or ferroptosis. The realignment of redox balance is crucial for how tumour cells tolerate high ROS levels. This review focuses on the biochemistry of key molecules involved in redox regulation, such as reduced glutathione (GSH), thioredoxins (TXN1 and TXN2), and NADPH. It examines the mechanisms that control their abundance under normal physiological conditions and during the various stages of cancer progression, including initiation, progression, metastasis, and post-therapy recurrence.

NF-kB represents a family of transcription factors composed of heterodimer or homodimer combinations of p50, p52, p65/RelA, RelB, and c-Rel subunits. These factors act as an inducible first-line defence against infection and other harmful agents (Perkins, 2007). While NF-kB coordinates an adaptive response to eliminate invading pathogens by inducing the expression of cytokines, chemokines, receptors, and tissue repair, it also regulates the expression of antioxidant genes (Morgan and Liu, 2011) Constitutive activation of NF-kB is commonly observed in many cancers. In this context, NF-kB promotes the survival, proliferation, and metastasis of tumour cells by upregulating the expression of anti-apoptotic genes, cyclins, matrix metalloproteinases (MMPs), cell adhesion molecules, and pro-angiogenic genes (Perkins, 2012). Additionally, it induces a metabolic shift to glycolysis and influences the tumour microenvironment by directing the pro-tumorigenic actions of immune cells.

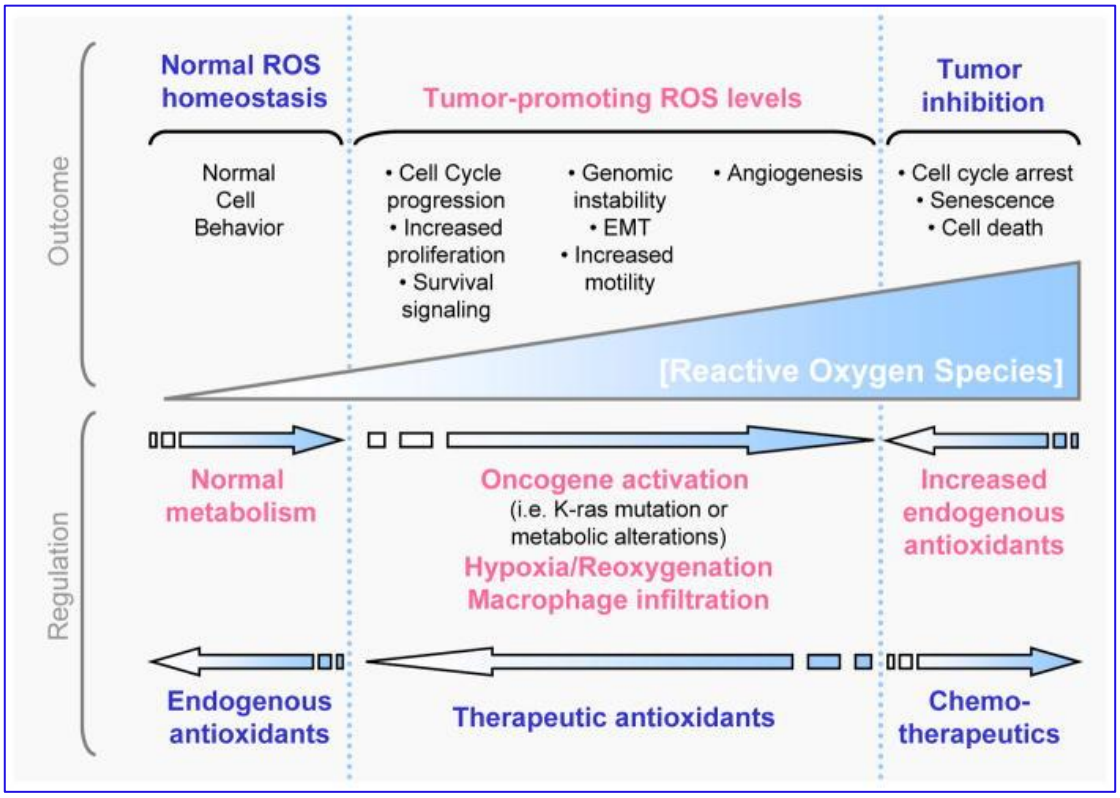

Figure 2.15. Role of oxidative stress in carcinogenesis; Source (Liou & Storz, 2010)

ROS-sensitive signalling pathways are consistently elevated in various types of cancers, where they play roles in cell growth, proliferation, differentiation, protein synthesis, glucose metabolism, cell survival, and inflammation. Among reactive oxygen species, hydrogen peroxide, in particular, functions as a second messenger in cellular signalling. H_2O_2 regulates protein activity by reversibly oxidizing its targets, including protein tyrosine phosphatases, protein tyrosine kinases, receptor tyrosine kinases, and transcription factors. In the following paragraphs, we delve into the ROS-mediated regulation of the mitogen-activated protein (MAP) kinase/Erk cascade, phosphoinositide-3-kinase (PI3K)/Akt-regulated signalling cascades, as well as the IκB kinase (IKK)/nuclear factor κ-B (NFκB)-activating pathways (Hayes et al., 2020).

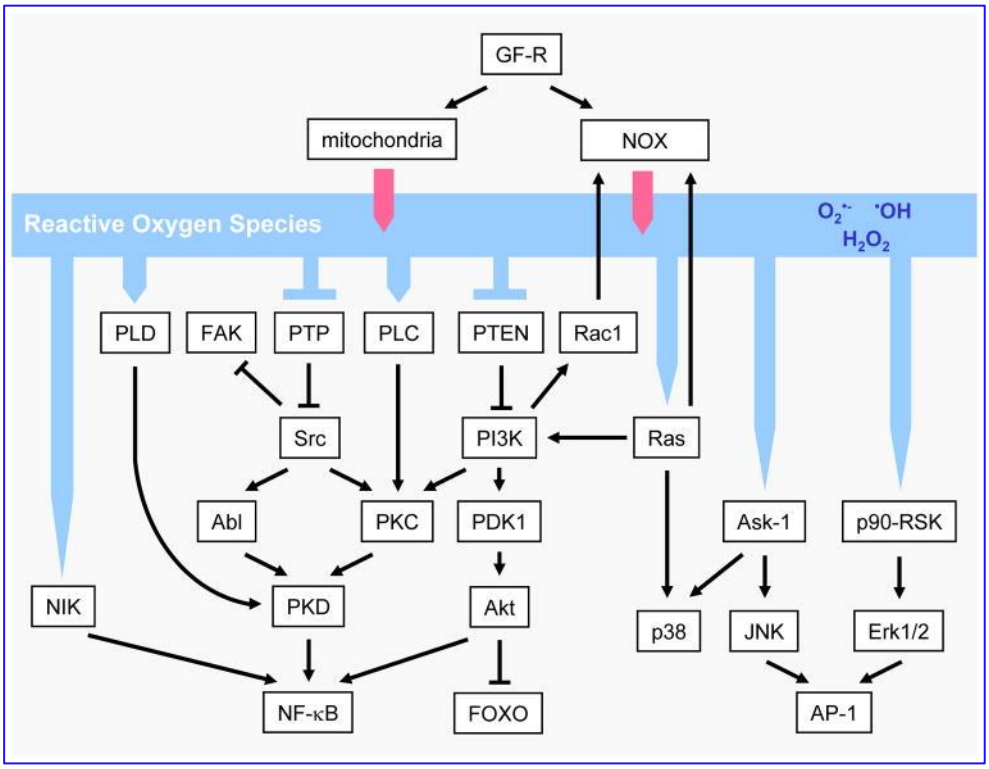

Figure 2.16. ROS-induced cellular signalling; Sourced from (Liou & Storz, 2010)

2.23. Preclinical ovarian cancer models

Future high-quality translational research on EOC is expected to focus on improving the understanding of disease biology, identifying correlates of response and resistance to therapy, and providing new targeted cancer therapies. The ultimate goal is to develop more effective methods for detecting and treating this lethal disease. Proper selection of preclinical models and careful study design are essential for achieving these ambitious objectives and making preclinical data translatable to clinical practice.

In EOC studies, three species are most commonly used: mouse, rat, and laying hen. The laying hen is distinctive as the only model that allows observation of early events in disease progression, making it well-suited for chemoprevention studies. In contrast, rodent models are the gold standard for studying tumour growth and response to drug compounds, despite limitations such as ethical controversies, species-specific differences between animals and humans, low-throughput drug optimization, and high

costs. The most widely used rodent models in EOC research include xenograft, syngeneic, and genetically engineered models (Ciucci et al., 2022a).

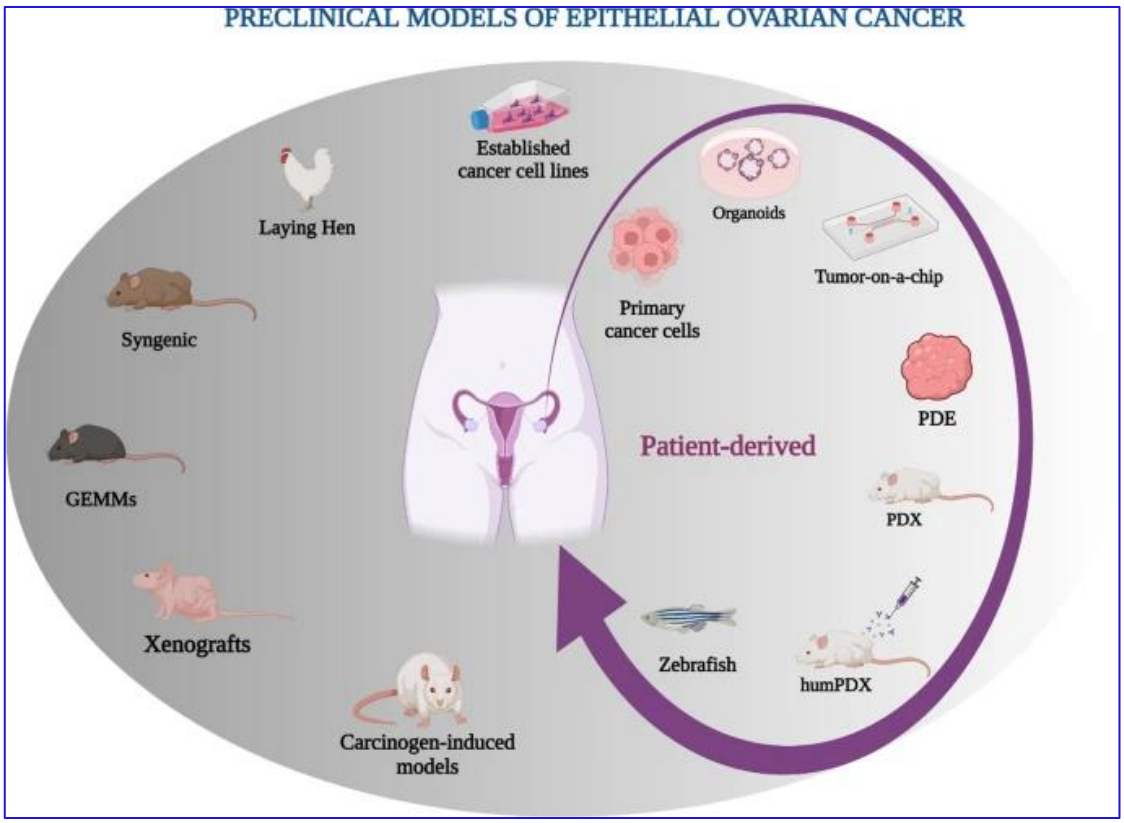

Figure 2.17. A brief overview of different preclinical models for ovarian cancer research.

PDE patient-derived explants, *PDX* patient-derived xenograft, *humPDX* humanized PDX, *GEMMs* genetically engineered mouse models; Source (Ciucci et al., 2022).

For xenograft and syngeneic models in the context of EOC, three important factors need to be considered:

i. Tumor cell source (established or primary cancer cell line, or surgical resections).

ii. Location of transplanted tumor cells (orthotopic vs. heterotopic).

iii. Immune status of the host (mouse immune system, immunocompromised, or human immune system).

The two major methods of engraftment are subcutaneous (SC) and intraperitoneal (IP) injections. Subcutaneous engraftment of cancerous cells or tissues confines tumor

formation to the implantation site, allowing it to grow within weeks and develop histology similar to the original tumour. This method can be readily quantified with calipers, making it suitable for drug response studies. Intraperitoneal injection creates a disseminated cancer model that mimics the metastatic behaviour of EOC, with cancer foci quickly forming within the peritoneum, and on the liver and spleen surfaces, similar to advanced stages of human EOC. Only a suspension of established or patient-derived cancer cell lines can be injected via IP (Ciucci et al., 2022).

In orthotopic mouse models, tumour cells are transplanted into the anatomical location from which they were originally derived, such as the ovarian bursae (IB, intrabursal) (Ciucci et al., 2022). Additionally, Greenaway and colleagues demonstrated that orthotopic grafting of ID8 cells into C57BL/6 mice induces the formation of epithelial ovarian tumours and secondary lesions throughout the peritoneal cavity between 80 and 90 days post-injection. These tumours exhibit cytological and architectural features resembling serous carcinoma, along with extensive abdominal ascites. However, no preclinical model can fully replicate the complexity of EOC as seen in patients, including their interindividual variability in drug response. A practical approach involves utilising a combination of in vitro, ex vivo, and in vivo experimental platforms to enhance the predictive power of experimental systems. This approach aims to improve the impact of cancer research in EOC (Ciucci et al., 2022).

CHAPTER 3

Scope of work
&
objectives of the study

Despite significant advancements in the diagnosis and chemotherapy of ovarian cancer, it remains one of the most lethal gynaecological malignancies, characterised by high recurrence and mortality rates. The standard treatment for epithelial ovarian cancer (EOC) involves cytoreductive surgery combined with platinum-based chemotherapy. However, mortality rates have not significantly improved, underscoring the urgent need for new therapies and alternative targets to combat this disease (Kurnit et al., 2021). The challenge of early detection persists, resulting in the majority of cases being diagnosed in advanced stages. While surgery and chemotherapy stand as primary treatments for advanced cases, chemotherapy resistance poses significant hurdles (Ciucci et al., 2022). Therefore, the imperative to pursue new targets or novel compounds with enhanced selective toxicity remains paramount in the quest for effective ovarian cancer treatment.

Future high-quality translational research on epithelial ovarian cancer (EOC) is expected to focus on several key areas:

i. Improving Understanding of Disease Biology: Gaining deeper insights into the biological mechanisms of EOC.

ii. Identifying Correlates of Response and Resistance to Therapy: Discovering biomarkers and factors that influence how patients respond to or resist treatment.

iii. Providing New Targeted Cancer Therapies: Developing novel targeted therapies aimed at more effectively treating EOC.

Natural products have garnered considerable attention for their potential in fighting cancer. Many natural compounds target cellular molecules that confer chemoresistance to conventional chemotherapy (Huang et al., 2021). Among these, bacterial toxins and enzymes are well-recognized for their anticancer properties, as they can induce cell death and modulate critical cellular processes such as apoptosis, differentiation, and proliferation. When used alone or in combination with existing anticancer drugs or radiation, bacterial toxins can enhance the efficacy of cancer therapy (Ab Mutalib et al., 2020; Carswell et al., 1975; Trivanović et al., 2021). Natural bacterial products can also be purified relatively cost-effectively compared to chemically synthesised drugs (P. Li et al., 2012; Sahayasheela et al., 2022). In this regard, our study aims to identify proteases from environmental microbial isolates capable of inducing apoptosis in ovarian cancer cells.

❖ **The objectives are**

1. Isolation, purification and characterisation of microbial proteases from environmental sources.

2. Studying the microbial protease-induced apoptosis in ovarian cancer cells.

3. Deciphering the microbial protease-induced major bio-signalling pathways.

4. Investigating the therapeutic effectiveness and potential toxicity of microbial proteases against ovarian cancer in an *in vivo* setup.

CHAPTER 4

Material & Methods

4.1. RESOURCE AVAILABILITY

4.1.1. Materials availability

This study did not generate any new unique reagents.

4.1.2. Data and code availability

• Data: The data presented in this study are available in the article and supplemental information.

• Code: NCBI GenBank accession number of *Bacillus altitudinis* strain GDL-186 https://www.ncbi.nlm.nih.gov/nuccore/**OP738003.1**. The whole genome shotgun project of *Bacillus altitudinis* GDL 186 has been deposited at DDBJ/ENA/GenBank under the accession **JAZHFY000000000**.

4.2. EXPERIMENTAL MODEL AND STUDY PARTICIPANT DETAILS

4.2.1 Bacterial isolates and its growth conditions

A total of 200 bacterial isolates were isolated from salt farm of CSIR-CSMCRI, Bhavnagar (21°47'50'' N, 72°07'16'' E), Gujrat, India. All the isolates were stored in 25% glycerol at -80°C. Bacterial isolates were revived in nutrient broth (BD, USA; Cat# 234000) of pH 8.0 containing 2% NaCl (BD, USA; Cat# 234000). Initially, isolates were grown in 5.0 ml NB (primary culture) at 37°C in a shaker incubator till the OD_{600} reached 0.6. Secondary cultures were given in 1000 ml NB at a ratio of 1:100 and grown at 37°C in a shaker incubator for 18 h. The culture supernatant of the bacterial isolates was used for screening of protease.

4.2.2 Cell culture and treatments

Human ovarian cancer cells PA-1 (ATCC; Manassas, Virginia, United State; Cat# CRL-1572, RRID:CVCL_0479) and SKOV3 (ATCC; Manassas, Virginia, United State; Cat# HTB-77, RRID:CVCL_0532) were cultured (10-12 passage) and maintained in alpha-minimum essential medium (MEM-α) (Sigma; Cat# M0644) and RPMI-1640 (Gibco; Cat# 23400021) respectively with 10% FBS (Gibco; Cat# 10270106), 100 U/ml penicillin G and 100 µg/ml Streptomycin sulphate solution (Gibco, Cat # 15140122) at 37°C in presence of 5% CO_2 incubator. Human immortalised ovarian surface epithelial cells, IOSE (IOSE-364 from N. Auersperg and C. Salamanca, Vancouver, Canada, RRID: CVCL_5540) was maintained in MCDB-105 (Sigma

Aldrich; Cat# M6395) and Medium-199 (Gibco; Cat# 31100035) in 1: 1 ratio and supplemented as stated earlier. Here, the low-passage cultures of human ovarian surface epithelium cells (isolated by scraping from human ovarian surface tissue) were immortalised by transfecting with SV40 large-T antigen viral particle (D. Ghosh et al., 2023). Mouse ovarian carcinoma ID8 (MERCK Cat# SCC145, RRID: CVCL_IU14) cell line was cultured in DMEM high glucose medium (Gibco; Cat# 31600034) supplemented with 10% FBS, 100 U/ml penicillin G and 100 µg/ml Streptomycin sulphate and 1% AOF-ITS supplement (Merck; Cat# SCM 054) at 37°C in presence of 5% CO_2 incubator. All cell lines were supplied by Dr. Sib Sankar Roy (CSIR-IICB, Kolkata) as a gift. Cell lines were tested for mycoplasma contamination and validated by short tandem repeat (STR) polymorphism analysis performed by the Life code genomic technologies.

4.2.3 Mice for animal model experiments

The mice that were used in this study were healthy adult female C57BL/6 mice of approximately 22–25 g of weight (6-8 weeks old), bred and maintained in an animal colony as per the principles and guidelines of the ethical committee for animal care of NICED, supplied with food pellets and autoclaved water *ad libitum*. The experimental design of the present study was approved by the IAEC (License No: PRO/168/Jan 2022), NICED, Kolkata, India.

4.2.4 Rabbit for animal model experiments

Antiserum against Peptidase M84 was raised by immunising an adult male New Zealand White rabbit (bred and maintained in an animal colony of NICED).

4.2.5 Table 1: List of primers used in this study

Gene of interest	Forward Primer (5'-3')	Reverse Primer (5'-3')
Human *PAR-1*	GTAGTCAGCCTCCCACTAAAC	CACAGACACAAACAGCACATC
Human *PAR-2*	CCTCAGTGTGCAGAGGTATTG	AGCAGAATCAGCAGCCATATT
Human *PAR-3*	CCCATCATCCTTCCGATTCTAC	GTGGATGAGAGTCGTGTAACAG
Human *PAR-4*	GTCACTAGCAGAGGTCACTTTG	GCCTCTTAAAGTGCTGGGATTA
Human *GAPDH*	GGAGCGAGATCCCTCCAAAAT	GGCTGTTGTCATACTTCTCATGG
Bacterial *peptidase M84*	CACCATGAAAAAGCGTTCAGTC	TTATCTGTACCAAGCTTTATTA
Bacterial *DNA gyrase B*	CTCGAAGGACTAGAAGCGGT	ACTTCTACAGCAGGACGTCC

4.3. METHOD DETAILS

4.3.1. Azocasein assay

Azocasein assay was performed to determine the protease activity of the bacterial isolates as described earlier (Syngkon et al., 2010). Briefly, the overnight grown culture supernatants were mixed with 0.7% azocasein (prepared in 100 mM Tris-HCl; pH 8.0) (Sigma, Cat# A2765) followed by incubation at 37°C for 1 h. The reaction was stopped using 10% Tri Chloro Acetic Acid (Sigma; Cat# T6399) and kept at 4°C for 30 min. Precipitate was removed by centrifugation (12,000 rpm for 10 min). NaOH (500 mM) was added to the supernatant and absorbance was measured at 440 nm. Nutrient broth and purified haemagglutinin protease (HAP) from *Vibrio cholerae* C6709 were used as negative and positive controls respectively.

4.3.2. Purification and identification of protease

Peptidase M84 was purified from the culture supernatant of 'GDL-186'. Bacterial strain was grown in 1000 ml NB (containing 2% NaCl, pH 8.0) for 19 h at 37°C in a shaker incubator. After centrifugation at 12,000 rpm for 10 min at 4°C, the culture supernatant was salted out with 80% saturated ammonium sulphate (Sigma; Cat# A4915) and kept overnight (O/N) at 4°C. Protein pellet was collected by centrifugation at 14000 rpm at 4ºC and the pellet was dissolved in 25 mM Tris-Cl buffer, pH 8.0. The protein solution was dialysed against the same buffer for 48 h at 4°C using dialysis membrane (Himedia; Cat# LA395-30MT). Dialysed protein solution was concentrated using speed-vac vacuum centrifugation and run on DEAE-52 ion-exchange column (2.5 X 20 cm) pre-equilibrated with 25 mM Tris-Cl buffer, pH 8.0. Flow through or non-binding fraction was collected, concentrated and checked for protease activity. Binding fractions were collected using increasing concentration of NaCl (0.1 M - 0.5 M) solution. The eluted fractions were pooled, dialysed, concentrated and examined for protease activity. Non-binding fraction showing protease activity, was further pooled, concentrated and loaded into Sephadex G-75 gel filtration column (1.5 X 30 cm) with 25 mM Tris-HCl buffer of pH 8.0. Chromatograms were generated in the Bio-rad biologic duo-flow instrument. Fractions positive for protease activity were eluted, concentrated and analysed by SDS and Native-PAGE. The single band from Native-PAGE and two bands from SDS-PAGE were cut out from the gel and sent to C-CAMP, NCBS, Bangalore, India for identification by nano-LC-MS/MS-TOF (ESI-nanospray/FT-ICR/Orbitrap- Nano LC-MS/MS). Peptide sequence generated from MS/MS spectra was searched in NCBI and Uniprot databases for homology alignment.

4.3.3. Determination of physico-chemical characteristics of the purified protease

Inhibition of the protease activity with different inhibitors was performed in order to determine the type of the purified protease and the culture supernatant of isolate GDL-186. PMSF (10 mM) (Sigma; Cat# P7626), EDTA (10 mM) (Sigma; Cat# E9884) and 1,10 phenanthroline (10 mM) (Sigma, Cat# 131377) were used in the inhibition study as described in our previous study (Tapader *et al*, 2016).[76] 100 mM stocks of PMSF and 1,10 phenanthroline were prepared in isopropanol and methanol respectively and 500 mM stock of EDTA was prepared in water. 5.0 µg of purified protease was pre-incubated at 37°C for 1 h with each inhibitor. The residual protease activity was measured by azocasein assay.

The optimum pH for protease activity was determined using buffers of different pH ranging from 4.0–11.0. 5.0 µg of purified protease was dialysed overnight against 25 mM acetate buffer (pH 4.0–5.0), 25 mM phosphate buffer (pH 6.0–7.0), 25 mM Tris-HCl (pH 8.0–9.0), 25 mM glycine-NaOH buffer (pH 10.0–11.0) and activity were determined with azocasein assay.

To determine the optimum temperature for activity, 5.0 µg of the purified protease was incubated over a wide range of temperatures: 4°C, 25°C, 37°C, 50°C, 60°C and 70°C for 1 h and the enzyme activity was determined by azocasein assay as already described.

Gelatine zymography was performed to determine the substrate specificity of the purified protease as per the protocol described earlier (Tapader et al., 2016). For native zymography, samples were electrophoresed under non-reducing conditions without boiling using 7.5% Native-PAGE co-polymerised with 0.1% gelatin (Sigma; Cat# G2500). The gel was incubated after electrophoresis in renaturation buffer (2.5% Triton-X-100) for 1 h at room temperature (RT) with gentle shaking. The gel was then developed in development buffer containing 5 mM $CaCl_2$, 25 mM Tris-HCl (pH 8.0) for O/N at 37ºC with gentle shaking. The gel was visualised after staining using Coomassie Brilliant Blue G-250 (Himedia; Cat# ML046) and subsequent destaining.

The effect of zinc ion (Zn^{2+}) or zinc dependency of the protease was also examined. The enzyme (5 µg) was preincubated with different concentrations of $ZnCl_2$ ranging from 0.5 mM to 15 mM at 37°C for 1 h. The azocaseinolytic activity was evaluated as described above.

4.3.4. 16s-rRNA and whole genome sequencing

The protease positive bacterial isolate which showed significant apoptotic activity was identified by 16s rRNA sequencing. First, genomic DNA was isolated from O/N grown bacterial culture and run on 1.0% Agarose gel.16S rRNA gene was amplified by 27F 5'-AGAGTTTGATCCTGGCTCAG-3' and 1492R 5'-GGTTACCTTGTTACGACTT-3' primers.

The PCR reaction was as follows: 95°C for 10 min; 35 cycles of 95°C for 30 s, 55°C for 1 min, and 72°C for 1.5 min; and final extension at 72°C for 10 min. The PCR amplicon was purified to remove contaminants. Forward and reverse DNA sequencing reaction of PCR amplicon was carried out with forward primer and reverse primers using BDT v3.1 Cycle sequencing kit on ABI 3730xl Genetic Analyzer. Consensus sequence of 16S rRNA gene was generated from forward and reverse sequence data using aligner software. The 16S rRNA gene sequence was used to carry out BLAST with database of NCBI GenBank. Based on maximum identity score first ten sequences were selected and aligned using multiple alignment software program Clustal W. Distance matrix was generated and the phylogenetic tree was constructed using MEGA 7. The evolutionary history was inferred by using the Maximum Likelihood method based on the Kimura 2- parameter model. In addition to this, The DNA gyrase B gene sequence was used to carry out BLAST with database of NCBI GenBank. Based on maximum identity score first ten sequences were selected and aligned using multiple alignment software program Clustal W and NCBI. The evolutionary history was inferred by using the Neighbour joining method based on the Kimura 2- parameter model. Final confirmation of the isolate was validated by whole genome-based shotgun sequencing. Paired-end raw sequence reads were assessed for base quality and contamination by sequencing artifacts. Trimming of adapters and poor-quality sequences was performed for paired sequence reads with Trim Galore. Trimmed sequence reads were assembled into scaffolds with SPAdes. Taxonomic classification with Bracken and BLAST was used to identify closest genomic reference sequences. Sequences from draft genome assembly were mapped and ordered with RagTag. Annotation of assembled and ordered draft genome sequences was performed with Prokka. Genomic map plots were generated with Cgview from. gbk annotation file generated by Prokka. Kraken2 and Bracken are used to align the filtered reads to prebuilt standard reference (bacteria, viral, plasmid, human, UniVec_Core).

4.3.5. Identification of the isolate based on biochemical, microbiological and physiological characteristics

Phenotypic characteristics of the isolate, including motility, cell morphology, Gram staining, catalase, and oxidase production, among others, were investigated according to standard protocols. The fermentation of substrate belonging to carbohydrates and derivatives was determined as per standard protocols.

4.3.6. Raising of antisera against purified Peptidase M84

Antiserum against Peptidase M84 was raised by immunizing a New Zealand White rabbit (bred and maintained in an animal colony as per the principles and guidelines of the ethical committee

for animal care of NICED as described previously by Mondal et al., 2016. Intramuscular injection was given with 100 µg of purified Peptidase M84 emulsified with an equal volume of Freund's complete adjuvant (Sigma, USA; Cat# F5881). This was followed by four booster injections with 100.0 µg of Peptidase M84 and incomplete adjuvant (Sigma, USA; Cat# F5506) at 7-day intervals. Blood samples were collected from rabbits on day 0 and 3rd day after the final injection and were allowed to clot O/N at RT. Sera were collected and centrifuged (1,000 rpm, 5 min), diluted in autoclaved glycerol (Sigma, USA) and stored at -80°C until use at a dilution of 1:800 unless otherwise mentioned.

4.3.7. PCR to detect the gene encodes Peptidase M84 from *Bacillus altitudinis*

Genomic DNA was isolated from 1 ml of O/N bacterial culture using Promega Wizard genomic DNA purification kit (Cat# A1120) according to the manufacturer's protocol. 20 ng of genomic DNA was subjected to PCR amplification using GoTaq green master mix (Promega; Cat# M7122) in an automated thermal cycler (Bio-Rad, USA) to detect the presence of gene codes for Peptidase M84 using specific primers (mentioned in Table 1) under the following conditions: 10 min initial denaturation at 95°C followed by 35 cycles of 1 min denaturation at 95°C, 30 s, annealing at 55°C, followed by 1 min extension at 72°C and final 10 min extension at 72°C.

4.3.8. Cell viability and cell proliferation assay

The effect of Peptidase M84 on cellular viability and to determine the sub-lethal concentration of peptidase M84, MTT assay was done as per standard protocol (Kar et al., 2014). About $1X10^5$ live cells/well were seeded in a 96-well plate for viability assay. Trypan blue was used to determine cell viability. After 24 h of incubation, PA-1, SKOV3 and ID8 cells were treated with different concentrations of Peptidase M84 to determine the minimal inhibitory concentration (IC_{50}) value. After 24 h of protease treatment at different concentrations of 0.5 µg/ml – 5.0 µg/ml, MTT solution (0.8 mg/ml dissolved in serum free medium) was added to the cells and further incubated for 4 h in the dark at 37°C. The media containing MTT was removed and DMSO was added followed by incubation for 15 min in the dark. The absorbance was measured at 595 nm and mean of five replicates was taken to obtain IC_{50} value for subsequent experiments. The effect of Peptidase M84 on cell viability was also studied by immunofluorescence of ki-67 nuclear antigen in PA-1 and SKOV3 cells. Peptidase M84 treated (with 2.0 µg/ml for 18 h) and untreated PA-1 and SKOV3 cells were fixed with 4 % paraformaldehyde for 10 min at RT. Cells were then permeabilised with 0.1 % Triton X-100 in 0.1% sodium citrate solution and blocked with 5% serum. Cells were incubated O/N with anti-ki-67 primary antibody (1:200) at 4ºC in a

moist chamber. Cells were washed with (phosphate buffer saline) PBS and then incubated with Alexa 488 conjugated secondary antibody. Nuclei were stained with DAPI for 10 min at 37°C. Cells were then washed twice with PBS, mounting was done with 10% glycerol. Images were captured using Zeiss (LSM 710) confocal microscope.

4.3.9. Flow cytometry analysis to study apoptosis

Flow cytometry was performed for screening of apoptotic activity of protease positive bacterial culture supernatants. Cellular apoptosis was detected by double staining, FITC conjugated annexinV/propidium iodide (PI) staining, as described in our previous studies (Ray & Pal, 2016). Briefly, PA-1 cells (1×10^6) were seeded into 6 well tissue culture plates. Cells with 70% confluency were washed with PBS and starved in serum free media for 18 h. Cells were treated with filter sterilised protease positive bacterial supernatant for 18 h in complete medium. Untreated control cells were replaced with fresh media and incubated under similar conditions. After treatment, cells were harvested and flow cytometric analysis was done by using Annexin V and PI staining kit (BD, USA, Cat# 556547) as per the manufacturer's protocol. For protease inhibition studies bacterial culture supernatant was pre-incubated with both 10 mM EDTA and 10 mM PMSF before treatment.

Flow cytometry was also performed with the purified protease as described below. After treatment with purified Peptidase M84 at a concentration range between 1.0 µg/ml to 3.0 µg/ml for 18 h, PA-1, SKOV3, IOSE and ID8 cells were harvested by centrifugation and washed twice with PBS. Cells were re-suspended in 1X binding buffer (provided with BD annexin-V kit), stained with annexin V/PI and kept at RT for 15 mins. Cells were analysed by BD FACS Aria II using 'Cell Quest' software. For protease inhibition studies, Peptidase M84 was preincubated with either 10 mM EDTA or 10 mM PMSF before treatment.

4.3.10. Chromatin condensation assay

After treatment with 2.0 µg/ml of protease for 18 h, ovarian cancer cells were stained with Hoechst 33342 stain (2 µg/ml) and incubated for 10 min at 37°C, and images were taken under Zeiss confocal microscope. Condensed nucleus was counted against total number of nuclei in the field, and the percentage of apoptotic nuclei were calculated and plotted graphically (Deb et al., 2014).

4.3.11. Detection of ROS by DCFDA staining

In-situ ROS level was measured by oxidation of 2',7'- dichlorofluorescin diacetate (DCFDA) to highly fluorescent 2',7'-dichlorofluorescin (DCF). Peptidase M84 treated (2.0 µg/ml) PA-1, SKOV3, IOSE cells and ID8 (3.0 µg/ml) cells for 6 h and 18 h with their respective untreated controls were incubated with DCFDA at a working concentration of 20 µM for 20 min at 37°C, washed with PBS and subsequently the cell pellet was resuspended in 500 µl of PBS and then subjected to flow cytometry and analysed by BD FACS Aria II using 'Cell Quest' software. At least three independent experiments were conducted to validate our results and the MFI values of DCF was plotted.

4.3.12. Flow Cytometry Detection of JC-1 Fluorescence

JC-1 dye (Invitrogen, USA) staining to detect changes in mitochondrial membrane potential in ovarian cancer cells was done according to the protocol described by (Prasad et al., 2021). Briefly, PA-1 and SKOV3 cells ($1X10^6$) were harvested by centrifugation (5 min at 500×g) after Peptidase M84 treatment (2.0 µg/ml for 6 h and 18 h). Cells were then resuspended in 500 µl of PBS. JC-1 (5,50,6,60-tetrachloro-1,10,3,30-tetraethyl-imidacarbocyanine iodide) was added to a final concentration of 10.0 µg/ml from a stock solution of 5.0 mg/ml and cells were incubated in dark at 37°C for 30 min. Cells were then washed once and again resuspended in 500 µl of PBS. Cells were analysed in a BD FACS Aria II flow cytometer (BD Bioscience, San Jose, CA, USA). The ratio of the median value of green and red fluorescence was plotted for quantification.

4.3.13. Comet assay

DNA damage (single-strand breaks) was measured by alkaline comet assay (Singh et al., 1988). Briefly, PA-1 and SKOV3 control and Peptidase M84 treated (2.0 µg/ml for 18 h) cells were suspended in 0.6% (w/v) low melting agarose. Subsequently, cells were layered over a frosted microscopic slide previously coated with a layer of 0.75% normal melting agarose. The slides were then immersed in a lysis buffer of pH 10.0 and left overnight at 4°C. Slides were transferred into a horizontal electrophoresis chamber containing an alkaline solution (300 mM NaOH, 1 mM Na_2EDTA; pH 13.0). Pre-soaking for 20 min was done in order to unwind DNA. Electrophoresis was then carried out for 20 min (300 mA, 20 V). Slides were washed thrice with neutralizing buffer (Tris Buffer 0.4 M, pH 7.5) followed by staining with ethidium bromide (final concentration 40.0 µg/ml). Slides were examined under Axio observer 7 Apotome.2; objective-EC Plan-Neofluar 40X / 0.75 NA fluorescence microscope and image analysis was

done using comet assay software programme Komet 5.5. DNA damage was quantitated by tail moment measurement.

4.3.14. Western blotting (WB)

Western blot was done as described by (Das et al., 2022; Ray & Pal, 2016). Briefly, cultured cells were lysed with RIPA buffer and the concentration of protein samples was measured using BCA assay kit. Equal amount of protein was loaded onto SDS-PAGE for separation and then electrophoretically transferred to the PVDF membrane (Merck; Cat# IPVH00010). After transfer the membrane was blocked with 3% BSA (Sigma; Cat# A1470) in Tris-buffered-saline (TBS) and incubated overnight with primary antibody (1: 1000) against the protein of interest (as per requirement) at 4°C. The blot was washed with TBS-Twin 20 (TBST) buffer and incubated with HRP/AP-tagged secondary antibody for 2 h at RT. Proteins were either visualized by Bio-Rad gel documentation system using specific ECL substrate (Thermo scientific; Cat# 34580) for HRP tagged antibodies (Cell Signaling Technology Cat# 7076 and Cell Signaling Technology Cat# 7074) or using BCIP/NBT substrate (Bio-rad; Cat# 1706432) for AP tagged antibodies (Cell Signaling Technology Cat# 7056 and Cell Signaling Technology Cat# 7054).. Quantification of western blots was performed using GelQuant (Thermo Fisher Scientific, USA) and ImageJ (NIH, Bethesda, MD) software. At least three independent experiments were performed to confirm the findings and band intensities were normalised to loading controls.

4.3.15. Immunocytochemistry and confocal imaging

Peptidase M84 treated (2.0 µg/ml for 18 h) and untreated PA-1 and SKOV3 cells were fixed with 4% paraformaldehyde for 10 min at RT. Cells were then permeabilized with 0.1 % Triton X-100 in 0.1% sodium citrate solution and blocked with 5% FBS. Cells were incubated O/N with primary antibody (1:200) against the protein of interest (as per requirement) at 4°C in a moist chamber. Cells were washed with PBS and incubated with either Alexa 488 (Cell Signaling Technology Cat# 4408 and Cell Signaling Technology Cat# 4412) or Alexa 555 conjugated secondary antibody (Cell Signaling Technology Cat# 4413 and Cell Signaling Technology Cat# 4409) for 2 h at RT. Nuclei were stained with either DAPI or Hoechst 33342 (working concentration 1.0 µg/ml) for 10 min at 37°C. Cells were washed twice and mounting was done with 10% glycerol. Images were captured using confocal microscope (Zeiss 710); objective-Plan-Apochromat 63X / 1.40 NA. and all the other required analysis were done according to the procedure described by (Das et al., 2022).

4.3.16. Evaluation of intracellular cytochrome c by western blot and immunofluorescence

Subcellular fractionation to extract mitochondria free cytosol from PA-1 and SKOV3 cell lysates was performed. using the method described by (Dimauro et al., 2012). Briefly, $5x10^6$ cells were harvested after 18 h of protease treatment (2.0 µg/ml) by trypsinisation followed by the isolation of mitochondria-free cytosolic fraction to assess the release of cytochrome c. Concentration of cytochrome c in cytosolic fraction was measured by western blot in protease treated and untreated cells. Cytosolic GAPDH (mitochondria free) was used as loading control. To observe the intracellular cytochrome c distribution, co-localization-based immunofluorescence was used as described earlier (J. Li et al., 2020; Sun et al., 2008). Briefly, PA-1 and SKOV3 cells were treated with Peptidase M84 for 18 h at a concentration of 2.0 µg/ml. Untreated and treated cells were incubated with Mito Tracker dye (Mito Tracker Green FM; Molecular Probes; Thermo Fisher Scientific) at a working concentration of 100 nm for 40 min in a 37ºC incubator in dark. The slides were then fixed with 4% formaldehyde at RT for 15 min. The fixed slides were stained with anti-cytochrome c antibody (1:200) and kept O/N at 4°C in a moist chamber, followed by staining with Alexa 555 labelled secondary antibody (1:200) at RT for 2 h. Cells were stained with DAPI (1.0 µg/ml) for 10 min, washed twice and mounted with 10% glycerol in glass slides. Images were obtained using different excitation filters and merged. Co-localisation was quantified by calculating Pearson's co-efficient values.

4.3.17. mRNA expression level of different PARs upon Peptidase M84 treatment by quantitative Real-Time PCR (RT-qPCR)

RT-qPCR of PARs was done as described previously (Ray & Pal, 2016). Total cellular RNA was isolated from untreated and Peptidase M84 treated (2.0 µg/ml for 18 h) PA-1 and SKOV3 cells (about $1X\ 10^6$ cells for PA1 and $0.8X10^6$ cells for SKOV3) using RNA isolation kit (Zymo research; Cat# R1057). 2.0 µg of the total RNA was reverse transcribed using Revertaid first strand cDNA synthesis kit (Thermo scientific; Cat# K1622) to synthesize the cDNA first strand. Thereafter, the cDNA first strand was used in the subsequent amplification by Real-Time PCR with the primers described in Table S1. GAPDH was used as an internal control to normalize the results. Real-Time PCR was performed using SYBR green reagent (Eurogentec; Cat# UFRSMTBC101) in a total volume of 25 µl containing 10 pM of each primer (mentioned in Table S1), 12.5 µl of SYBR green reagent and 2.0 µl of cDNA. PCR reactions were carried out by using an ABI multicolour real time PCR detection system. The thermal cycling conditions used for Real Time PCR were: denaturation at 95ºC for 30 s followed by 35 cycles of 1 min

denaturation at 95º C, 30 s, annealing at 55ºC, followed by 1 min extension at 72ºC and final 10 min extension at 72ºC.

4.3.18. Immunoprecipitation

For immunoprecipitation (IP), cells were lysed in immunoprecipitation buffer [50 mM Tris-HCl, pH 7.5, 150 mM NaCl, 0.1% Triton X-100, 1% IGEPAL and 1 mM PMSF], and it was performed under denaturing conditions as described previously by Ray and Pal, 2016. Briefly, 2.0 µg/ml of Peptidase M84 was added to the PA-1 and SKOV3 cell medium and incubated for 30 min. The incubation media was removed after centrifugation and cells were fixed with 4% formaldehyde and the cell lysate was prepared using RIPA buffer. 500 µg of the total lysate was incubated with either PAR-1 antibody or antisera raised against Peptidase M84 for 5 h at 4ºC in a rotating shaker at a speed of 10 rpm. The lysate along with antibody was allowed to bind with A/G agarose beads and incubated O/N at 4ºC in a rotating shaker at a speed of 10 rpm. The lysates were centrifuged and washed twice with IP buffer to remove any non-specific bindings. Beads were boiled with SDS-protein loading dye for 10 min and subjected to electrophoresis. The proteins were transferred to a PVDF membrane and western blot was done with either anti-Peptidase M84 antibody (1:3000) or anti-PAR-1 antibody (1:1000). Immunoblots (IB) were developed using Veri Blot (Abcam Cat# ab131366) as per the manufacturer's instruction to observe the interaction between Peptidase M84 and PAR-1. In another experiment, beads were boiled with SDS-protein loading dye for 10 min and subjected to electrophoresis only. Proteins were visualised after Coomassie staining.

4.3.19. Nuclear cytosolic fractionation

To detect the nuclear translocation of NFκB subunits, PA-1 and SKOV3 ($5X10^6$) cells were treated with 2.0 µg/ml of Peptidase M84 for 18 h. Extraction of nuclear and cytosolic fractions of untreated and Peptidase M84 treated cells were performed using NE-PER™ Nuclear and Cytoplasmic Extraction Reagents (Thermo Scientific™, USA, Cat#78833) according to manufacturer's protocol. The fractions were used for western blotting to determine nuclear translocation of p50 and p65. Here, α-tubulin and Histone H3 were used as cytosolic and nuclear loading controls respectively.

4.3.20. Treatments of cells and siRNA transfection

The cells were first starved for at least 18 h with an incomplete medium prior to respective treatments. Scrambled (SCR) siRNA (Cat#sc-37007, Santa Cruz Biotechnology) was used as

control for knockdown studies. Lipofectamine 3000 was used as transfection reagent and transfection was performed according manufacturer's protocol. The transfection was done at 50–60% confluency and the transfection reagents were added in Opti-MEM (Gibco, USA; Cat# 31985062). medium and after 4 h of transfection the media was changed to respective media of treatment. PAR-1 si-RNA (CGGUCUGUUAUGUGUCUAUdTdT) was transfected for at least 48 hours for efficient knock down.

4.3.21. Flow cytometric analysis for apoptosis and ROS detection using inhibitors to study the signalling pathway

Quantitative evaluation of apoptosis and ROS was performed using the flow cytometry methods as described previously by Ray and Pal, 2016. PA-1 and SKOV3 cells ($1X10^6$ cells) were incubated with either 2.0 µg/ml of Peptidase M84 or pre-incubated for 1 h with 0.5 µM PAR1 inhibitor (ML161) or 3.0 µM of NFκB inhibitor (MG132), or 10.0 µM p38 inhibitor (SB203580) and then incubated with 2.0 µg /ml of Peptidase M84 for 18 h. Cells were washed with PBS and analysed to detect apoptosis by Annexin-V-FITC and PI dual staining based method. In-situ ROS was determined by DCFDA staining using FACS Aria II (Cell Quest software) as per the protocol described earlier.

4.3.22. Syngeneic mice model Syngeneic mice

Survival kinetics and body weight changes were studied by implanting $5X10^6$ number of ID8 cells (0.2 ml) into the peritoneal cavity of C57BL/6 female mice and allowed to multiply (Jan et al., 2006; Roby et al., 2000). The day of tumour implantation was assigned as day '0'. In the present study, the animals were randomised into six groups containing ten animals (n = 10) in each group. (i) **Group 1** normal set (non-tumour-bearing; untreated control); (ii) **Group 2** only tumour-bearing set (ID8 control); (iii) **Group 3** Peptidase M84-treated ID8 bearing set; where 3.0 µg /ml Peptidase M84 (12.0 µg / kg of body weight) was injected intraperitonially on the day after inoculation of ID8 cells and injected once in a week for seven successive weeks; (iv) **Group 4** Peptidase M84 pre-treated with 10 mM EDTA; tumour bearing set where Peptidase M84 was inhibited with 10 mM EDTA at 37ºC for 1 h and then injected into the peritoneum cavity of ID8 treated mouse for seven successive weeks (v) **Group 5** Only Buffer treated set (vehicle control) where 100 µl of 1X PBS buffer was injected intraperitonially once in a week for seven successive weeks. (vi) **Group 6** only Peptidase M84 treated group (protease control). The life span of each group of mice was evaluated by measuring the percentage of survival rate in each group at 10 days interval by using a formula: (Number of live animals in a group/number of initial animals in that group) X100

4.3.23. *In vivo* evaluation of cell viability

The effects of 3.0 µg/ml of Peptidase M84 were compared against control groups, where mice were randomised in six different groups as mentioned earlier. After 45 days and 60 days of tumour inoculation, mice were sacrificed to collect total cells from the peritoneum and cells viability was checked by trypan blue exclusion method as described previously by (Barua et al., 2020).

4.3.24. Collection of blood and serum samples

Blood samples from mice were collected as per the protocol reported previously (Barua et al., 2019). Before euthanasia, all animals were fasted for 4 h then the blood samples were collected by cardiac puncture into microcentrifuge tubes and left to clot. The serum was separated by centrifugation at 2000 X g for 15 min and stored at -20ºC until analysis.

4.3.25. Measurement of cellular ROS and liver and kidney toxicity in mice

Cellular ROS level was detected by biochemical analysis of different markers in serum samples of all groups of experimental mice as described above. Different biochemical parameters like lipid peroxidation (LPO), reduced glutathione (GSH), catalase (CAT) and superoxide dismutase (SOD) were measured in the serum of different groups of mice at day 0- and 45-days intervals after inoculation of cells using standard protocols as described earlier by Ray et al., 2016. Liver toxicity markers such as serum aspartate transaminase (AST), alanine aminotransferase (ALT) level and kidney toxicity markers such as urea and creatinine were analysed by automated clinical chemistry analyzer (AU400, Olympus, Japan) according to the manufacturer's protocol after 45 days of treatment.

4.3.26. Histology of liver and kidney tissue of mice

Histopathology and hematoxylin-eosin (HandE) staining of liver and kidney tissue was done as per protocol suggested by (Dasgupta et al., 2022). For the experimental purpose, euthanasia was done as per CPCSEA guidelines. The liver and kidney were harvested from all six groups of mice mentioned earlier after 45 days of tumour implantation. The tissues were fixed in 10 % buffered formalin. The fixed tissue was paraffin embedded and serially sectioned at 4.0 µm, and stained with hematoxylin and eosin (H&E). Tissue Sections were viewed under 40X magnification of Zeiss Axiovert 40 C microscope.

4.3.27. Isolation of peritoneal exudate macrophages (PEMΦ) and treatment

To assess the cytotoxic effects of purified protease on normal healthy cells of mice the peritoneal exudate macrophages (PEMΦ) were isolated from 6-8 weeks of old C57BL/6 female mice as described previously (Chakraborty & Bhaumik, 2020; Naskar et al., 2014). Briefly, Naive C57BL/6 mice were injected intraperitoneally once with 3.0 ml of a 4% (w/v) starch (Sigma, USA) solution. After 48 h, PEMΦ were collected by peritoneal washing with chilled PBS followed by centrifugation of the exudate and resuspension of cell pellet in RPMI-1640 medium supplemented with 10% FBS (Gibco, USA), 100 U penicillin/ml, and 100 µg streptomycin/ml (Gibco, USA). Cells were then seeded into 6-well plates at $5X10^4$ cells/ml. The cells were then cultured for 48 h at 37ºC in a humidified 5% CO_2 incubator to dampen any residual effects of the starch. Non-adherent cells were removed thereafter by gentle washing with serum-free medium. The remaining adherent cells were treated with 3.0 µg/ml of Peptidase M84 for 18 h. The untreated and treated cells were collected by gentle scraping for use in the FITC conjugated annexin V/ (PI) dual staining-based apoptosis detection assay by flow cytometry as per the protocol described earlier.

4.3.28. Statistical analysis

All experiments were replicated at least thrice (n=3). All animal experimental groups contained either 10 or 6 animals. The experimental results were expressed as mean ± standard deviation. All statistical analysis was done by applying Student's t-test (unpaired two-tailed) and bar graphs were plotted using Microsoft Office Excel 2021. In all panels, ns (non-significant) $p>0.05$, *$p\leq0.05$, **$p\leq0.01$, and ***$p\leq0.001$. In each panel, error bars were calculated based on results obtained from a minimum of three independent experiments.

CHAPTER 5

Results

5.1. The culture supernatant from isolate GDL-186 which showed similarity with *Bacillus altitudinis*, triggered apoptosis in ovarian cancer cells

- High extracellular protease activity was recorded for 12 isolates (GDL-184, GDL-185, GDL-186, GDL-187, GDL-188, GDL-191, GDL-201, GDL-71, GDL-213, BSF-4, BSF-80, and BSF-32) screened from 200 environmental isolates (Figure 5.1.A and 5.1.B). We initially assessed the apoptosis-inducing potential of sterile supernatants from these isolates in PA-1 cells using flow cytometry. Notably, PA-1 cells treated with the GDL-186 supernatant underwent significant apoptosis (Figure 5.1.C and 5.1.D).

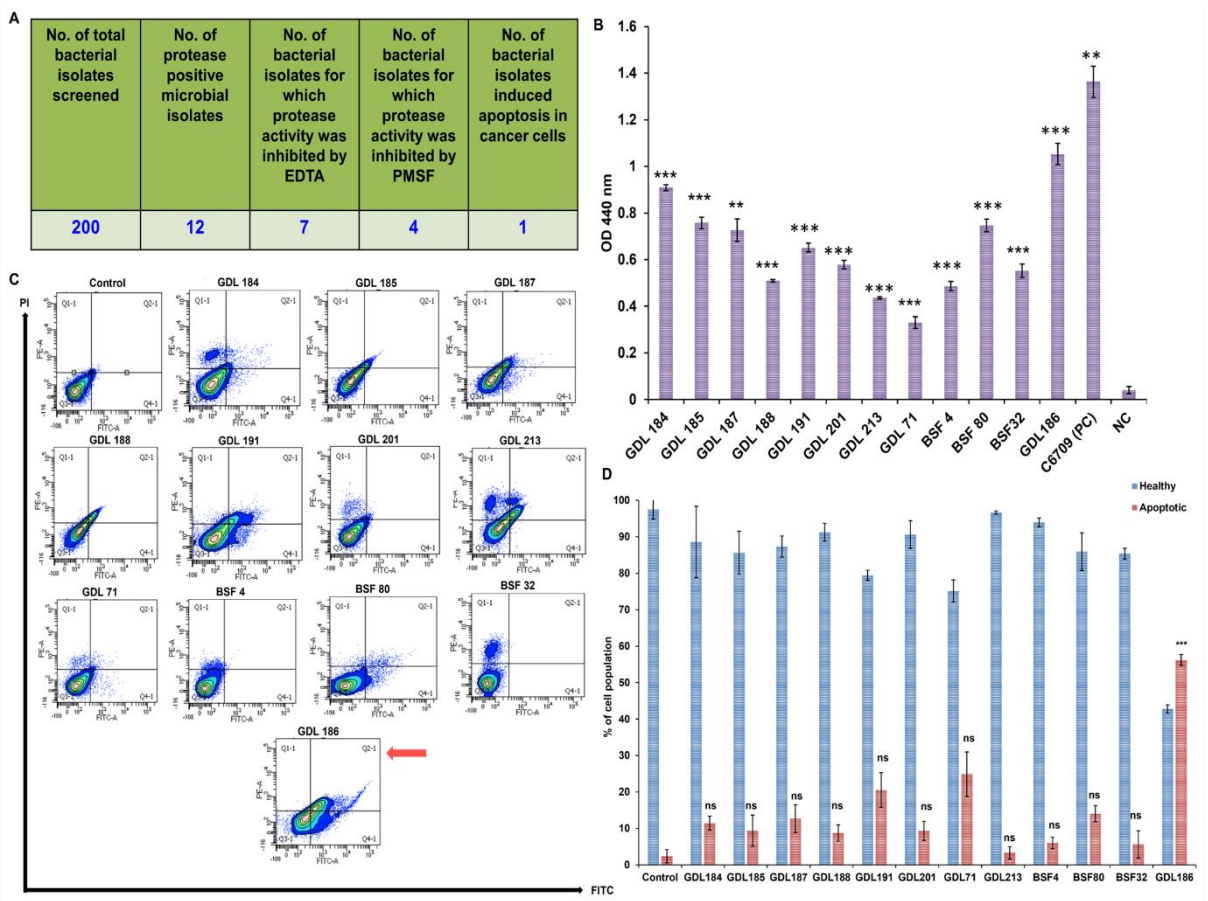

No. of total bacterial isolates screened	No. of protease positive microbial isolates	No. of bacterial isolates for which protease activity was inhibited by EDTA	No. of bacterial isolates for which protease activity was inhibited by PMSF	No. of bacterial isolates induced apoptosis in cancer cells
200	12	7	4	1

Figure 5.1. Screening of 200 bacterial isolates from environmental sources for extracellular protease activity and apoptosis-inducing ability. **(A and B)** Results of azocasein assay are represented in tabular and in graphical form. Culture supernatant of *Vibrio cholerae* EL Tor strain C6709 and nutrient broth were used as positive and negative controls, respectively. **(C)** Annexin V/PI based flow-cytometric analysis to

assess the apoptosis-inducing ability of the culture supernatant of the protease-secreting isolates in PA-1 cells. In each display, the lower right quadrant is for early apoptotic cells (Annexin V+/PI), the upper right is for late apoptotic cells (Annexin V+/PI+), the upper left is for necrotic population (Annexin V-/PI+) and lower left is for healthy cells (Annexin V-/PI-). The culture supernatant of GDL-186 isolate (marked with an arrow) shows significant apoptosis. **(D)** The aforementioned results are graphically represented in the bar diagram. All statistical analysis was done by applying the Student's t-test (unpaired two-tailed). Data are expressed in ±SEM. In all panels, ns $p > 0.05$, $*p \leq 0.05$, $**p \leq 0.01$, and $***p \leq 0.001$.

- We performed bacterial growth curve analysis for isolates individually and found isolates were reaching the stationary phases by 18-20 hours. So, it is nearly impossible for the isolates to secrete protease after the 20th hour of their growth phase. For this reason, we set the limit of the bacterial stationary phase for a maximum 20th hours for our experimental purpose (Fig. 5.2.A). So, we have set the threshold period depending on the maximum yield of the protease. The GDL-186 culture supernatant not only induced apoptosis in PA-1 cells but also proteolytically degraded azocasein. Based on these observations, we decided to purify and characterise the supernatant for its protease-like properties. Initially, treatment with EDTA and 1,10-phenanthroline inhibited the proteolytic activity of the crude supernatant, whereas PMSF and EGTA had no effect (Figure 5.2.B and C). This suggested that GDL-186 produced an extracellular zinc-dependent metalloprotease. This finding was corroborated when the GDL-186 supernatant also induced apoptosis in SKOV3 cells. However, no significant apoptosis was observed in either PA-1 or SKOV3 cells when treated with GDL-186 supernatant pre-incubated with EDTA and PMSF (Figure 5.2.D - G). The significant decrease in apoptotic cells suggests that GDL-186 induces apoptosis through a protease-mediated mechanism.

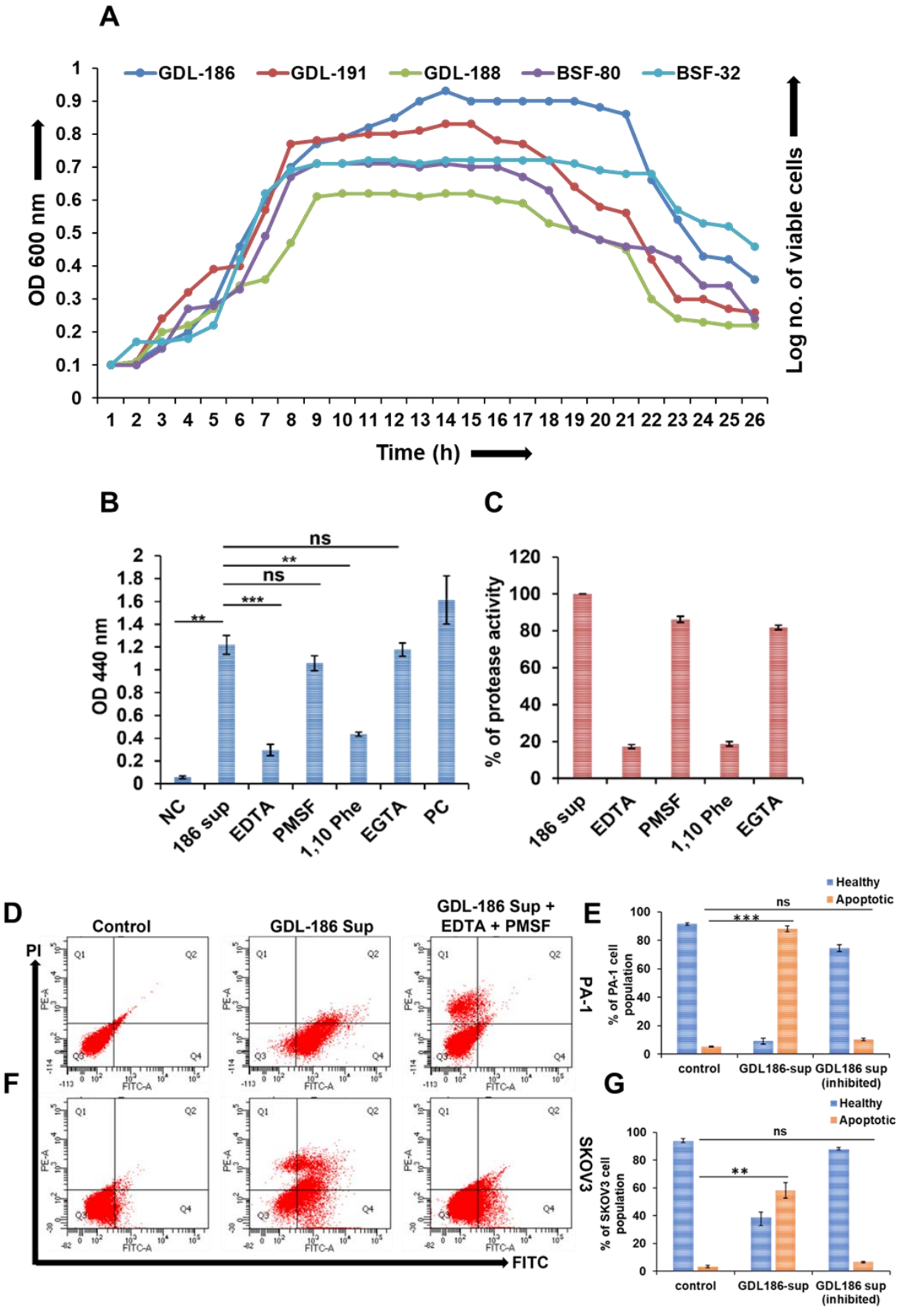

Figure 5.2. Zinc dependent Protease-secreting environmental isolates

(A) Growth curves of 5 representative isolates among the 12 protease-secreting isolates. **(B and C)** Azocasein assay shows protease activity in the culture supernatant of *Bacillus altitudinis* strain GDL-186. Here culture supernatant from *Vibrio cholerae* C6709 was used as positive control (PC) and nutrient broth was used as negative control (NC). **(D-G)** Flow cytometric studies to detect apoptosis with overnight-grown culture supernatant from isolate GDL-186 in PA-1 and SKOV3 cells indicate the presence of a microbial extracellular protease with apoptosis-inducing capabilities. Overnight grown culture supernatant of isolate GDL-186 priorly incubated with EDTA and PMSF failed to induce apoptosis in PA-1 and SKOV3 cells. These results are also graphically represented. All statistical analysis was done by applying the Student's t-test (two-tailed). Data are expressed in ± SEM. In all panels, ns $p>0.05$, *$p\leq0.05$, **$p\leq0.01$, 20 and ***$p\leq0.001$. In each panel, error bars were calculated based on results obtained from a minimum of three independent experiments.

- Next, GDL-186 was identified as a Bacillus species, showing 100% sequence homology of its 16S rRNA with *Bacillus altitudinis* in NCBI Blast results. The gene sequence was submitted to NCBI GenBank under accession number **OP738003.1** (Figure 5.3.A and B). DNA gyrase B sequence homology analysis further confirmed the identity of GDL-186 (Figure 5.4.A - C). Biochemical, microbiological, and morphological studies supported these findings. GDL-186 did not grow on MacConkey agar plates containing crystal violet. Phenotypic analysis showed medium-sized rod-shaped cells with aerobic growth, white to off-white moist colonies, motility, and endospore formation. The isolate was gram-positive bacilli, and tested positive for oxidase and catalase. It metabolized D-arabinose, D-glucose, starch, fructose, and lactose (Figure 5.5.A - F). Additional biochemical tests, including indole production, citrate utilization, triple sugar iron, lysine iron agar, and oxidative fermentation, confirmed the environmental isolate as a Bacillus species (Figure 5.6.A and B). The definitive identification of the isolate was achieved through whole genome sequencing, with the sequence deposited at DDBJ/ENA/GenBank under the accession **JAZHFY000000000**. Collectively, these results confirm that isolate GDL-186 belongs to the *Bacillus altitudinis*.

A

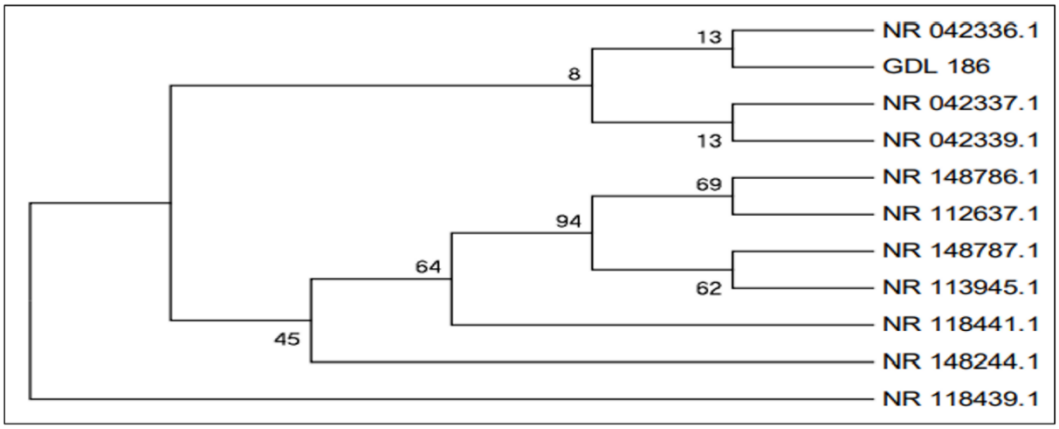

B

GDL_186		0.000	0.001	0.000	0.000	0.002	0.000	0.002	0.002	0.002	0.001
NR_042337.1	0.000		0.001	0.000	0.000	0.002	0.000	0.002	0.002	0.002	0.001
NR_148244.1	0.001	0.001		0.001	0.001	0.002	0.001	0.002	0.002	0.002	0.001
NR_042339.1	0.000	0.000	0.001		0.000	0.002	0.000	0.002	0.002	0.002	0.001
NR_042336.1	0.000	0.000	0.001	0.000		0.002	0.000	0.002	0.002	0.002	0.001
NR_148786.1	0.005	0.005	0.006	0.005	0.005		0.002	0.001	0.001	0.001	0.002
NR_118439.1	0.000	0.000	0.001	0.000	0.000	0.005		0.002	0.002	0.002	0.001
NR_148787.1	0.006	0.006	0.005	0.006	0.006	0.002	0.006		0.001	0.001	0.002
NR_112637.1	0.004	0.004	0.005	0.004	0.004	0.001	0.004	0.001		0.001	0.001
NR_113945.1	0.004	0.004	0.005	0.004	0.004	0.002	0.004	0.001	0.001		0.002
NR_118441.1	0.001	0.001	0.001	0.001	0.001	0.004	0.001	0.005	0.003	0.005	

Figure 5.3. Identification of the environmental isolate secreting apoptotic protease based on 16S rRNA

(A) Molecular phylogenetic analysis and the evolutionary history are inferred by using the maximum likelihood method based on the Kimura 2 parameter model. The 'NR' number stands for the respective NCBI accession numbers. **(B)** Estimates of evolutionary divergence between sequences. The number of base substitutions per site from between sequences is shown. Standard error estimate(s) are shown above the diagonal. Analyses were conducted using the Kimura 2-parameter model.

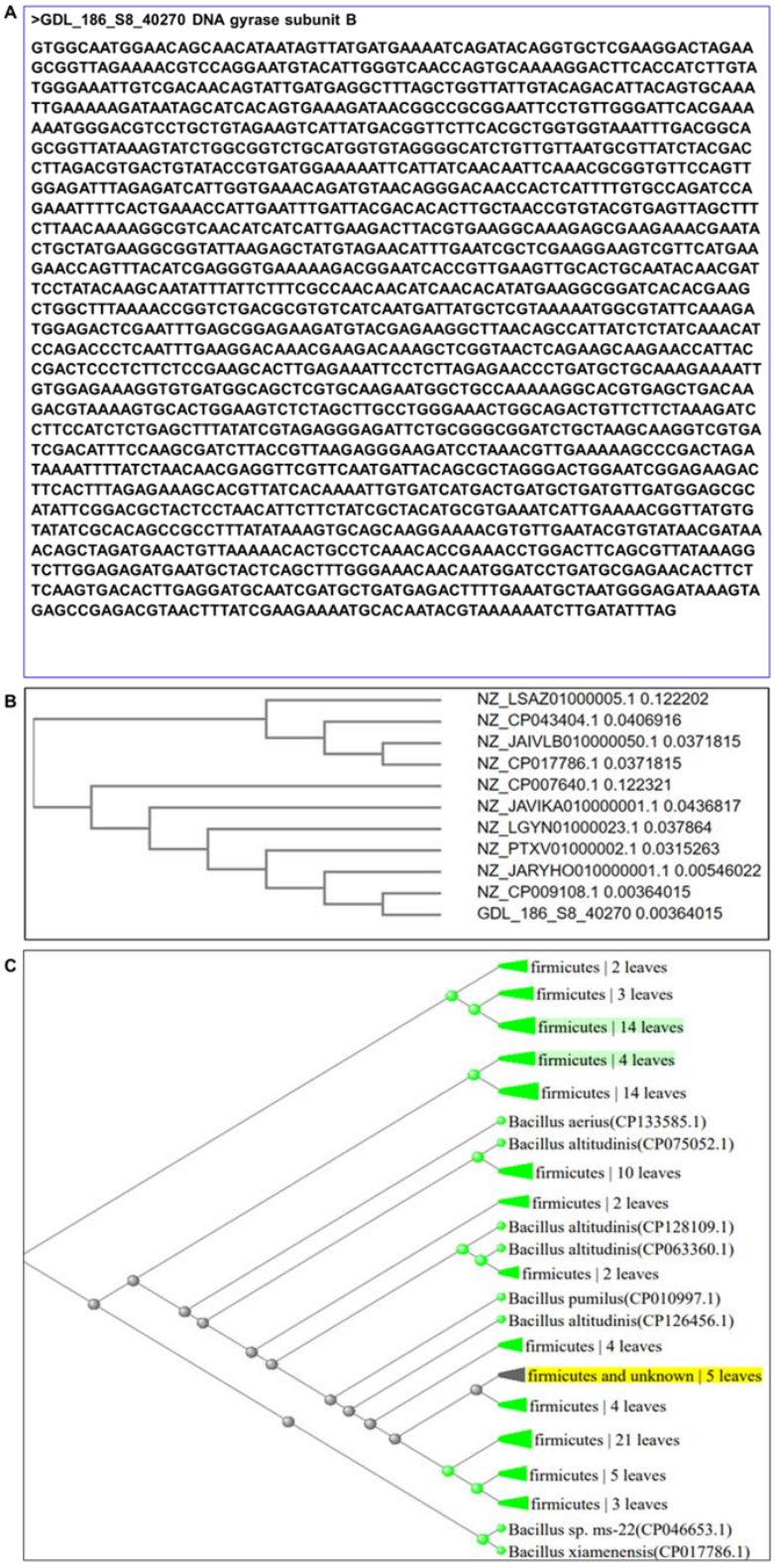

Figure 5.4. Identification of the environmental isolate secreting apoptotic protease based on DNA gyrase B (A) Gene sequence of DNA gyrase B. **(B and C)** Molecular phylogenetic analysis based on DNA gyrase B subunit of Bacillus species and the evolutionary history is inferred by using the neighbour-joining method based on the Kimura 2 parameter model using Clustal omega and NCBI blast respectively. The 'NR' number stands for the respective NCBI accession numbers.

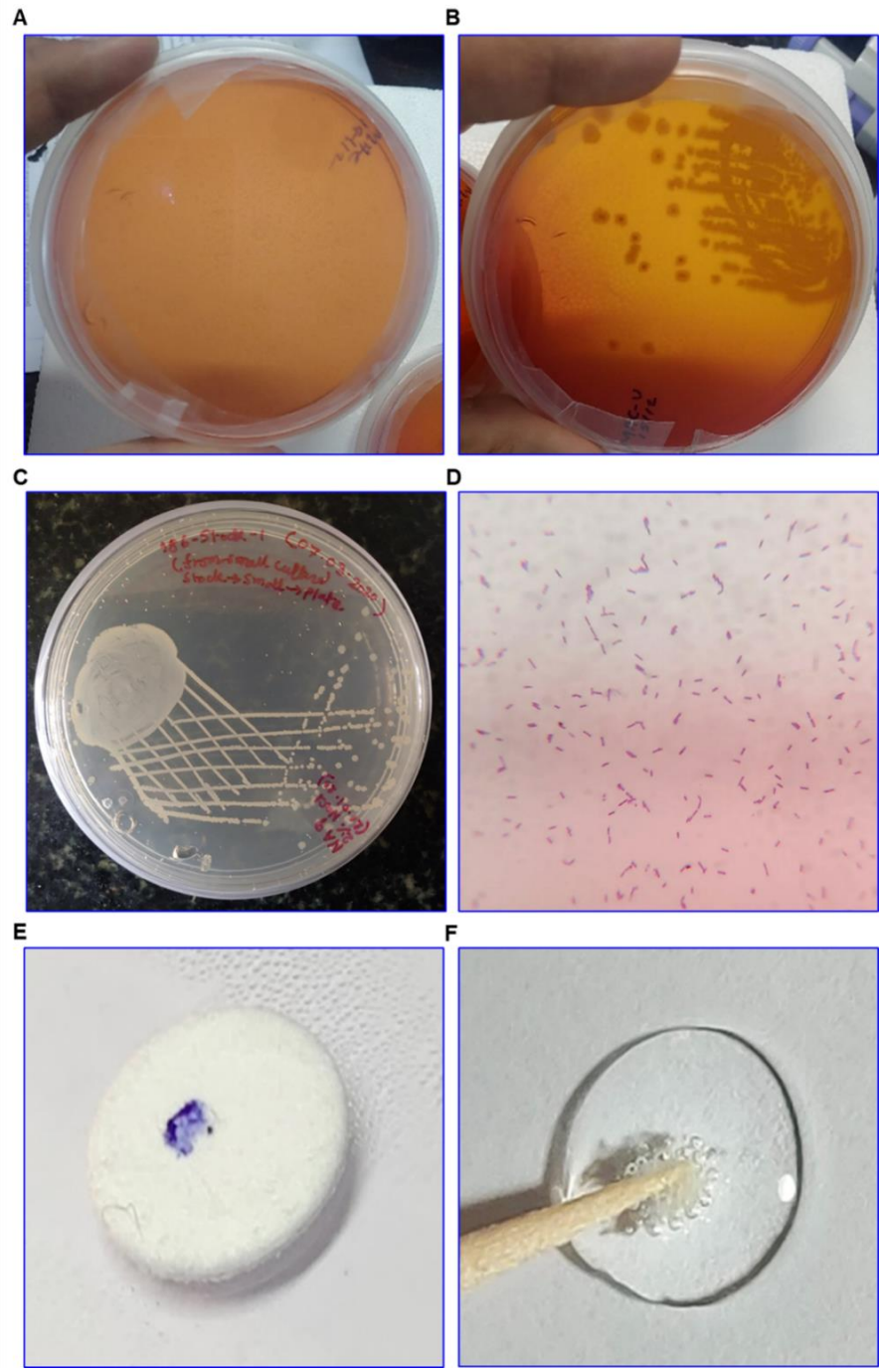

Figure 5.5. Qualitative analysis for the isolate GDL-186

(A and B) Macconkey agar plates show pink nucleated bacterial single colonies in the plate without added crystal violet. The yellow colour appeared due to lactose fermentation by the bacterium. **(C)** White to off-white coloured creamy, moist, glossy, round-shaped single bacterial colonies in nutrient agar plates of pH 9.0 containing 2% NaCl. **(D)** Microscopic (100X) observation of the Gram staining of the bacteria shows purplish violet-coloured medium-sized rod-shaped cells arranged singly also some in chains. **(E)** The blue spot on the disk shows the isolate is oxidase-positive. **(F)** Bubble formation of serum shows catalase positivity of the isolate.

A

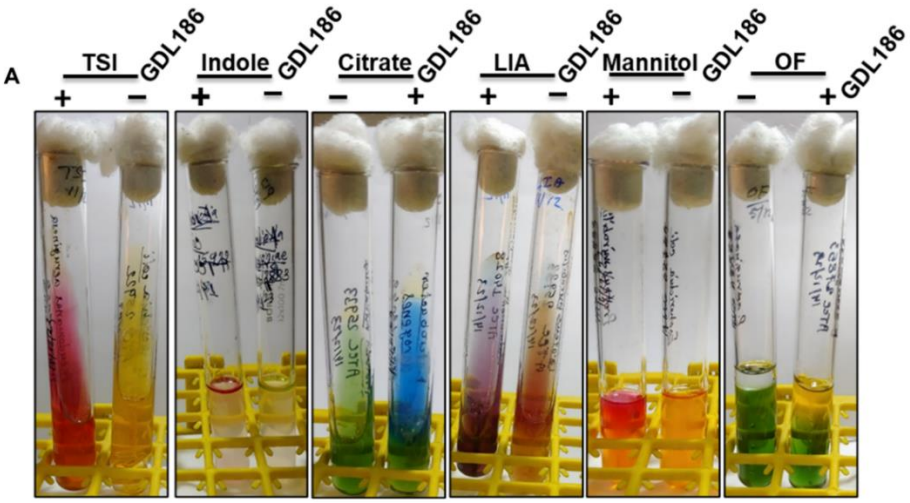

B

Biochemical / Microbiological properties/ Carbon source utilisation	Status
Gram character	Gram positive
Cell size	Medium rods
Cell arrangement	Arranged singly, some in chains
Motility	Positive
Colony morphology	White to off-white coloured, glossy, circular
Pigmentation	White
Lactose	Positive
D-Mannitol	Negative
D-Glucose	Positive
D-Arabinose	Positive
Starch	Positive
Fructose	Positive
Triple Sugar Iron Agar	Acid Positive, Gas Negative
Hydrogen Sulphide Gas	Negative
Lysine Iron Agar	Acid Positive, Gas Negative
Oxidase	Positive
Catalase	Positive
Citrate	Positive
Indole	Negative
Oxidative fermentation	Positive

Figure 5.6. Biochemical characteristics of *Bacillus altitudinis* isolate GDL-186

(A and B) Major biochemical and microbiological tests reveal the characteristics of the isolate GDL-186. Here, *Escherichia coli* and *Pseudomonas aeruginosa* were used as control organisms for the biochemical tests.

5.2. Purification and identification of secreted protease named Peptidase M84 from *Bacillus altitudinis* GDL-186

- We concentrated the probable protease-containing culture supernatant through dialysis and examined the resultant non-binding and binding fractions for proteolytic activity (Figure 5.7.A and B). Interestingly, protease activity was observed in the non-binding fraction (Figure 5.7.C). This fraction was pooled, concentrated, and further analysed using gel filtration chromatography on a Sephadex G-75 column. Two fractions, indicated by two distinct peaks in the chromatogram, were eluted (Figure 5.7.D). The first fraction (G75 '1') exhibited higher protease activity compared to the second (G75 '2') (Figures 5.7.E). The first peak from the Sephadex G-75 elution was pooled, concentrated, and analysed using SDS-PAGE (15%). Two major bands, around 25 kDa and 16 kDa, were distinctly observed. Upon pre-incubation with EDTA, only a single band at 25 kDa remained (Figure 5.8.A). Additionally, this fraction showed a single band in Native PAGE (10%) (Figure 5.8.B). These bands were further characterised by nano-LC-MS/MS-TOF, revealing that the peptide sequence was homologous to "Peptidase M84" from *Bacillus altitudinis* (Figure 5.8.C). This enzyme typically contains a consensus amino acid sequence HExxH and a Met-turn motif "CLMNY" downstream of its active site, where histidines and glutamic acid function as zinc ligands and catalytic bases, respectively.

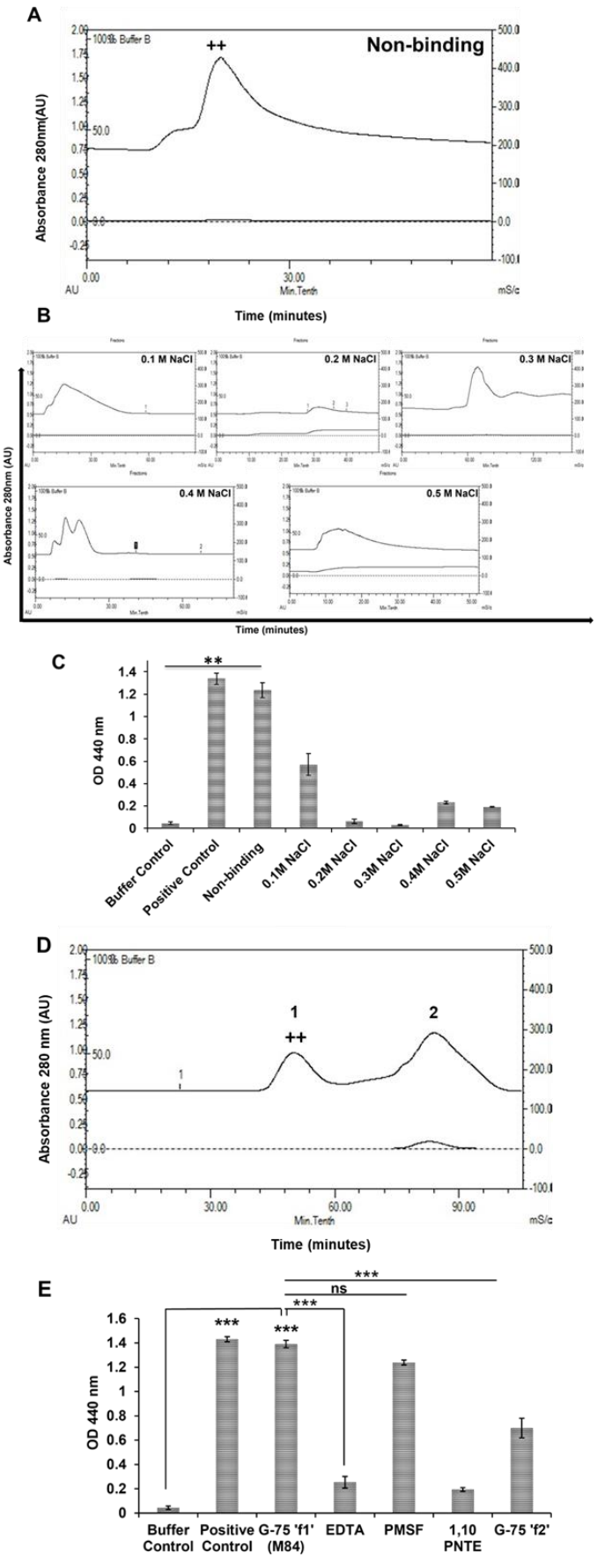

Figure 5.7. Purification of secreted protease from *Bacillus altitudinis* GDL-186

(A) Chromatogram of DEAE-52 anion exchange chromatography of the ammonium sulphate precipitated crude protein fraction from GDL-186 culture supernatant. **(B)** Chromatogram profile of DEAE-52 ion-exchange chromatogram profile of binding fractions of the crude protein extract from the culture supernatant of *Bacillus altitudinis* strain GDL-186 eluted by a gradient of NaCl (0.1 M – 0.5 M)**. (C)** Azocasein assay with protein fractions (5.0 µg) obtained from DEAE-52 column shows higher protease activity in the non-binding fraction (++) as compared to the NaCl (0.1 M–0.5 M) eluted binding fractions. **(D)** The chromatogram of the G-75 gel filtration chromatography shows separation of the non-binding fraction, represented as two individual peaks (G-75'1' and G-75'2'). **(E)** Azocasein assay with G-75 fractions shows maximum protease activity in the G-75 '1' (++) fraction. EDTA and 1,10-phenanthroline inhibit this activity. All statistical analysis was done by applying Student's t test (two-tailed). Data are expressed in ±SEM. In all panels, ns $p > 0.05$, $*p \leq 0.05$, $**p \leq 0.01$, and $***p \leq 0.001$. In each panel, error bars were calculated based on results obtained from a minimum of three independent experiments

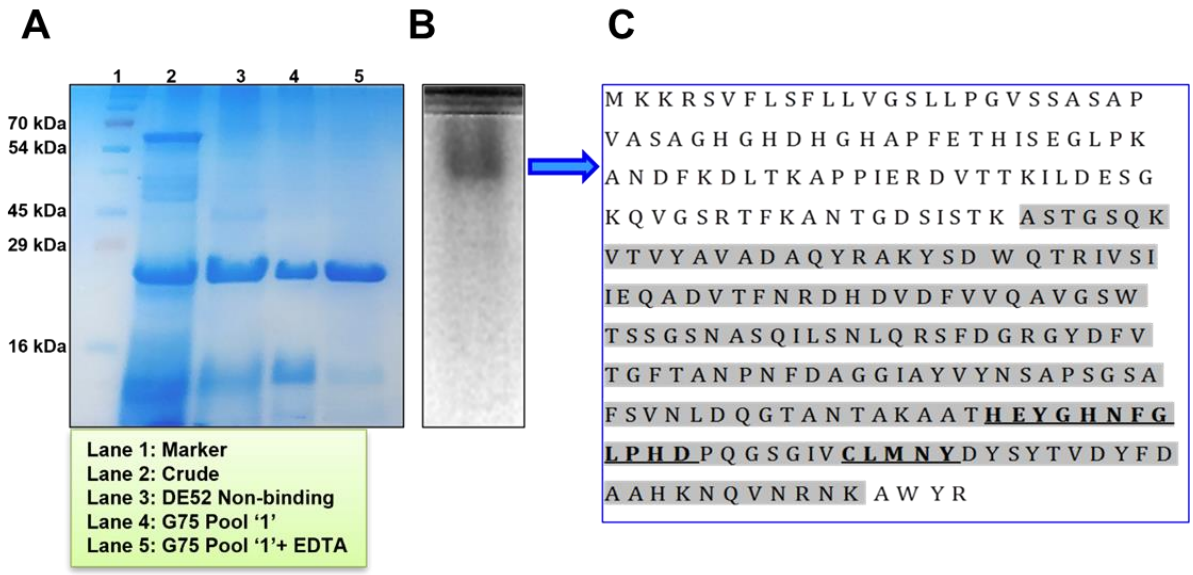

Figure 5.8. Identification of Peptidase M84

(A) 15% SDS-PAGE profile of the purified protease shows two major bands near 25 kDa and 16 kDa, which upon pre-incubation with EDTA shows a single band at 25 kDa. **(B)** 12% Native-PAGE profile of the purified protease (G-75 "1") shows a single band. **(C)** Protein bands were identified by Nano-LC-MS/MS-TOF peptide sequencing which exhibited homology with "Peptidase M84". The peptides

showing homology are with the background colour. The active sites and the zinc-binding domains of the protease are underlined.

5.3. Inhibition of the protease activity revealed the metallo-protease nature of Peptidase M84 which was optimally active at normal physiological pH and temperature

- Purified Peptidase M84 was also proteolytically active against azocasein. This activity was yet again inhibited by EDTA and 1,10- phenanthroline but remained unaltered with PMSF (Figure 5.7.E). Inhibition studies once again confirmed that this purified Peptidase M84 was a zinc-containing metallo-protease. Peptidase M84 exhibited maximum activity against azocasein at temperatures ranging from 37ºC to 40ºC which decreased gradually at 50ºC–60ºC. In line with this, Peptidase M84 showed suboptimal activity at temperatures ranging from 4ºC to 25ºC. At higher temperatures (60ºC–70ºC), the proteolytic activity was almost completely abolished (Figure 5.9.A). Peptidase M84 showed proteolytic activity over a wide range of pH values (from 4.0 to 11.0). Although the optimal and the minimal activities of Peptidase M84 were recorded at pH 8.0 and pH 4.0, respectively, the enzyme kept 80–90% activity at pH 7.0–10.0 (Figure 5.9.B). We also evaluated the effect of Zn^{2+} on the azocaseinolytic activity of Peptidase M84. We observed that the Peptidase M84 protease activity was gradually increased with the Zn^{2+} concentration starting from 0.5 mM up to 2 mM. Interestingly, this activity was decreased in the presence of higher concentrations (5 mM and above) of $Zn^{2+.}$ This activity was completely abolished by pre-treatment with EDTA or 1,10-phenanthroline. (Figures 5.9.C and D) This can be explained by the binding of Zn^{2+} to non-catalytic ion-binding sites of metzincins, triggering a conformational change resulting in the loss of proteolytic activity or the precipitating effect induced by $Zn^{2+.}$ Studies suggested that the addition of excess Zn^{2+} decreased the proteolytic activity of metzincins over the pH range from 7.0 to 9.0, pointing to this effect on $Zn(OH)_2$ precipitation on the protein (Gomes et al., 2015). Based on this, we can conclude the protease activity of Peptidase M84 is dependent on Zn^{2+}. Additionally, the native gelatine zymogram profile revealed Peptidase M84 to be proteolytically active against gelatine. A clear hollow zone due to gelatine degradation was attained in Native PAGE (with 0.1% gelatine) followed by Coomassie staining (Figure 5.9.E). Besides, the full-length

amplified 813 bp gene encoded Peptidase M84 of *Bacillus altitudinis* was also detected in 0.8% agarose gel after PCR amplification (Figures 5.9.F). The molecular phylogenetic tree of Peptidase M84 sequence derived from NCBI blast showed the distribution of the M84 metallo-proteases in Bacillus species (Figure 5.10.A and B)

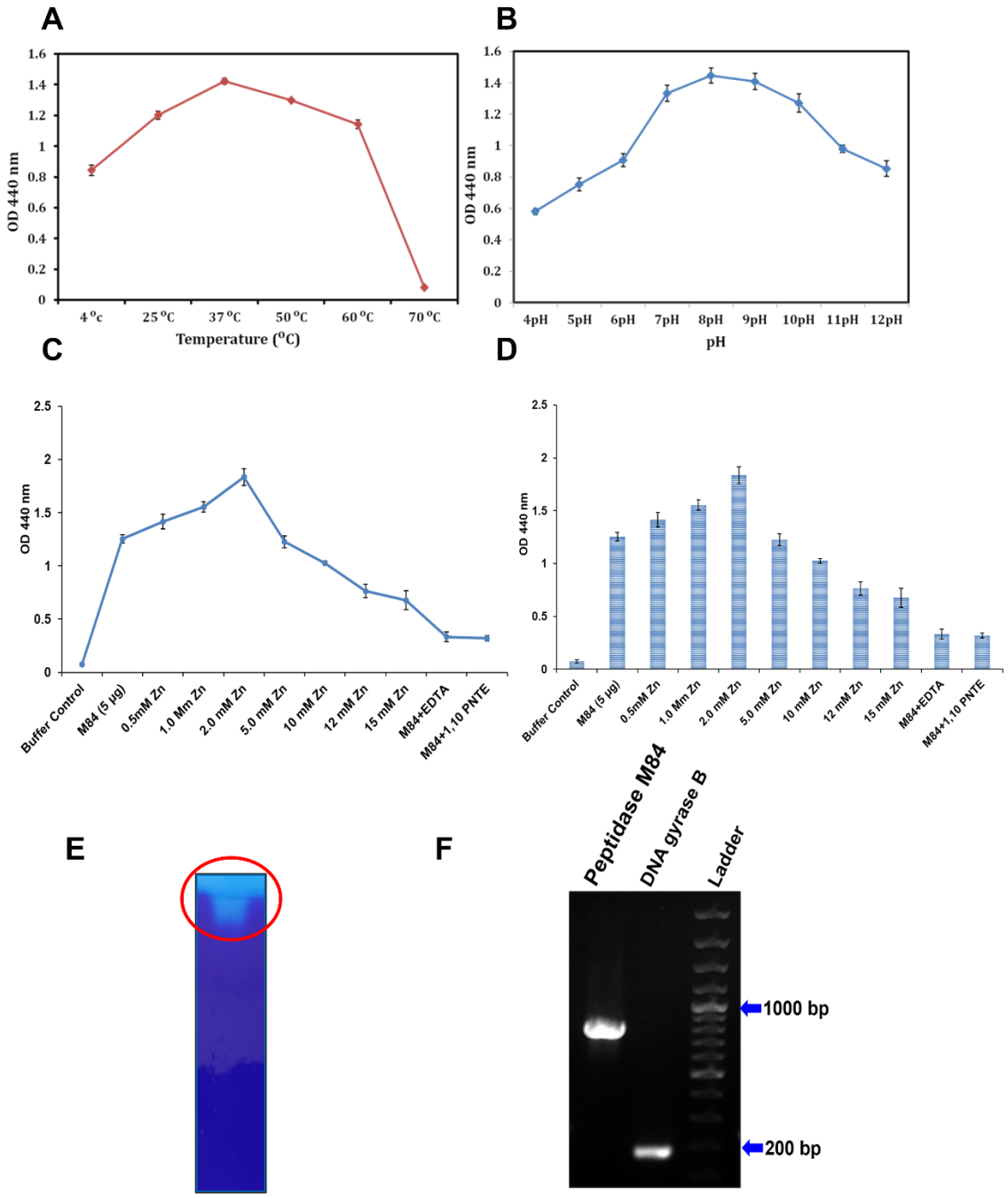

Figure 5.9. Identification of Peptidase M84

(A and B) Determination of the optimum temperature and pH of Peptidase M84. **(C and D)** Azocasein assay shows zinc-dependent proteolytic activity of Peptidase M84. **(E)** Native gelatine zymogram profile of purified Peptidase M84 shows proteolytic degradation of gelatine. **(F)** PCR amplification of the full-length (813bp) peptidase M84 gene (Lane 1) and DNA gyrase B gene (Lane 2) from *Bacillus altitudinis* strain GDL-186. All statistical analysis was done by applying Student's t-test (two-tailed). Data are expressed in ± SEM. In all panels, ns $p>0.05$, *$p\leq0.05$, 55 **$p\leq0.01$, and ***$p\leq0.001$. In each panel, error bars were calculated based on results obtained from a minimum of three independent experiments.

A

>GDL_186_S8_36590 peptidase M84

ATGAAAAAGCGTTCAGTCTTTTTGTCATTTTTATTGGTAGGTAGTTTG
TTACCGGGGGTAAGTTCAGCTTCAGCACCAGTTGCAAGTGCAGGTC
ATGGGCATGATCATGGTCATGCACCGTTCGAAACACATATTAGTGAA
GGGTTGCCAAAGGCAAACGATTTTAAAGATTTGACGAAGGCACCTC
CTATTGAAAGAGATGTGACAACAAAAATTTTAGACGAGTCTGGTAAA
CAGGTAGGGTCTAGAACCTTTAAAGCAAATACAGGAGATTCGATTTC
AACAAAAGCTAGTACAGGCAGTCAGAAAGTGACCGTCTATGCAGTA
GCTGATGCGCAGTATCGTGCGAAATATAGTGATTGGCAGACGCGCA
TTGTCAGCATCATTGAGCAAGCGGATGTGACATTTAACCGTGATCAT
GATGTGGACTTTGTTGTACAAGCTGTAGGGTCTTGGACGTCTTCAGG
ATCAAATGCATCACAAATTTTGTCTAACCTTCAGCGTAGCTTTGATGG
CAGAGGATACGATTTTGTCACAGGATTTACAGCAAATCCAAACTTTG
ATGCTGGCGGAATCGCTTATGTTTACAATAGTGCACCGAGCGGAAGT
GCATTCAGTGTCAACCTTGATCAAGGAACAGCGAATACAGCAAAAG
CGGCTACACATGAATACGGCCATAACTTTGGTTTGCCGCATGACCCT
CAAGGCAGCGGAATTGTCTGCTTAATGAATTATGATTATTCTTACACT
GTCGATTACTTCGATGCGGCTCATAAAAATCAAGTGAACCGTAATAA
AGCTTGGTACAGATAA

B

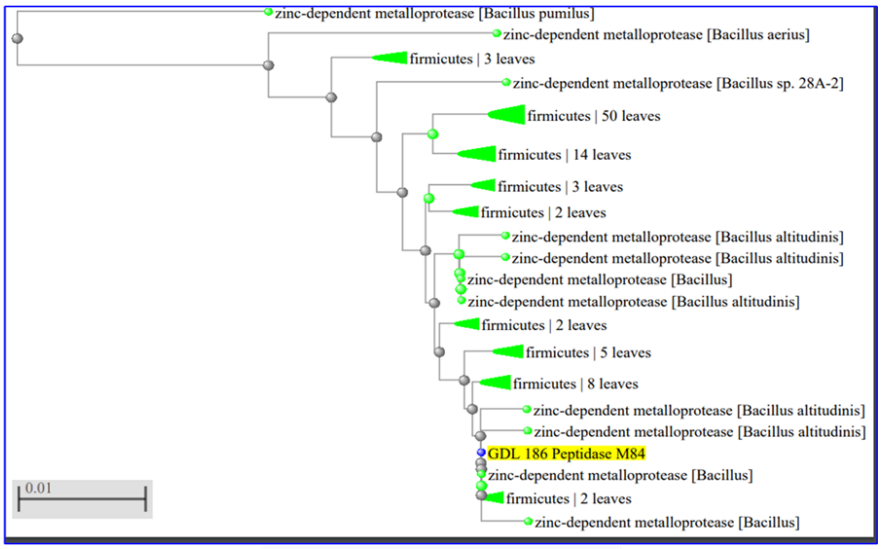

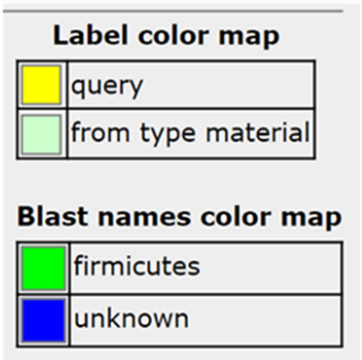

Figure 5.10. Molecular and phylogenetic analysis of DNA gyrase B and Peptidase M84 genes from *Bacillus altitudinis* GDL-186

(A) The gene sequence of Peptidase M84. **(B)** Molecular phylogenetic tree for Peptidase M84 from *Bacillus altitudinis* GDL-186 derived from NCBI constraint-based multiple alignment tool (COBALT) analysis.

5.4. Peptidase M84 exhibited apoptosis and suppressed the proliferation of ovarian cancer cells but had no such impact on IOSE cells.

- The MTT cell viability assay demonstrated a gradual decrease in the percentage of viable ovarian cancer cells with increasing concentrations of Peptidase M84, ranging from 0.5 µg/ml to 5.0 µg/ml. The *in vitro* safe dose (IC_{50}) of Peptidase M84 was determined to be **2.0 µg/ml** for PA-1 and SKOV3 cells, and **3.0 µg/ml** for ID8 cells (Figure 5.11.A – C). These concentrations were also used to detect apoptosis and study bio-signalling pathways in these cell lines.

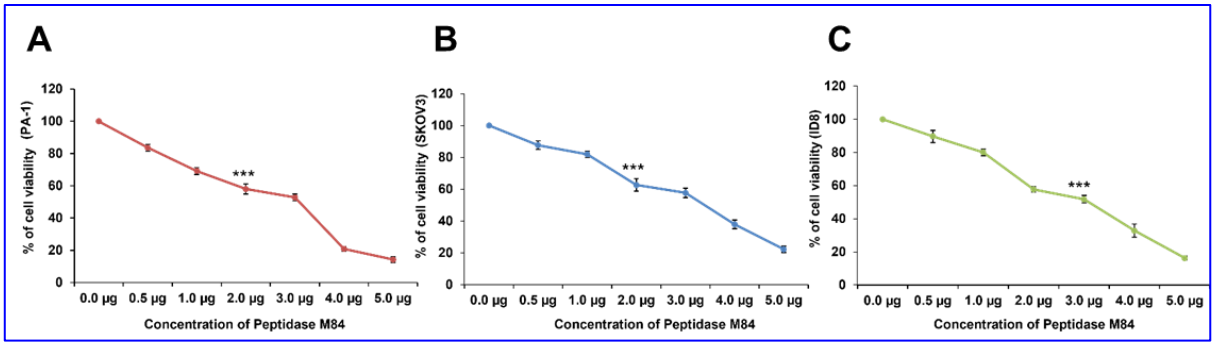

Figure 5.11. Cytotoxic and apoptotic effects of Peptidase M84 on ovarian cancer cells

(A-C) MTT assay shows the IC_{50} value of Peptidase M84 in PA1, SKOV3 and ID8 cells.

- Peptidase M84 treatment also altered the morphology of PA-1 and SKOV3 cells. At lower concentrations, Peptidase M84 caused cell distension, while higher concentrations induced cell rounding after 18 hours of treatment (Figure 5.12.A). During apoptosis, chromatin becomes highly condensed and fragmented, forming apoptotic bodies (Deb et al., 2014). This was confirmed by Hoechst 33342 staining, which showed distinct chromatin condensation in Peptidase M84-treated PA-1, SKOV3, and ID8 cells, with percentages of condensed nuclei at 43.66%, 38.33%, and 44.33% respectively, compared to 13%, 10.6%, and 11.33% in control cells (Figure 5.12.B and C). This indicates that Peptidase M84-treated cells had condensed, bright nuclei, while untreated control cells had less condensed chromatin.

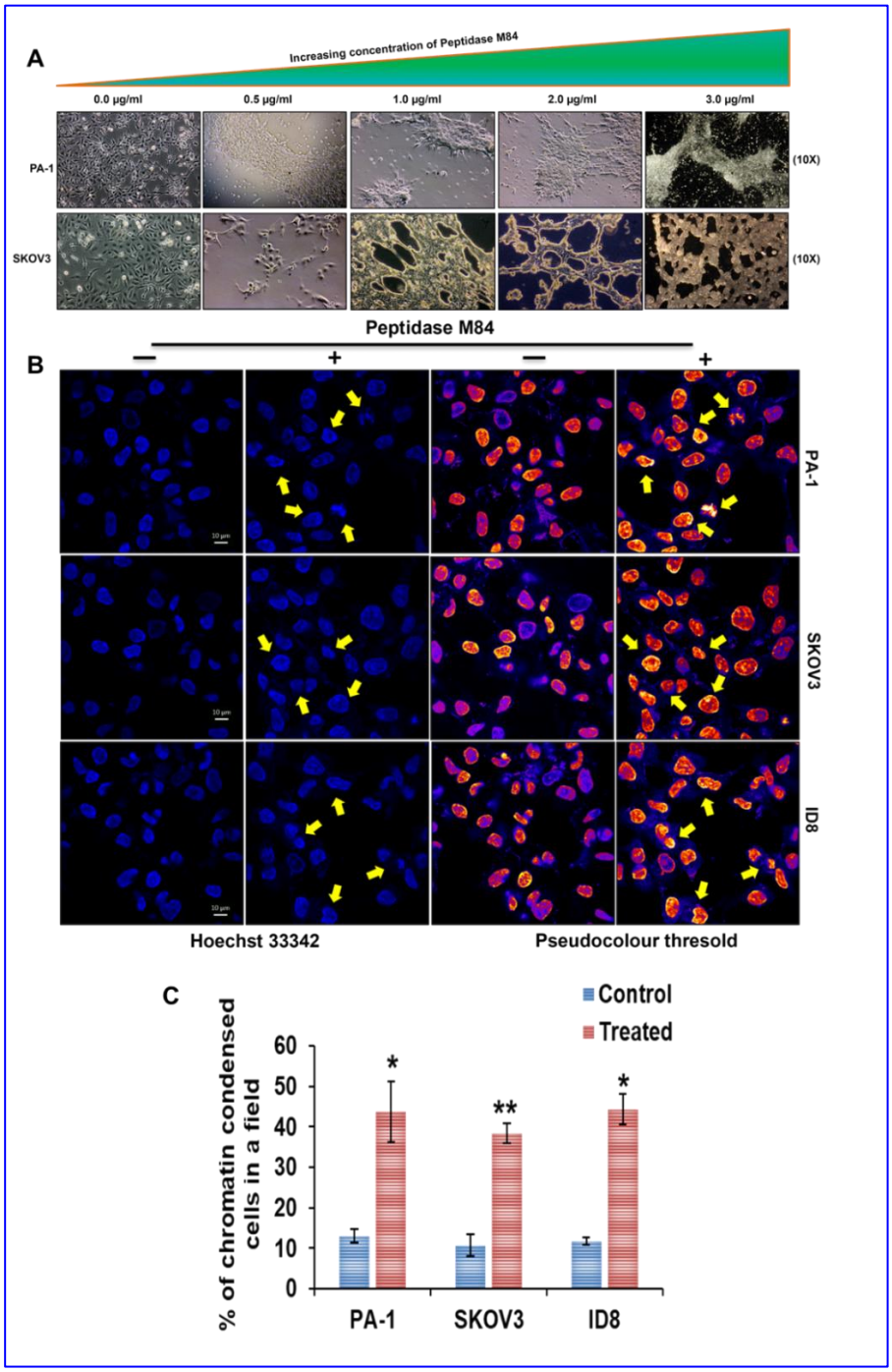

Figure 5.12. Peptidase M84 induced cellular changes in ovarian cancer cells (A) PA-1 and SKOV3 cells were treated with different concentrations of Peptidase M84 for 18 h. Cells were observed with a phase-contrast microscope. Cell distending and rounding effects of Peptidase M84 are noticed in lower and higher concentrations respectively. **(B and C)** Cells were stained with Hoechst 33342 after treatment with Peptidase M84. The representative images of Hoechst 33342 stained nuclei (arrow) are shown. The percentage of condensed nuclei is represented graphically. All statistical analysis was done by applying Student's t test (two-tailed). Data are expressed in ±SEM. In all panels, ns $p > 0.05$, $*p \leq 0.05$, $**p \leq 0.01$, and $***p \leq 0.001$. Scale bars: 10 µm.

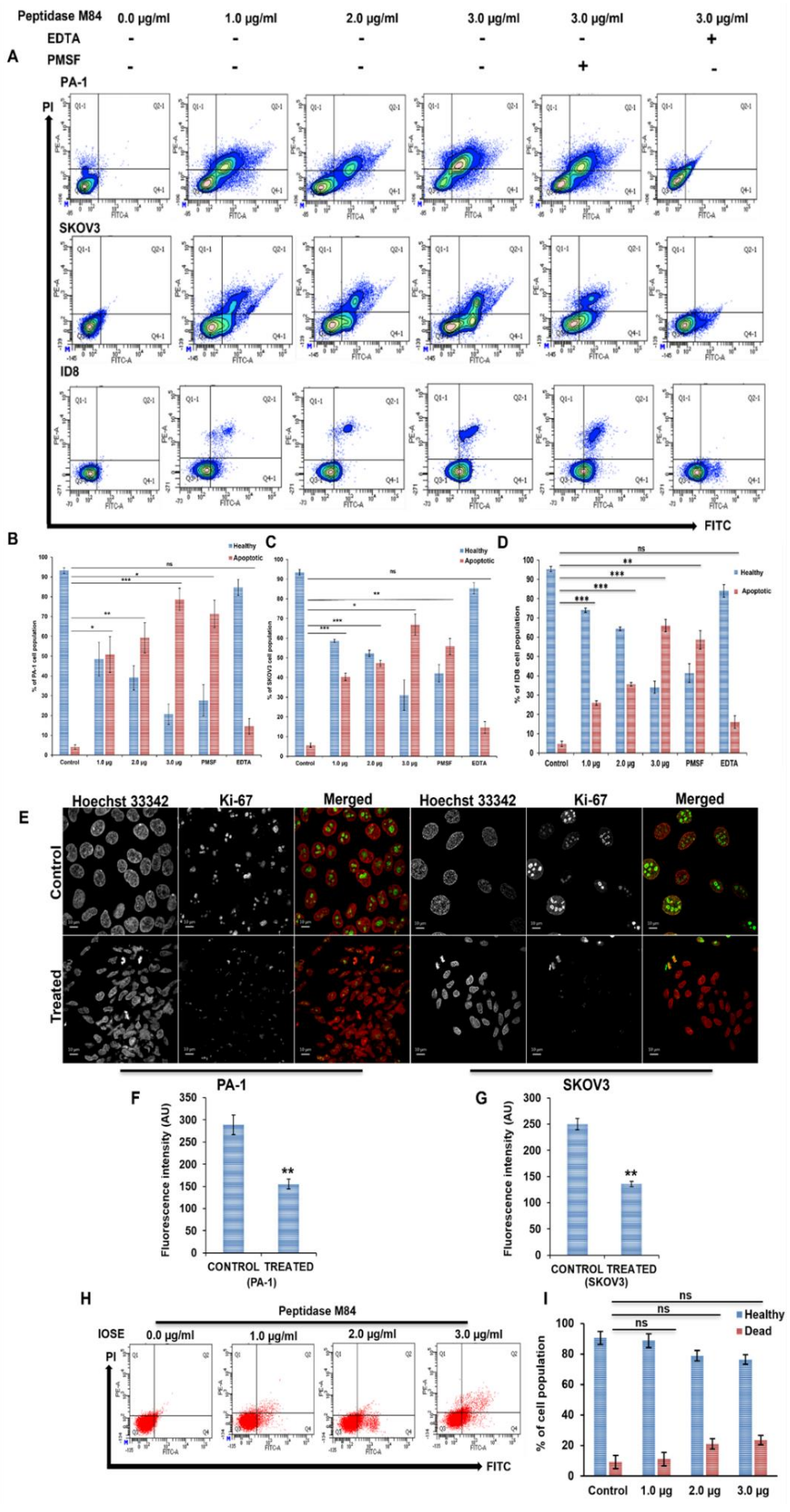
Peptidase M84
0.0 µg/ml
1.0 µg/ml
2.0 µg/ml
3.0 µg/ml
3.0 µg/ml
3.0 µg/ml
EDTA
PMSF
A
PA-1
SKOV3
ID8
PI
FITC
B
C
D
Healthy
Apoptotic
Control
1.0 µg
2.0 µg
3.0 µg
PMSF
EDTA
E
Hoechst 33342
Ki-67
Merged
Control
Treated
F
PA-1
Fluorescence intensity (AU)
CONTROL TREATED
(PA-1)
G
SKOV3
CONTROL TREATED
(SKOV3)
H
Peptidase M84
IOSE
0.0 µg/ml
1.0 µg/ml
2.0 µg/ml
3.0 µg/ml
PI
FITC
I
Healthy
Dead
% of cell population
Control
1.0 µg
2.0 µg
3.0 µg

Figure 5.13. Detection of cytotoxicity and apoptosis in Peptidase M84 treated ovarian cancer cells and human ovarian normal epithelial cells (IOSE). (A) Flow cytometric analysis of Peptidase M84 treated PA1, SKOV3, and ID8 cells shows dose-dependent apoptosis. EDTA inhibition significantly reduces the effect while PMSF treatment does not affect cell viability. **(B–D)** Bar diagrams show the percentage of healthy and apoptotic cell populations. **(E–G)** Confocal imaging of nuclear Ki-67 (green) coupled with bar diagrams of mean fluorescence intensity (MFI) (calculated in Fiji) shows a significant reduction in PA-1 and SKOV3 cell proliferation due to Peptidase M84 treatment. **(H and I)** Flow cytometric analysis of the Peptidase M84 treated IOSE and PEMV cells shows no significant apoptosis as compared to the untreated cells. Bar diagrams of the data are also being presented. All statistical analysis was done by applying Student's t test (two-tailed). Data are expressed in ±SEM. In all panels, ns $p > 0.05$, $*p \leq 0.05$, $**p \leq 0.01$, and $***p \leq 0.001$. Scale bars: 10 μm.

- To further investigate the cytotoxic effect of Peptidase M84, PA-1, SKOV3, and ID8 cells were treated with doses ranging from 1.0 μg/ml to 3.0 μg/ml for 18 h. Flow cytometry analysis showed that Peptidase M84 induced significant apoptosis in these cell lines compared to untreated cells. The inhibition of protease activity with EDTA significantly reduced the percentage of apoptotic cells, while PMSF had no effect (Figure 5.13.A – D). These findings indicate that the metalloprotease activity of purified Peptidase M84 promotes apoptosis in human and mouse ovarian cancer cells.
- Ki-67 protein, a proliferation marker for human tumour cells, is highly expressed in all stages of the cell cycle except G_0 and in dead cells (Scholzen & Gerdes, 2000). Lower levels of Ki-67 were observed in Peptidase M84-treated PA-1 and SKOV3 cells compared to untreated cells, indicating that Peptidase M84 significantly inhibited cancer cell proliferation (Figure 5.13.E – G). In contrast, higher levels of nuclear Ki-67 in untreated control cells indicated rapid proliferation and increased survivability.
- To evaluate specificity, the effect of Peptidase M84 was tested on IOSE cells at similar doses. Nearly all cells remained viable even at a 3.0 μg/ml concentration, demonstrating that Peptidase M84 selectively induces apoptosis in malignant ovarian cells without affecting normal cells (Figure 5.13.H and I). Based on these

findings, we were motivated to explore the detailed molecular mechanisms underlying Peptidase M84-induced apoptosis in ovarian cancer cells.

5.5. Peptidase M84 augmented ROS generation and activated the intrinsic canonical pathway of apoptosis in ovarian cancer cells

- Excessive production of reactive oxygen species (ROS) can surpass the cellular antioxidant capacity, leading to oxidative stress. This stress influences various signalling pathways and can cause oxidative damage, ultimately resulting in cell death (Higuchi et al., 1998; Von Harsdorf et al., 1999). In this study, we monitored the oxidative stress induced by Peptidase M84 using DCFDA staining. ROS stimulation converts DCFH to the fluorescent DCF upon oxidation. Peptidase M84 treatment increased ROS generation in PA-1, SKOV3, and ID8 cells, as indicated by higher mean fluorescence intensity levels of DCF compared to untreated cells over time (6 hours and 18 hours) (Figure 5.14.A – C). This increase in ROS may trigger apoptotic signals. In contrast, Peptidase M84 did not promote ROS generation in IOSE cells (Figure 5.14.E – G).
- Further, we assessed changes in mitochondrial membrane potential ($\Delta\psi m$) using JC-1 dye uptake patterns. Peptidase M84 treatment caused alterations in $\Delta\psi m$ in PA-1 and SKOV3 cells. A decrease in $\Delta\psi m$, a hallmark of apoptosis, was evident as an increased ratio of green to red fluorescence intensity in a time-dependent manner (6 hours and 18 hours) compared to untreated control cells (Figure 5.15.A and B).
- To investigate DNA damage, we performed a comet assay on PA-1 and SKOV3 cells following 18 hours of Peptidase M84 treatment. This treatment significantly induced comet tail moment in these ovarian cancer cells compared to untreated controls (Figure 5.16.A and B).
- We also examined the expression profiles of key regulatory proteins to understand the apoptotic mechanisms induced by Peptidase M84. Our results showed downregulation of the anti-apoptotic protein Bcl-2 and upregulation of the pro-apoptotic marker Bax in PA-1 and SKOV3 cells. Additionally, Peptidase M84 treatment activated caspase 9 and caspase 3 and increased cleaved PARP levels. However, caspase 8 expression levels remained unchanged, indicating that the extrinsic (FADD-caspase 8) apoptosis pathway was not involved (Figure 5.17.A and

B). Interestingly, normal IOSE cells treated with Peptidase M84 did not show caspase 3 activation (Figure 5.17.C and D).

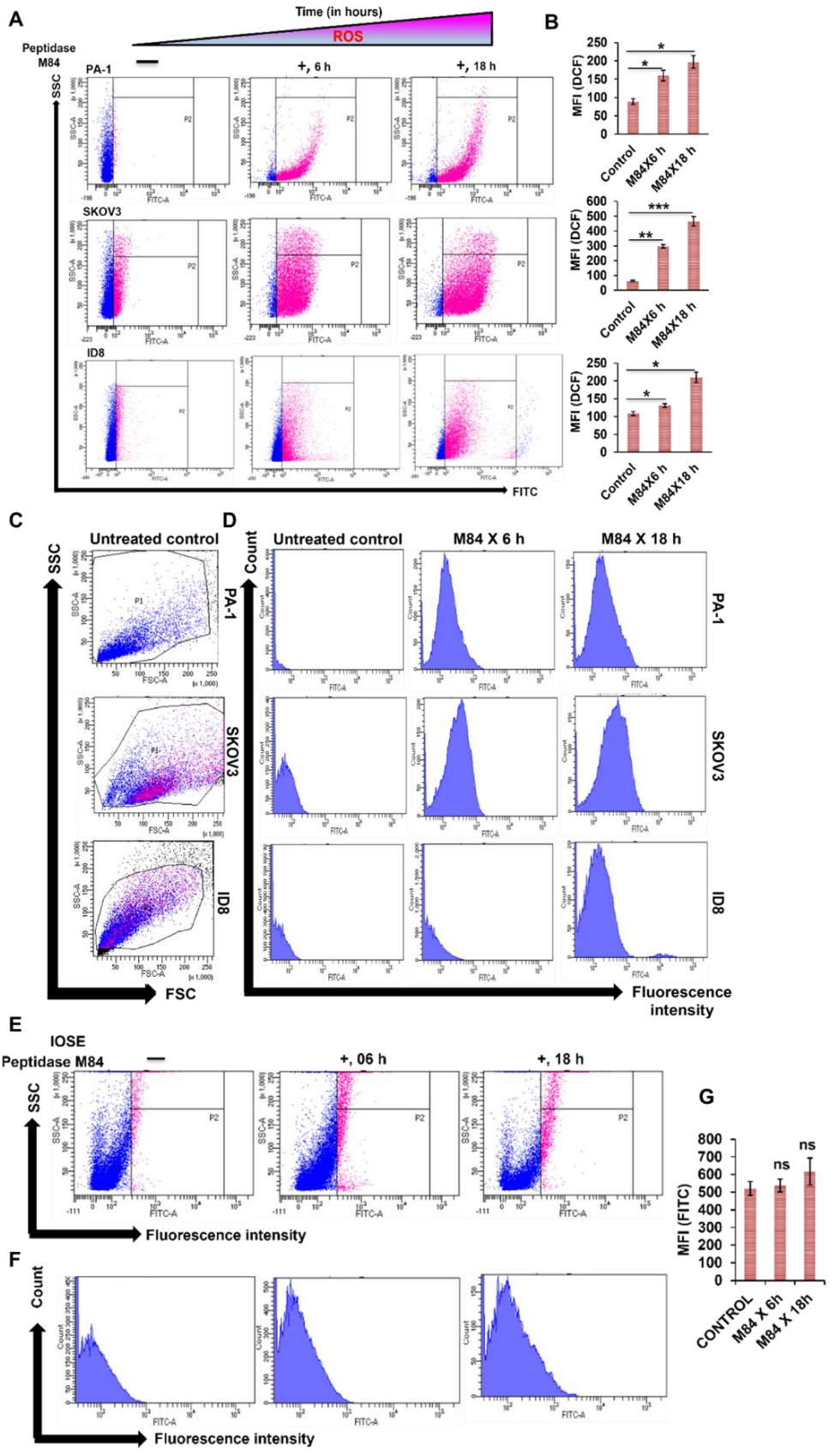

Figure 5.14. Peptidase M84 induced ROS generation in ovarian cancer cells. (A) A time-dependent ROS generation was examined by DCFDA staining in PA-1, SKOV3, and ID8 cells after Peptidase M84 treatment. Quadrant "P2" represents cells producing ROS. **(B)** Bar diagrams represent the MFI of DCF. **(C and D)** Detection of time-dependent ROS generation in PA-1, SKOV3 and ID8 cells with the respective gating patterns of untreated cells after Peptidase M84 treatment by DCFDA staining. **(E and F)** Detection of ROS generation in normal IOSE cells after Peptidase M84 treatment by DCFDA staining. No significant ROS generation is found even after 18 h of treatment. **(G)** Bar diagram of mean fluorescence intensity of DCF is represented. All statistical analysis was done by applying Student's t test (two-tailed). Data are expressed in ±SEM. In all panels, ns $p > 0.05$, $*p \leq 0.05$, $**p \leq 0.01$, and $***p \leq 0.001$.

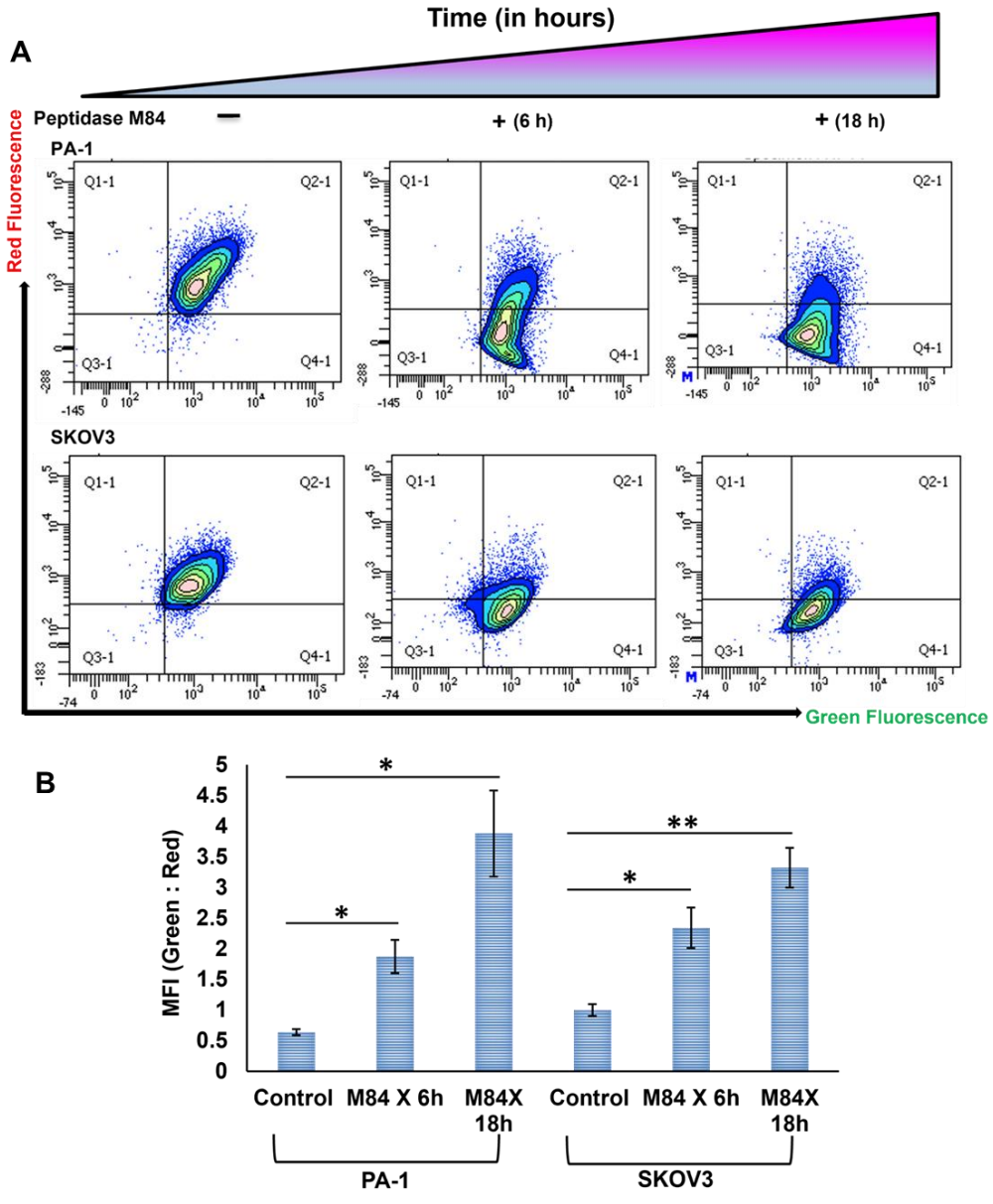

Figure 5.15. M84 induced mitochondrial damage in ovarian cancer cells.

(A and B) JC-1 staining data with bar diagrams of MFI (green: red) show the disruption of mitochondrial membrane potential with time in Peptidase M84 treated PA-1 and SKOV3 cells. Cell population positive for green fluorescence signified disrupted mitochondrial membrane potential. All statistical analysis was done by applying Student's t test (two-tailed). Data are expressed in ±SEM. In all panels, ns $p > 0.05$, ∗$p \leq 0.05$, ∗∗$p \leq 0.01$, and ∗∗∗$p \leq 0.001$

.

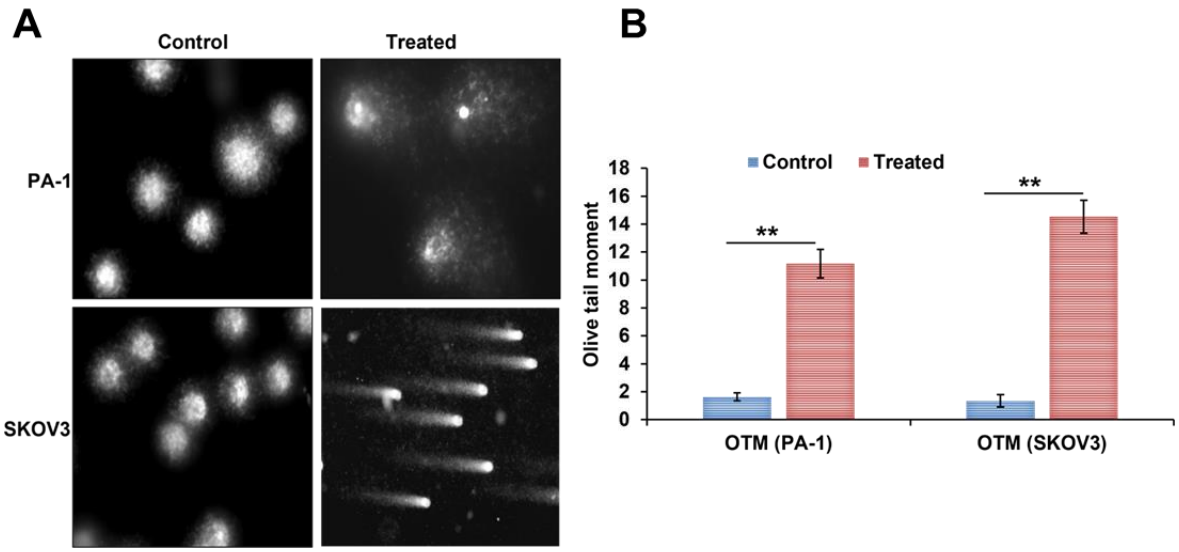

Figure 5.16. Peptidase M84 induced DNA damage in ovarian cancer cells

(A) Comet assay represents an increase in the comet tail length in Peptidase M84 treated PA-1 and SKOV3 cells. **(B)** The bar diagram represents the olive tail moment of cells. All statistical analysis was done by applying Student's t test (two-tailed). Data are expressed in ±SEM. In all panels, ns $p > 0.05$, ∗$p \leq 0.05$, ∗∗$p \leq 0.01$, and ∗∗∗$p \leq 0.001$.

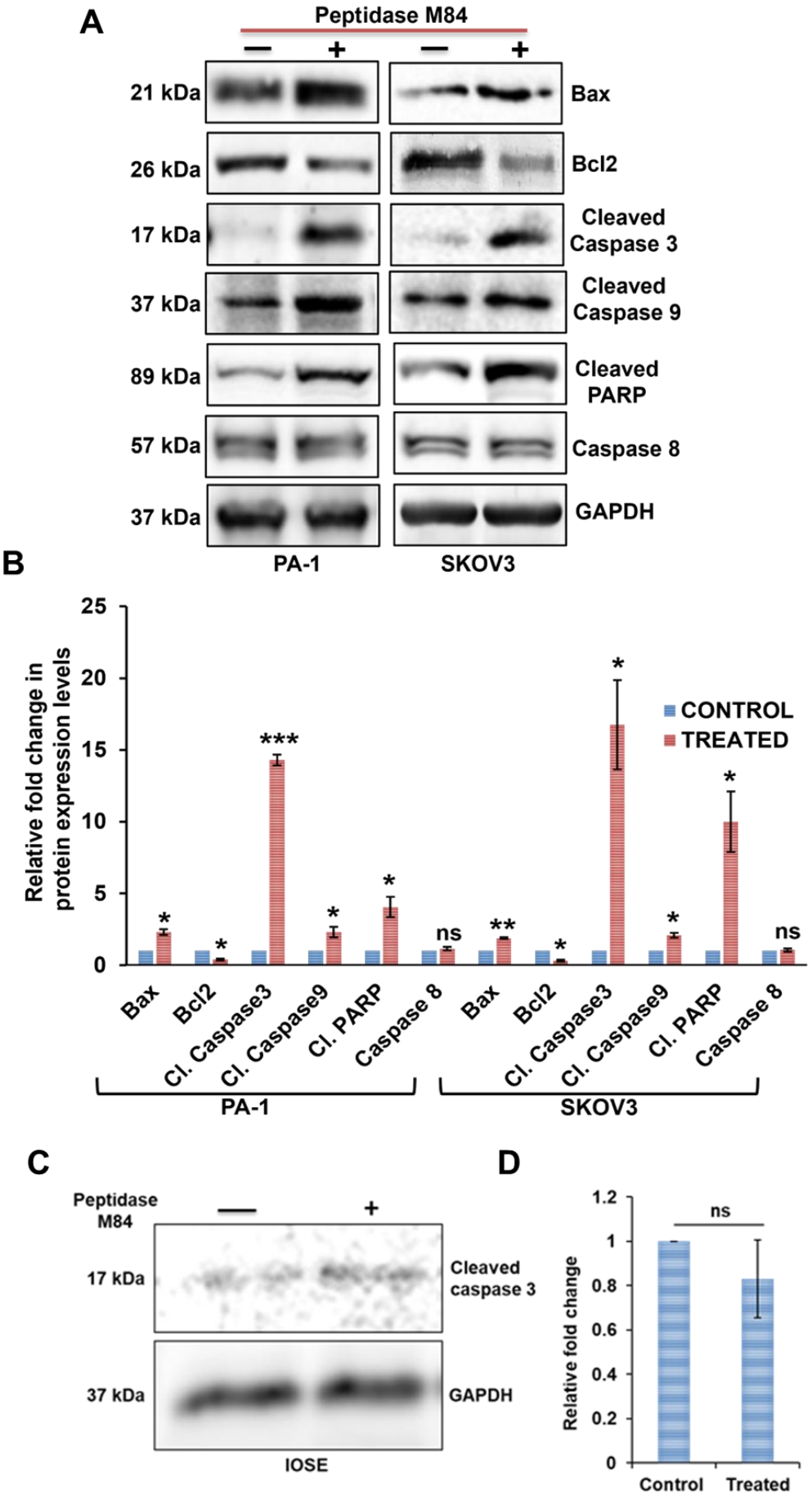
A
Peptidase M84
—
+
—
+
21 kDa
Bax
26 kDa
Bcl2
17 kDa
Cleaved Caspase 3
37 kDa
Cleaved Caspase 9
89 kDa
Cleaved PARP
57 kDa
Caspase 8
37 kDa
GAPDH
PA-1
SKOV3
B
Relative fold change in protein expression levels
25
20
15
10
5
0
CONTROL
TREATED
***
*
ns
**
Bax
Bcl2
Cl. Caspase3
Cl. Caspase9
Cl. PARP
Caspase 8
PA-1
SKOV3
C
Peptidase M84
17 kDa
Cleaved caspase 3
37 kDa
GAPDH
IOSE
D
Relative fold change
1.2
1
0.8
0.6
0.4
0.2
0
ns
Control
Treated

Figure 5.17. Peptidase M84 alters the balance between major pro-apoptotic and anti-apoptotic proteins. **(A and B)** The immunoblots represent expression levels of major proteins of the intrinsic apoptotic pathway in Peptidase M84 induced and un-induced PA-1 and SKOV3 cells. Densitometric analysis for relative protein expression is plotted as a histogram. **(C and D)** Western blot and densitometric bar diagram show no significant cleavage of Caspase 3 in Peptidase M84 treated IOSE cells. Data are expressed in ± SEM. In all panels, ns $p > 0.05$, $*p \leq 0.05$, $**p \leq 0.01$, and $***p \leq 0.001$. Densitometric analysis was performed on ImageJ and Gel Quant. Band intensities were normalized to loading controls GAPDH. Pearson's coefficient was calculated in Fiji (https://imagej.net/software/fiji/).

- Mitochondrial cytochrome c, which functions as an electron carrier in the respiratory chain, translocates to the cytosol during apoptosis to activate specific caspases (Bossy-Wetzel, 1998). We observed a significant increase in cytosolic cytochrome c levels in Peptidase M84-treated PA-1 and SKOV3 cells, as confirmed by densitometric and immunofluorescence data (Figure 5.18.A and B). Damaged mitochondria were detected using mitotracker green FM staining, showing decreased green fluorescence intensity. Additionally, the co-localization between cytochrome c and mitochondria was reduced in treated PA-1 and SKOV3 cells compared to untreated cells. Released cytochrome c appeared as punctate red signals throughout the cytosol and around the nucleus. Pearson's coefficient values confirmed the significant reduction in co-localization between mitochondria and cytochrome c in Peptidase M84-treated cells (Figure 5.18.C – E).

- In summary, our findings indicate that Peptidase M84 from *Bacillus altitudinis* activates the intrinsic pathway of apoptosis in ovarian cancer cells.

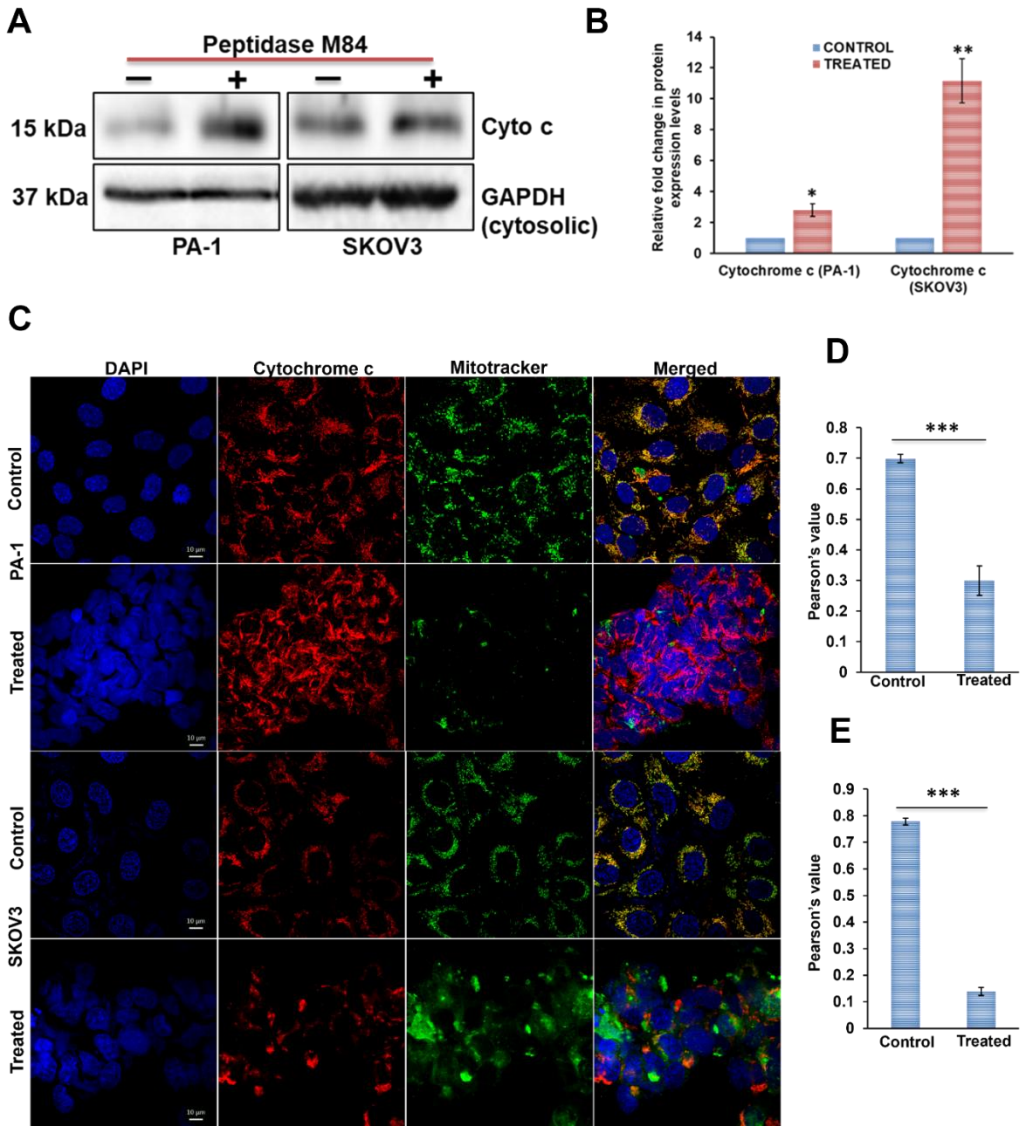

Figure 5.18. Peptidase M84 induces cytochrome c release from damaged mitochondria of ovarian cancer cells. (A and B) Immunoblot with bar diagram of densitometry scan of cytochrome c in the mitochondria-free cytosolic fraction in Peptidase M84 treated PA-1 and SKOV3 cells depict the release of cytochrome c from mitochondria. **(C-E)** Immunofluorescence along with bar diagrams of Pearson's co-efficient values show a reduction in co-localization between mitochondria (green) and cytochrome c (red) due to Peptidase M84 treatment in PA-1 and SKOV3 cells. Data are expressed in ± SEM. In all panels, ns $p > 0.05$, $*p \leq 0.05$, $**p \leq 0.01$, and $***p \leq 0.001$. Scale bars: 10 µm. Band intensities were normalized to loading controls GAPDH. Pearson's coefficient was calculated in Fiji (https://imagej.net/software/fiji/).

5.6. Peptidase M84 specifically interacted with PAR-1 and caused overexpression of PAR-1 in ovarian cancer cells however not in healthy ovarian epithelial cells

- Real-time PCR data revealed a significant overexpression of PAR-1 in PA-1 and SKOV3 cells. Specifically, there was a 4-fold and 7-fold upregulation of PAR-1 mRNA levels in PA-1 and SKOV3 cells, respectively, compared to other PARs (Figure 5.19.A). This time-dependent overexpression occurred 6 and 18 hours after Peptidase M84 treatment (Figure 5.19.B). Immunoblotting confirmed nearly a 2-fold increase in PAR-1 expression in PA-1 and SKOV3 cells and an almost 3.5-fold increase in ID8 cells after 18 h of Peptidase M84 treatment. In contrast, IOSE cells showed no significant change in PAR-1 expression, with almost no detectable PAR-1 expression. Densitometric scan analysis highlighted the differences in PAR-1 expression levels between treated and untreated cells (Figure 5.19.C and D). Immunofluorescence also demonstrated a significant increase in PAR-1 expression in PA-1 and SKOV3 cells following Peptidase M84 treatment (Figure 5.19.E – H). These findings suggest that Peptidase M84 does not induce apoptosis in normal cells due to ineffective modulation of PAR-1.
- To identify the receptor for Peptidase M84 and elucidate their physical interaction, we performed immunoprecipitation. The results showed that Peptidase M84 specifically bound and interacted with PAR-1 in PA-1 and SKOV3 cells. A 50 kDa PAR-1 band was observed in western blots when PAR-1 was immunoprecipitated with Peptidase M84-specific antisera. Additionally, bands corresponding to Peptidase M84 (25 kDa and 16 kDa) were detected when Peptidase M84 was immunoprecipitated with an anti-PAR-1 antibody (Figure 5.19.I – J). Furthermore, co-localisation based confocal imaging validated the binding and interaction between Peptidase M84 and PAR-1. Increased Pearson's coefficient values in Peptidase M84-treated (30 min) PA-1 and SKOV3 cells, compared to untreated cells, indicated a probable interaction between PAR-1 and Peptidase M84 (Figure 5.19.K – M and Figure 5.20.A and B). These findings were further supported by western blots using antisera against Peptidase M84, which showed two major bands at 25 kDa and 16 kDa, consistent with the 15% SDS-PAGE profile of purified Peptidase M84 (Figure 5.21.A). In addition to this SDS-PAGE also showed the presence of both Peptidase M84 and PAR-1 in Coomassie-stained gel due to interaction (Figure 5.21.B).

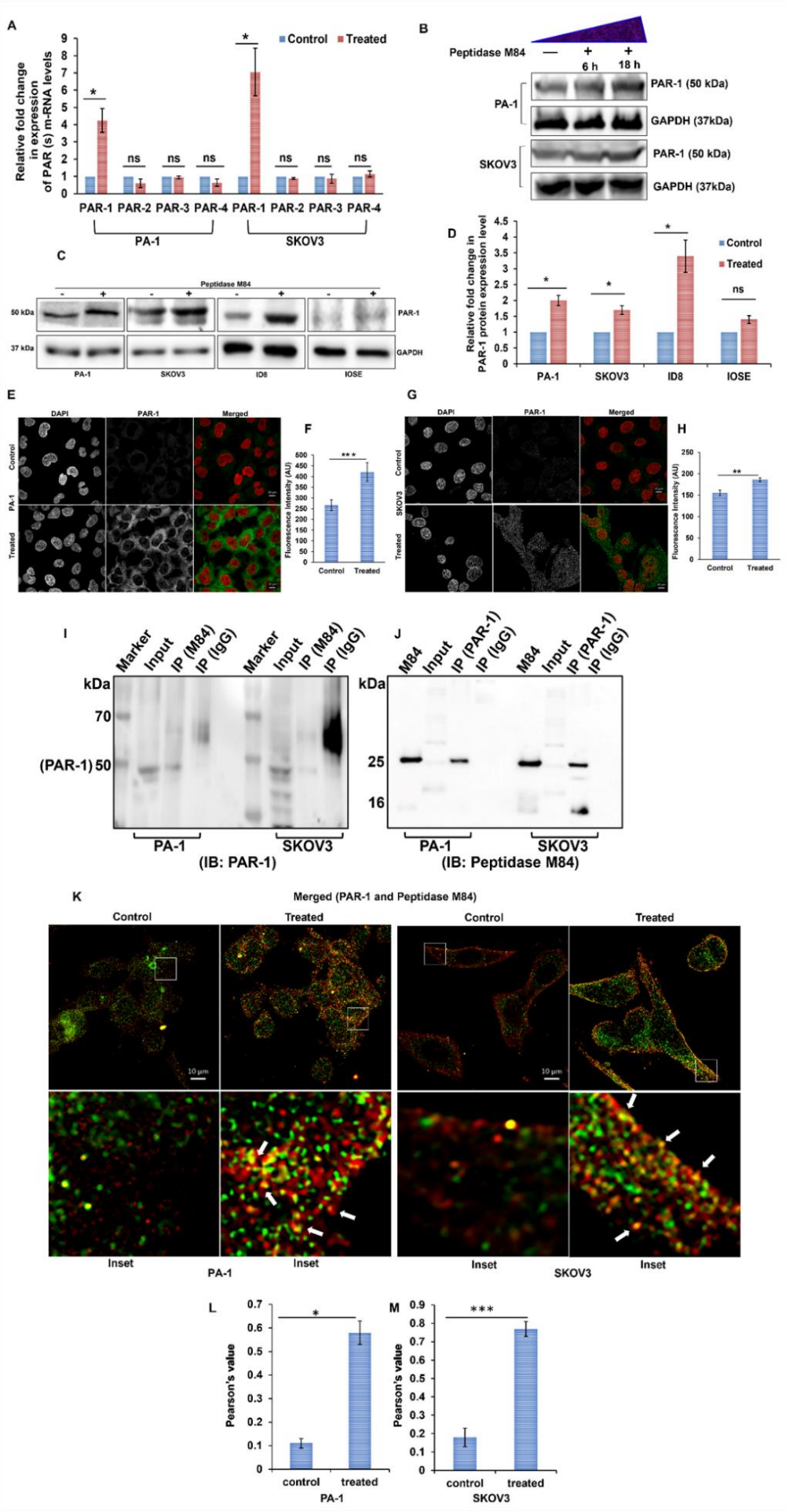
A
Relative fold change in expression of PAR (s) m-RNA levels
Control
Treated
PAR-1 PAR-2 PAR-3 PAR-4 PAR-1 PAR-2 PAR-3 PAR-4
PA-1
SKOV3
B
Peptidase M84
6 h
18 h
PA-1
SKOV3
PAR-1 (50 kDa)
GAPDH (37kDa)
C
Peptidase M84
50 kDa
37 kDa
PAR-1
GAPDH
PA-1
SKOV3
ID8
IOSE
D
Relative fold change in PAR-1 protein expression level
Control
Treated
PA-1
SKOV3
ID8
IOSE
E
DAPI
PAR-1
Merged
Control
PA-1
Treated
F
Fluorescence Intensity (AU)
Control
Treated
G
DAPI
PAR-1
Merged
Control
SKOV3
Treated
H
Fluorescence Intensity (AU)
Control
Treated
I
Marker
Input
IP (M84)
IP (IgG)
kDa
70
(PAR-1) 50
PA-1
SKOV3
(IB: PAR-1)
J
M84
Input
IP (PAR-1)
IP (IgG)
kDa
25
16
PA-1
SKOV3
(IB: Peptidase M84)
K
Merged (PAR-1 and Peptidase M84)
Control
Treated
Control
Treated
10 µm
Inset
Inset
Inset
Inset
PA-1
SKOV3
L
Pearson's value
control
treated
PA-1
M
Pearson's value
control
treated
SKOV3

Figure 5.19. Peptidase M84 induces overexpression and activation of PAR-1 in ovarian cancer cells. (A) Real-time PCR analysis of PAR-1, PAR-2, PAR3, and PAR-4 genes in Peptidase M84 treated and untreated PA1 and SKOV3 cells. Ct values are normalized to GAPDH expression, and 2^{-ddct} values are calculated (n = 3). **(B)** Western blot shows a time-dependent increase in PAR-1 expression levels in Peptidase M84 treated PA-1 and SKOV3 cells. **(C and D)** Western blot together with bar diagram of densitometry scan of PAR-1 expression in Peptidase M84 treated (18 h) and untreated PA-1, SKOV3, ID8, and IOSE cells. **(E–H)** Confocal imaging with respective bar diagrams of MFI of PAR-1 expression levels (green) in PA-1 and SKOV3 cells.(I) Co-immunoprecipitation study of PAR-1 and Peptidase M84 reveals the interaction between PAR-1 and Peptidase M84 in both PA-1 and SKOV3 cells. Here, whole-cell lysates (WCL) from these cells were loaded as inputs. **(J)** Bands of Peptidase M84 are observed in IB when Peptidase M84 was immunoprecipitated with PAR-1. Here, purified Peptidase M84 from *B. altitudinis* was loaded as input. **(K)** Confocal imaging revealed co-localization between Peptidase M84 (green) and PAR-1(red) in Peptidase M84 treated PA-1 and SKOV3 cells. **(L and M)** Bar diagrams showed Pearson's co-efficient values. In each panel, error bars were calculated based on results obtained from a minimum of three independent experiments. All statistical analysis was done by applying the Student's t test (two-tailed). In all panels, ns $p > 0.05$, $*p \leq 0.05$, $**p \leq 0.01$, and $***p \leq 0.001$. Data are expressed in ±SEM. Scale bars: 10 μm. Densitometric analysis was performed on ImageJ and Gel Quant softwares. Band intensities were normalized to loading controls GAPDH. Pearson's co-efficient was calculated in Fiji (https://imagej.net/software/fiji/).

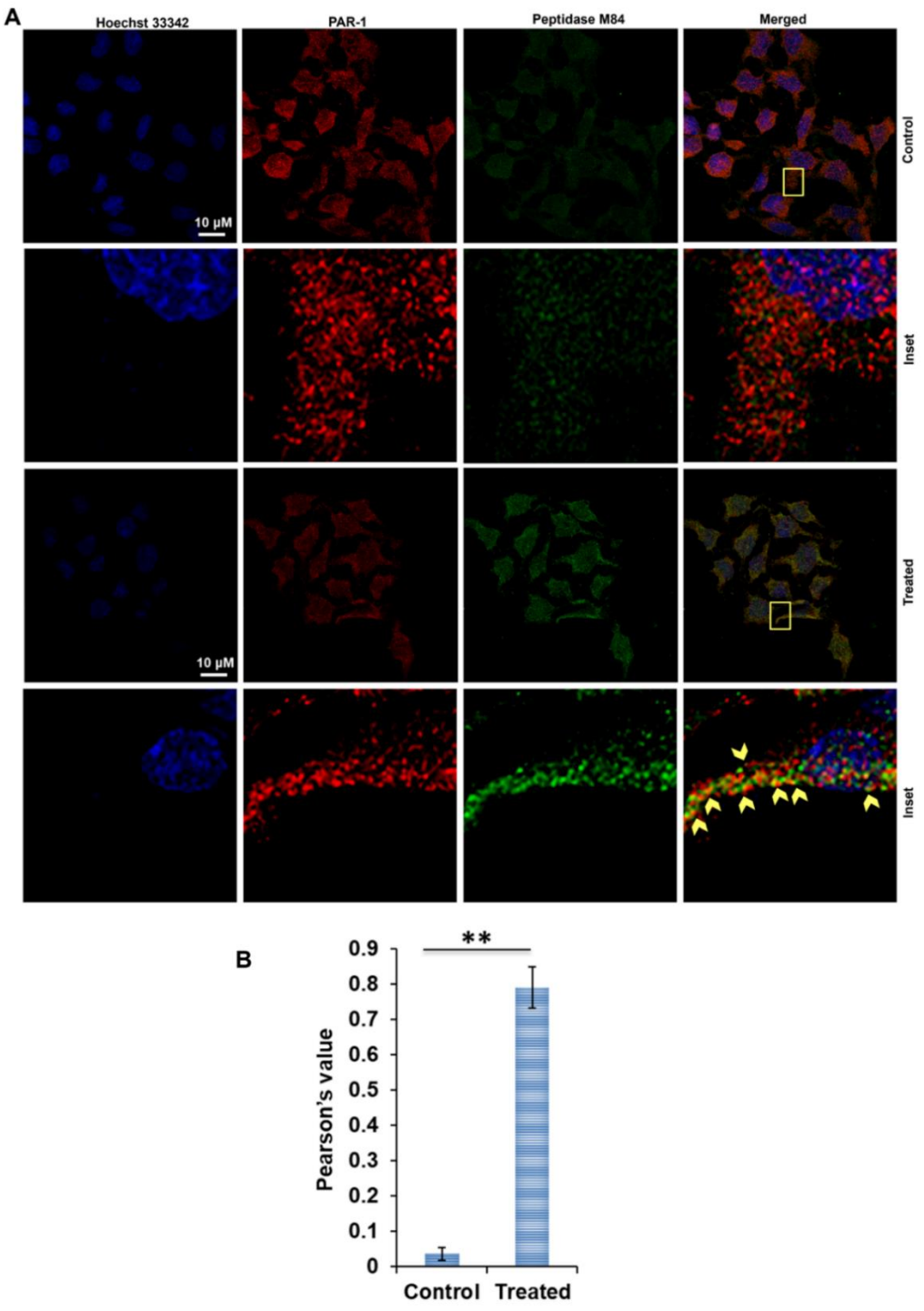

Figure 5.20. Peptidase M84 binds with PAR-1 (A) Confocal imaging reveals co-localisation between Peptidase M84 (green) and PAR-1(red) in Peptidase M84 treated PA-1 cells. **(B)** Bar diagrams showing Pearson's co-efficient values. In each panel, error bars were calculated based on results obtained from a minimum of three independent experiments. All statistical analysis was done by applying the Student's t-test (two-tailed). In all panels, ns $p>0.05$, *$p\leq0.05$, **$p\leq0.01$, and ***$p\leq0.001$. Data are expressed in ± SEM. Scale bars: 10 µm.

A

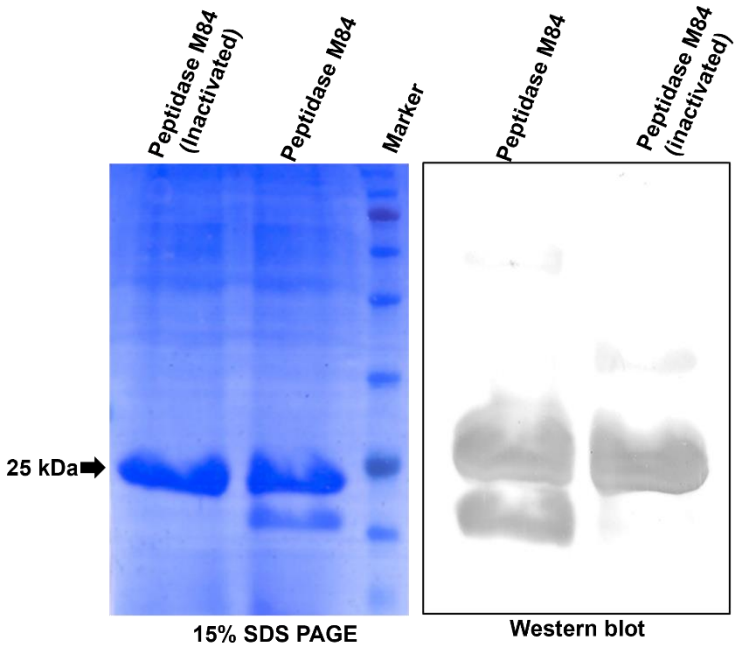

B

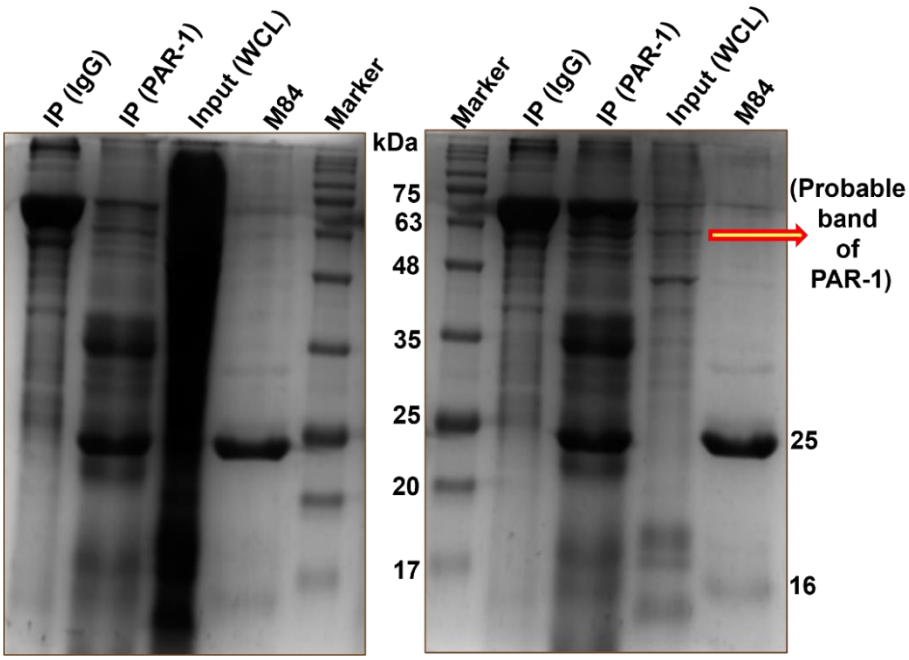

Figure 5.21. Determination of the interaction between PAR-1 and Peptidase M84 by gel electrophoresis. (A) Detection of two major bands of purified Peptidase M84 from *Bacillus altitudinis* strain GDL-186 by western blot using anti-Peptidase M84 antisera raised in rabbit. **(B)** SDS PAGE showed presence of both PAR-1 and Peptidase M84 in the gel after the interaction.

5.7. Peptidase M84 persuaded PAR-1 dependent apoptosis in ovarian cancer cells by triggering NFκB and MAPK signalling mediated ROS generation

- Thrombin-mediated PAR-1 activation generally regulates major signalling pathways, such as p38 MAPK and NF-kB, which ultimately trigger further ROS generation (Marin et al., 2001; Ray et al., 2016; Tapader et al., 2018). In this study, immunoblots of cytosolic and nuclear fractions of PA-1 and SKOV3 cells showed that Peptidase M84 treatment promoted the nuclear translocation of p50 and p65 proteins, suggesting the activation of NF-kB signalling. We observed significant expression of p50 and p65 proteins in the nuclear fraction of Peptidase M84 treated cells compared to untreated cells. Densitometry analysis represented the ratio of protein expression between the nucleus and cytosol of Peptidase M84 induced and uninduced cells. Histone H3 (a nuclear protein) and alpha-tubulin (a cytosolic protein) were used as loading controls (Figures 5.22.A and B). Immunofluorescence imaging of Peptidase M84 treated and untreated cells further supported our findings, showing prominent nuclear translocation of the same proteins. There was an increase in the ratio of nuclear to cytosolic mean fluorescence intensity of p50 and p65 proteins in Peptidase M84 treated cells (Figures 5.22. C–G).

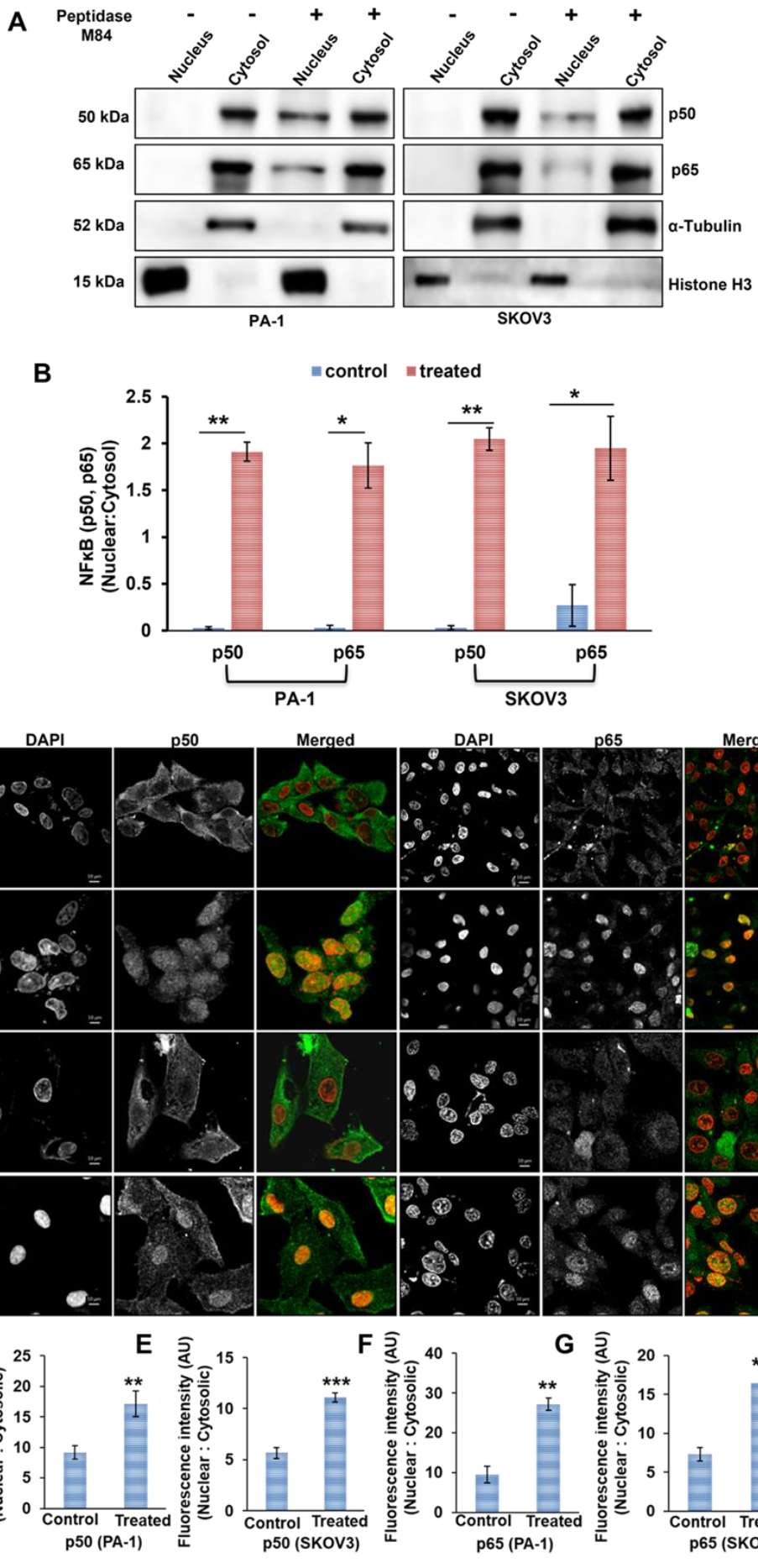
A
Peptidase M84
Nucleus
Cytosol
50 kDa
65 kDa
52 kDa
15 kDa
p50
p65
α-Tubulin
Histone H3
PA-1
SKOV3
B
control
treated
NFκB (p50, p65) (Nuclear:Cytosol)
C
DAPI
p50
Merged
p65
PA1
SKOV3
Control
Treated
D
E
F
G
Fluorescence intensity (AU) (Nuclear : Cytosolic)
p50 (PA-1)
p50 (SKOV3)
p65 (PA-1)
p65 (SKOV3)

Figure 5.22. Peptidase M84 induces nuclear localisation of p50 and p65 in ovarian cancer cells.

(A and B) Western blot and bar diagram of densitometric scan (nucleus: cytosol) indicate enhanced nuclear translocation of p50 and p65 after Peptidase M84 treatment in PA-1 and SKOV3 cells. Histone H3 and α-tubulin are loading controls. **(C–G)** Immunofluorescence shows Peptidase M84 induced nuclear translocation of p50 (green) and p65 (green) in PA-1 and SKOV3 cells. Bar diagrams represent the ratio of the MFI of nucleus to cytosol of cells. In each panel, error bars were calculated based on results obtained from a minimum of three independent experiments. All statistical analysis was done by applying the Student's t-test (two-tailed). In all panels, ns $p>0.05$, *$p\leq0.05$, **$p\leq0.01$, and ***$p\leq0.001$. Data are expressed in ± SEM. Scale bars: 10 μm.

- Results from immunoblots showed that the levels of p-p38 and phospho-ERK1/2 significantly increased and decreased, respectively, due to Peptidase M84 treatment, while the total cellular levels of p38 and ERK1/2 remained unchanged. Thus, our report revealed that Peptidase M84 modulated MAP kinase pathways in ovarian cancer cells (Figures 5.23. A and B). Immunofluorescence also indicated an overall increase in phospho-p38 (p-p38) expression levels in Peptidase M84 treated cells (Figures 5.23. C - E).

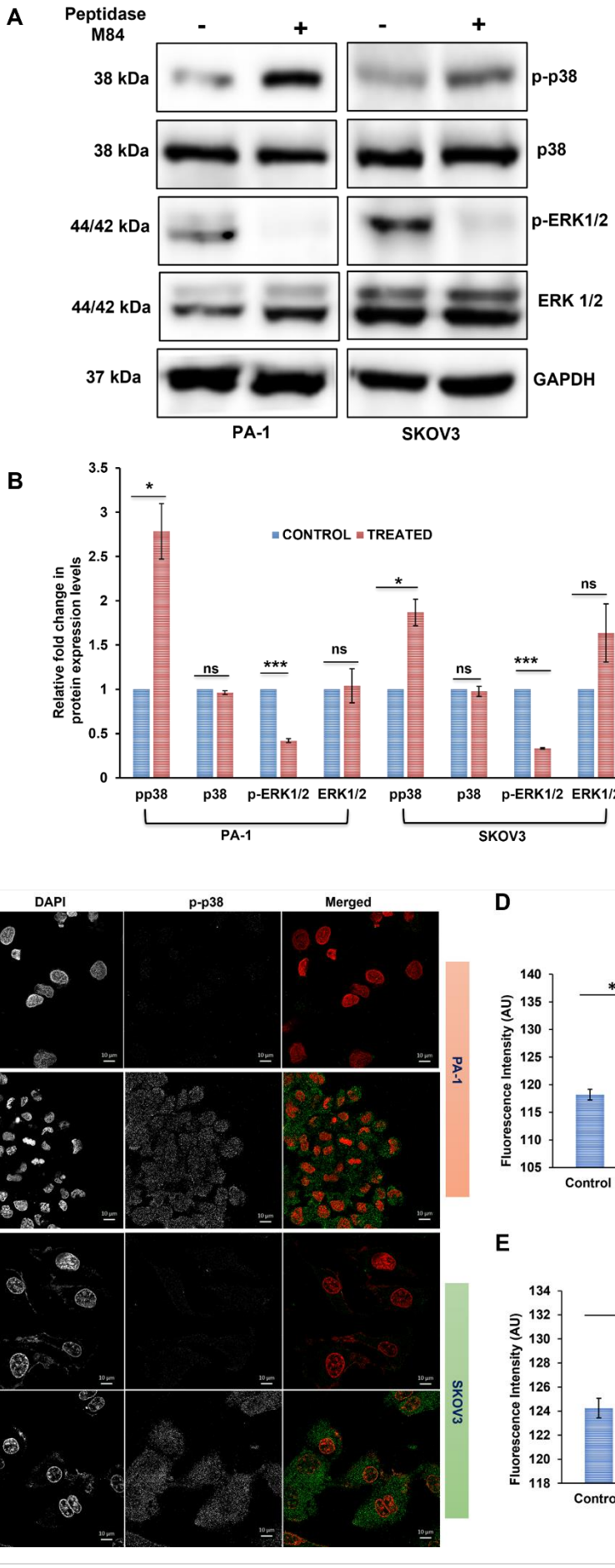
A
Peptidase M84
-
+
-
+
38 kDa
p-p38
38 kDa
p38
44/42 kDa
p-ERK1/2
44/42 kDa
ERK 1/2
37 kDa
GAPDH
PA-1
SKOV3
B
CONTROL
TREATED
Relative fold change in protein expression levels
pp38
p38
p-ERK1/2
ERK1/2
PA-1
SKOV3
C
DAPI
p-p38
Merged
Control
Treated
PA-1
SKOV3
D
Fluorescence Intensity (AU)
Control
Treated
E
Fluorescence Intensity (AU)
Control
Treated

Figure 5.23. Peptidase M84 treatment altered MAPK pathway in ovarian cancer cells.

(A and B) Western blot with bar diagram of densitometric scan show significant upregulation in phospho-p38 and down-regulation in phospho-ERK-1/2 expression levels in Peptidase M84 treated PA-1 and SKOV3 cells. Here, GAPDH is used as loading control **(C)** Immunofluorescence-based confocal imaging shows upregulation of p-p38 (green) expression levels in PA-1 and SKOV3 cells. **(D and E)** Bar diagrams represent the mean fluorescence intensity of p-p38 levels in PA-1 and SKOV3 cells. In each panel, error bars were calculated based on results obtained from a minimum of three independent experiments. All statistical analysis was done by applying the Student's t-test (two-tailed). In all panels, ns $p>0.05$, *$p\leq0.05$, **$p\leq0.01$, and ***$p\leq0.001$. Data are expressed in ± SEM. Scale bars: 10 μm.

- We aimed to determine whether the interaction between Peptidase M84 and PAR-1 directly induced apoptotic signalling in ovarian cancer cells. Peptidase M84 treatment of PA-1 and SKOV3 cells showed cellular apoptosis. When these cells were pretreated with the PAR-1 inhibitor (ML161) followed by Peptidase M84 treatment for 18 hours, apoptosis was absent. Furthermore, knockdown of PAR-1 was achieved by si-RNA transfection for 48 hours in PA-1 and SKOV3 cells (Figures 4.24. A and B). These PAR-1 silenced cells behaved like untreated cells even after Peptidase M84 treatment. Hence, our data illustrated that Peptidase M84 induced apoptosis in ovarian cancer cells in a PAR-1-dependent manner (Figures 5.24. C - E).

- We found that Peptidase M84 augmented ROS levels in ovarian cancer via activation of MAP kinase and NF-kB. To confirm whether these signalling pathways were directly responsible for cellular apoptosis, PA-1 and SKOV3 cells were pre-incubated with either an NF-kB inhibitor (MG132), a p38 inhibitor (SB203580), or both, followed by Peptidase M84 treatment for 18 hours. When cells were pre-incubated with MG132, only 58% of PA-1 and 49% of SKOV3 cells showed apoptosis. Cells pre-incubated with SB203580 showed apoptosis in 51% of PA-1 and 41% of SKOV3 cells. Notably, the majority of the cells undergoing apoptosis under these conditions were mostly in the early apoptotic phase. Interestingly, when both inhibitors were applied together, no significant apoptosis was observed.

Furthermore, no significant apoptosis was observed when cells were incubated with the ROS quencher NAC prior to protease treatment. This observation suggested the major involvement of ROS in Peptidase M84 induced apoptosis in ovarian cancer cells (Figures 5.24. C - E).

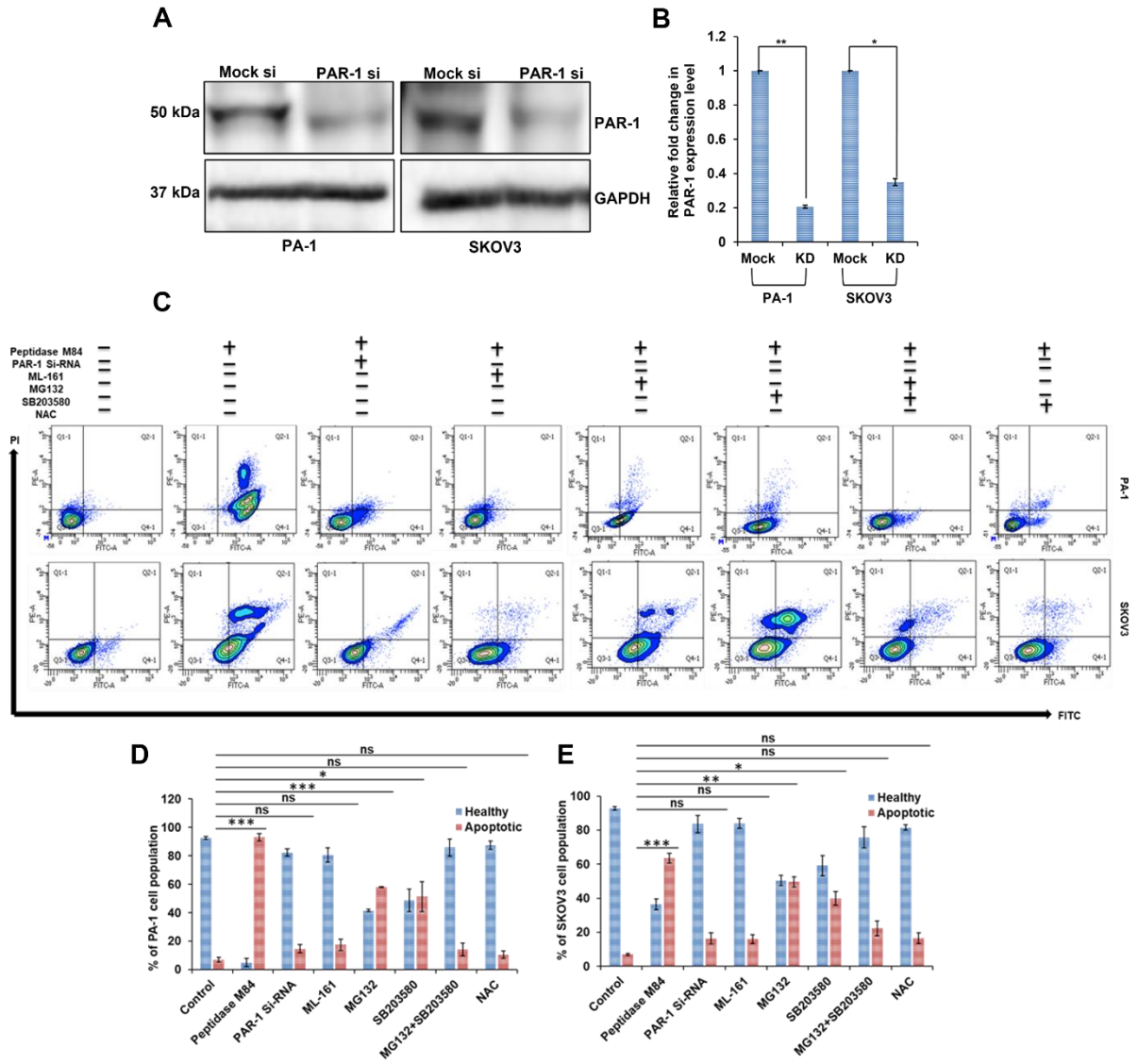

Figure 5.24. Effect of signalling inhibitors on Peptidase M84 induced apoptosis in ovarian cancer cells. **(A and B)** Western blot coupled with a bar diagram of the densitometric scan shows downregulation in PAR-1 protein expression levels after 48 h of si-RNA treatment in PA-1and SKOV3 cells. **(C)** Peptidase M84 mediated cellular apoptosis is analysed by FACS in the presence and absence of different signalling

inhibitors (PAR-1, NF-κB, p38, and ROS) and PAR-1 si-RNA in PA-1 (upper panel) and SKOV3 (lower panel) cells. **(D and E)** The above results are graphically represented in the bar diagram. In each panel, error bars were calculated based on results obtained from a minimum of three independent experiments. All statistical analysis was done by applying Student's t test (two-tailed). In all panels, ns $p > 0.05$, $*p \leq 0.05$, $**p \leq 0.01$, and $***p \leq 0.001$. Data are expressed in ±SEM. Densitometric analysis was performed on ImageJ and Gel Quant. Band intensities were normalised to loading controls. Fluorescence intensity and Pearson's co-efficient values were measured manually by drawing lines along the entire length of each nucleus or cytosol and calculating them using Fiji (https://imagej.net/software/fiji/).

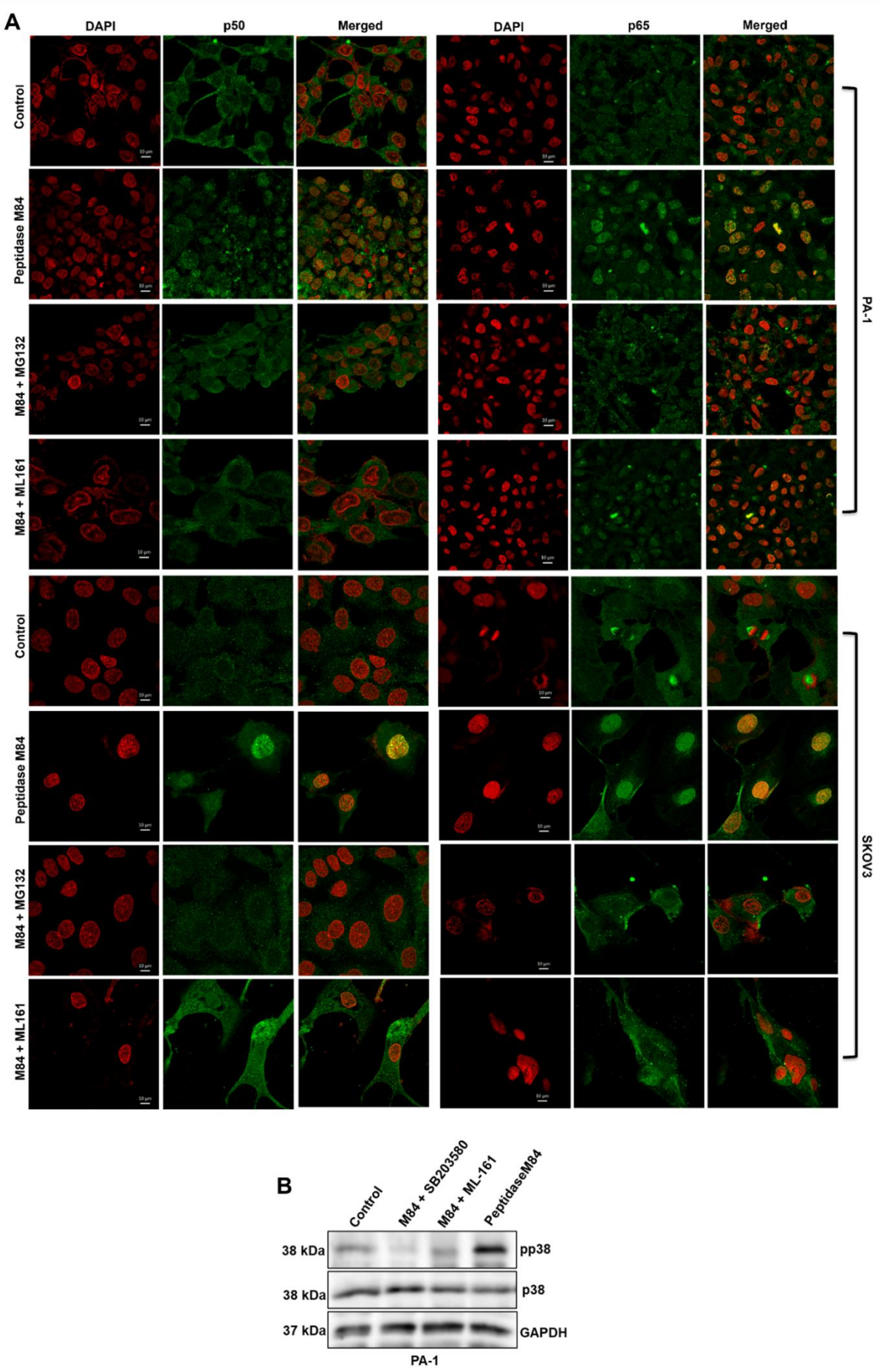
A
DAPI
p50
Merged
DAPI
p65
Merged
Control
Peptidase M84
M84 + MG132
M84 + ML161
PA-1
Control
Peptidase M84
M84 + MG132
M84 + ML161
SKOV3
B
Control
M84 + SB203580
M84 + ML-161
PeptidaseM84
38 kDa
pp38
38 kDa
p38
37 kDa
GAPDH
PA-1

Figure 5.25. Effect of PAR-1 inhibition on NFκB and MAPK signalling in Peptidase M84 treated ovarian cancer cells.

(A) Immunofluorescence-based confocal imaging shows PAR-1 inhibitor ML161 inhibits nuclear translocation of p50 (green) and p65 (green) in Peptidase M84 treated PA-1 and SKOV3 cells. Here, MG132 is used as a positive control. **(B)** Western blot shows PAR-1 inhibitor ML161 effectively inhibits phosphorylation of p38 even after Peptidase M84 treatment. Here, SB203580 is used as a positive control. All statistical analysis was done by applying the Student's t-test (two-tailed). In all panels, ns $p>0.05$, *$p\leq0.05$, **$p\leq0.01$, and ***$p\leq0.001$. Data are expressed in ± SEM. Scale bars: 10 μm. Densitometric analysis was performed on ImageJ and Gel Quant software. Band intensities were normalised to loading controls GAPDH. Fluorescence intensity was measured using Fiji (https://imagej.net/software/fiji/).

- We noticed that ML161 pre-treatment inhibited Peptidase M84 mediated nuclear translocation of p50 and p65 (Figure 5.25.A). Immunoblots also confirmed that Peptidase M84 induced phosphorylation of p38 was inhibited by ML161 pre-treatment in PA-1 cells, while the total p38 concentration remained consistent (Figure 5.25.B). Therefore, Peptidase M84 mediated NF-kB and MAP kinase pathways were regulated by PAR-1 activity alterations.

- We previously stated that Peptidase M84 treatment promoted ROS generation in ovarian cancer cells. Interestingly, cells pre-treated with ML161 displayed no significant ROS generation even after Peptidase M84 treatment for 18 hours. Inhibition studies with MG132 and SB203580 further confirmed that blocking NF-κB and p38, either individually or together, impaired further ROS production in ovarian cancer cells (Figures 5.26. A - C). Hence, Peptidase M84 induced PAR-1 dependent activation of both NF-κB and p38 to enhance ROS levels in ovarian cancer cells. Taken together, our data illustrated that Peptidase M84 induced apoptosis by effectively targeting PAR-1 with the specific involvement of p38, NF-κB, and ROS.

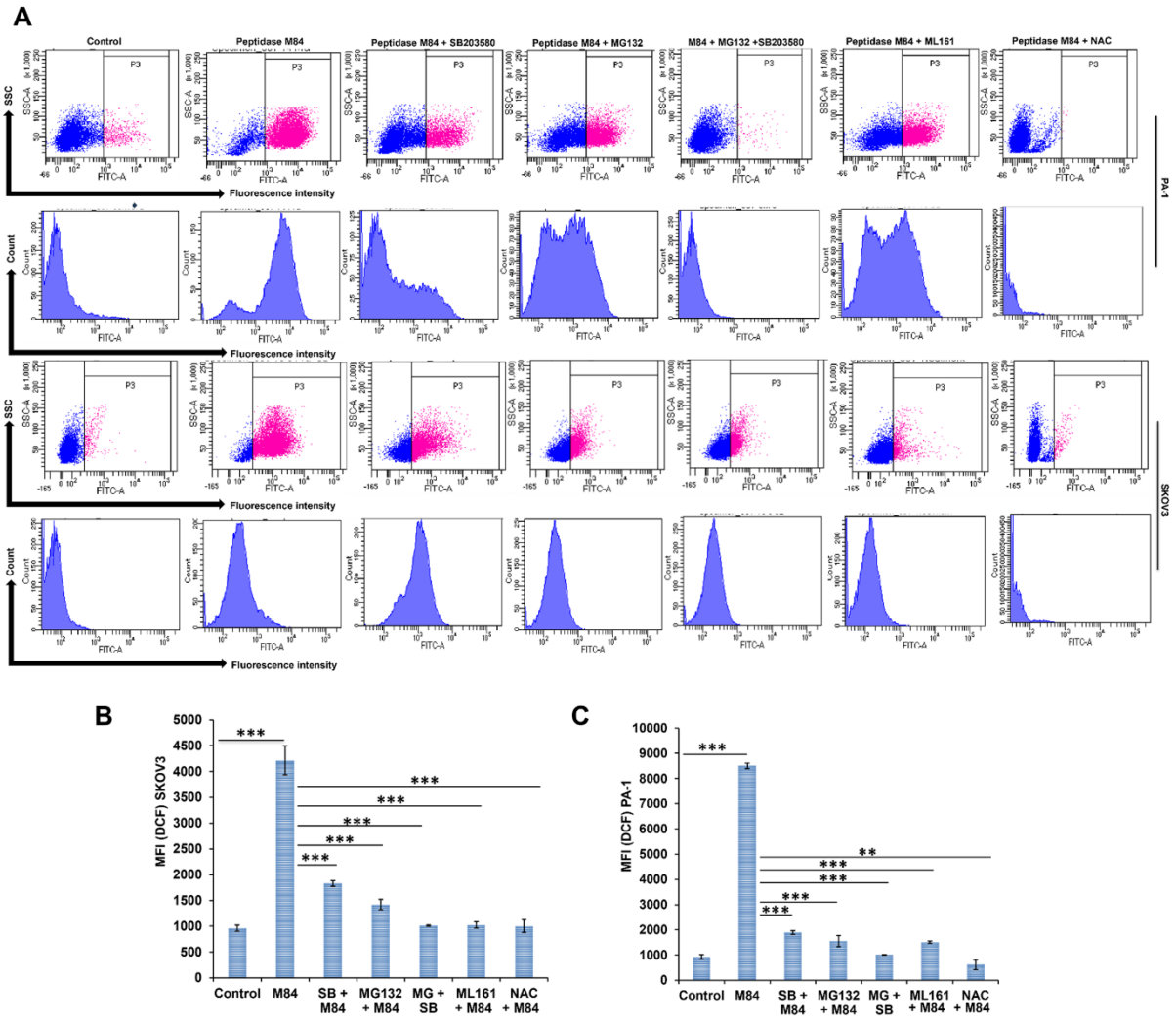

Figure 5.26. Effect of signalling inhibitors on Peptidase M84 induced ROS generation in ovarian cancer cells.

(A) PAR-1 inhibitor (ML161), NFκB inhibitor (MG132) and p38 inhibitor (SB203580) inhibit ROS generation in Peptidase M84 treated PA-1 and SKOV3 cells. MG132 and SB203580 individually inhibit ROS generation partially. When both inhibitors are used together ROS generation is completely blocked. Pre-treatment of ML161 completely blocks ROS generation. Cells pre-treated with 2 mM NAC are used as a negative control. **(B and C)** Bar diagrams represent the mean fluorescence intensity of DCF in PA-1 and SKOV3 cells. All statistical analysis was done by applying the Student's t-test (two-tailed). In all panels, ns $p>0.05$, *$p\leq0.05$, **$p\leq0.01$, and ***$p\leq0.001$. Data are expressed in ± SEM.

5.8. Investigation on the therapeutic effectiveness and potential toxicity of microbial proteases against ovarian cancer in an *in vivo* setup. Peptidase M84 treatment improved the survival of ID8 bearing mice and impeded body weight increase due to ascites accumulation and also affected the viability of ID8 cells *in vivo*. Peptidase M84 treatment improved the survival of ID8 bearing mice and impeded body weight increase due to ascites accumulation and also affected the viability of ID8 cells *in vivo*.

- Tumours were induced intraperitoneally with ID8 cells ($5X10^6$), and the survival rate and changes in body weight were observed in C57BL/6 mice (Figure 5.27.A). In the ID8 control group, the survival rate was 60% after 30 days and 10% after 60 days. However, when 3.0 μg/ml Peptidase M84 was injected at a weekly interval for 7 successive weeks, the survival rate increased to 90% after 30 days and 70% after 60 days (Figure 5.28.A). The body weight of the ID8 control group increased from 25 g (at 0 days) to 45 g (after 60 days of tumour inoculation). In contrast, no significant changes in body weight were observed in the Peptidase M84 treated group and the buffer control group (Figures 5.28.B; 5.29.A and B). Inactivated Peptidase M84 (EDTA treated) failed to improve the survival rate of ID8-induced mice and also resulted in an increase in body weight.

- Furthermore, viable ID8 cells were assessed by trypan blue staining. Initially, ID8 cells ($5X10^6$) were inoculated into the peritoneal cavity of mice, and there was a gradual proliferation of viable ID8 cells in the tumour control group. However, Peptidase M84 treatment led to a significant decline in the count of viable ID8 cells after 45 and 60 days. In contrast, Peptidase M84 inactivated by EDTA did not affect the viability of ID8 cells at all (Figures 5.30. A and B). Overall, our findings elucidated that the antitumor property of Peptidase M84 was linked to its proteolytic activity.

A

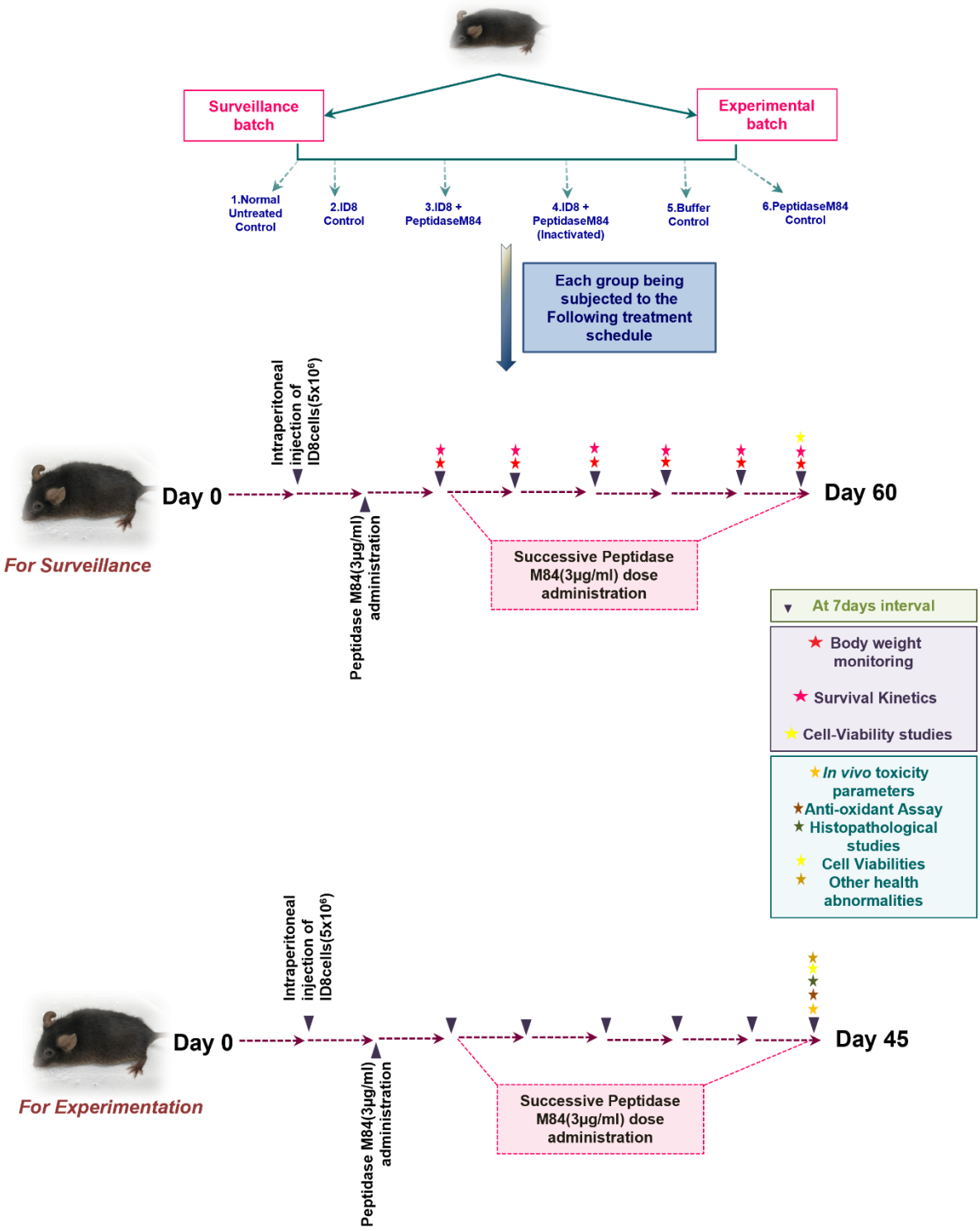

Figure 5.27. (A) Illustration of the in vivo study to determine the anticancer potential and non-toxicity of Peptidase M84.

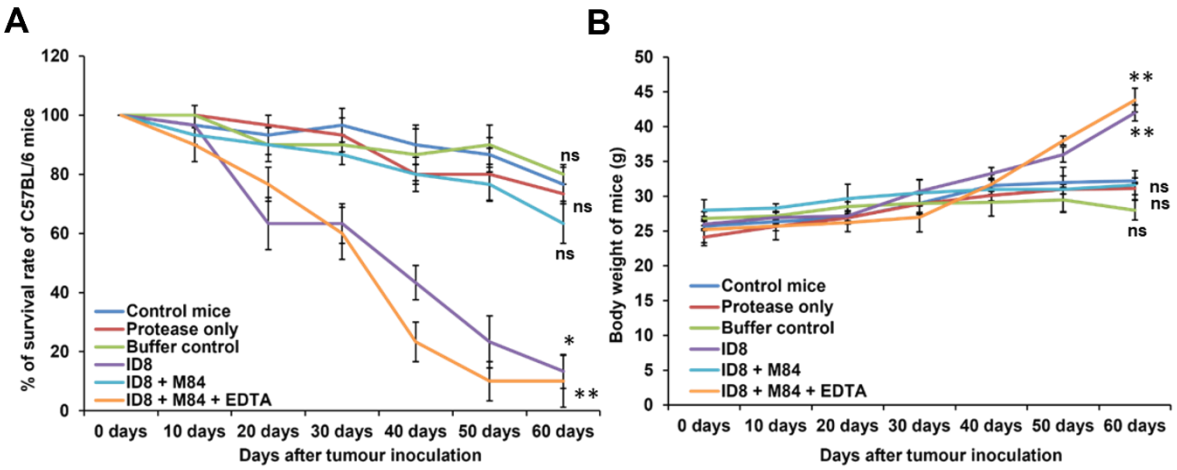

Figure 5.28. Effect of Peptidase M84 on mice survival and body weight.

(A) Peptidase M84 treatment shows promising improvement in survival rate in ID8 mice model. Peptidase M84 in the presence of EDTA shows a similar mortality rate as tumour control group. **(B)** Line graph shows body weight after Peptidase M84 administration in mice. In each panel, error bars were calculated based on results obtained from a minimum of three independent experiments (n = 3). All statistical analysis was done by applying Student's t test (two-tailed). Data are expressed in ±SEM. In all panels, ns $p > 0.05$, $*p \leq 0.05$, $**p \leq 0.01$, and $***p \leq 0.001$.

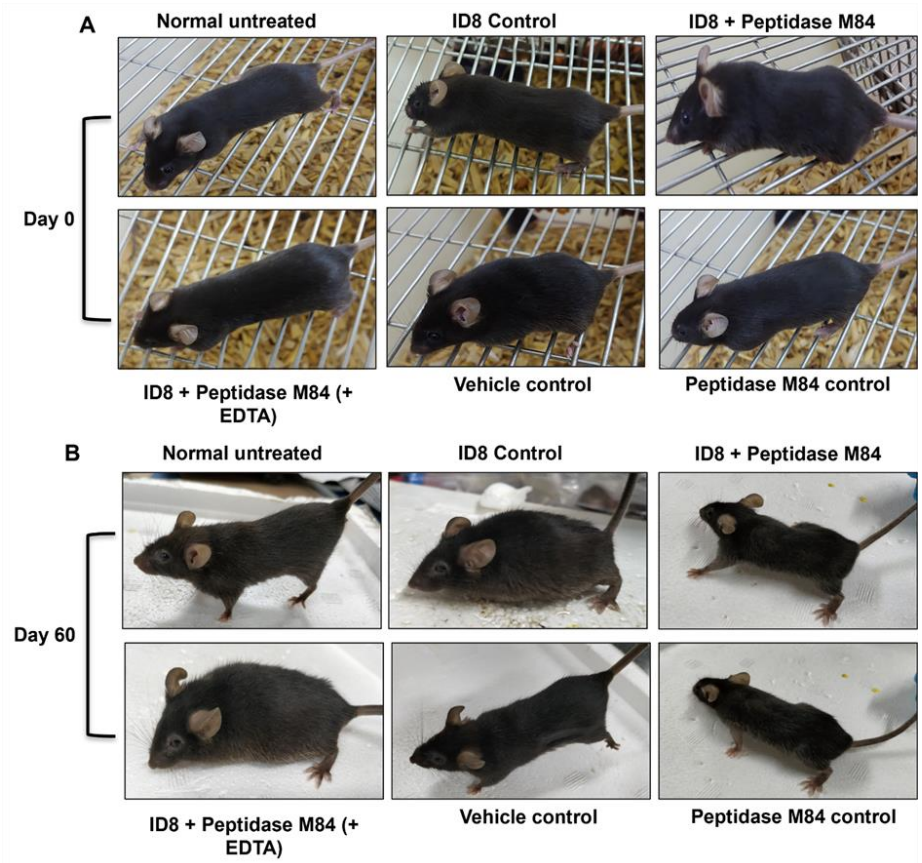

Figure 5.29. Ascites regression by Peptidase M84 in ID8 induced intraperitoneal mice model.

(A and B) An increase in body weight is observed in ID8 control and Inactivated Peptidase M84 treated ID8 bearing group after 60 days of tumour inoculation. The untreated control group, buffer control group, Peptidase M84 control group and ID8 bearing mice treated with Peptidase M84 group show no such increase in body weight after 60 days of tumour cell inoculation.

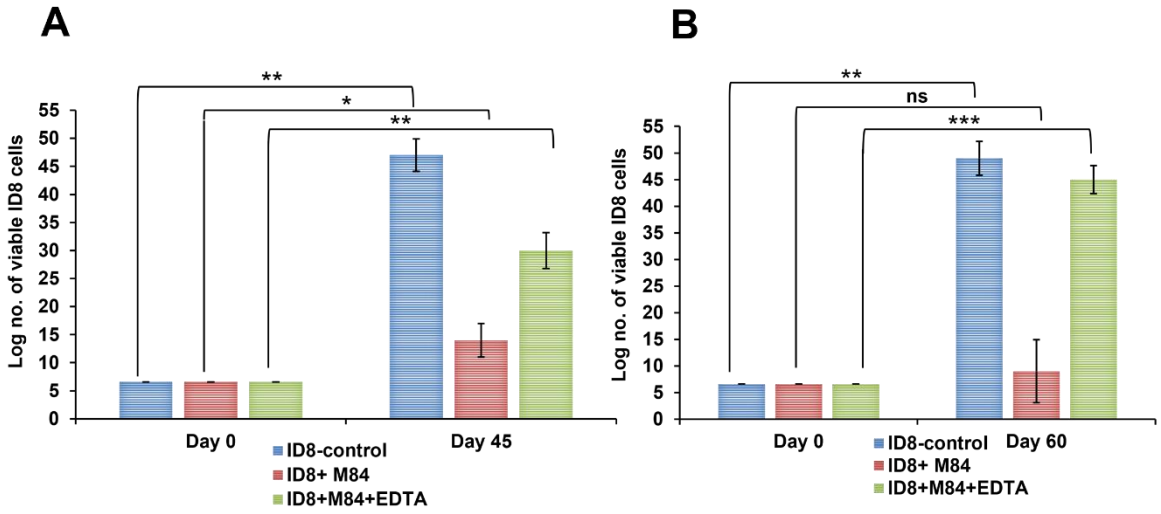

Figure 5.30. Peptidase M84 affected viability of ID8 cell *in vivo*

(A and B) Viable ID8 cells were measured at different time points by the trypan blue exclusion method.

5.9. Studies based on the biochemical index of the liver and kidney of mice revealed peptidase M84 did not cause any significant toxicity. Peptidase M84 treatment showed recovery of the damaged architecture of liver and kidney tissue of host system and did not cause any significant toxicity.

- After 45 days of treatment, experiments were conducted to assess the impact of Peptidase M84 on oxidative stress by examining various detoxifying enzymes and lipid peroxidation (LPO) levels in serum samples from mice. The LPO level in serum serves as an indicator of cellular oxidative stress. Interestingly, in group-3, where Peptidase M84 was administered, the number of viable ID8 cells decreased significantly compared to group-2, indicating the induction of oxidative stress by Peptidase M84 itself. Moreover, the LPO level in group-3 was lower than that in the tumour control group-2. Remarkably, after 45 days of Peptidase M84 treatment, the LPO level in group-3 returned to normal levels, similar to group-1 (Figure 5.31.A). Additionally, the levels of catalase, superoxide dismutase (SOD), and glutathione (GSH) in serum were initially low due to excessive oxidative stress. However, following 45 days of Peptidase M84 treatment in group-3, the number of viable ID8 cells decreased significantly compared to group-2, accompanied by an increase in the levels of these enzymes in group-3. Furthermore, in group-4, which received Peptidase M84 treatment, the levels of catalase, GSH, and SOD in serum were similar to those in group-2 after 45 days of treatment. Notably, when normal animals were treated with Peptidase M84 (group-6), there were no significant differences observed in any of the aforementioned biochemical markers (Figure 5.31. B - D). These findings suggest that Peptidase M84 induces apoptosis in ID8 cells through oxidative stress-mediated damage.

- A 45-day chronic toxicity study was conducted on C57BL/6 mice to assess any potential adverse effects of exposure to Peptidase M84. Changes in biochemical parameters, including serum glutamate oxaloacetate transaminase (SGOT/AST) and serum glutamate pyruvate transaminase (SGPT/ALT) levels (indicative of drug-induced liver injury), as well as creatinine and urea levels (indicative of toxin-induced impaired renal function), were monitored. In the tumour control group, there was a significant increase in ALT and AST activity, along with a notable

decrease in creatinine and urea levels compared to the normal group. However, in the group treated solely with Peptidase M84, no significant differences were observed in any of the aforementioned indexes compared to the normal untreated group. These findings indicate that treatment with Peptidase M84 at a concentration of 3.0 µg/ml (equivalent to **12.0 µg/kg of body weight**) for up to 45 days did not lead to hepatotoxicity or nephrotoxicity (Figures 5.31. E - H).

- Histopathological analysis further confirmed these results, demonstrating that Peptidase M84 did not induce any significant toxicity, as all parameters related to liver and kidney toxicity remained within the normal range. These findings provide reassurance regarding the safety profile of Peptidase M84 in prolonged exposure scenarios. In our study, histopathological examination was conducted on kidney and liver tissues from all six groups of experimental animals after 45 days of treatment. We utilized haematoxylin-eosin staining to evaluate whether any discrepancies existed compared to the biochemical markers. Histopathological analysis of normal liver sections revealed a healthy morphology of hepatocytes, while normal kidney tissues exhibited healthy glomeruli, vessels, and tubules. Conversely, the tumour control group (group-2) displayed disrupted architecture, characterized by moderate to dense inflammation with damaged hepatocytes in the liver and extensively damaged glomerular structure in the kidney (Figure 5.31.I). However, following treatment with Peptidase M84 (group-3), this damage was observed to be reversed, with a restoration of healthy tissue structure in both the liver and kidney. Comparison with the untreated control group revealed no noticeable anomalies in the histopathology of the kidney and liver tissues in the Peptidase M84 treated groups (group-3 and group-4) after 45 days of continual treatment. The morphology of the liver in mice treated solely with Peptidase M84 closely resembled that of the untreated group, with no significant changes observed. Additionally, the liver morphology in group-6 (protease control and vehicle control group) showed no discernible difference from that of the untreated control. Furthermore, the absence of a radial distribution pattern of hepatocytes around the central vein, along with the presence of Kupffer cells and fine tissue integrity in the liver tissue, indicates the absence of chronic toxicity. Similarly, notable differences were not observed in renal corpuscles and glomerular tufts of kidney tissue after 45 days of constant

treatment with Peptidase M84 compared to the untreated group. Additionally, the absence of tubular dilation, glomerular infiltration, and necrosis suggests the absence of acute inflammation (Figure 5.31.J).

- Peptidase M84 also showed no significant effect on mouse PEMΦ cells *in vitro* (Figure 5.32. A and B). These findings imply that treatment with 3.0 µg/ml (equivalent to 12.0 µg/kg of body weight) of Peptidase M84 for the specified period is significantly non-toxic and non-hazardous to normal mouse tissues, without affecting mouse survival.

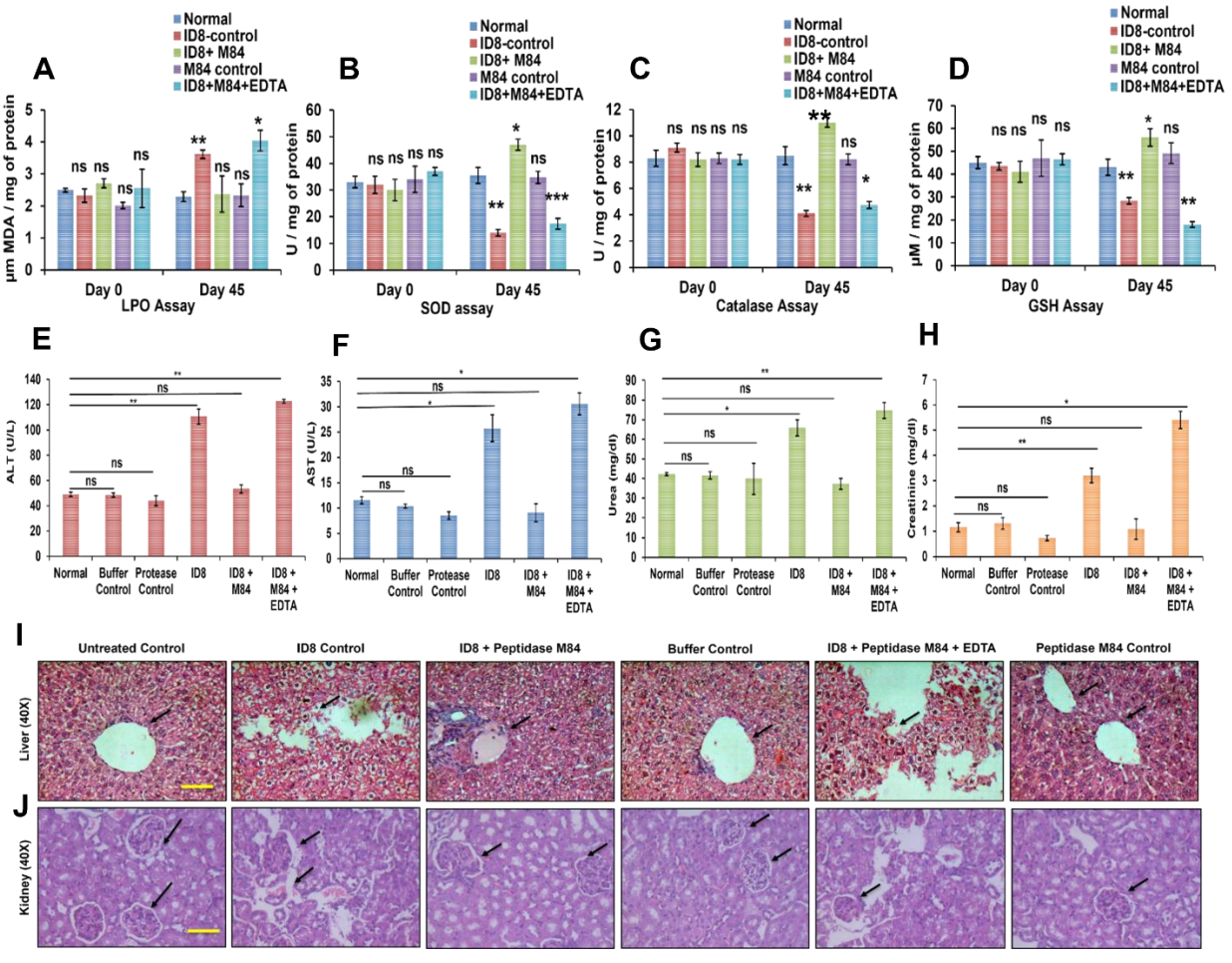

Figure 5.31. Major biochemical and histological parameters in mice.

(A-D) Biochemical parameters of cellular oxidative stress (LPO, SOD, CAT, and GSH) were measured in serum samples of mice. The results are graphically represented. **(E-**

H) Liver and kidney functionality test (ALT, AST, urea, and creatinine) was performed in serum samples of mice. The results are graphically represented. **(I and J)** Histological studies H & E staining showed that Peptidase M84 treatment improved the damaged architecture of the liver and kidney tissue caused by tumour induction. While arrows indicated intact membrane integrity in control and Peptidase M84 treated set and disrupted tissue architectures in ID8 control and Peptidase M84-pre-treated with EDTA set. In each panel, error bars were calculated based on results obtained from a minimum of three independent experiments (n = 3). All statistical analysis was done by applying Student's t test (two-tailed). Data are expressed in ±SEM. In all panels, ns $p > 0.05$, ∗$p \leq 0.05$, ∗∗$p \leq 0.01$, and ∗∗∗$p \leq 0.001$. Scale bars: standard.

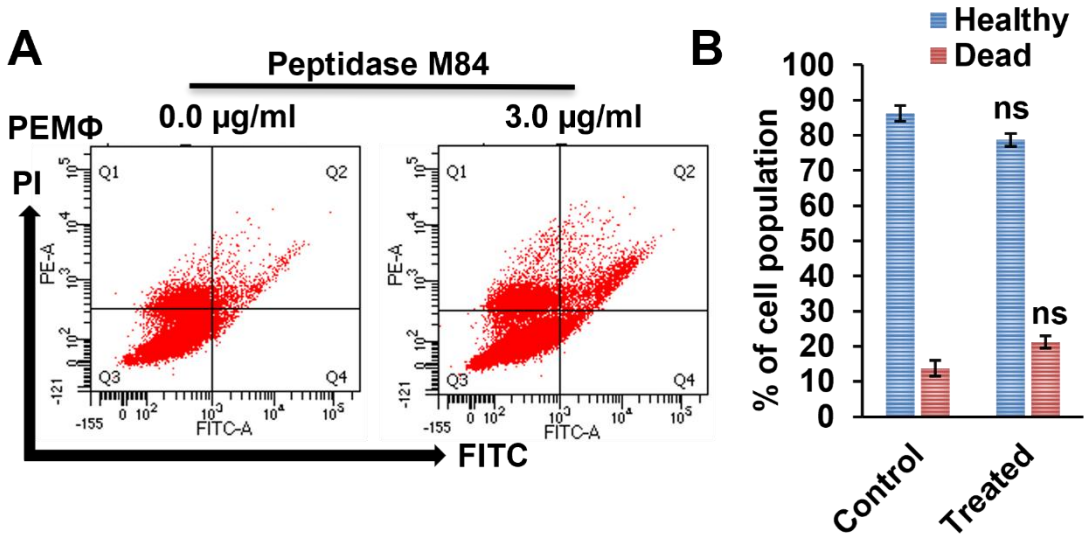

Figure 5.32. Effect of Peptidase M84 in mouse PEMΦ

(A, B) Flow cytometric analysis of the Peptidase M84 treated PEMΦ cells shows no significant apoptosis as compared to the untreated cells in similar doses. Bar diagrams of the data are also being presented. All statistical analysis was done by applying Student's t-test (two-tailed). Data are expressed in ± SEM. In all panels, ns $p>0.05$, *$p\leq0.05$, **$p\leq0.01$, and ***$p\leq0.001$. In each panel, error bars were calculated based on results obtained from a minimum of three independent experiments.

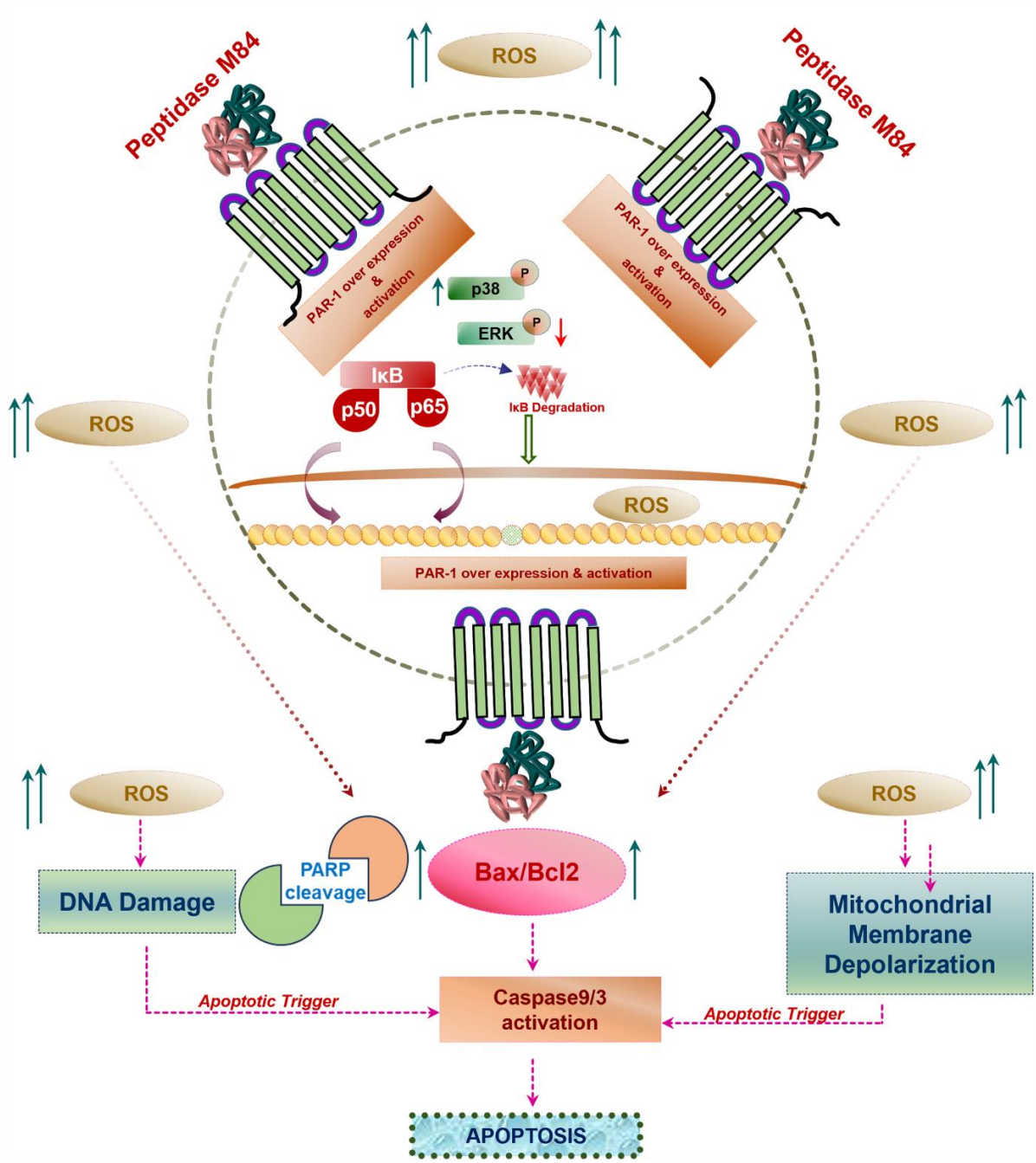

Figure 5.33. Schematic representation of Peptidase M84 induced apoptosis in ovarian cancer cells. Peptidase M84 induced activation and overexpression of PAR-1 thus enhancing cellular ROS and activation of NF-κB, p38 followed by downregulation of pERK1/2. ROS mediated DNA damage induced changes in mitochondrial membrane potential and triggered the release of mitochondrial cytochrome c which subsequently activated caspase 3 ultimately promoting Bax, Bcl2 mediated intrinsic pathway of apoptosis. Enhanced ROS level in malignant cells allows to meet the threshold level of cellular ROS that affect cell survival earlier than the normal healthy cells ultimately triggering apoptotic cell death.

CHAPTER 6

Discussion

The emerging complexities and side effects associated with conventional chemotherapy necessitate the search for new therapeutic agents for ovarian cancer treatment. In this study, we developed a novel approach to isolate and characterise proteases from environmental microbial sources with apoptotic properties to curb the growth of ovarian cancer cells. We screened over 200 environmental isolates and selected a protease-secreting isolate, identified as *Bacillus altitudinis*, labelled "GDL-186." *Bacillus altitudinis* was first isolated from high-altitude air samples in India (Shivaji et al., 2006), was found to secrete extracellular proteases that induce apoptosis in ovarian cancer cells.

Bacillus species are well-known for their extracellular alkaline protease secretion, which has significant industrial relevance. In our quest to find a protease with pro-apoptotic properties, we identified Peptidase M84, a key secretory metallo-protease from *Bacillus altitudinis*. Previous reports have indicated the anti-proliferative activity of organic extracts from *Bacillus altitudinis* MTCC13046 against human hepatocellular carcinoma cells (Asharaf and Chakraborty, 2022).

In our study, SDS-PAGE analysis of the purified protease revealed two major bands at 25 kDa and 16 kDa. These bands corresponded to the amino acid sequences of Peptidase M84 from *Bacillus altitudinis*, as found in the Uniprot (ID: A0A5D4PNG4) and NCBI databases. This protease contains a conserved metallo-protease domain with three histidine residues at its active site, similar to the metzincin metallo-protease from *Bacillus intermedius* (Sabirova et al., 2010). Optimal protease activity for Peptidase M84 was observed at physiological pH (7.0–9.0) and temperature (37°C–40°C), with activity inhibited by EDTA and 1,10-phenanthroline, confirming its classification as a Zn^{2+}-dependent metalloprotease. LC-MS/MS peptide blast analysis revealed the presence of Peptidase M84-like proteases in other closely related Bacillus species, including *Bacillus aerophilus, Bacillus xiamenensis*, and *Bacillus intermedius* (Sabirova et al., 2010). However, the anticancer effects of these proteases had not been well elucidated. Our study reports for the first time the apoptotic effects of this protease from *Bacillus altitudinis* GDL-186, demonstrating high selective toxicity towards ovarian cancer cells. Previous studies primarily focused on the biophysical and microbiological properties of Peptidase M84, leaving its potential pro-apoptotic effects unexplored. Our work paves the way for further research into the therapeutic potential of this protease.

For many decades, established cancer-derived cell lines have been invaluable experimental tools for studying cancer biology, identifying correlates of response and resistance to existing therapies, and testing the therapeutic efficacy of potential new treatments. These cell lines are relatively easy to manipulate, inexpensive to use, and provide rapid experimental results. Commonly used cell lines to study EOC are PA1 and SKOV3. Peptidase M84 triggered apoptosis in both human and mouse ovarian adenocarcinoma cells in a dose-dependent manner. This pro-apoptotic response was confirmed to be due to its proteolytic activity, as it was inhibited by EDTA treatment. Notably, Peptidase M84 did not have any significant effect on the normal IOSE and PEMΦ cells used in this study. Additionally, Peptidase M84 demonstrated anti-proliferative properties by reducing the expression levels of Ki-67, a proliferative antigen (Scholzen & Gerdes, 2000), in PA-1 and SKOV3 cells. These findings prompted further investigation into the detailed molecular mechanisms underlying Peptidase M84-induced apoptosis in ovarian cancer cells.

The canonical intrinsic pathway of apoptosis relies on the delicate balance between the pro-apoptotic protein Bax and the anti-apoptotic protein Bcl2 (J. Yang et al., 1997). We observed a significant increase in the Bax to Bcl2 ratio, along with a rise in cytosolic mitochondrial cytochrome c concentrations and activation of caspase 9 and caspase 3 following Peptidase M84 treatment in both SKOV3 and PA-1 cells. These findings indicate that Peptidase M84 specifically induces the intrinsic apoptosis pathway in these malignant ovarian cells.

Enhanced oxidative stress, due to higher ROS production and impaired redox balance, is essential for the survival of neoplastic cells, unlike normal healthy cells (Hayes et al., 2020; Perillo et al., 2020). Consistent with this, we noted that Peptidase M84 abnormally increased intracellular ROS levels in PA-1, SKOV3, and ID8 cells in a time-dependent manner, leading to their apoptotic death. In contrast, Peptidase M84 did not cause any such changes in normal IOSE cells, where ROS levels remained very low compared to the malignant setups. This observation was further confirmed by the inhibition of ROS following pre-incubation with NAC (a cellular ROS quencher) before Peptidase M84 treatment in ovarian cancer cells.

Overproduction and accumulation of ROS are known to modify nucleotides, break DNA strands, and facilitate chromosomal rearrangements, contributing to the deregulation of

various signalling pathways (Srinivas et al., 2019). Peptidase M84 treatment induced ROS-mediated DNA damage in ovarian cancer cells, prompting us to check the status of mitochondrial membrane potential using JC-1 staining. ROS overproduction is positively associated with mitochondrial membrane depolarization and reduced cell viability (Bossy-Wetzel, 1998). Disruption of the mitochondrial membrane potential was evident in JC-1-stained ovarian cancer cells treated with Peptidase M84. This finding aligned with the observed increase in cytochrome c in the cytosolic fractions of treated ovarian cancer cells, suggesting it had leaked from a depolarized mitochondrial membrane to trigger apoptosis cascades involving caspases, the apoptosome complex, and PARP (Bossy-Wetzel, 1998; Goldstein et al., 2000). The enzymatic activity of PARP increases under stressed conditions. Intact PARP expression is associated with the DNA repair system, which helps cancer cells evade apoptotic death. The presence of cleaved PARP and a decrease in Bcl-2 disrupt the apoptotic balance and drive the cell toward apoptosis by limiting cell repair (Rath et al., 2016). We found that Peptidase M84 induces PARP cleavage in ovarian cancer cells, which correlated with increased DNA damage. This PARP-activating feature of Peptidase M84 is promising, given that the FDA has approved Olaparib (AZD2281), a PARP inhibitor, for conventional ovarian cancer treatment (Kim et al., 2015).

The major signalling pathways of proteases are initiated by the cleavage of PARs, which play a crucial role in both cancer progression and apoptosis of malignant cells in a context-dependent manner (Soh et al., 2010). PAR-1 has been reported to be overexpressed in human ovarian cancer tissues compared to normal ovarian cells (Flynn & Buret, 2004; Grisaru-Granovsky et al., 2005). Gingipain-R (RgpB), a cysteine protease isolated from *Porphyromonas gingivalis*, was the earliest reported microbial protease that acted by cleaving a model peptide representing a cleavage site of PAR-2 (Lourbakos et al., 1998). In our study, we observed an overexpression of PAR-1 at both the transcriptional and translational levels in Peptidase M84-treated ovarian cancer cells compared to untreated cells. Interestingly, no significant change in PAR-1 expression was observed in Peptidase M84-treated normal ovarian epithelial cells. Evidence has identified PAR-1 as a tumour promoter, as it is associated with the induction of angiogenesis, invasion, and metastasis in ovarian and breast adenocarcinoma cells, as well as in xenograft models (Agarwal et al., 2008; Boire et al., 2005). However, thrombin has been found to mediate apoptosis in a dose-dependent manner through the

modulation of PAR-1 in tumour cells (Zain et al., 2000). Previously, we reported that the metalloprotease HAP from *V. cholerae* could cause overexpression of PAR-1 by inducing its cleavage (Ray & Pal, 2016). This paradox is not limited only to PAR-1. Other biomolecules, such as granulocyte/macrophage colony-stimulating factor, RAR-b2, E-cadherin, CD44, α/β-catenin, and CAV1, have also been reported to have contrasting functions in tumorigenesis (Deb et al., 2014; Patra, 2008). To understand the relationship between changes in PAR-1 expression and apoptosis in the presence of Peptidase M84 in ovarian cancer cells, we performed gene knockdown, signalling inhibition, and immunoprecipitation studies. Our findings demonstrated that Peptidase M84 could specifically bind to and interact with PAR-1. Furthermore, Peptidase M84 failed to induce apoptosis in PAR-1 silenced ovarian cancer cells. Additionally, ML161, a PAR-1-mediated Gq signalling inhibitor (Gandhi et al., 2019), significantly reduced apoptosis in Peptidase M84-treated cells. This suggests that Peptidase M84 induces PAR-1 activation through Gq signalling. The cumulative data strengthened the possible correlation between PAR-1 and the induction of apoptosis, establishing PAR-1 as a novel oncogenic target for Peptidase M84-mediated apoptosis in ovarian cancer cells. PAR-1 has also emerged as a promising target for chemotherapeutic drugs in recent years. PAR-1 targeting drugs, such as vorapaxar and atopaxar, have entered clinical trials (X. Liu et al., 2017).

Thrombin-mediated PAR-1 activation regulates major signalling pathways, such as p38 MAPK (Marin et al., 2001) and NF-kB (Rahman et al., 2002). In this study, inhibition experiments using NF-kB and p38 inhibitors confirmed the involvement of these pathways in Peptidase M84-mediated apoptosis in PA-1 and SKOV3 cells. Pre-treatment with inhibitors of NF-kB, p38, and ROS significantly reduced cellular apoptosis even after Peptidase M84 treatment, compared to the absence of any prior inhibition. Interestingly, Peptidase M84 treatment not only upregulated p38 phosphorylation but also downregulated p-ERK1/2 in these cells. The blockade of the AKT/ERK pathway and enhanced phosphorylation levels of p38 significantly contribute to apoptosis in response to various stimuli in cancer cells (C. Yang et al., 2020). Furthermore, NF-kB regulates gene expression involved in cellular processes such as proliferation, stress responses, and apoptosis under different conditions (Oeckinghaus & Ghosh, 2009). Additionally, ROS can either activate or repress NF-kB signalling depending on the phase and context (Lingappan, 2018; Nakajima &

Kitamura, 2013). We observed that cellular ROS levels gradually increased over time with Peptidase M84 treatment in ovarian cancer cells. Peptidase M84 promoted PAR-1 dependent activation of p38 and NF-kB signalling, which augmented cellular ROS levels. Inhibition of these pathways attenuated ROS levels in ovarian cancer cells. Phosphorylation of p38, a major component of the MAPK pathway, is linked with ROS generation and cell proliferation (Kulisz et al., 2002; Tapader et al., 2018). However, when p-p38 levels exceed a critical threshold in conjunction with downregulation of ERK, cells experience immense stress leading to apoptosis (Berra et al., 1998). In normal IOSE cells, there was no significant expression of PAR-1, resulting in lower ROS levels even after Peptidase M84 treatment, as there was no effective alteration in PAR-1 activity or expression. Consequently, Peptidase M84 failed to trigger the intrinsic apoptotic pathway in normal IOSE cells.

In light of these findings, we established that PAR-1, NF-kB, p38, ERK1/2, and ROS collaboratively regulate Peptidase M84-induced apoptosis in ovarian cancer cells. A collective understanding of anticancer therapy using microbial proteases will aid in selecting and developing effective strategies for the prevention, treatment, and better management of the deadly disease known as cancer. Numerous models of oxidative stress have been extensively studied to investigate the effects of oxidant stress on NF-κB-related activities. Conversely, ROS can also regulate the activation or repression of NF-κB signalling in a phase- and context-dependent manner. Reports have shown that H_2O_2 significantly decreases the ability of TNF to induce IKK activity, resulting in the inhibition of I-κB degradation and NF-κB activation. ROS-induced oxidation of upstream kinases impacts the NF-κB pathway (Lingappan, 2018; Sies, 2015; Tapader et al., 2018). In our earlier studies on PAR-1-mediated apoptosis in colon carcinoma signalling, we observed ROS as an end product of apoptotic signalling through the activation of NF-κB and MAPK by HAP from *Vibrio cholerae*. Our current study on ovarian cancer cells observed almost complete inhibition of apoptosis when Peptidase M84-treated cells were pre-incubated with the ROS quencher, NAC, and partial inhibition when NF-κB and p38 inhibitors were individually applied. However, we also observed an increase in ROS generation in ovarian cancer cells as an early response (6 h) to Peptidase M84 treatment, which significantly increased in a time-dependent manner (18 h). Nuclear localisation of NF-κB p50 and p65 was observed after 18 h of Peptidase M84 treatment. These findings suggest a cyclic regulatory pathway between

NF-κB activation and oxidative stress, where increased ROS levels promote more nuclear translocation of NF-κB, and conversely, activated NF-κB triggers more ROS generation, creating a feedback loop. These results indicate that NF-κB, p38, ERK1/2, and cellular ROS levels regulate apoptosis by playing decisive roles either individually or collaboratively in Peptidase M84-induced apoptosis in ovarian cancer cells. The levels of cellular ROS and nuclear p50-p65 are much lower in normal cells compared to cancer cells. Therefore, Peptidase M84 does not activate the intrinsic pathway of apoptosis via the same signalling cascade as described above. Phosphorylation of p38, a major component of the MAPK pathway, is associated with cell proliferation and excessive ROS generation in the majority of events. However, when excessive phospho-p38 levels surpass critical threshold levels, immense stress is exerted on cells, ultimately triggering cell death. In our previous study, we established that HAP from *Vibrio cholerae* C6709 induces cellular ROS levels that activate the intrinsic pathway of apoptosis in EAC cells. Since the expression level of PAR-1 in normal healthy cells is lower than in malignant cells, there is no significant activation of the NF-κB and MAP kinase pathways. Consequently, the burden of cellular ROS levels is lower in normal cells, failing to activate the intrinsic pathway of apoptosis (Figure 5.33). Here, we describe the mechanism of Peptidase M84-mediated apoptosis of ovarian cancer cells while leaving normal healthy cells unaltered in the same environment. Due to the activation of PAR-1 by Peptidase M84 in malignant cells, it can be utilised as a therapeutic agent in cancer therapy. A focused approach and combined efforts would accelerate the advancement of new anticancer drugs with greater efficacy.

To validate our findings *in vivo*, we investigated the role of Peptidase M84 in a syngeneic mouse model using the ID8 cell line, a spontaneous murine ovarian adenocarcinoma model. This cell line is advantageous due to its ability to develop tumours in both solid and ascitic forms (Jan et al., 2006; Roby et al., 2000). Our study found that Peptidase M84 treatment in ID8-bearing mice inhibited body weight increase, likely due to reduced ascites formation. Additionally, Peptidase M84 treatment increased the survival rate of these mice compared to the tumour control group, suggesting that Peptidase M84 impacts cancer cell viability *in vivo*. When Peptidase M84 was pre-treated with EDTA, it was ineffectual, indicating that its antitumor activity is dependent on its proteolytic function. In ID8-bearing mice, Peptidase M84 treatment significantly increased cellular ROS levels. This rise in oxidative stress was

corroborated by increased levels of GSH, SOD, and catalase, along with reduced LPO titters, compared to control mice. Moreover, the reduction in viable ID8 cell count in the peritoneum indicated that Peptidase M84 decreased tumour cell survivability and enhanced the effectiveness of chemotherapy. Histopathological studies showed that the cellular architecture and morphology of liver and kidney tissues were not affected by Peptidase M84, indicating it is non-toxic to normal tissues. Furthermore, Peptidase M84 treatment appeared to restore damaged tissue morphology in ID8-bearing mice. The lower levels of SGOT, SGPT, urea, and creatinine in the Peptidase M84-treated group compared to the control group further validated our findings. No significant mortality or toxic symptoms were observed in the protease control group. Thus, our findings demonstrated that Peptidase M84 reduces cancer cell proliferation through oxidative stress-mediated apoptosis without harming normal healthy cells *in vivo*.

Peptidase M84 shows significant promise as a new antitumor agent, meriting further exploration. Additional research in various experimental models and clinical settings is necessary to establish Peptidase M84 as an anticancer drug. This could potentially expand the scope for a durable targeted therapy for ovarian cancer.

CHAPTER 7

Summary

- In pursuit of isolating novel anticancer proteases from environmental microbial isolates, we have screened, purified and identified an extracellular metallo-protease from *Bacillus altitudinis* named Peptidase M84.

- This protease selectively triggered apoptosis in human ovarian adenocarcinoma cells (PA-1, SKOV3) and mouse ovarian carcinoma cells (ID8), in addition to exhibiting no significant effect on normal human epithelial ovarian cell (IOSE) and mouse peritoneal macrophage (PEMΦ) cell viabilities.

- Protease activated receptor-1 (PAR-1); a GPCR which is reported to be overexpressed in ovarian cancer cells was identified as a novel target of Peptidase M84.

- We observed that Peptidase M84 interacted with PAR-1. This induced PAR-1 overexpression and activation along with activating its downstream signalling effectors NFκB and MAPK to promote excessive reactive oxygen species (ROS) generation in ovarian cancer cells. This disrupted mitochondrial membrane potential, allowed the cytosolic release of mitochondrial cytochrome c, increased the Bax (pro-apoptotic) to Bcl-2 (anti-apoptotic) ratio and promoted DNA damage to evoke apoptotic death of the ovarian cancer cells. Peptidase M84 also reduced nuclear ki-67 expression in these malignant cells to render an anti-proliferative role.

- In *in vivo* set-up, weekly intraperitoneal administration of Peptidase M84 (12.0 µg/kg body-weight) in the syngeneic mice model significantly diminished ascitic fluid accumulation through induction of oxidative stress, increasing murine survival rates by 60%. Peptidase M84 is also significantly non-toxic to the host.

- Collectively, our *in vitro* and *in vivo* findings suggested that Peptidase M84 triggered PAR-1 mediated oxidative stress to act as an apoptosis inducer in ovarian cancer cells. This established Peptidase M84 as a promising drug candidate for receptor mediated targeted-therapy of ovarian cancer. Therefore, Peptidase M84 may be employed for its chemotherapeutic efficacy in future for ovarian cancer amelioration.

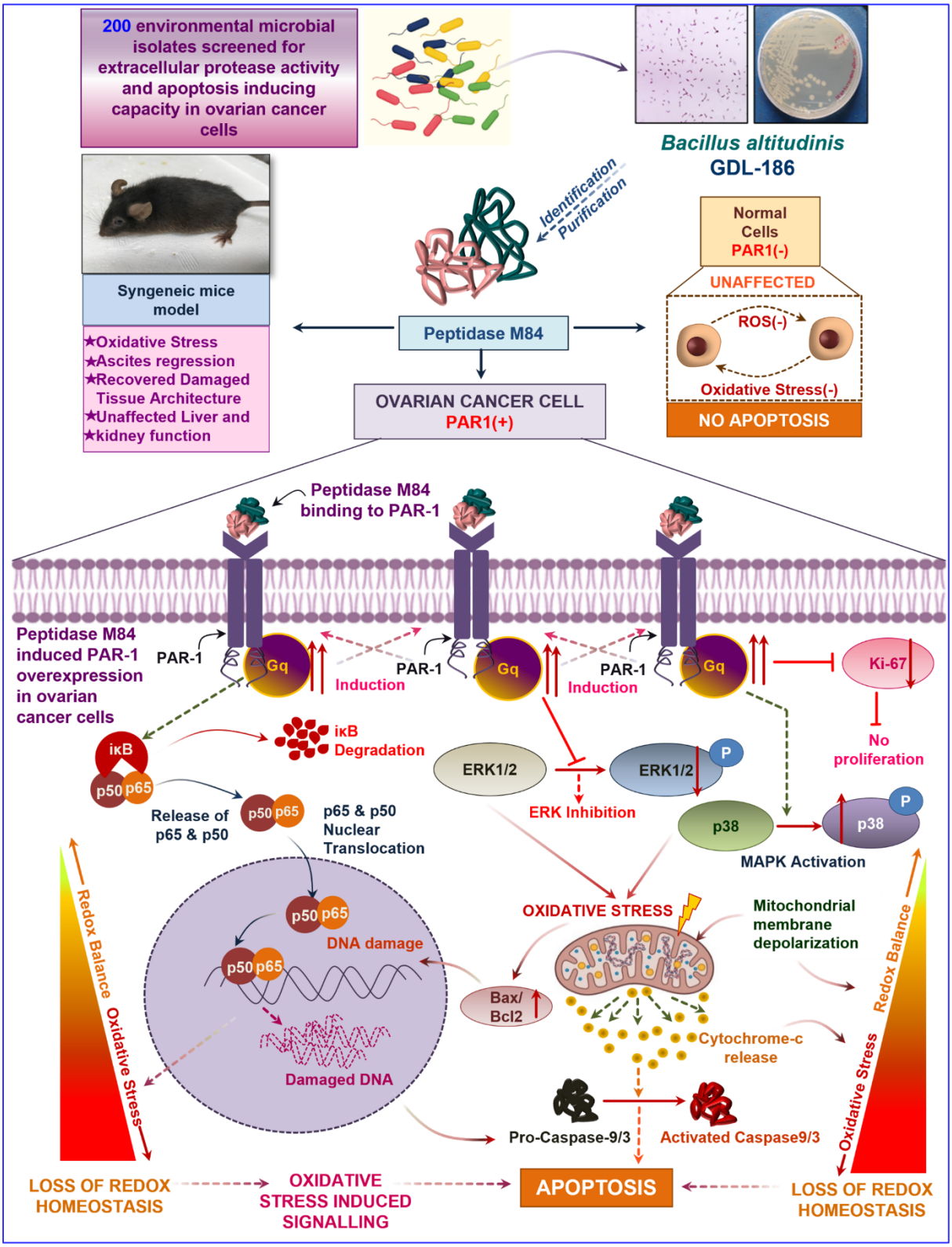

Figure 7.1. Peptidase M84 derived from *Bacillus altitudinis* induced ROS-dependent apoptosis in ovarian cancer cells by targeting PAR-1

CHAPTER 8

References

Ab Mutalib, N.-S., Wong, S. H., Ser, H.-L., Duangjai, A., Law, J. W.-F., Ratnakomala, S., Tan, L. T.-H., & Letchumanan, V. (2020). Bioprospecting of Microbes for Valuable Compounds to Mankind. *Progress In Microbes & Molecular Biology*, *3*(1). https://doi.org/10.36877/pmmb.a0000088

Agarwal, A., Covic, L., Sevigny, L. M., Kaneider, N. C., Lazarides, K., Azabdaftari, G., Sharifi, S., & Kuliopulos, A. (2008). Targeting a metalloprotease-PAR1 signaling system with cell-penetrating pepducins inhibits angiogenesis, ascites, and progression of ovarian cancer. *Molecular Cancer Therapeutics*, *7*(9), 2746–2757. https://doi.org/10.1158/1535-7163.MCT-08-0177

Akter, S., Rahman, Md. A., Hasan, M. N., Akhter, H., Noor, P., Islam, R., Shin, Y., Rahman, Md. H., Gazi, Md. S., Huda, M. N., Nam, N. M., Chung, J., Han, S., Kim, B., Kang, I., Ha, J., Choe, W., Choi, T. G., & Kim, S. S. (2022). Recent Advances in Ovarian Cancer: Therapeutic Strategies, Potential Biomarkers, and Technological Improvements. *Cells*, *11*(4), 650. https://doi.org/10.3390/cells11040650

Alrumman, S. A., Mostafa, Y. S., Al-izran, K. A., Alfaifi, M. Y., Taha, T. H., & Elbehairi, S. E. (2019). Production and Anticancer Activity of an L-Asparaginase from Bacillus licheniformis Isolated from the Red Sea, Saudi Arabia. *Scientific Reports*, *9*(1), 3756. https://doi.org/10.1038/s41598-019-40512-x

Balachandran, C., Duraipandiyan, V., & Ignacimuthu, S. (2012). Purification and characterization of protease enzyme from actinomycetes and its cytotoxic effect on cancer cell line (A549). *Asian Pacific Journal of Tropical Biomedicine*, *2*(1), S392–S400. https://doi.org/10.1016/S2221-1691(12)60195-6

Barua, A., Choudhury, P., Maity, J. K., Mandal, S. B., Mandal, S., & Saha, P. (2019). Chemotherapeutic potential of novel non-toxic nucleoside analogues on EAC ascitic tumour cells. *Free Radical Research*, *53*(1), 57–67. https://doi.org/10.1080/10715762.2018.1551999

Barua, A., Choudhury, P., Mandal, S., Panda, C., & Saha, P. (2020). Therapeutic potential of xanthones from Swertia chirata in breast cancer cells. *Indian Journal of Medical Research*, *152*(3), 285. https://doi.org/10.4103/ijmr.IJMR_1153_18

Berra, E., Diaz-Meco, M. T., & Moscat, J. (1998). The Activation of p38 and Apoptosis by the Inhibition of Erk Is Antagonized by the Phosphoinositide 3-Kinase/Akt Pathway. *Journal of Biological Chemistry*, *273*(17), 10792–10797. https://doi.org/10.1074/jbc.273.17.10792

Boire, A., Covic, L., Agarwal, A., Jacques, S., Sherifi, S., & Kuliopulos, A. (2005). PAR1 Is a Matrix Metalloprotease-1 Receptor that Promotes Invasion and Tumorigenesis of Breast Cancer Cells. *Cell*, *120*(3), 303–313. https://doi.org/10.1016/j.cell.2004.12.018

Bossy-Wetzel, E. (1998). Mitochondrial cytochrome c release in apoptosis occurs upstream of DEVD-specific caspase activation and independently of mitochondrial transmembrane depolarization. *The EMBO Journal*, *17*(1), 37–49. https://doi.org/10.1093/emboj/17.1.37

Brett M., R., Jennifer B., P., Thomas A., S., Brett M., R., Jennifer B., P., & Thomas A., S. (2017). Epidemiology of ovarian cancer: A review. *Cancer Biology & Medicine*, *14*(1), 9–32. https://doi.org/10.20892/j.issn.2095-3941.2016.0084

Carneiro, B. A., & El-Deiry, W. S. (2020). Targeting apoptosis in cancer therapy. *Nature Reviews Clinical Oncology*, *17*(7), 395–417. https://doi.org/10.1038/s41571-020-0341-y

Carswell, E. A., Old, L. J., Kassel, R. L., Green, S., Fiore, N., & Williamson, B. (1975). An endotoxin-induced serum factor that causes necrosis of tumors. *Proceedings of the National Academy of Sciences*, *72*(9), 3666–3670. https://doi.org/10.1073/pnas.72.9.3666

Chakrabarty, A. M., Bernardes, N., & Fialho, A. M. (2014). Bacterial proteins and peptides in cancer therapy: Today and tomorrow. *Bioengineered*, *5*(4), 234–242. https://doi.org/10.4161/bioe.29266

Chakraborty, M., & Bhaumik, M. (2020). Prenatal arsenic exposure interferes in postnatal immunocompetence despite an absence of ongoing arsenic exposure. *Journal of Immunotoxicology*, *17*(1), 135–143. https://doi.org/10.1080/1547691X.2020.1767238

Chaudhry, G.-S., Md Akim, A., Sung, Y. Y., & Sifzizul, T. M. T. (2022). Cancer and apoptosis: The apoptotic activity of plant and marine natural products and their potential as targeted cancer therapeutics. *Frontiers in Pharmacology*, *13*, 842376. https://doi.org/10.3389/fphar.2022.842376

Chin, A. C., Vergnolle, N., MacNaughton, W. K., Wallace, J. L., Hollenberg, M. D., & Buret, A. G. (2003). Proteinase-activated receptor 1 activation induces epithelial apoptosis and increases intestinal permeability. *Proceedings of the National Academy of Sciences*, *100*(19), 11104–11109. https://doi.org/10.1073/pnas.1831452100

Ciucci, A., Buttarelli, M., Fagotti, A., Scambia, G., & Gallo, D. (2022a). Preclinical models of epithelial ovarian cancer: Practical considerations and challenges for a meaningful application. *Cellular and Molecular Life Sciences*, *79*(7), 364. https://doi.org/10.1007/s00018-022-04395-y

Ciucci, A., Buttarelli, M., Fagotti, A., Scambia, G., & Gallo, D. (2022b). Preclinical models of epithelial ovarian cancer: Practical considerations and challenges for a meaningful application. *Cellular and Molecular Life Sciences*, *79*(7), 364. https://doi.org/10.1007/s00018-022-04395-y

Craik, C. S., Page, M. J., & Madison, E. L. (2011). Proteases as therapeutics. *Biochemical Journal*, *435*(1), 1–16. https://doi.org/10.1042/BJ20100965

Cristea, M., Han, E., Salmon, L., & Morgan, R. J. (2010). Review: Practical considerations in ovarian cancer chemotherapy. *Therapeutic Advances in Medical Oncology*, *2*(3), 175–187. https://doi.org/10.1177/1758834010361333

Das, R., Kamal, I. M., Das, S., Chakrabarti, S., & Chakrabarti, O. (2022). MITOL-mediated DRP1 ubiquitylation and degradation promotes mitochondrial hyperfusion in a CMT2A-linked MFN2 mutant. *Journal of Cell Science*, *135*(2), jcs257808. https://doi.org/10.1242/jcs.257808

Dasgupta, S., Kar, K., Barua, A., Ghosh, D., Kabi, B., Dewan, K., & Chandra, A. (2022). A significantly non-toxic novel Cobalt(III) Schiff base complex induces apoptosis via G2-M cell cycle arrest in human breast cancer cell line MCF-7. *Life Sciences*, *308*, 120963. https://doi.org/10.1016/j.lfs.2022.120963

Deb, M., Sengupta, D., Kar, S., Rath, S. K., Parbin, S., Shilpi, A., Roy, S., Das, G., & Patra, S. K. (2014). Elucidation of caveolin 1 both as a tumor suppressor and metastasis promoter in light of epigenetic modulators. *Tumor Biology*, *35*(12), 12031–12047. https://doi.org/10.1007/s13277-014-2502-z

Di Lorenzo, G., Ricci, G., Severini, G. M., Romano, F., & Biffi, S. (2018). Imaging and therapy of ovarian cancer: Clinical application of nanoparticles and future perspectives. *Theranostics*, *8*(16), 4279–4294. https://doi.org/10.7150/thno.26345

Dimauro, I., Pearson, T., Caporossi, D., & Jackson, M. J. (2012). A simple protocol for the subcellular fractionation of skeletal muscle cells and tissue. *BMC Research Notes*, *5*(1), 513. https://doi.org/10.1186/1756-0500-5-513

Flynn, A. N., & Buret, A. G. (2004). Proteinase-activated receptor 1 (PAR-1) and cell apoptosis. *Apoptosis*, *9*(6), 729–737. https://doi.org/10.1023/B:APPT.0000045784.49886.96

Furman, M., Krueger, L., Frelinger, A. L., Barnard, M., Mascelli, M., Nakada, M., & Michelson, A. (2000). GPIIb-IIIa Antagonist-induced Reduction in Platelet Surface Factor V/Va Binding and Phosphatidylserine Expression in Whole Blood. *Thrombosis and Haemostasis*, *84*(09), 492–498. https://doi.org/10.1055/s-0037-1614050

Furman, M., Nurden, P., Berndt, M., Nurden, A., Benoit, S., Barnard, M., Ofosu, F., & Michelson, A. (2000). The Cleaved Peptide of PAR1 Results in a Redistribution of the Platelet Surface GPIb-

IX-V Complex to the Surface-Connected Canalicular System. *Thrombosis and Haemostasis*, *84*(11), 897–903. https://doi.org/10.1055/s-0037-1614134

Gandhi, D. M., Rosas, R., Greve, E., Kentala, K., D.-R. Diby, N., Snyder, V. A., Stephans, A., Yeung, T. H. W., Subramaniam, S., DiMilo, E., Kurtenbach, K. E., Arnold, L. A., Weiler, H., & Dockendorff, C. (2019). The parmodulin NRD-21 is an allosteric inhibitor of PAR1 Gq signaling with improved anti-inflammatory activity and stability. *Bioorganic & Medicinal Chemistry*, *27*(17), 3788–3796. https://doi.org/10.1016/j.bmc.2019.06.043

Gerszten, R. E., Chen, J., Ishli, M., Ishil, K., Wang, L., Nanevicz, T., Turck, C. W., Vu, T.-K. H., & Coughlin, S. R. (1994). Specificity of the thrombin receptor for agonist peptide is defined by its extracellular surface. *Nature*, *368*(6472), 648–651. https://doi.org/10.1038/368648a0

Ghosh, A., Saha, D. R., Hoque, K. M., Asakuna, M., Yamasaki, S., Koley, H., Das, S. S., Chakrabarti, M. K., & Pal, A. (2006). Enterotoxigenicity of Mature 45-Kilodalton and Processed 35-Kilodalton Forms of Hemagglutinin Protease Purified from a Cholera Toxin Gene-Negative *Vibrio cholerae* Non-O1, Non-O139 Strain. *Infection and Immunity*, *74*(5), 2937–2946. https://doi.org/10.1128/IAI.74.5.2937-2946.2006

Ghosh, D., Pakhira, S., Ghosh, D. D., Roychoudhury, S., & Roy, S. S. (2023). Ets1 facilitates EMT/invasion through Drp1-mediated mitochondrial fragmentation in ovarian cancer. *iScience*, *26*(9), 107537. https://doi.org/10.1016/j.isci.2023.107537

Goldstein, J. C., Waterhouse, N. J., Juin, P., Evan, G. I., & Green, D. R. (2000). The coordinate release of cytochrome c during apoptosis is rapid, complete and kinetically invariant. *Nature Cell Biology*, *2*(3), 156–162. https://doi.org/10.1038/35004029

Gomes, M. S. R., Naves De Souza, D. L., Guimaraes, D. O., Lopes, D. S., Mamede, C. C. N., Gimenes, S. N. C., Ache, D. C., Rodrigues, R. S., Yoneyama, K. A. G., Borges, M. H., De Oliveira, F., & Rodrigues, V. M. (2015). Biochemical and functional characterization of Bothropoidin: The first haemorrhagic metalloproteinase from Bothrops pauloensis snake venom. *Journal of Biochemistry*, *157*(3), 137–149. https://doi.org/10.1093/jb/mvu058

Grisaru-Granovsky, S., Salah, Z., Maoz, M., Pruss, D., Beller, U., & Bar-Shavit, R. (2005). Differential expression of *Protease activated receptor 1* (*Par1*) and pY397FAK in benign and malignant human ovarian tissue samples. *International Journal of Cancer*, *113*(3), 372–378. https://doi.org/10.1002/ijc.20607

Hayes, J. D., Dinkova-Kostova, A. T., & Tew, K. D. (2020). Oxidative Stress in Cancer. *Cancer Cell*, *38*(2), 167–197. https://doi.org/10.1016/j.ccell.2020.06.001

Higuchi, M., Honda, T., Proske, R. J., & Yeh, E. T. (1998). Regulation of reactive oxygen species-induced apoptosis and necrosis by caspase 3-like proteases. *Oncogene*, *17*(21), 2753–2760. https://doi.org/10.1038/sj.onc.1202211

Huang, M., Lu, J.-J., & Ding, J. (2021). Natural Products in Cancer Therapy: Past, Present and Future. *Natural Products and Bioprospecting*, *11*(1), 5–13. https://doi.org/10.1007/s13659-020-00293-7

Jan, M. M., Yockman, J. W., Anderson, M. L., Kieback, D. G., & Kim, S. W. (2006). Comparison of ID8 MOSE and VEGF-modified ID8 Cell Lines in an Immunocompetent Animal Model for Human Ovarian Cancer. *ANTICANCER RESEARCH*.

Kamath, L., Meydani, A., Foss, F., & Kuliopulos, A. (n.d.). *Signaling from Protease-activated Receptor-1 Inhibits Migration and Invasion of Breast Cancer Cells1,2*.

Kar, S., Sengupta, D., Deb, M., Shilpi, A., Parbin, S., Rath, S. K., Pradhan, N., Rakshit, M., & Patra, S. K. (2014). Expression profiling of DNA methylation-mediated epigenetic gene-silencing factors in breast cancer. *Clinical Epigenetics*, *6*(1), 20. https://doi.org/10.1186/1868-7083-6-20

Kim, G., Ison, G., McKee, A. E., Zhang, H., Tang, S., Gwise, T., Sridhara, R., Lee, E., Tzou, A., Philip, R., Chiu, H.-J., Ricks, T. K., Palmby, T., Russell, A. M., Ladouceur, G., Pfuma, E., Li, H., Zhao,

L., Liu, Q., … Pazdur, R. (2015). FDA Approval Summary: Olaparib Monotherapy in Patients with Deleterious Germline *BRCA* -Mutated Advanced Ovarian Cancer Treated with Three or More Lines of Chemotherapy. *Clinical Cancer Research*, *21*(19), 4257–4261. https://doi.org/10.1158/1078-0432.CCR-15-0887

Kulisz, A., Chen, N., Chandel, N. S., Shao, Z., & Schumacker, P. T. (2002). Mitochondrial ROS initiate phosphorylation of p38 MAP kinase during hypoxia in cardiomyocytes. *American Journal of Physiology-Lung Cellular and Molecular Physiology*, *282*(6), L1324–L1329. https://doi.org/10.1152/ajplung.00326.2001

Kurnit, K. C., Fleming, G. F., & Lengyel, E. (2021). Updates and New Options in Advanced Epithelial Ovarian Cancer Treatment. *Obstetrics & Gynecology*, *137*(1), 108–121. https://doi.org/10.1097/AOG.0000000000004173

Lheureux, S., Karakasis, K., Kohn, E. C., & Oza, A. M. (2015). Ovarian cancer treatment: The end of empiricism? *Cancer*, *121*(18), 3203–3211. https://doi.org/10.1002/cncr.29481

Li, G., Yi, X., Du, S., Gong, L., Wu, Q., Cai, J., Sun, S., Cao, Y., Chen, L., Xu, L., & Wang, Z. (2023). Tumour-derived exosomal piR-25783 promotes omental metastasis of ovarian carcinoma by inducing the fibroblast to myofibroblast transition. *Oncogene*, *42*(6), 421–433. https://doi.org/10.1038/s41388-022-02560-y

Li, J., Cui, J., Li, Z., Fu, X., Li, J., Li, H., Wang, S., & Zhang, M. (2020). ORP8 induces apoptosis by releasing cytochrome□c from mitochondria in non-small cell lung cancer. *Oncology Reports*. https://doi.org/10.3892/or.2020.7517

Li, P., Li, X., Saravanan, R., Li, C. M., & Leong, S. S. J. (2012). Antimicrobial macromolecules: Synthesis methods and future applications. *RSC Advances*, *2*(10), 4031. https://doi.org/10.1039/c2ra01297a

Lingappan, K. (2018). NF-κB in oxidative stress. *Current Opinion in Toxicology*, *7*, 81–86. https://doi.org/10.1016/j.cotox.2017.11.002

Liou, G.-Y., & Storz, P. (2010). Reactive oxygen species in cancer. *Free Radical Research*, *44*(5), 479–496. https://doi.org/10.3109/10715761003667554

Liu, X., Yu, J., Song, S., Yue, X., & Li, Q. (2017). Protease-activated receptor-1 (PAR-1): A promising molecular target for cancer. *Oncotarget*, *8*(63), 107334–107345. https://doi.org/10.18632/oncotarget.21015

Liu, Y., Tong, L., Luo, Y., Li, X., Chen, G., & Wang, Y. (2018). Resveratrol inhibits the proliferation and induces the apoptosis in ovarian cancer cells via inhibiting glycolysis and targeting AMPK/mTOR signaling pathway. *Journal of Cellular Biochemistry*, *119*(7), 6162–6172. https://doi.org/10.1002/jcb.26822

Liu, Z., Jing, C., & Kong, F. (2024). From clinical management to personalized medicine: Novel therapeutic approaches for ovarian clear cell cancer. *Journal of Ovarian Research*, *17*(1), 39. https://doi.org/10.1186/s13048-024-01359-7

Maeda, H., Molla, A., Sakamoto, K., Murakami, A., & Matsumura, Y. (n.d.). *Cytotoxicity of Bacterial Proteases in Various Tumor Cells Mediated through Â«2-Macroglobulin Receptor*.

Marin, V., Farnarier, C., Grès, S., Kaplanski, S., Su, M. S.-S., Dinarello, C. A., & Kaplanski, G. (2001). The p38 mitogen-activated protein kinase pathway plays a critical role in thrombin-induced endothelial chemokine production and leukocyte recruitment. *Blood*, *98*(3), 667–673. https://doi.org/10.1182/blood.V98.3.667

McCarthy, E. F. (n.d.). *THE TOXINS OF WILLIAM B. COLEY AND THE TREATMENT OF BONE AND SOFT-TISSUE SARCOMAS*.

Mhatre, A., Koroth, J., Manjunath, M., Kumar S, S., Gawari, R., & Choudhary, B. (2023). Multi-omics analysis of the Indian ovarian cancer cohort revealed histotype-specific mutation and gene

expression patterns. *Frontiers in Genetics*, *14*, 1102114. https://doi.org/10.3389/fgene.2023.1102114

Moschetta, M., Boussios, S., Rassy, E., Samartzis, E. P., Funingana, G., & Uccello, M. (2020). Neoadjuvant treatment for newly diagnosed advanced ovarian cancer: Where do we stand and where are we going? *Annals of Translational Medicine*, *8*(24), 1710–1710. https://doi.org/10.21037/atm-20-1683

Mußbach, F., Henklein, P., Westermann, M., Settmacher, U., Böhmer, F.-D., & Kaufmann, R. (2015). Proteinase-activated receptor 1- and 4-promoted migration of Hep3B hepatocellular carcinoma cells depends on ROS formation and RTK transactivation. *Journal of Cancer Research and Clinical Oncology*, *141*(5), 813–825. https://doi.org/10.1007/s00432-014-1863-4

Nag, N., Ray, T., Tapader, R., Gope, A., Das, R., Mahapatra, E., Saha, S., Pal, A., Prasad, P., & Pal, A. (2024). Metallo-protease Peptidase M84 from *Bacillus altitudinis* induces ROS-dependent apoptosis in ovarian cancer cells by targeting PAR-1. *iScience*, *27*(6), 109828. https://doi.org/10.1016/j.isci.2024.109828

Nakajima, S., & Kitamura, M. (2013). Bidirectional regulation of NF-κB by reactive oxygen species: A role of unfolded protein response. *Free Radical Biology and Medicine*, *65*, 162–174. https://doi.org/10.1016/j.freeradbiomed.2013.06.020

Naskar, D., Maiti, G., Chakraborty, A., Roy, A., Chattopadhyay, D., & Sen, M. (2014). Wnt5a–Rac1–NF-κB Homeostatic Circuitry Sustains Innate Immune Functions in Macrophages. *The Journal of Immunology*, *192*(9), 4386–4397. https://doi.org/10.4049/jimmunol.1302817

Oeckinghaus, A., & Ghosh, S. (2009). The NF- B Family of Transcription Factors and Its Regulation. *Cold Spring Harbor Perspectives in Biology*, *1*(4), a000034–a000034. https://doi.org/10.1101/cshperspect.a000034

Oldham, W. M., & Hamm, H. E. (2008). Heterotrimeric G protein activation by G-protein-coupled receptors. *Nature Reviews Molecular Cell Biology*, *9*(1), 60–71. https://doi.org/10.1038/nrm2299

Park, B. T., Na, K. H., Jung, E. C., Park, J. W., & Kim, H. H. (2009). Antifungal and Anticancer Activities of a Protein from the Mushroom Cordyceps militaris. *The Korean Journal of Physiology and Pharmacology*, *13*(1), 49. https://doi.org/10.4196/kjpp.2009.13.1.49

Patra, S. K. (2008). Dissecting lipid raft facilitated cell signaling pathways in cancer. *Biochimica et Biophysica Acta (BBA) - Reviews on Cancer*, *1785*(2), 182–206. https://doi.org/10.1016/j.bbcan.2007.11.002

Pereira, F. V., Ferreira-Guimarães, C. A., Paschoalin, T., Scutti, J. A. B., Melo, F. M., Silva, L. S., Melo, A. C. L., Silva, P., Tiago, M., Matsuo, A. L., Juliano, L., Juliano, M. A., Carmona, A. K., Travassos, L. R., & Rodrigues, E. G. (2014). A Natural Bacterial-Derived Product, the Metalloprotease Arazyme, Inhibits Metastatic Murine Melanoma by Inducing MMP-8 Cross-Reactive Antibodies. *PLoS ONE*, *9*(4), e96141. https://doi.org/10.1371/journal.pone.0096141

Perillo, B., Di Donato, M., Pezone, A., Di Zazzo, E., Giovannelli, P., Galasso, G., Castoria, G., & Migliaccio, A. (2020). ROS in cancer therapy: The bright side of the moon. *Experimental & Molecular Medicine*, *52*(2), 192–203. https://doi.org/10.1038/s12276-020-0384-2

Prasad, P., Ghosh, S., & Roy, S. S. (2021). Glutamine deficiency promotes stemness and chemoresistance in tumor cells through DRP1-induced mitochondrial fragmentation. *Cellular and Molecular Life Sciences*, *78*(10), 4821–4845. https://doi.org/10.1007/s00018-021-03818-6

Punj, V., Bhattacharyya, S., Saint-Dic, D., Vasu, C., Cunningham, E. A., Graves, J., Yamada, T., Constantinou, A. I., Christov, K., White, B., Li, G., Majumdar, D., Chakrabarty, A. M., & Das Gupta, T. K. (2004). Bacterial cupredoxin azurin as an inducer of apoptosis and regression in human breast cancer. *Oncogene*, *23*(13), 2367–2378. https://doi.org/10.1038/sj.onc.1207376

Rao, M. B., Tanksale, A. M., Ghatge, M. S., & Deshpande, V. V. (1998). Molecular and Biotechnological Aspects of Microbial Proteases. *Microbiology and Molecular Biology Reviews*, *62*(3), 597–635. https://doi.org/10.1128/MMBR.62.3.597-635.1998

Rath, S. K., Deb, M., Sengupta, D., Kari, V., Kar, S., Parbin, S., Pradhan, N., & Patra, S. K. (2016). Silencing of ZRF1 impedes survival of estrogen receptor positive MCF-7 cells and potentiates the effect of curcumin. *Tumor Biology*, *37*(9), 12535–12546. https://doi.org/10.1007/s13277-016-5114-y

Ray, T., Chakrabarti, M. K., & Pal, A. (2016). Hemagglutinin protease secreted by V. cholerae induced apoptosis in breast cancer cells by ROS mediated intrinsic pathway and regresses tumor growth in mice model. *Apoptosis*, *21*(2), 143–154. https://doi.org/10.1007/s10495-015-1194-1

Ray, T., & Pal, A. (2016). PAR-1 mediated apoptosis of breast cancer cells by V. cholerae hemagglutinin protease. *Apoptosis*, *21*(5), 609–620. https://doi.org/10.1007/s10495-016-1229-2

Razzaq, A., Shamsi, S., Ali, A., Ali, Q., Sajjad, M., Malik, A., & Ashraf, M. (2019). Microbial Proteases Applications. *Frontiers in Bioengineering and Biotechnology*, *7*, 110. https://doi.org/10.3389/fbioe.2019.00110

Roby, K. F., Taylor, C. C., Sweetwood, J. P., Cheng, Y., Pace, J. L., Tawfik, O., Persons, D. L., Smith, P. G., & Terranova, P. F. (2000). Development of a syngeneic mouse model for events related to ovarian cancer. *Carcinogenesis*, *21*(4), 585–591. https://doi.org/10.1093/carcin/21.4.585

Rojas, V., Hirshfield, K., Ganesan, S., & Rodriguez-Rodriguez, L. (2016). Molecular Characterization of Epithelial Ovarian Cancer: Implications for Diagnosis and Treatment. *International Journal of Molecular Sciences*, *17*(12), 2113. https://doi.org/10.3390/ijms17122113

Sabirova, A. R., Rudakova, N. L., Balaban, N. P., Ilyinskaya, O. N., Demidyuk, I. V., Kostrov, S. V., Rudenskaya, G. N., & Sharipova, M. R. (2010). A novel secreted metzincin metalloproteinase from *Bacillus intermedius*. *FEBS Letters*, *584*(21), 4419–4425. https://doi.org/10.1016/j.febslet.2010.09.049

Sahayasheela, V. J., Lankadasari, M. B., Dan, V. M., Dastager, S. G., Pandian, G. N., & Sugiyama, H. (2022). Artificial intelligence in microbial natural product drug discovery: Current and emerging role. *Natural Product Reports*, *39*(12), 2215–2230. https://doi.org/10.1039/D2NP00035K

Scholzen, T., & Gerdes, J. (2000). The Ki-67 protein: From the known and the unknown. *Journal of Cellular Physiology*, *182*(3), 311–322. https://doi.org/10.1002/(SICI)1097-4652(200003)182:3<311::AID-JCP1>3.0.CO;2-9

Shankar, R., Upadhyay, P. K., & Kumar, M. (2021). Protease Enzymes: Highlights on Potential of Proteases as Therapeutics Agents. *International Journal of Peptide Research and Therapeutics*, *27*(2), 1281–1296. https://doi.org/10.1007/s10989-021-10167-2

Sheng, Y.-N., Luo, Y.-H., Liu, S.-B., Xu, W.-T., Zhang, Y., Zhang, T., Xue, H., Zuo, W.-B., Li, Y.-N., Wang, C.-Y., & Jin, C.-H. (2020). Zeaxanthin Induces Apoptosis via ROS-Regulated MAPK and AKT Signaling Pathway in Human Gastric Cancer Cells. *OncoTargets and Therapy*, *Volume 13*, 10995–11006. https://doi.org/10.2147/OTT.S272514

Shivaji, S., Chaturvedi, P., Suresh, K., Reddy, G. S. N., Dutt, C. B. S., Wainwright, M., Narlikar, J. V., & Bhargava, P. M. (2006). Bacillus aerius sp. Nov., Bacillus aerophilus sp. Nov., Bacillus stratosphericus sp. Nov. And Bacillus altitudinis sp. Nov., isolated from cryogenic tubes used for collecting air samples from high altitudes. *International Journal of Systematic and Evolutionary Microbiology*, *56*(7), 1465–1473. https://doi.org/10.1099/ijs.0.64029-0

Siegel, R. L., Miller, K. D., & Jemal, A. (2020). Cancer statistics, 2020. *CA: A Cancer Journal for Clinicians*, *70*(1), 7–30. https://doi.org/10.3322/caac.21590

Sies, H. (2015). Oxidative stress: A concept in redox biology and medicine. *Redox Biology*, *4*, 180–183. https://doi.org/10.1016/j.redox.2015.01.002

Singh, N. P., McCoy, M. T., Tice, R. R., & Schneider, E. L. (1988). A simple technique for quantitation of low levels of DNA damage in individual cells. *Experimental Cell Research*, *175*(1), 184–191. https://doi.org/10.1016/0014-4827(88)90265-0

Song, P., Zhang, X., Wang, S., Xu, W., Wang, F., Fu, R., & Wei, F. (2023). Microbial proteases and their applications. *Frontiers in Microbiology*, *14*, 1236368. https://doi.org/10.3389/fmicb.2023.1236368

Srinivas, U. S., Tan, B. W. Q., Vellayappan, B. A., & Jeyasekharan, A. D. (2019). ROS and the DNA damage response in cancer. *Redox Biology*, *25*, 101084. https://doi.org/10.1016/j.redox.2018.101084

Sun, L., Xie, P., Wada, J., Kashihara, N., Liu, F., Zhao, Y., Kumar, D., Chugh, S. S., Danesh, F. R., & Kanwar, Y. S. (2008). Rap1b GTPase Ameliorates Glucose-Induced Mitochondrial Dysfunction. *Journal of the American Society of Nephrology*, *19*(12), 2293–2301. https://doi.org/10.1681/ASN.2008030336

Syngkon, A., Elluri, S., Koley, H., Rompikuntal, P. K., Saha, D. R., Chakrabarti, M. K., Bhadra, R. K., Wai, S. N., & Pal, A. (2010). Studies on a Novel Serine Protease of a ΔhapAΔprtV Vibrio cholerae O1 Strain and Its Role in Hemorrhagic Response in the Rabbit Ileal Loop Model. *PLoS ONE*, *5*(9), e13122. https://doi.org/10.1371/journal.pone.0013122

Tapader, R., Basu, S., & Pal, A. (2019). Secreted proteases: A new insight in the pathogenesis of extraintestinal pathogenic Escherichia coli. *International Journal of Medical Microbiology*, *309*(3–4), 159–168. https://doi.org/10.1016/j.ijmm.2019.03.002

Tapader, R., Bose, D., Basu, P., Mondal, M., Mondal, A., Chatterjee, N. S., Dutta, P., Basu, S., Bhadra, R. K., & Pal, A. (2016). Role in proinflammatory response of YghJ, a secreted metalloprotease from neonatal septicemic Escherichia coli. *International Journal of Medical Microbiology*, *306*(7), 554–565. https://doi.org/10.1016/j.ijmm.2016.06.003

Tapader, R., Bose, D., Dutta, P., Das, S., & Pal, A. (2018). SslE (YghJ), a Cell-Associated and Secreted Lipoprotein of Neonatal Septicemic Escherichia coli, Induces Toll-Like Receptor 2-Dependent Macrophage Activation and Proinflammation through NF-κB and MAP Kinase Signaling. *Infection and Immunity*, *86*(9), e00399-18. https://doi.org/10.1128/IAI.00399-18

Toh, E., Baryalai, P., Nadeem, A., Aung, K. M., Chen, S., Persson, K., Persson, J. L., Uhlin, B. E., & Wai, S. N. (2022). Bacterial protein MakA causes suppression of tumour cell proliferation via inhibition of PIP5K1α/Akt signalling. *Cell Death & Disease*, *13*(12), 1024. https://doi.org/10.1038/s41419-022-05480-7

Torre, L. A., Trabert, B., DeSantis, C. E., Miller, K. D., Samimi, G., Runowicz, C. D., Gaudet, M. M., Jemal, A., & Siegel, R. L. (2018). Ovarian cancer statistics, 2018. *CA: A Cancer Journal for Clinicians*, *68*(4), 284–296. https://doi.org/10.3322/caac.21456

Trivanović, D., Pavelić, K., & Peršurić, Ž. (2021). Fighting Cancer with Bacteria and Their Toxins. *International Journal of Molecular Sciences*, *22*(23), 12980. https://doi.org/10.3390/ijms222312980

Vachher, M., Sen, A., Kapila, R., & Nigam, A. (2021). Microbial therapeutic enzymes: A promising area of biopharmaceuticals. *Current Research in Biotechnology*, *3*, 195–208. https://doi.org/10.1016/j.crbiot.2021.05.006

Vimal, A., & Kumar, A. (2017). Biotechnological production and practical application of L-asparaginase enzyme. *Biotechnology and Genetic Engineering Reviews*, *33*(1), 40–61. https://doi.org/10.1080/02648725.2017.1357294

Von Harsdorf, R., Li, P.-F., & Dietz, R. (1999). Signaling Pathways in Reactive Oxygen Species–Induced Cardiomyocyte Apoptosis. *Circulation*, *99*(22), 2934–2941. https://doi.org/10.1161/01.CIR.99.22.2934

Xu, Y., Kersten, R. D., Nam, S.-J., Lu, L., Al-Suwailem, A. M., Zheng, H., Fenical, W., Dorrestein, P. C., Moore, B. S., & Qian, P.-Y. (2012). Bacterial Biosynthesis and Maturation of the Didemnin Anti-cancer Agents. *Journal of the American Chemical Society*, *134*(20), 8625–8632. https://doi.org/10.1021/ja301735a

Yang, C., Luo, J., Luo, X., Jia, W., Fang, Z., Yi, S., & Li, L. (2020). Morusin exerts anti-cancer activity in renal cell carcinoma by disturbing MAPK signaling pathways. *Annals of Translational Medicine*, *8*(6), 327–327. https://doi.org/10.21037/atm.2020.02.107

Yang, J., Liu, X., Bhalla, K., Kim, C. N., Ibrado, A. M., Cai, J., Peng, T.-I., Jones, D. P., & Wang, X. (1997). Prevention of Apoptosis by Bcl-2: Release of Cytochrome c from Mitochondria Blocked. *Science*, *275*(5303), 1129–1132. https://doi.org/10.1126/science.275.5303.1129

Yap, H. Y. Y., Tan, N. H., Ng, S. T., Tan, C. S., & Fung, S. Y. (2018). Molecular attributes and apoptosis-inducing activities of a putative serine protease isolated from Tiger Milk mushroom (*Lignosus rhinocerus*) sclerotium against breast cancer cells *in vitro*. *PeerJ*, *6*, e4940. https://doi.org/10.7717/peerj.4940

Zahaf, N.-I., & Schmidt, G. (2017). Bacterial Toxins for Cancer Therapy. *Toxins*, *9*(8), 236. https://doi.org/10.3390/toxins9080236

Zain, J., Huang, Y.-Q., Feng, X., Nierodzik, M. L., Li, J.-J., & Karpatkin, S. (2000). Concentration-dependent dual effect of thrombin on impaired growth/apoptosis or mitogenesis in tumor cells. *Blood*, *95*(10), 3133–3138. https://doi.org/10.1182/blood.V95.10.3133

Zania, P., Gourni, D., Aplin, A. C., Nicosia, R. F., Flordellis, C. S., Maragoudakis, M. E., & Tsopanoglou, N. E. (2009). Parstatin, the Cleaved Peptide on Proteinase-Activated Receptor 1 Activation, Is a Potent Inhibitor of Angiogenesis. *Journal of Pharmacology and Experimental Therapeutics*, *328*(2), 378–389. https://doi.org/10.1124/jpet.108.145664

Zhang, J., Zhao, X., Wang, S., Wang, N., Han, J., Jia, L., & Ren, X. (2015). Monitoring therapeutic response of human ovarian cancer to trastuzumab by SPECT imaging with 99m Tc-peptide-Z HER2:342. *Nuclear Medicine and Biology*, *42*(6), 541–546. https://doi.org/10.1016/j.nucmedbio.2015.02.002

Zhang, Y., Luo, G., Li, M., Guo, P., Xiao, Y., Ji, H., & Hao, Y. (2019). Global patterns and trends in ovarian cancer incidence: Age, period and birth cohort analysis. *BMC Cancer*, *19*(1), 984. https://doi.org/10.1186/s12885-019-6139-6

Zhu, J. W., Charkhchi, P., & Akbari, M. R. (2022). Potential clinical utility of liquid biopsies in ovarian cancer. *Molecular Cancer*, *21*(1), 114. https://doi.org/10.1186/s12943-022-01588-8

Zo, M. (n.d.). Apoptosis regulators and their role in tumorigenesis. *Biochimica et Biophysica Acta*.

❖ Publications and Proceedings

List of Publications arising from the thesis

• **Nag N**, Ray T, Tapader R, Gope A, Das R, Mahapatra E, Saha S, Pal A, Prasad P, Pal A. Metallo-protease Peptidase M84 from *Bacillus altitudinis* induces ROS-dependent apoptosis in ovarian cancer cells by targeting PAR-1. iScience. 2024 Apr 26;27(6):109828. doi: 10.1016/j.isci.2024.109828. PMID: 38799586; PMCID: PMC11126781.

Additional Work (Not in Thesis)

• Barua, A., Choudhury, P., **Nag, N**., Nath, A., Kundagrami, S., Pal, A., Panda, CK., Saha P. Xanthone from *Swertia chirata* exerts chemotherapeutic potential against 597 colon carcinoma. Current Science. 2022.122(1):47–55. doi: https://doi: 10.18520/cs/v122/i1/47-55.

• Mahapatra E, Saha A, **Nag N**, Gope A, Vernekar M, Chakrabarti J, Pal A, Sengupta S and Mukherjee S. Deregulated PI3K/Akt/mTOR Pathway Reprograms HGSOC related Cholesterol Profiles to Promote Carboplatin Insensitivity. (Under review).

• Barua, A., Mallick, S., **Nag, N**., Nath, A., Pal, A., Banerjee, S., Chemotherapeutic potential of anthocyanin isolated from red rice. (Under review).

• Ray T, Roy P, **Nag N**, Tapader R, Saha S and Pal A. *Vibrio cholerae* hemagglutinin protease: A novel microtubule targeting agent to kill colon cancer cells by triggering lysosomal and proteasomal cascades and induced apoptosis in explant culture of colon and gastrointestinal cancer tissues of human clinical samples. (Under review).

• **Nag N** and Pal A. Peptidase M84 impedes ovarian cancer cell survival by inhibiting epithelial to mesenchymal transition in a PAR-2 dependent manner. (Manuscript under preparation).

• Tapader R, Singh N, **Nag N**, Saha S, Ray T, Bhowmick M and Pal A. Maternal immunization with SslE (YghJ), a surface-associated and secreted lipoprotein of *Escherichia coli*, confers systemic and mucosal protection against neonatal septicemic *E. coli* in a murine model of early-onset sepsis. (Manuscript under preparation).

• Saha, S., Ray, T., Tapader, R., **Nag, N**., Gope, A., Pal, A., Non-canonical activation of PAR-1 induced by PFISED peptide triggers autophagy in breast cancer cells. (Manuscript under preparation)

❖ Conference and symposium attended

Oral Presentations

- **Niraj Nag** and Amit Pal "Peptidase M84 from *Bacillus altitudinis* induces apoptosis in ovarian cancer cells in a PAR-1/ROS dependent manner". International Conference on Traditional Medicine & Phytopharmaceuticals and 11th International Congress of Society for Ethnopharmacology organized by CSIR-IIIM, Jammu, India. **(2024)**

- **Niraj Nag** and Amit Pal "Anticarcinogenic effects of Peptidase M84 from *Bacillus altitudinis*". National conference on "Sustainable health science for future generations" organized by ISCA-Kolkata chapter and University of Kalyani. **(2022)**

Poster Presentations

- **Niraj Nag**, Tanusree Ray and Amit Pal. **Best poster award** for the poster entitled "Overexpression of PAR-1 by Peptidase M84, a secreted metallo-protease from *Bacillus altitudinis* induces apoptosis in ovarian cancer cells in a caspase cascade dependent manner. International Conference on Advances in Molecular Diagnostics and Precision Medicine (AMDP) in association with Cancercon 2022, Organized by Anna University, Chennai, India. **(2022)**

Niraj Nag and Amit Pal. "Microbial Protease Mediated Induction of Apoptosis in Human Colon Cancer Cells" 16th Asian Conference on Dirrhoeaeal Disease and Nutrition (ASCODD), organised by ICMR-NICED, India in association with ICDDRB Bangladesh, in Kolkata, India. **(2022)**

- **Niraj Nag** and Amit Pal. "Purification and Identification of Peptidase M84, an Extracellular Metallo-Protease from *Bacillus altitudinis* as an Apoptotic Molecule Against Ovarian Cancer Cells; Protease Activated Receptor-1 is a Putative Target". 11th annual conference of Asian Pacific Organization of Cancer Prevention (APOCP), Kolkata, India. **(2022)**

Workshops

- Two-day flow cytometry workshop organised by NIPER, Kolkata. **(2022)**

iScience

CellPress
OPEN ACCESS

Article

Metallo-protease Peptidase M84 from *Bacillus altitudinis* induces ROS-dependent apoptosis in ovarian cancer cells by targeting PAR-1

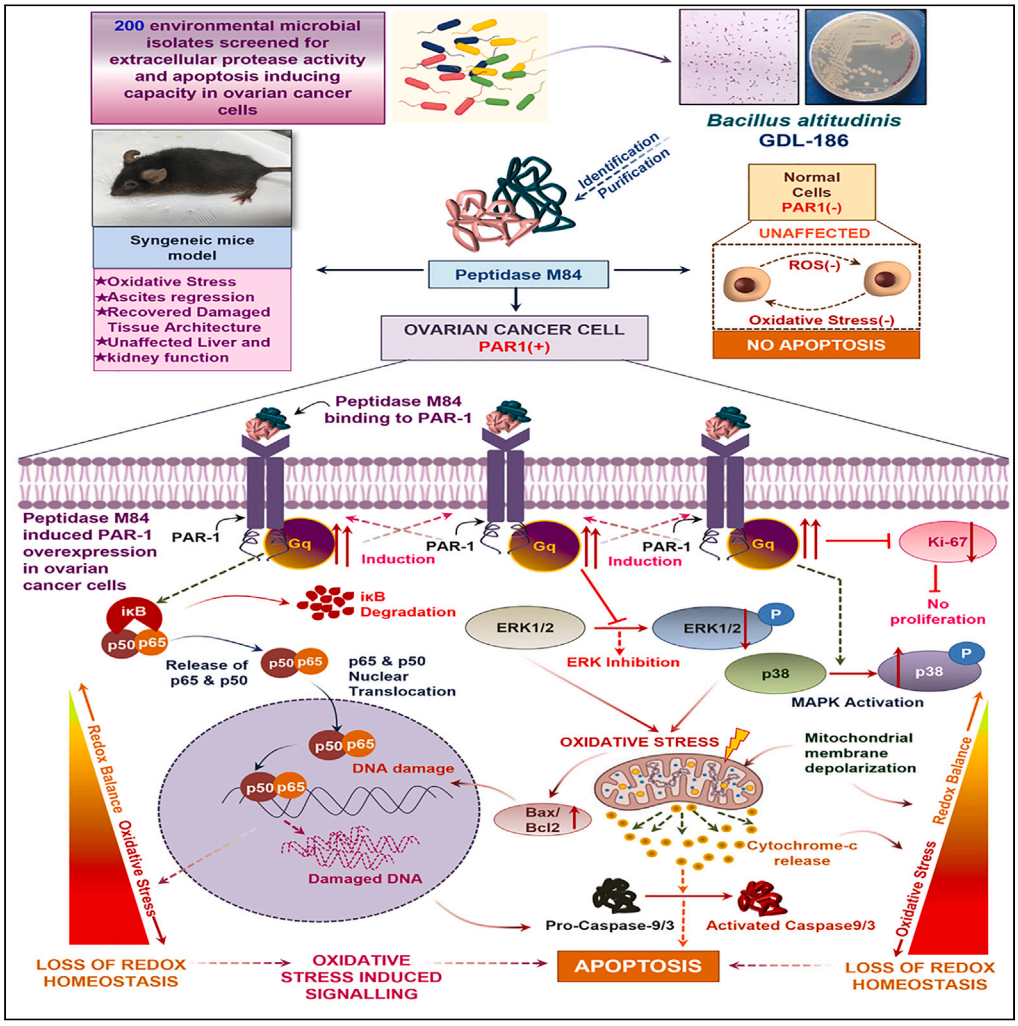

Niraj Nag, Tanusree Ray, Rima Tapader, ..., Ananda Pal, Parash Prasad, Amit Pal

palamit.app@gmail.com

Highlights

Bacillus altitudinis derived Peptidase M84 possesses anti-cancer properties

It triggered ROS-dependent apoptosis in PAR-1-positive ovarian cancer cells

PAR-1 negative normal healthy cells were unaffected with Peptidase M84 treatment

Peptidase M84 potentiated PAR-1 targeted ovarian cancer therapy

Nag et al., iScience *27*, 109828
June 21, 2024
https://doi.org/10.1016/j.isci.2024.109828

iScience

CellPress
OPEN ACCESS

Article

Metallo-protease Peptidase M84 from *Bacillus altitudinis* induces ROS-dependent apoptosis in ovarian cancer cells by targeting PAR-1

Niraj Nag,[1] Tanusree Ray,[1] Rima Tapader,[1] Animesh Gope,[2] Rajdeep Das,[3] Elizabeth Mahapatra,[4] Saibal Saha,[1] Ananda Pal,[2] Parash Prasad,[5] and Amit Pal[1,6,*]

SUMMARY

We have purified Peptidase M84 from *Bacillus altitudinis* in an effort to isolate anticancer proteases from environmental microbial isolates. This metallo-protease had no discernible impact on normal cell survival, but it specifically induced apoptosis in ovarian cancer cells. PAR-1, a GPCR which is reported to be overexpressed in ovarian cancer cells, was identified as a target of Peptidase M84. We observed that Peptidase M84 induced PAR-1 overexpression along with activating its downstream signaling effectors NF-κB and MAPK to promote excessive reactive oxygen species (ROS) generation. This evoked apoptotic death of the ovarian cancer cells through the intrinsic route. In *in vivo* set-up, weekly intraperitoneal administration of Peptidase M84 in syngeneic mice significantly diminished ascites accumulation, increasing murine survival rates by 60%. Collectively, our findings suggested that Peptidase M84 triggered PAR-1-mediated oxidative stress to act as an apoptosis inducer. This established Peptidase M84 as a drug candidate for receptor mediated targeted-therapy of ovarian cancer.

INTRODUCTION

In spite of remarkable improvements in chemotherapy regimens to treat ovarian cancer, it still remains one of the most lethal gynecological malignancies with a high recurrence and mortality rate.[1] Although cytoreductive surgery accompanied with platinum-based chemotherapy is the admissible treatment for epithelial ovarian cancer (EOC), the mortality rates have not improved markedly.[1–3] For instance, ovarian cancer is ranked eighth among the top ten common malignancies affecting Indian females as per Globocan 2018. Therefore, new therapies and alternative targets need to be developed to combat ovarian cancer.

In this regard, the anticancer potentials of natural products have been extensively explored for their differential effects as "cytoprotectors" to normal cells and "cytotoxics" to cancer cells. Predominantly, natural products exhibit this dual role by targeting several key molecules which in many instances impart resistance to conventional chemotherapy.[4–6] Herein, microorganisms supply structurally diverse natural products in abundance, serving the purpose of drug discovery. Extraction and purification of natural bacterial products are relatively cost-effective compared to chemically synthesized drugs.[7,8] Bacterial toxins and enzymes have been acknowledged for their anti-cancer effects. Reports are suggestive of their role as modulators of various cellular processes like apoptosis, differentiation, and proliferation. Bacterial products alone or when conjugated with other available anticancer drugs or irradiation can improve the efficiency of cancer therapy.[9–11] Didemnin B from *Tridemnum solidum* was among the earliest anti-cancer drugs of marine origin to enter clinical studies.[12] Similarly, Azurin from *Pseudomonas aeruginosa* and MakA from *Vibrio cholerae* have already shown promising anticancer effects.[13–15] Microbial proteases are reported to play their role through several mechanisms such as the inactivation of antimicrobial peptides,[16] disruption of the defensive mucosal barrier,[17] and elicitation of apoptosis in target cells.[18] For example, a protease obtained from *Serratia mercescens kums 3958* was reported to cause significant tumor regression when injected into solid tumors in BALB/c mice.[19,20] Previously, we have also reported bacterial subtilisin, a serine protease capable of potentiating apoptosis via ubiquitin mediated tubulin degradation pathway in breast cancer cells.[21] L-asparaginase (ASNase) is a pharmaceutically and clinically important microbial enzyme, isolated from different environmental sources that showed hopeful outcomes in cancer therapy as well.[22,23] Studies on extracellular metallo-protease arazyme from *Serratia proteamaculans* stated that it could

[1]Division of Molecular Pathophysiology, ICMR-National Institute of Cholera and Enteric Diseases (ICMR-NICED), P-33, CIT Road, Scheme-XM, Beliaghata, Kolkata, West Bengal 700010, India
[2]Division of Clinical Medicine, ICMR-National Institute of Cholera and Enteric Diseases (ICMR-NICED), P-33, CIT Road, Scheme-XM, Beliaghata, Kolkata, West Bengal 700010, India
[3]Molecular Cell Biology of Autophagy Lab, The Francis Crick Institute, 1, Midland Road, London NW1 1AT, UK
[4]Department of Environmental Carcinogenesis and Toxicology, Chittaranjan National Cancer Institute, 37, S.P. Mukherjee Road, Kolkata, West Bengal 700026, India
[5]Division of Experimental Hematology and Cancer Biology, Cincinnati Children's Hospital and Medical Center, 3333 Burnet Avenue, Cincinnati 45229-3026, OH, USA
[6]Lead contact
*Correspondence: palamit.app@gmail.com
https://doi.org/10.1016/j.isci.2024.109828

effectively inhibit metastatic murine melanoma via MMP-8 cross-reactive antibody stimulation.[24] These findings revealed a possible mechanism of cytotoxic action of microbial proteases on cancer cells.

Oxidative stress serves as a key modulator of signaling pathways involved in cellular survival and death depending on the cellular threshold levels of ROS. Dynamic redox homeostasis is thus a characteristic of exorbitantly growing cancer cells. Hence, most cytotoxic cancer drugs are observed to promote cell death by inducing oxidative stress, either directly or indirectly.[25,26] Higher levels of cellular reactive oxygen species (ROS) persuade mitochondria dependent conventional intrinsic pathway of apoptosis following caspase-9 activation.[26,27] Proteases can induce bio-signalling pathways and control cellular functions through the cleavage of protease-activated receptors (PARs), a notable G-protein coupled receptors (GPCRs).[28] The subtypes of PARs, ranging from PAR 1–4, have been found to be overexpressed in cancer cells with respect to healthy normal cells.[29] PARs play important roles in the apoptosis of cancer cells and carcinogenesis depending on the stimuli.[30–33] Studies demonstrated the differential expression pattern of PAR-1 in both transcriptional and translational levels in ovarian carcinoma tissue samples, while, negligible or none in the normal ovarian surface epithelium.[34] Moreover, PAR-1 agonists also showed apoptosis in intestinal epithelial cells.[35] Nevertheless, the molecular mechanism by which overexpression of PAR-1 can perturb the viability of cancer cells remains a less examined area of cancer research. PAR-1 activation can trigger ROS generation in cancer cells.[36,37] However, both PAR-1 and ROS are also reported to be associated with the activation of NF-κB and MAP kinases imparting apoptosis of cancer cells.[37,38] Therefore, PAR-1 mediated ROS targeting therapy using proteases may be proven to be advantageous to selectively kill cancer cells.

The objective of our study, therefore involved screening of environmental microbial isolates to identify a naturally occurring microbial protease with apoptosis capacitating potentials and deciphering its anticancer mechanism. In this study, we report that Peptidase M84, an extracellular metallo-protease purified from an environmental isolate of gram-positive *Bacillus altitudinis* can augment oxidative stress by altering PAR-1 activity to trigger apoptotic signaling in human and mice ovarian carcinoma cells with high selective toxicity. Our present study provides a deeper insight into the mechanism underlying Peptidase M84-induced apoptosis in ovarian cancer cells in a PAR-1/ROS-dependent manner which was not elucidated previously. Thus, Peptidase M84 may be employed for its chemotherapeutic efficacy in the future for ovarian cancer amelioration.

RESULTS

The culture supernatant from isolate GDL-186 which showed similarity with *Bacillus altitudinis*, triggered apoptosis in PA-1 cells

High extracellular protease activity was recorded for the 12 isolates (GDL-184, GDL-185, GDL-186, GDL-187, GDL-188, GDL-191, GDL-201, GDL-71, GDL-213, BSF-4, BSF-80, and BSF-32) screened out of 200 environmental isolates (Figures 1A and 1B). Initially, we assessed the apoptosis inducing potentials of the sterile supernatants extracted from these isolates among PA-1 cells by flow cytometry after treatment. Herein, PA-1 cells, specifically treated with GDL-186 supernatant underwent apoptosis significantly (Figures 1C and 1D). This was reconfirmed when the GDL-186 supernatant also successfully induced apoptosis in SKOV3 cells additionally. Contrarily, no apoptosis inductions were noted among both PA-1 and SKOV3 cells upon treatment with GDL-186 supernatant pre-incubated with EDTA and PMSF. A significant decrease in the percentage of apoptotic PA-1 and SKOV3 cells was enumerated, denoting protease mediated apoptosis inducing property of GDL-186 isolate (Figures S1A–S1D). Thereafter, we identified GDL-186 as a *Bacillus* species after deciphering 100% sequence homology of their 16S rRNA with that of *Bacillus altitudinis* strain in NCBI Blast results. The gene sequence was submitted to NCBI GenBank under accession number OP738003.1. (Figures S1E and S1F). We also confirmed the identity of the GDL-186 isolate based on DNA gyrase B sequence homology analysis (Figures S1G and S1H). In addition to this, some major biochemical, microbiological, and morphological studies further strengthened our observation of the isolate GDL-186. We observed no growth of this isolate in Macconkey agar plates containing crystal violet. Following this, the phenotypic results of this isolate showed medium-sized rod-shaped cells with aerobic growth, white to off-white-coloured moist colonies, motile and endospore-forming. This isolate was found as gram-positive bacilli also positive for oxidase and catalase. The biochemical profile illustrated that this isolate metabolizes D-arabinose, D-glucose, starch, fructose, and lactose. Other biochemical characterizations for indole, citrate utilization, triple sugar iron, lysine iron agar, and oxidative fermentation tests confirmed the environmental isolate as *Bacillus* sp. The identity of the isolate was definitively confirmed by whole genome sequencing, with the sequence deposited at DDBJ/ENA/GenBank under the accession JAZHFY000000000. All these results indicated that the isolate GDL-186 belonged to the Bacillus genus (Figures S2A–S2F, S3A, and S3B).

Purification and identification of secreted protease named Peptidase M84 from *Bacillus altitudinis* GDL-186

GDL-186 culture supernatant proteolytically degraded azocasein alongside inducing apoptosis in PA-1 cells. On this basis, we decided to purify and characterize this supernatant for its typical protease-like behavior. Firstly, EDTA and 1, 10- phenanthroline treatment inhibited the proteolytic activity of these crude supernatants which remained unaltered in PMSF and EGTA's presence. This hinted at GDL-186 being an extracellular zinc-dependent metallo-protease (Figures S4A and S4B). Next, the probable protease was concentrated following dialysis where the resultant non-binding and binding fractions were examined for proteolytic activity (Figures 2A and S4C) Interestingly, the non-binding fraction was observed to exhibit protease activity (Figure 2B). This was therefore pooled, concentrated, and analyzed by gel filtration (sephadex G-75). Two fractions (indicated as two different peaks in the chromatogram) were eluted from the G-75 column of which the first fraction showed higher protease activity compared to the second (Figures 2C and 2D). The first peak of sephadex G-75 elution was hence pooled, concentrated, and further analyzed in SDS-PAGE (15%). Two major bands around 25 kDa and 16 kDa molecular weights were distinctly observed which upon EDTA pre-incubation resulted in a single band at 25 kDa only (Figure 2E). This fraction of G-75 also showed single

A

No. of total bacterial isolates screened	No. of protease positive microbial isolates	No. of bacterial isolates for which protease activity was inhibited by EDTA	No. of bacterial isolates for which protease activity was inhibited by PMSF	No. of bacterial isolates induced apoptosis in cancer cells
200	12	7	4	1

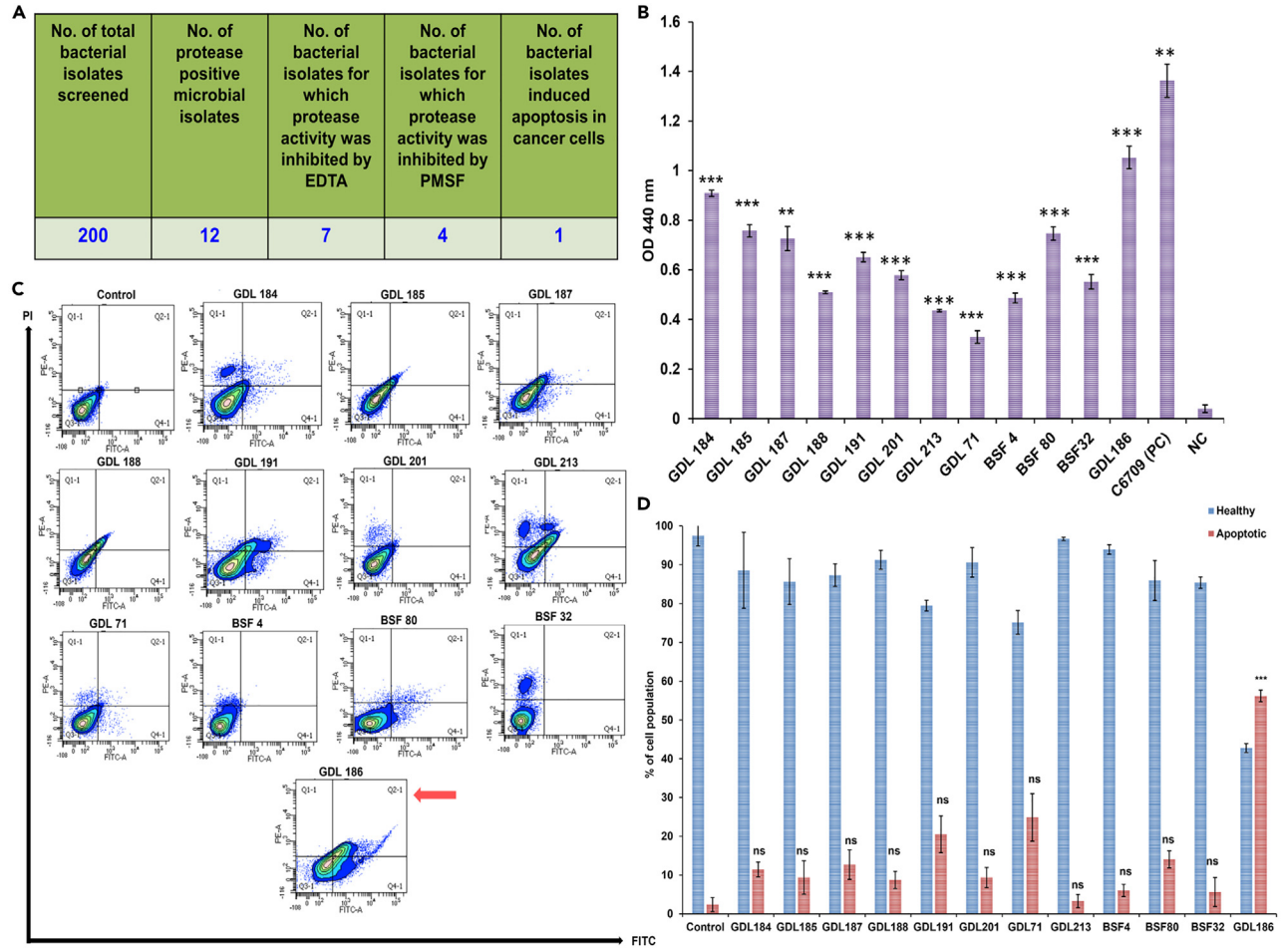

Figure 1. Screening of 200 bacterial isolates from environmental sources for extracellular protease activity and apoptosis inducing ability

(A) Results of azocasein assay are represented in tabular form (B) Results of azocasein assay are represented in graphical form. Culture supernatant of *Vibrio cholerae* EL Tor strain C6709 and nutrient broth were used as positive and negative controls, respectively.

(C) Annexin V/PI based flow-cytometric analysis to assess the apoptosis inducing ability of the culture supernatant of the protease-secreting isolates in PA-1 cells. In each display the lower right quadrant is for early apoptotic cells (Annexin V+/PI), the upper right is for late apoptotic cells (Annexin V+/PI+), the upper left is for necrotic population (Annexin V-/PI+) and lower left is for healthy cells (Annexin V-/PI-). The culture supernatant of GDL-186 isolate (marked with an arrow) shows significant apoptosis.

(D) The aforementioned results are graphically represented in the bar diagram. All statistical analysis was done by applying the Student's t test (unpaired two-tailed). Data are expressed in ±SEM. In all panels, (non-significant) ns $p > 0.05$, *$p \leq 0.05$, **$p \leq 0.01$, and ***$p \leq 0.001$. Error bars were calculated based on results obtained from a minimum of three independent experiments ($n = 3$). See also Figures S1–S3 and S13.

band in Native PAGE (10%) (Figure 2F). These bands were further characterized by nano-LC-MS/MS-TOF where the generated peptide sequence was homologous to "Peptidase M84" from *Bacillus altitudinis*. (Figure 2G). This enzyme typically consists of a consensus amino acid sequence HExxH and a Met-turn motif "CLMNY" in downstream of its active site. The histidines and glutamic acid act as zinc ligands and catalytic base, respectively.[39]

Inhibition of the protease activity revealed the metallo-protease nature of Peptidase M84 which was optimally active at normal physiological pH and temperature

Purified Peptidase M84 was also proteolytically active against azocasein. This activity was yet again inhibited by EDTA and 1,10- phenanthroline but remained unaltered with PMSF (Figure 2D). Inhibition studies once again confirmed that this purified Peptidase M84 was a zinc-containing metallo-protease. Additionally, native gelatin zymogram profile revealed Peptidase M84 to be proteolytically active against gelatin. A clear hollow zone due to gelatin degradation was attained in Native PAGE (with 0.1% gelatin) followed by Coomassie staining (Figure S4D). Peptidase M84 showed proteolytic activity over a wide range of pH values (from 4.0 to 11.0). Although, the optimal and the minimal activities of Peptidase M84 were recorded at pH 8.0 and pH 4.0, respectively, the enzyme kept 80–90% activity at pH 7.0–10.0 (Figure 2H). In line with

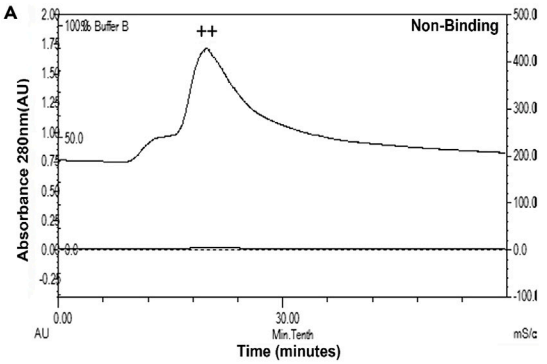
A
Non-Binding
++
Absorbance 280nm(AU)
Time (minutes)

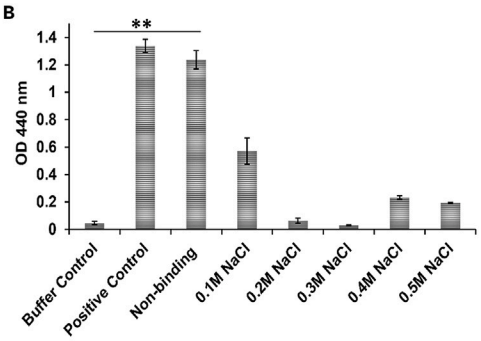
B
**
OD 440 nm
Buffer Control
Positive Control
Non-binding
0.1M NaCl
0.2M NaCl
0.3M NaCl
0.4M NaCl
0.5M NaCl

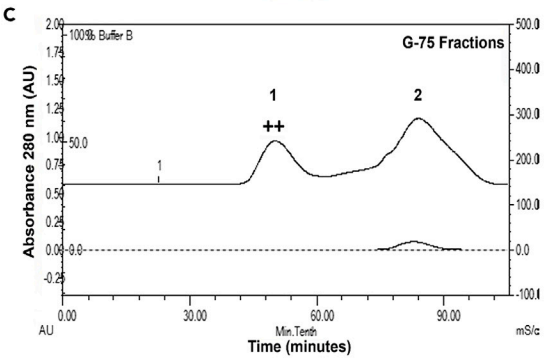
C
G-75 Fractions
1
2
++
Absorbance 280 nm (AU)
Time (minutes)

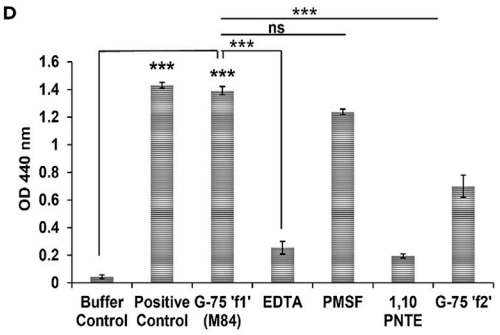
D
***
ns
***
OD 440 nm
Buffer Control
Positive Control
G-75 'f1' (M84)
EDTA
PMSF
1,10 PNTE
G-75 'f2'

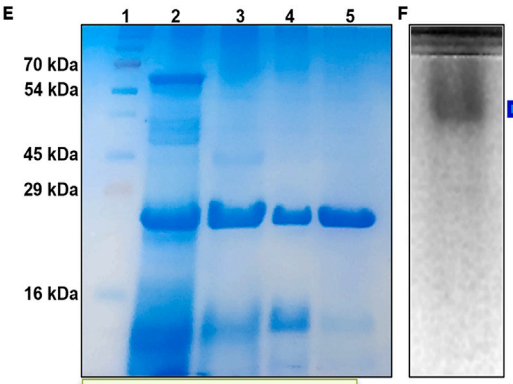
E
1 2 3 4 5
70 kDa
54 kDa
45 kDa
29 kDa
16 kDa
F
Lane 1: Marker
Lane 2: Crude
Lane 3: DE52 Non-binding
Lane 4: G75 Pool '1'
Lane 5: G75 Pool '1'+ EDTA

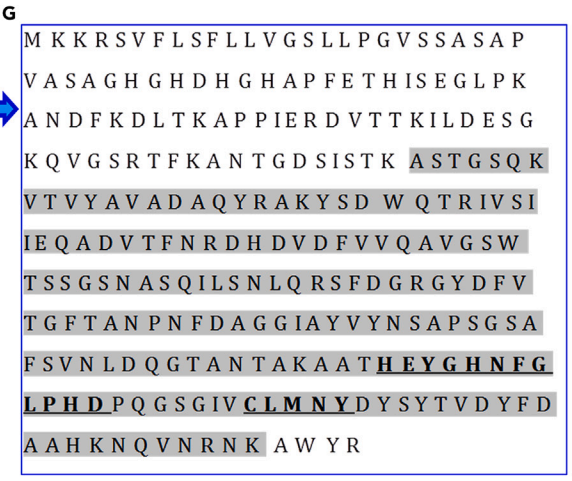
G
M K K R S V F L S F L L V G S L L P G V S S A S A P
V A S A G H G H D H G H A P F E T H I S E G L P K
A N D F K D L T K A P P I E R D V T T K I L D E S G
K Q V G S R T F K A N T G D S I S T K A S T G S Q K
V T V Y A V A D A Q Y R A K Y S D W Q T R I V S I
I E Q A D V T F N R D H D V D F V V Q A V G S W
T S S G S N A S Q I L S N L Q R S F D G R G Y D F V
T G F T A N P N F D A G G I A Y V Y N S A P S G S A
F S V N L D Q G T A N T A K A A T H E Y G H N F G
L P H D P Q G S G I V C L M N Y D Y S Y T V D Y F D
A A H K N Q V N R N K A W Y R

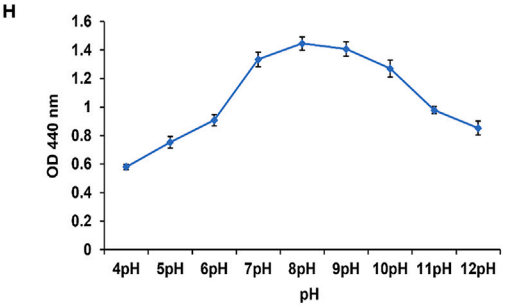
H
OD 440 nm
4pH 5pH 6pH 7pH 8pH 9pH 10pH 11pH 12pH
pH

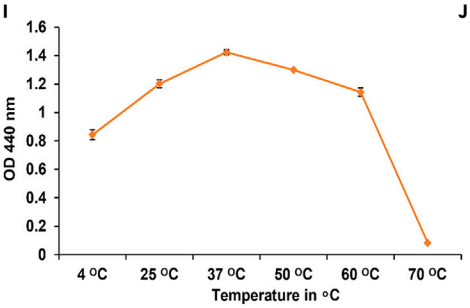
I
OD 440 nm
4 °C 25 °C 37 °C 50 °C 60 °C 70 °C
Temperature in °C

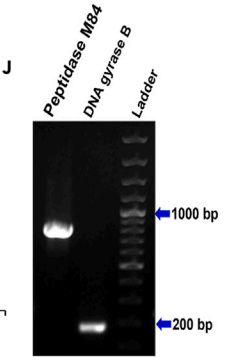
J
Peptidase M84
DNA gyrase B
Ladder
1000 bp
200 bp

Figure 2. Purification and identification of Peptidase M84 from *Bacillus altitudinis* GDL-186

(A) Chromatogram of DEAE-52 anion exchange chromatography of the ammonium sulfate precipitated crude protein fraction from GDL-186 culture supernatant.
(B) Azocasein assay with protein fractions (5.0 μg) obtained from DEAE-52 column shows higher protease activity in the non-binding fraction (++) as compared to the NaCl (0.1 M–0.5 M) eluted binding fractions.
(C) The chromatogram of the G-75 gel filtration chromatography shows separation of the non-binding fraction, represented as two individual peaks (G-75"f1" and G-75"f2").
(D) Azocasein assay with G-75 fractions shows maximum protease activity in the G-75 "f1" (++) fraction. This activity is inhibited by EDTA and 1,10-phenanthroline.
(E) 15% SDS-PAGE profile of the purified protease shows two major bands near 25 kDa and 16 kDa, which upon pre-incubation with EDTA shows a single band at 25 kDa.
(F) 12% Native-PAGE profile of the purified protease (G-75 "f1") shows a single band.
(G) Protein bands were identified by Nano-LC-MS/MS-TOF peptide sequencing which exhibited homology with "Peptidase M84". The peptides showing homology are with the background color. The active sites and the zinc-binding domains of the protease are underlined.
(H and I) Determination of the optimum pH and temperature of Peptidase M84.
(J) PCR amplification of the full-length (813bp) peptidase M84 gene (Lane 1) and DNA gyrase B gene (Lane 2) from *Bacillus altitudinis* strain GDL-186. All statistical analysis was done by applying Student's t test (two-tailed). Data are expressed in ±SEM. In all panels, ns $p > 0.05$, *$p \leq 0.05$, **$p \leq 0.01$, and ***$p \leq 0.001$. In each panel, error bars were calculated based on results obtained from a minimum of three independent experiments ($n = 3$). See also Figures S4 and S5.

this, Peptidase M84 exhibited maximum activity against azocasein at temperatures ranging from 37°C to 40°C which decreased gradually at 50°C–60°C. This protease showed suboptimal activity at temperatures ranging from 4°C to 25°C. At higher temperature (60°C–70°C), the proteolytic activity was almost completely abolished (Figure 2I).

We also evaluated the effect of Zn^{2+} on the azocaseinolytic activity of Peptidase M84. We observed that the Peptidase M84 protease activity was gradually increased with the Zn^{2+} concentration starting from 0.5 mM up to 2 mM. Interestingly, this activity was decreased in the presence of higher concentrations (5 mM and above) of Zn^{2+}. This activity was completely abolished by pre-treatment with EDTA or 1,10-phenanthroline. (Figures S4E and S4F) This can be explained by the binding of Zn^{2+} to non-catalytic ion-binding sites of metzincins, triggering a conformational change that results in the loss of proteolytic activity or by the precipitating effect induced by Zn^{2+}. Studies suggested that the addition of excess Zn^{2+} decreased the proteolytic activity of metzincins over the pH range from 7.0 to 9.0, pointing to this effect on $Zn(OH)_2$ precipitation on the protein.[40] Based on this, we can conclude the protease activity of Peptidase M84 is dependent on Zn^{2+}. Besides, the full-length amplified 813 bp gene encoded Peptidase M84 of *Bacillus altitudinis* was also detected in 0.8% agarose gel after PCR amplification (Figures 2J, S5A, and S5B). The molecular phylogenetic tree of Peptidase M84 derived from NCBI blast showed the distribution of the M84 metallo-proteases in Bacillus species (Figure S5C).

Peptidase M84 exhibited apoptosis and suppressed the proliferation of ovarian cancer cells but had no such impact on IOSE and PEMΦ cells

MTT cell viability assay showed a gradual depletion in the percentage of viable ovarian cancer cells with increasing concentrations of Peptidase M84, ranging between 0.5 μg/mL and 5.0 μg/mL. The *in vitro* safe dose (IC_{50}) of Peptidase M84 was found to be 2.0 μg/mL for PA-1 and SKOV3 cells. Furthermore, Peptidase M84 showed IC_{50} 3.0 μg/mL against ID8 cells (Figures S6A–S6C). These concentrations aligned with the concentrations used to detect apoptosis and study the bio-signalling pathways in the aforementioned cell lines.

Next, in order to investigate the cytotoxic effect of Peptidase M84, PA-1, SKOV3, and ID8 cells were treated with doses ranging between 1.0 μg/mL and 3.0 μg/mL for 18 h. Flow cytometry showed that Peptidase M84 caused significant apoptosis in these cell lines as compared to untreated cells. Inhibition of protease activity by EDTA showed a significant reduction in the percentage of apoptotic cells. However, this percentage was not affected by PMSF. These results clearly indicated that purified Peptidase M84 by virtue of its metalloprotease activity could promote cell death by inducing apoptosis in human and mouse ovarian cancer cells (Figures 3A–3D).

Ki-67 protein is considered as a proliferation marker for human tumor cells. Higher expression of nuclear Ki-67 is found in all stages of cell cycle not including the G0 stage and dead cells.[41] We noticed a lower abundance of Ki-67 in Peptidase M84 treated PA-1 and SKOV3 cells as compared to the untreated cells indicating that Peptidase M84 significantly restrained cancer cell proliferation. Contrarily, higher levels of nuclear Ki-67 in untreated control cells indicated rapid proliferation and increased survivability (Figures 3E–3G).

Peptidase M84 treatment also altered the morphology of PA-1 and SKOV3 cells. Peptidase M84 treatment showed a cell-distending effect at lower concentrations. A cell rounding effect was observed when cells were treated with increasing concentrations of Peptidase M84 for 18 h (Figure S6D).

During apoptosis, highly condensed inert and fragmented chromatin gets packaged into apoptotic bodies.[42] Herein, these became distinct upon Hoechst 33342 staining which indicated apoptotic induction. In Peptidase M84 treated PA-1, SKOV3, and ID8 cells, the percentage of condensed nuclei were 43.66, 38.33, and 44.33%, respectively, whereas the respective control cells were shown to be 13%, 10.6%, and 11.33% (Figures S6E and S6F). The result indicated that nuclei of Peptidase M84 treated cells exhibited condensed and bright nuclei while the untreated control cells showed less amount of condensed chromatin.

To understand the specificity, the effect of Peptidase M84 was evaluated on IOSE cells and PEMΦ cells in a similar range of doses of Peptidase M84. Almost all cells remained viable even at a concentration of 3.0 μg/mL of Peptidase M84. Therefore, Peptidase M84 selectively triggered apoptosis in malignant ovarian cells but not in normal cells (Figures 3H, 3I, S6G, and S6H). The respective gating patterns associated with these data are represented in Figure S13.

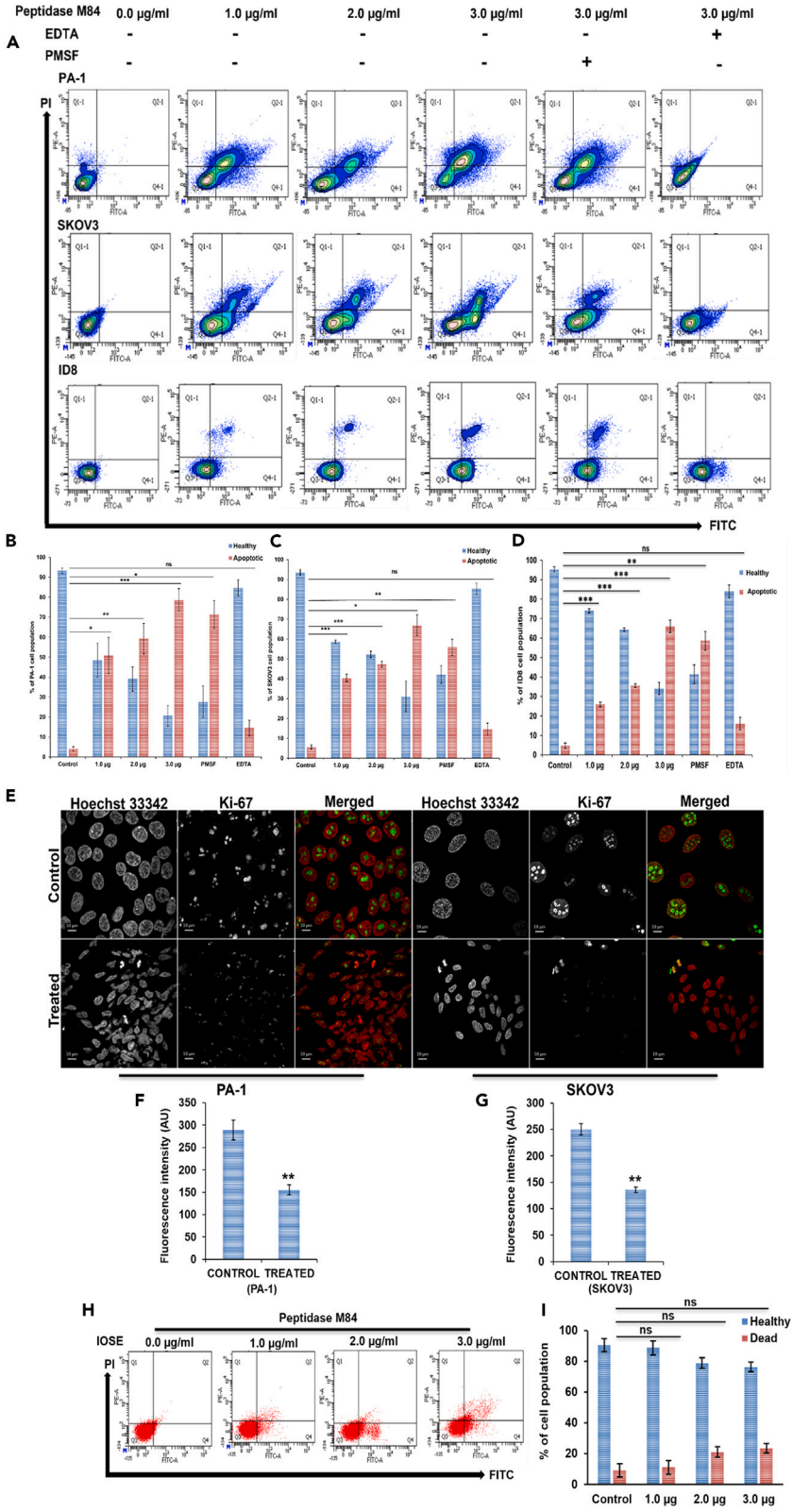
Peptidase M84
0.0 μg/ml
1.0 μg/ml
2.0 μg/ml
3.0 μg/ml
3.0 μg/ml
3.0 μg/ml
A
EDTA
PMSF
PA-1
PI
SKOV3
ID8
FITC
B
C
D
Healthy
Apoptotic
Control
1.0 μg
2.0 μg
3.0 μg
PMSF
EDTA
E
Hoechst 33342
Ki-67
Merged
Control
Treated
F
PA-1
Fluorescence intensity (AU)
CONTROL TREATED
(PA-1)
G
SKOV3
CONTROL TREATED
(SKOV3)
H
IOSE
I
Dead
% of cell population

Figure 3. Detection of cytotoxicity and apoptosis in Peptidase M84 treated ovarian cancer cells and human ovarian normal epithelial cells (IOSE) and in mouse peritoneal macrophage (PEMΦ) cells

(A) Flow cytometric analysis of Peptidase M84 treated PA1, SKOV3, and ID8 cells shows dose-dependent apoptosis. EDTA inhibition significantly reduces the effect while PMSF treatment does not affect cell viability.

(B–D) Bar diagrams show the percentage of healthy and apoptotic cell populations.

(E–G) Confocal imaging of nuclear Ki-67 (green) coupled with bar diagrams of mean fluorescence intensity (MFI) (calculated in Fiji) show a significant reduction in PA-1 and SKOV3 cell proliferation due to Peptidase M84 treatment.

(H and I) Flow cytometric analysis of the Peptidase M84 treated IOSE and PEMΦ cells shows no significant apoptosis as compared to the untreated cells. Bar diagrams of the data are also being presented. All statistical analysis was done by applying Student's t test (two-tailed). Data are expressed in ±SEM. In all panels, ns $p > 0.05$, *$p \leq 0.05$, **$p \leq 0.01$, and ***$p \leq 0.001$. In each panel, error bars were calculated based on results obtained from a minimum of three independent experiments ($n = 3$). Scale bars: 10 μm. See also Figures S6 and S13.

Peptidase M84 augmented ROS generation and activated the intrinsic canonical pathway of apoptosis in ovarian cancer cells

Excessive production of ROS overtakes the cellular antioxidant capacity. It results in oxidative stress, which ultimately contributes to the regulation of a wide range of signaling pathways and can impart oxidative damage mediated cell death.[43,44] The oxidative stress related to Peptidase M84 treatment was monitored by staining with DCFDA. Under the stimulation of ROS, DCFH is converted to fluorescent DCF upon oxidation. Peptidase M84 treatment showed an increase in ROS generation in PA-1, SKOV3, and ID8 cells, depicted as an increase in the mean fluorescence intensity level of DCF in comparison to untreated cells with time (6 h and 18 h). This could lead to initiating apoptotic signals (Figures 4A, 4B, S7A, and S7B). In contrast, Peptidase M84 failed to promote ROS generation in IOSE cells (Figures 4C–4E).

JC-1 dye uptake pattern suggested that Peptidase M84 also caused alterations in mitochondrial membrane potential ($\Delta\Psi$m) in PA-1 and SKOV3 cells. A decrease in $\Delta\Psi$m is considered as a major hallmark of apoptosis.[45] An increase in the ratio of green fluorescence to red fluorescence intensity levels clearly indicated disrupted $\Delta\Psi$m in Peptidase M84 treated cells in a time-dependent manner (6 h and 18 h) as compared to the untreated control cells (Figures 4F and 4G).

Herein, comet assay was performed to detect DNA damage in PA-1 and SKOV3 cells as a result of Peptidase M84 treatment as genotoxicity tests predominantly contribute to cancer research. We observed that Peptidase M84 treatment for 18 h gave a prominent induction of comet tail moment in ovarian cancer cells with respect to control untreated cells (Figures S7C–S7E).

Next, we examined the quantitative expression profiles of some prime regulatory proteins to study the possible molecular mechanism of apoptotic cascade induced by Peptidase M84. We observed that Peptidase M84 treatment resulted in the down-regulation of anti-apoptotic Bcl-2 levels and upregulation of pro-apoptotic marker Bax in PA-1 and SKOV3 cells concerning the untreated cells. Our results also revealed activation of caspase 9 and caspase 3 and upregulation of cleaved PARP expression levels by Peptidase M84. However, a consistent profile of caspase 8 expression levels indicated non-involvement of extrinsic (FADD-Caspase 8) apoptosis pathway in response to Peptidase M84 treatment in these cells (Figures 4H and 4I). Interestingly, no activation of caspase 3 was observed in Peptidase M84 treated normal IOSE cells (Figures S7F and S7G).

Mitochondrial cytochrome *c* functions as an electron carrier in the respiratory chain,[46] translocates to the cytosol in Peptidase M84 treated cells undergoing apoptosis, where it participates in the activation of specific caspases. We found an increase in the cytochrome *c* expression levels in cytosolic fraction devoid of mitochondria in translational levels in Peptidase M84 treated PA-1 and SKOV3 cells compared to the untreated cells. Densitometric data showed that the increase was highly significant. (Figures 4J and 4K).

Immunofluorescence data also supported this observation. Damaged mitochondria due to Peptidase M84 treatment were observed with mitotracker green FM staining. We also noticed a depletion in green fluorescence intensity levels in these cells. There was a reduction in co-localization between cytochrome *c* and mitochondria in PA-1 and SKOV3 cells treated with Peptidase M84 as compared to the untreated cells. Released cytochrome *c* was found to be distributed in punctate (red) form throughout the cytosol and around the nucleus of cells. Pearson's co-efficient values showed a significant reduction in co-localization between mitochondria and cytochrome *c* in Peptidase M84 treated PA-1 and SKOV3 cells (Figures 4L–4N).

Taken together, our findings implicated the activation of the intrinsic pathway of apoptosis in ovarian cancer cells by Peptidase M84 from *B. altitudinis*.

Peptidase M84 specifically interacted with PAR-1 and caused overexpression of PAR-1 in human and mouse ovarian cancer cells however not in human healthy ovarian epithelial cells

Real-time PCR data represented overexpression of PAR-1 in PA-1 and SKOV3 cells. We found almost 4-fold and 7-fold upregulation of PAR-1 mRNA levels in PA-1 and SKOV3 cells, respectively, as compared to the other PARs. (Figure 5A).

A time-dependent (6 h and 18 h) overexpression of PAR-1 was observed in PA-1 and SKOV3 cells after Peptidase M84 treatment (Figure 5B). Immunoblots also confirmed almost 2-fold increase in PAR-1 expression levels in PA-1 and SKOV3 cells and nearly 3.5-fold overexpression in ID8 cells after Peptidase M84 treatment (18 h) (Figures 5C and 5D). Importantly, no significant change was observed in the PAR-1 expression in IOSE cells (Figures 5C and 5D). Almost no expression of PAR-1 was observed in IOSE cells. Densitometric scan analysis depicted the intensity differences between PAR-1 expression levels in Peptidase M84 treated and untreated cells (Figure 5D). Immunofluorescence imaging also showed a significant increase in PAR-1 expression due to Peptidase M84 treatment in PA-1 and SKOV3 cells (Figures 5E–5H). This supports the fact that Peptidase M84 is unable to induce apoptosis in normal cells via effective modulation of PAR-1.

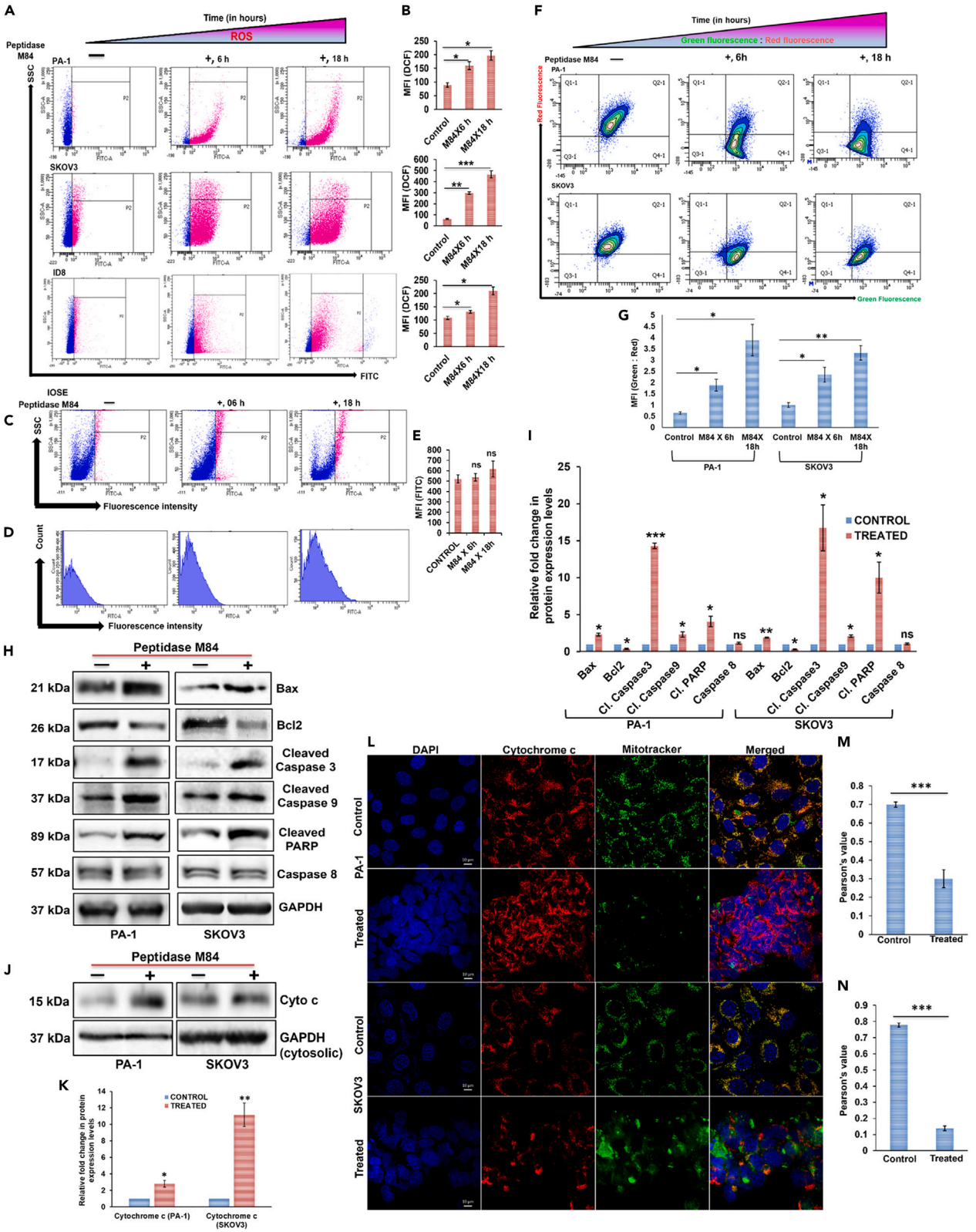
A
Time (in hours)
ROS
Peptidase M84
PA-1
+, 6 h
+, 18 h
SKOV3
ID8
SSC
FITC
B
MFI (DCF)
Control
M84X6 h
M84X18 h
C
IOSE
Peptidase M84
+, 06 h
+, 18 h
Fluorescence intensity
D
Count
Fluorescence intensity
E
MFI (FITC)
CONTROL
M84 X 6h
M84 X 18h
ns
F
Time (in hours)
Green fluorescence : Red fluorescence
Peptidase M84
+, 6h
+, 18 h
Red Fluorescence
Green Fluorescence
G
MFI (Green : Red)
Control
M84 X 6h
M84X 18h
PA-1
SKOV3
I
Relative fold change in protein expression levels
CONTROL
TREATED
Bax
Bcl2
Cl. Caspase3
Cl. Caspase9
Cl. PARP
Caspase 8
H
Peptidase M84
21 kDa
Bax
26 kDa
Bcl2
17 kDa
Cleaved Caspase 3
37 kDa
Cleaved Caspase 9
89 kDa
Cleaved PARP
57 kDa
Caspase 8
37 kDa
GAPDH
PA-1
SKOV3
J
Peptidase M84
15 kDa
Cyto c
37 kDa
GAPDH (cytosolic)
PA-1
SKOV3
K
Relative fold change in protein expression levels
CONTROL
TREATED
Cytochrome c (PA-1)
Cytochrome c (SKOV3)
L
DAPI
Cytochrome c
Mitotracker
Merged
Control
Treated
PA-1
SKOV3
M
Pearson's value
Control
Treated
N
Pearson's value
Control
Treated

Figure 4. Ovarian cancer cells undergo ROS-dependent intrinsic pathway due to Peptidase M84 treatment

(A) A time-dependent ROS generation was examined by DCFDA staining in PA-1, SKOV3, and ID8 cells after Peptidase M84 treatment. Quadrant "P2" represents cells producing ROS.

(B) Bar diagrams represent the MFI of DCF.

(C and D) Detection of ROS generation in normal IOSE cells after Peptidase M84 treatment by DCFDA staining. No significant ROS generation is found even after 18 h of treatment.

(E) Bar diagram of mean fluorescence intensity of DCF is represented.

(F and G) JC-1 staining data with bar diagrams of MFI (green: red) show the disruption of mitochondrial membrane potential with time in Peptidase M84 treated PA-1 and SKOV3 cells. Cell population positive for green fluorescence signified disrupted mitochondrial membrane potential.

(H and I) The immunoblots represent expression levels of major proteins of the intrinsic apoptotic pathway in Peptidase M84 induced and un-induced PA-1 and SKOV3 cells. Densitometric analysis for relative protein expression is plotted as a histogram.

(J and K) Immunoblot with bar diagram of densitometry scan of cytochrome *c* in the mitochondria-free cytosolic fraction in Peptidase M84 treated PA-1 and SKOV3 cells depict the release of cytochrome *c* from mitochondria.

(L–N) Immunofluorescence along with bar diagrams of Pearson's co-efficient values show a reduction in co-localization between mitochondria (green) and cytochrome *c* (red) due to Peptidase M84 treatment in PA-1 and SKOV3 cells. In each panel, error bars were calculated based on results obtained from a minimum of three independent experiments. All statistical analysis was done by applying Student's t test (two-tailed). Data are expressed in ±SEM. In all panels, ns $p > 0.05$, *$p \leq 0.05$, **$p \leq 0.01$, and ***$p \leq 0.001$. Scale bars: 10 μm. Densitometric analysis was performed on ImageJ and Gel Quant softwares. Band intensities were normalized to loading controls GAPDH. Pearson's co-efficient was calculated in Fiji (https://imagej.net/software/fiji/). See also Figures S7 and S13.

Next, we proceeded with immunoprecipitation to identify the receptor of Peptidase M84 and to elucidate the physical interaction between them. The outcome revealed Peptidase M84 specifically bound and interacted with PAR-1 when PA-1 and SKOV3 cells. A band of PAR-1 (50 kDa) was observed in western blot when PAR-1 was immunoprecipitated with Peptidase M84 specific antisera (Figure 5I). Additionally, bands of Peptidase M84 (25 kDa and 16 kDa) were also observed when Peptidase M84 was immunoprecipitated with anti-PAR-1 antibody (Figure 5J). In this context, another western blot with the raised antisera against Peptidase M84 showed two major bands at 25 kDa and 16 kDa. These bands were similar to that in 15% SDS-PAGE profile of purified Peptidase M84 (Figure S7H). Furthermore, binding and interaction between Peptidase M84 and PAR-1 were also validated by co-localization based confocal imaging. An increase in Pearson's co-efficient values in Peptidase M84 treated (30 min) PA-1 and SKOV3 cells as compared to untreated cells indicated the possible interaction between PAR-1 and Peptidase M84 (Figures 5K–5M, S8A, and S8B).

Peptidase M84 persuaded PAR-1 dependent apoptosis in ovarian cancer cells by triggering NF-κB and MAPK signaling mediated ROS generation

Thrombin-mediated PAR-1 activation generally regulates major signaling pathways such as p38 MAPK and NF-κB which ultimately triggers further ROS generation.[47–49] Likewise, in this study immunoblots of cytosolic and nuclear fractions of PA-1 and SKOV3 cells showed Peptidase M84 treatment promoted nuclear translocation p50 and p65 proteins, suggesting the activation of NF-κB signaling. We observed significant expression of p50 and p65 proteins in the nuclear fraction of Peptidase M84 treated cells as compared to untreated cells. Densitometry represented the ratio of protein expression between nucleus to cytosol of Peptidase M84 induced and un-induced cells. Histone H3 (nuclear protein) and alpha-tubulin (cytosolic protein) were used as loading controls (Figures 6A and 6B) Immunofluorescence imaging of Peptidase M84 treated and untreated cells further supported our findings and showed prominent nuclear translocation of the same proteins. There was an increase in the ratio of nuclear to cytosolic mean fluorescence intensity of p50 and p65 proteins in Peptidase M84 treated cells (Figures 6C–6G).

Immunofluorescence also indicated the overall increase of phospho-p38 (p-p38) expression levels in Peptidase M84 treated cells (Figures S9A–S9C). Results obtained from immunoblot also depicted the level of p–p38 and phospho-ERK1/2 was significantly increased and decreased respectively due to Peptidase M84 treatment. However, the entire cellular p38 and ERK1/2 levels remained unaltered. Thus, our report revealed that Peptidase M84 also modulated MAP kinase pathways in ovarian cancer cells (Figures 6H and 6I).

We aimed to decipher whether the interaction between Peptidase M84 and PAR-1 directly persuaded apoptotic signaling in ovarian cancer cells. Peptidase M84 treatment on PA-1 and SKOV3 cells showed cellular apoptosis. When these cells were priorly treated with PAR-1 inhibitor (ML161) followed by Peptidase M84 treatment for 18 h, there was an absence of apoptosis. Furthermore, knockdown of PAR-1 was achieved by si-RNA transfection for 48 h in PA-1 and SKOV3 cells (Figures S9D and S9E). These PAR-1 silenced cells behaved like untreated cells even after Peptidase M84 treatment. Hence, our data illustrated that Peptidase M84-induced apoptosis in ovarian cancer cells in a PAR-1 dependent manner (Figures 6J–6L).

We found that Peptidase M84 augmented ROS levels in ovarian cancer via activation of MAP kinase and NF-κB. To confirm whether these signaling pathways were directly responsible for cellular apoptosis, PA-1 and SKOV3 cells were pre-incubated with either NF-κB inhibitor (MG132) or p38 inhibitor (SB203580) or both followed by Peptidase M84 treatment for 18 h. When cells were pre-incubated with MG132 only 58% of PA-1 and 49% of SKOV3 cells showed apoptosis. Cells pre-incubated with SB203580 only 51% of PA-1 and 41% of SKOV3 cells showed apoptosis. Importantly, the majority of the cells undergoing apoptosis under the aforementioned conditions were mostly in the early apoptotic phase. Interestingly, when both inhibitors were applied together no significant apoptosis was noticed. Furthermore, no significant apoptosis was noticed when cells were incubated with ROS quencher (NAC) prior to protease treatment. This observation suggested the major involvement of ROS in Peptidase M84 induced apoptosis in ovarian cancer cells (Figures 6J–6L). We noticed that ML161 pre-treatment inhibited the Peptidase M84 mediated nuclear translocation of p50 and p65 (Figure S10A). Immunoblot also confirmed that Peptidase

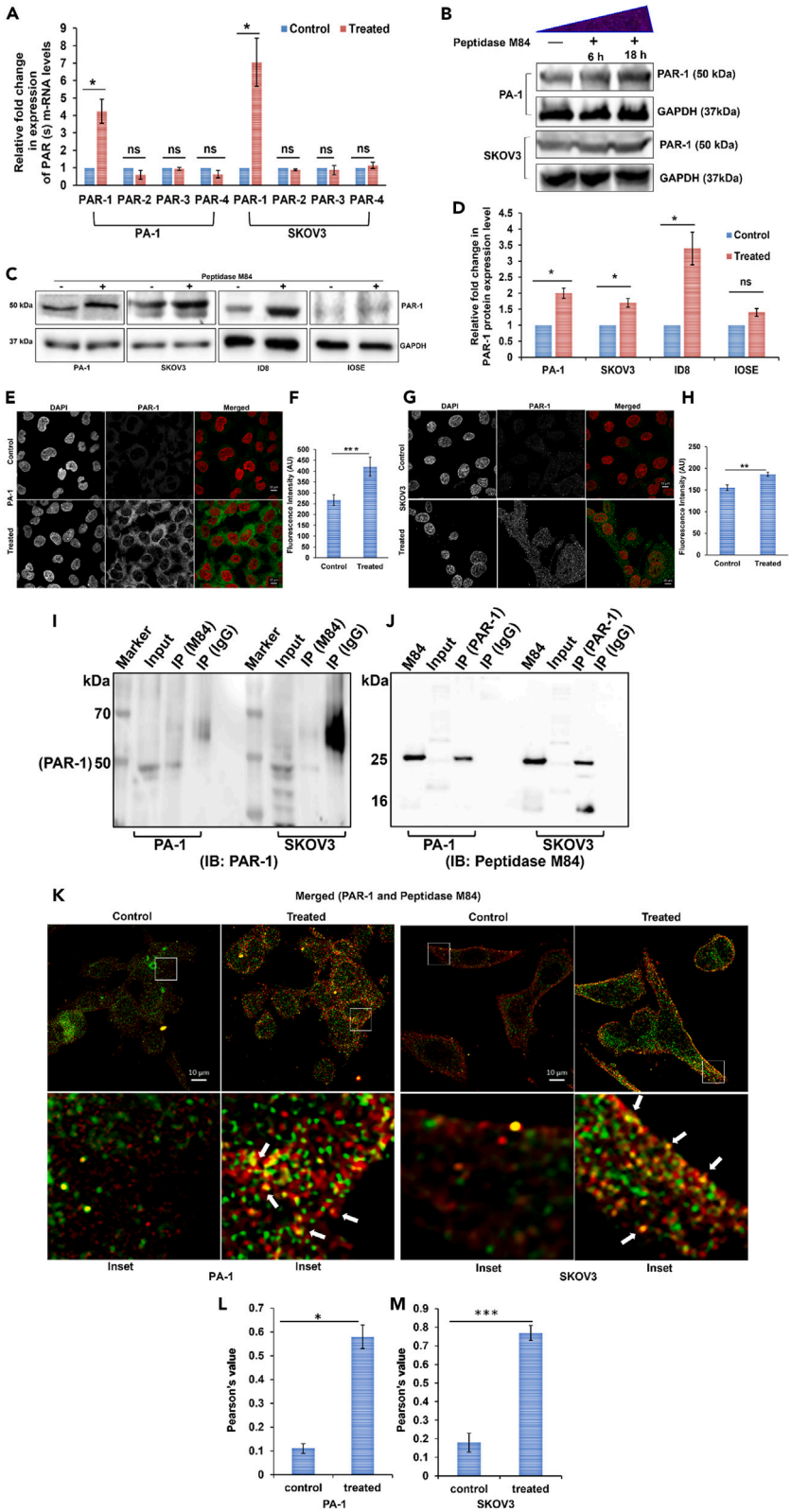
A
Relative fold change in expression of PAR (s) m-RNA levels
Control
Treated
PAR-1 PAR-2 PAR-3 PAR-4 PAR-1 PAR-2 PAR-3 PAR-4
PA-1
SKOV3
B
Peptidase M84
6 h
18 h
PA-1
PAR-1 (50 kDa)
GAPDH (37kDa)
SKOV3
PAR-1 (50 kDa)
GAPDH (37kDa)
C
Peptidase M84
50 kDa
37 kDa
PAR-1
GAPDH
PA-1
SKOV3
ID8
IOSE
D
Relative fold change in PAR-1 protein expression level
Control
Treated
PA-1
SKOV3
ID8
IOSE
E
DAPI
PAR-1
Merged
Control
PA-1
Treated
F
Fluorescence Intensity (AU)
Control
Treated
G
DAPI
PAR-1
Merged
Control
SKOV3
Treated
H
Fluorescence Intensity (AU)
Control
Treated
I
Marker
Input
IP (M84)
IP (IgG)
kDa
70
(PAR-1) 50
PA-1
SKOV3
(IB: PAR-1)
J
M84
Input
IP (PAR-1)
IP (IgG)
kDa
25
16
PA-1
SKOV3
(IB: Peptidase M84)
K
Merged (PAR-1 and Peptidase M84)
Control
Treated
Inset
PA-1
SKOV3
L
Pearson's value
control
treated
PA-1
M
Pearson's value
control
treated
SKOV3

Figure 5. Peptidase M84 persuaded apoptosis in ovarian cancer cells by modulating PAR-1

(A) Real-time PCR analysis of *PAR-1*, *PAR-2*, *PAR3*, *and PAR-4* genes in Peptidase M84 treated and untreated PA1 and SKOV3 cells. Ct values are normalized to *GAPDH* expression, and 2^{-ddct} values are calculated ($n = 3$).

(B) Western blot shows a time-dependent increase in PAR-1 expression levels in Peptidase M84 treated PA-1 and SKOV3 cells.

(C and D) Western blot together with bar diagram of densitometry scan of PAR-1 expression in Peptidase M84 treated (18 h) and untreated PA-1, SKOV3, ID8, and IOSE cells.

(E–H) Confocal imaging with respective bar diagrams of MFI of PAR-1 expression levels (green) in PA-1 and SKOV3 cells.

(I) Co-immunoprecipitation study of PAR-1 and Peptidase M84 reveals the interaction between PAR-1 and Peptidase M84 in both PA-1 and SKOV3 cells. Here, whole-cell lysates (WCL) from these cells were loaded as inputs.

(J) Bands of Peptidase M84 are observed in IB when Peptidase M84 was immunoprecipitated with PAR-1. Here, purified Peptidase M84 from *B. altitudinis* was loaded as input.

(K) Confocal imaging revealed co-localization between Peptidase M84 (green) and PAR-1(red) in Peptidase M84 treated PA-1 and SKOV3 cells.

(L and M) Bar diagrams showed Pearson's co-efficient values. In each panel, error bars were calculated based on results obtained from a minimum of three independent experiments. All statistical analysis was done by applying the Student's t test (two-tailed). In all panels, ns $p > 0.05$, *$p \leq 0.05$, **$p \leq 0.01$, and ***$p \leq 0.001$. Data are expressed in ±SEM. Scale bars: 10 μm. Densitometric analysis was performed on ImageJ and Gel Quant softwares. Band intensities were normalized to loading controls GAPDH. Pearson's co-efficient was calculated in Fiji (https://imagej.net/software/fiji/). See also Figures S7 and S8.

M84 induced phosphorylation of p38 was inhibited by ML161 pre-treatment in PA-1 cells. However, the total p38 concentration remained consistent (Figure S10B). Therefore, Peptidase M84 mediated NF-κB and MAP kinase pathways were regulated by PAR-1 activity alterations.

We have stated earlier that Peptidase M84 treatment promoted ROS generation in ovarian cancer cells. Interestingly, cells pre-treated with ML-161 displayed no significant ROS generation even after Peptidase M84 treatment for 18 h. Inhibition studies with MG132 and SB203580 further strengthened that blockade of NF-κB and p38 either individually or together impaired further ROS production in ovarian cancer cells (Figures S11A–S11C). Hence, Peptidase M84 induced PAR-1 dependent activation of both NF-κB and p38 to enhance ROS levels in ovarian cancer cells. Taken together our data illustrated that Peptidase M84 induced apoptosis by effectively targeting PAR-1 in accordance with the specific involvement of p38, NF-κB, and ROS.

Peptidase M84 treatment improved the survival of ID8 bearing mice and impeded body weight increase due to ascites accumulation and also affected the viability of ID8 cells *in vivo*

Tumor was induced intraperitoneally with ID8 cells (5×10^6) and the survival rate and the alterations in body weight were observed in C57BL/6 mice (Figure 7A). In the ID8 control mice, the rate of survival was 60% after 30 days and 10% after 60 days. When 3.0 μg/mL Peptidase M84 was injected at a weekly interval for 7 successive weeks the rate of survival was increased to 90% after 30 days and 70% after 60 days (Figure 7B). The body weight of ID8 control group enhanced from 25 g (0 days) to 45 g (after 60 days of tumor inoculation). On the other hand, in Peptidase M84 treated group and buffer control group no significant alterations in body weight were noticed (Figures 7C, S12A, and S12B). Inactivated Peptidase M84 (EDTA treated) failed to ameliorate the survival rate of ID8 induced mice and also showed an increase in body weight (Figure 7C).

In addition, viable ID8 cells were evaluated by trypan blue staining. At the inception of this investigation ID8 cells (5×10^6) were inoculated in the peritoneum cavity of mice and there was a gradual proliferation of viable ID8 cells in tumor control group. Peptidase M84 treatment caused a significant decline in the count of viable ID8 cells after 45^{th} and 60^{th} days. Peptidase M84 inactivated by EDTA did not affect the viability of ID8 cells at all (Figures 7D and 7E). Altogether our findings elucidated that the antitumour property of Peptidase M84 was linked to its proteolytic activity.

Peptidase M84 augmented oxidative stress in mice

To evaluate the Peptidase M84 mediated oxidative stress, biochemical tests were performed with different phase II detoxifying enzymes and LPO in the serum samples of mice. The level of LPO in serum is considered a marker for cellular oxidative stress. After 45 days of treatment, the number of viable ID8 cells significantly lessened in group-3 as compared to group-2 and the level of LPO in the serum was also found to be lowered in group-3 than to that of tumor control group-2. This indicated that Peptidase M84 itself could induce oxidative stress. After 45 days of Peptidase M84 treatment, the LPO level in group-3 was at normal levels as compared to group-1. The LPO levels of group-4 were found similar to group-2 after 45 days of treatment (Figure 7F).

The levels of catalase, SOD, and GSH in serum were relatively low because of excessive oxidative stress. After 45 days of Peptidase M84 treatment, the number of viable ID8 cells significantly declined in group-3 compared to group-2 and an increase in the levels of these enzymes was found in group-3 than to group-2. In addition to the aforementioned observations, the levels of catalase, GSH, and SOD in serum of group-4 were noticed as similar to group-2 after 45 days of treatment. Interestingly, there was no significant difference observed in any of the aforementioned biochemical markers when normal animals were treated with Peptidase M84 (group-6) (Figures 7G–7I). These observations clearly pointed out that Peptidase M84 triggered apoptosis in ID8 cells via oxidative stress-mediated damage.

Studies based on the biochemical index of the liver and kidney of mice revealed peptidase M84 did not cause any significant toxicity

To observe any adverse effects of exposure to Peptidase M84, a chronic toxicity study for 45 days was also been performed on experimental C57BL/6 mice. Alterations in the level of biochemical parameters, such as SGOT (AST), SGPT (ALT) (parameters for drug-induced liver injury),

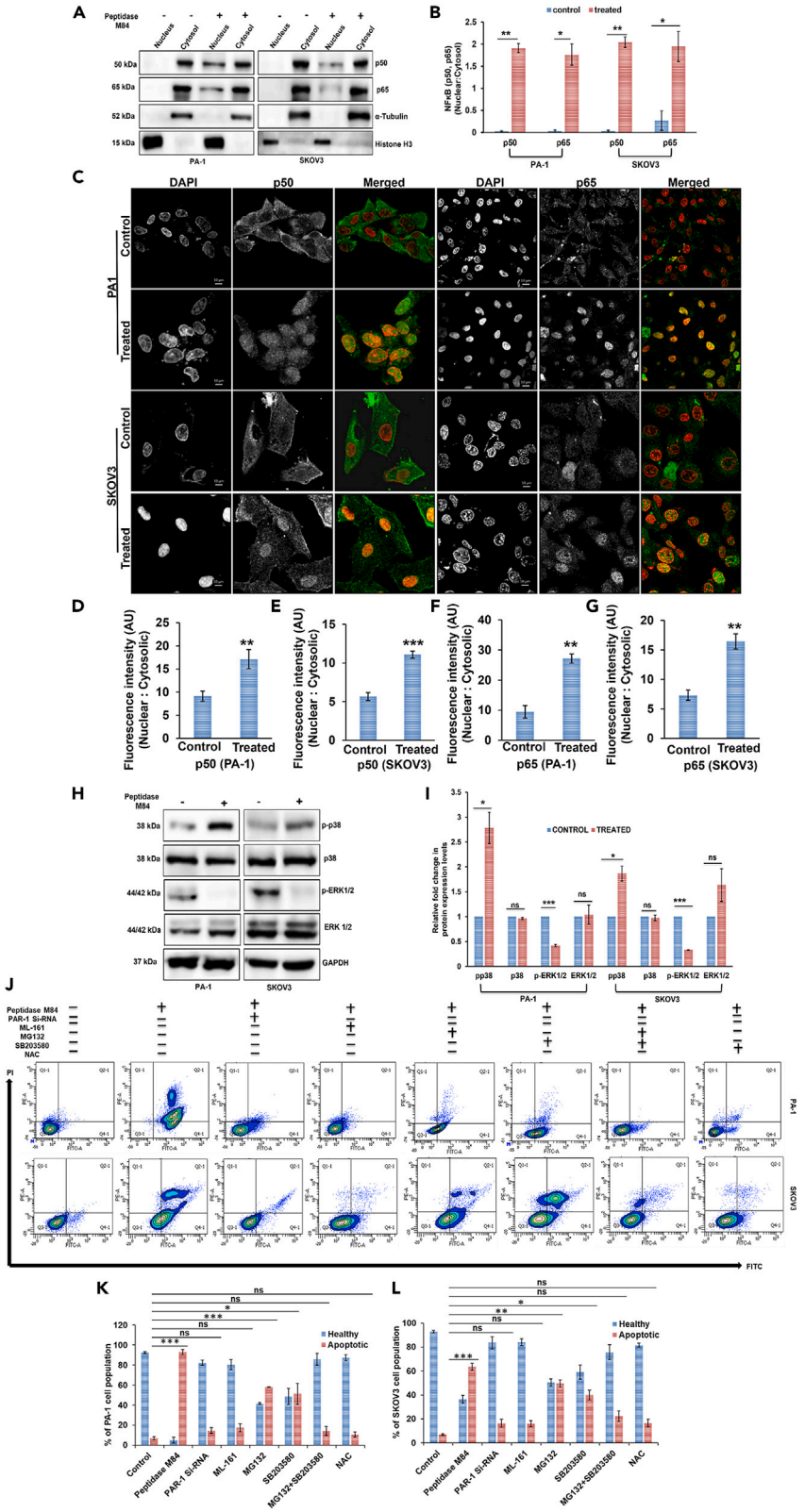
A
Peptidase M84
Nucleus
Cytosol
50 kDa
65 kDa
52 kDa
15 kDa
p50
p65
α-Tubulin
Histone H3
PA-1
SKOV3
B
control
treated
NF-κB (p50, p65) (Nuclear/Cytosol)
p50
p65
PA-1
SKOV3
C
DAPI
p50
Merged
p65
PA1
SKOV3
Control
Treated
D
Fluorescence intensity (AU) (Nuclear : Cytosolic)
p50 (PA-1)
E
p50 (SKOV3)
F
p65 (PA-1)
G
p65 (SKOV3)
H
38 kDa
44/42 kDa
37 kDa
p-p38
p38
p-ERK1/2
ERK 1/2
GAPDH
I
CONTROL
TREATED
Relative fold change in protein expression levels
pp38
p-ERK1/2
ERK1/2
J
Peptidase M84
PAR-1 Si-RNA
ML-161
MG132
SB203580
NAC
PI
FITC
PA-1
SKOV3
K
% of PA-1 cell population
Healthy
Apoptotic
Control
Peptidase M84
PAR-1 Si-RNA
ML-161
MG132
SB203580
MG132+SB203580
NAC
L
% of SKOV3 cell population

Figure 6. Peptidase M84 triggers PAR-1 induced apoptosis in ovarian cancer cells via NF-κB, MAPK, and ROS-dependent manner

(A and B) Western blot and bar diagram of densitometric scan (nucleus: cytosol) indicate enhanced nuclear translocation of p50 and p65 after Peptidase M84 treatment in PA-1 and SKOV3 cells. Histone H3 and α-tubulin are loading controls.

(C–G) Immunofluorescence shows Peptidase M84 induced nuclear translocation of p50 (green) and p65 (green) in PA-1 and SKOV3 cells. Bar diagrams represent the ratio of the MFI of nucleus to cytosol of cells.

(H and I) Western blot with bar diagram of densitometric scan show significant upregulation in phospho-p38 and down-regulation in phospho-ERK-1/2 expression levels in Peptidase M84 treated PA-1 and SKOV3 cells. Here, GAPDH is used as loading control (J) Peptidase M84 mediated cellular apoptosis is analyzed by FACS in the presence and absence of different signaling inhibitors (PAR-1, NF-κB, p38, and ROS) and PAR-1 si-RNA in PA-1 (upper panel) and SKOV3 (lower panel) cells. (K and L) The above results are graphically represented in the bar diagram. In each panel, error bars were calculated based on results obtained from a minimum of three independent experiments. All statistical analysis was done by applying Student's t test (two-tailed). In all panels, ns $p > 0.05$, *$p \leq 0.05$, **$p \leq 0.01$, and ***$p \leq 0.001$. Data are expressed in ±SEM. Scale bars: 10 μm. Densitometric analysis was performed on ImageJ and Gel Quant softwares. Band intensities were normalized to loading controls. Fluorescence intensity and Pearson's co-efficient values were measured manually by drawing lines along the entire length of each nucleus or cytosol and calculating them using Fiji (https://imagej.net/software/fiji/). See also Figures S9–S11 and S13.

or creatinine and urea (parameters for toxin-induced impaired renal function) in the serum sample of experimental mice implicate hepatotoxicity and nephrotoxicity. ALT and AST activity was significantly upregulated and creatinine and urea levels were reduced significantly in the tumor control group when compared to the normal group. However, no such significant difference was noticed in all the aforementioned indexes in the only protease treated group with respect to normal untreated group. Our results deciphered that both liver and kidney toxicity parameters remained within the normal range after treatment with 3.0 μg/mL (12.0 μg/kg of body weight) of Peptidase M84 for up to 45 days of continual treatment (Figures 7J–7M). No adverse effects were observed concerning normal untreated mice. Upon evaluating the chronic toxicity of Peptidase M84, it did not cause any significant toxicity as all the parameters for liver and kidney toxicity lied within normal limit. We further validated those findings by histopathological analysis.

Peptidase M84 treatment showed recovery of the damaged architecture of liver and kidney tissue of host system and did not cause any significant toxicity

In the current investigation, histopathological examination was executed on sections from kidney and liver tissues of all six groups of experimental animals after 45 days of treatment using hematoxylin-eosin staining to assess whether there was any inconsistency with the biochemical markers. Histopathological sections of normal liver unraveled healthy morphology of hepatocytes; normal kidney tissues displayed healthy glomeruli, vessels, and tubules. However, tumor control group (group-2) showed disrupted architecture with moderate to dense inflammation with damaged hepatocytes in the liver and extensively damaged glomerular structure in the kidney. After Peptidase M84 treatment (group-3) this damage was observed to be recovered and healthy tissue structure prevailed in the liver and kidney tissue. In comparison with the untreated control group, no noticeable anomalies in the histopathology of the kidney and liver of the Peptidase M84 treated group-3 and group-4 were detected, following 45 days of continual treatment. Morphology of the liver of only Peptidase M84 treated mice was almost similar to the untreated group. Morphology of the livers from group-6 showed no significant change from that of the untreated control. As observed in untreated control, in addition to the radial distribution pattern of hepatocytes encircling the central vein was obvious in the protease control and vehicle control group after treatment. Radially arranged hepatocytes (HCs) lacking Kupffer cells (KCs) and fine integrity in the liver tissue, depict the absence of any chronic toxicity (Figure 7N).

Notable differences after 45 days of constant treatment with Peptidase M84 between renal corpuscles (RCs) and glomerular tufts of kidney tissue were not found when compared to the untreated group. Moreover, paucity of tubular dilation, glomerular infiltration, and necrosis indicated the non-existence of acute inflammation (Figure 7O). Hence, this implies that 3.0 μg/mL (12.0 μg/kg of body weight) of Peptidase M84 for the mentioned period is significantly non-toxic, non-hazardous to normal tissue of mice and does not affect the survival of mice (Figures 7N and 7O).

DISCUSSION

Emerging complexities and side effects associated with conventional chemotherapy necessitate the quest for new therapeutic agents for ovarian cancer treatment. In this study, we designed a novel approach to isolate and characterize proteases of environmental microbial origin for apoptotic properties to curb the growth of ovarian cancer cells. For this purpose, we assessed over 200 environmental isolates to finally select a protease secreting strain "GDL-186" which was identified as *Bacillus altitudinis*. Reported to be first isolated from air samples of high altitudes in India, *Bacillus altitudinis* was found to secrete extracellular proteases potentiating apoptosis in ovarian cancer cells in our study.[50] Popularly, *Bacillus* spp. is widely studied for its extracellular alkaline protease secreting properties which also make it industrially important.[51] In our attempt to find a protease with pro-apoptotic properties, we identified Peptidase M84 which is a key secretory metallo-protease of *Bacillus altitudinis*.[52] A recent report revealed the anti-proliferative activity of the organic extract of *Bacillus altitudinis* MTCC13046 against human hepatocellular carcinoma cells.[53] We obtained two major bands at 25 kDa and 16 kDa in SDS-PAGE for this purified protease which was homologous to the amino acid sequences of Peptidase M84 from *Bacillus altitudinis* in Uniprot (ID: A0A5D4PNG4) and NCBI databases. This protease is comprised of a conserved metallo-protease domain with three histidine residues in its active site, which is also reported to be present in metzincin metallo-protease from *Bacillus intermedius*.[39] The optimal protease activity of Peptidase M84 was observed in normal physiological pH (7.0–9.0) and temperature (37°C–40°C) that got inhibited by EDTA and 1,10 phenanthroline. This aided us to characterize

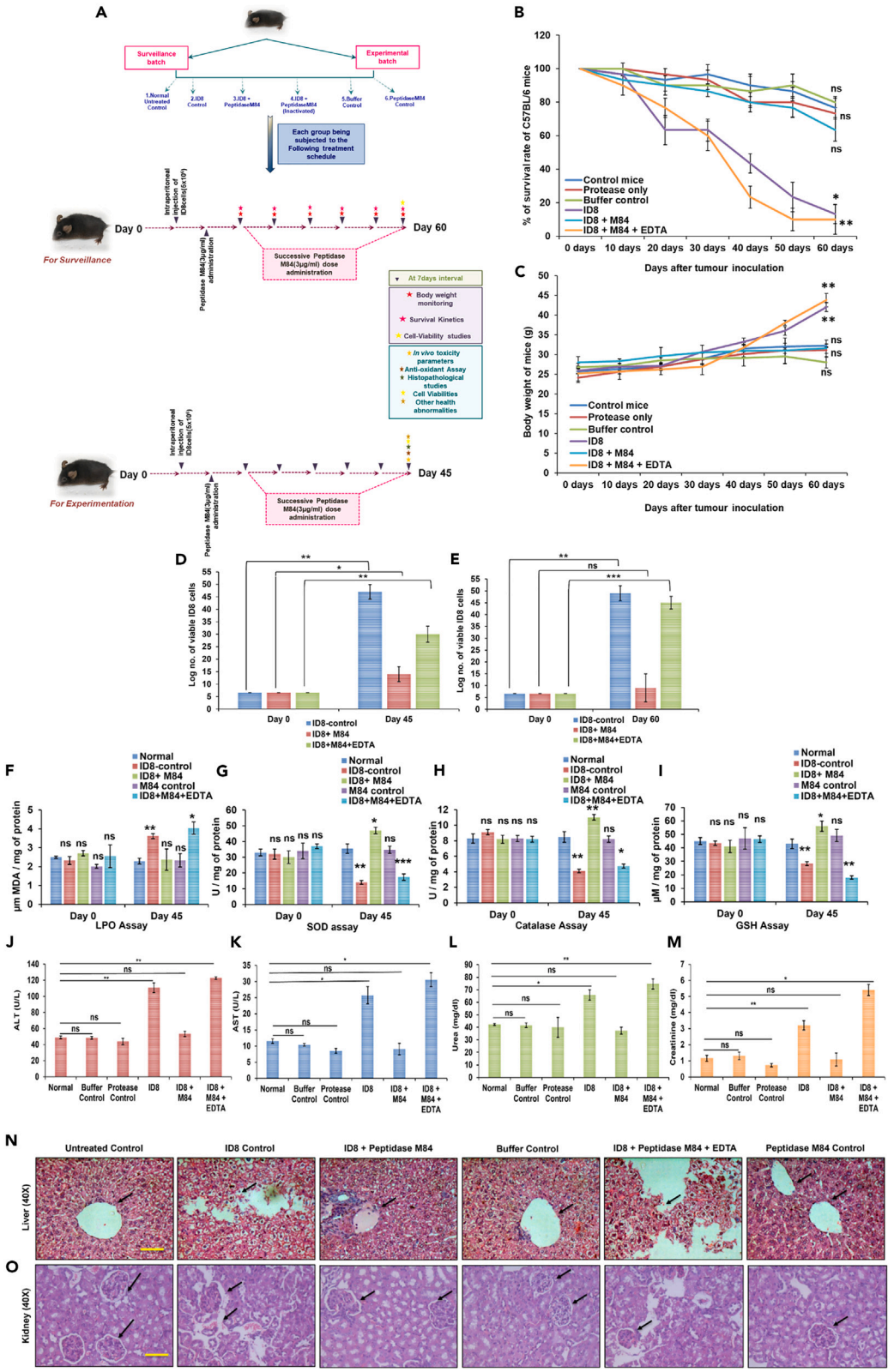
A
Surveillance batch
Experimental batch
1.Normal Untreated Control
2.ID8 Control
3.ID8 + PeptidaseM84
4.ID8 + PeptidaseM84 (Inactivated)
5.Buffer Control
6.PeptidaseM84 Control
Each group being subjected to the Following treatment schedule
Intraperitoneal injection of ID8cells(5x10⁶)
Day 0
Day 60
For Surveillance
Peptidase M84(3µg/ml) administration
Successive Peptidase M84(3µg/ml) dose administration
At 7days interval
Body weight monitoring
Survival Kinetics
Cell-Viability studies
In vivo toxicity parameters
Anti-oxidant Assay
Histopathological studies
Cell Viabilities
Other health abnormalities
Day 45
For Experimentation
B
% of survival rate of C57BL/6 mice
Control mice
Protease only
Buffer control
ID8
ID8 + M84
ID8 + M84 + EDTA
0 days 10 days 20 days 30 days 40 days 50 days 60 days
Days after tumour inoculation
C
Body weight of mice (g)
Days after tumour inoculation
D
Log no. of viable ID8 cells
Day 0
Day 45
ID8-control
ID8+ M84
ID8+M84+EDTA
E
Log no. of viable ID8 cells
Day 0
Day 60
F
µm MDA / mg of protein
LPO Assay
G
U / mg of protein
SOD assay
H
U / mg of protein
Catalase Assay
I
µM / mg of protein
GSH Assay
Normal
ID8-control
ID8+ M84
M84 control
ID8+M84+EDTA
J
A.L.T (U/L)
K
A.S.T (U/L)
L
Urea (mg/dl)
M
Creatinine (mg/dl)
Normal
Buffer Control
Protease Control
ID8
ID8 + M84
ID8 + M84 + EDTA
N
Untreated Control
ID8 Control
ID8 + Peptidase M84
Buffer Control
ID8 + Peptidase M84 + EDTA
Peptidase M84 Control
Liver (40X)
O
Kidney (40X)

Figure 7. Effect of Peptidase M84 on histological, biochemical parameters, survival rate, and body weight of tumor induced mice

(A) Illustration of the *in vivo* study to determine the anticancer potential and non-toxicity of Peptidase M84.

(B) Peptidase M84 treatment shows promising improvement in survival rate in ID8 mice model. Peptidase M84 in the presence of EDTA shows a similar mortality rate as tumor control group.

(C) Line graph shows body weight after Peptidase M84 administration in mice.

(D and E) Viable ID8 cells were measured at different time points by the trypan blue exclusion method.

(F–I) Biochemical parameters of cellular oxidative stress (LPO, SOD, CAT, and GSH) were measured in serum samples of mice. The results are graphically represented.

(J–M) Liver and kidney functionality test (ALT, AST, urea, and creatinine) was performed in serum samples of mice. The results are graphically represented.

(N and O) Histological studies (HandE staining) showed that Peptidase M84 treatment improved the damaged architecture of the liver and kidney tissue caused by tumor induction. While arrows indicated intact membrane integrity in control and Peptidase M84 treated set and disrupted tissue architectures in ID8 control and Peptidase M84-pre-treated with EDTA set. In each panel, error bars were calculated based on results obtained from a minimum of three independent experiments ($n = 3$). All statistical analysis was done by applying Student's t test (two-tailed). Data are expressed in $\pm$SEM. In all panels, ns $p > 0.05$, *$p \leq 0.05$, **$p \leq 0.01$, and ***$p \leq 0.001$. Scale bars: standard See also Figure S12.

Peptidase M84 as a Zn^{2+}-dependent metalloprotease. The LC-MS/MS peptide blast analysis showed the presence of Peptidase M84-like protease in other closely related Bacillus species such as *Bacillus aerophilus*, *Bacillus xiamenensis*, and *Bacillus intermedius*. However, the functional aspects especially the anticancer effects of these proteases were not elucidated well earlier. In this study, we report the apoptotic effects of this protease from an environmental isolate of *Bacillus altitudinis GDL-186* with high selective toxicity in ovarian cancer cells. Earlier studies majorly illustrated the biophysical and microbiological aspects of Peptidase M84. So, at present it is difficult to comment whether the previously identified Peptidase M84-like protease had any pro-apoptotic effect or not. Our work, in the present scenario, has definitely paved the way for further study in this direction in days to come. Previously, a polypeptide PBN118 isolated from a marine Bacillus was reported to be similar to the Peptidase M84 from *Bacillus pumilus*. PBN118 prevented migration and suppressed invasion of human hepatocellular carcinoma cells.[54]

Peptidase M84, here also triggered apoptosis in both human and mouse ovarian adenocarcinoma cells in a dose-dependent manner. Moreover, this pro-apoptotic response of Peptidase M84 was inhibited by EDTA treatment which helped us confirm that its apoptotic response was a result of its proteolytic activity. Interestingly, Peptidase M84 did not show any significant effect on IOSE and PEMΦ cells which were the normal cells used in this study. Additionally, Peptidase M84 turned out to be anti-proliferative in nature when it reduced the expression levels of Ki-67, a proliferative antigen in PA-1 and SKOV3 cells. Based on these findings, we were intrigued to decipher the detailed molecular mechanisms underlying the Peptidase M84 induced apoptosis in ovarian cancer cells. Since more than 90% of all ovarian malignancies are classified as EOC including the aggressive high-grade serous carcinoma category,[1] we considered that initial testing of Peptidase M84 for its apoptosis-inducing capabilities in *in vitro* setup could enable the designing of a better treatment rationale.

The canonical intrinsic pathway of apoptosis depends on the delicate balance between pro-apoptotic Bax and anti-apoptotic Bcl2.[55] We observed a significant increase in Bax to Bcl2 ratio, and a rise in cytosolic mitochondrial cytochrome *c* concentrations in addition to caspase 9 and 3 activation following Peptidase M84 treatment in SKOV3 as well as PA-1 cells. These observations delineated an induction of intrinsic apoptosis pathway in these malignant ovarian cells by Peptidase M84 specifically. Enhanced oxidative stress owing to the production of higher ROS and impaired redox balance is intrinsic to the sustenance of any neoplastic cells unlike a normal healthy cell.[25,26] In coherence with this fact, we also noted that Peptidase M84 abnormally increased intracellular ROS levels in PA1, SKOV3, and ID8 cells in a time-dependent manner which resulted in their apoptotic death. Contrastingly, Peptidase M84 failed to impart any such change in normal IOSE cells where ROS was quantitated to be very less with respect to the *in vitro* malignant setups. This observation was further confirmed by the inhibition of ROS by pre-incubation with NAC (a cellular ROS quencher) before treatment with Peptidase M84 in ovarian cancer cells. Overproduction and accumulation of ROS are known to modify nucleotides, break DNA strands, and facilitate chromosomal rearrangements, contributing to the deregulation of a wide range of signaling pathways.[56] Peptidase M84 treatment induced ROS-mediated DNA damage in ovarian cancer cells which intrigued us to check the status of mitochondrial membrane potential by JC-1 staining as ROS overproduction is always positively associated with mitochondrial membrane depolarization and reduced cell viability. A disruption in mitochondrial membrane potential by increased cellular ROS was apparent in JC1-stained ovarian cancer cells. These findings aligned with a rise of cytochrome *c* as detected in the cytosolic fractions of Peptidase M84 treated ovarian cancer cells which might have leaked out of a depolarized mitochondrial membrane to trigger apoptosis cascades involving caspases, apoptosome complex, and PARP.[46,57] Enzymatic activity of PARP is found to be increased in the cells under stressed conditions. Intact PARP expression is associated with DNA repair system which in turn saves the cancer cells from apoptotic cell death. The presence of cleaved PARP and a decrease in Bcl-2 muddle the apoptotic balance and drive the cell toward the gateway of apoptosis, as it restricts cell repair.[58] We evidenced Peptidase M84 to induce PARP cleavage in ovarian cancer cells which corroborated with an increased DNA damage. This PARP activating feature of Peptidase M84 is promising enough since the FDA has approved Olaparib (AZD2281) which is a PARP inhibitor for conventional ovarian cancer treatment.[59]

The major signaling pathways of proteases are initiated by the cleavage of PARs which play an important role both in cancer progression and apoptosis of malignant cells in a cue-based manner.[28] PAR-1 was reported to be overexpressed in explants of human ovarian cancer tissues compared to normal ovarian cells.[29,34] Gingipain-R (RgpB) a cysteine protease isolated from *Porphyromonas gingivalis* was the earliest reported microbial protease that acted by cleaving a model peptide representing a cleavage site of PAR-2.[60] We noted an overexpression of PAR-1 at both transcriptional and translational levels in Peptidase M84 treated ovarian cancer cells compared to their untreated counterparts. Interestingly, no significant alteration in the expression level of PAR-1 in Peptidase M84 treated normal ovarian epithelial cells was seen. Several evidence identified PAR-1 as a tumor promoter as it was associated with the induction of angiogenesis, invasion, and also metastasis

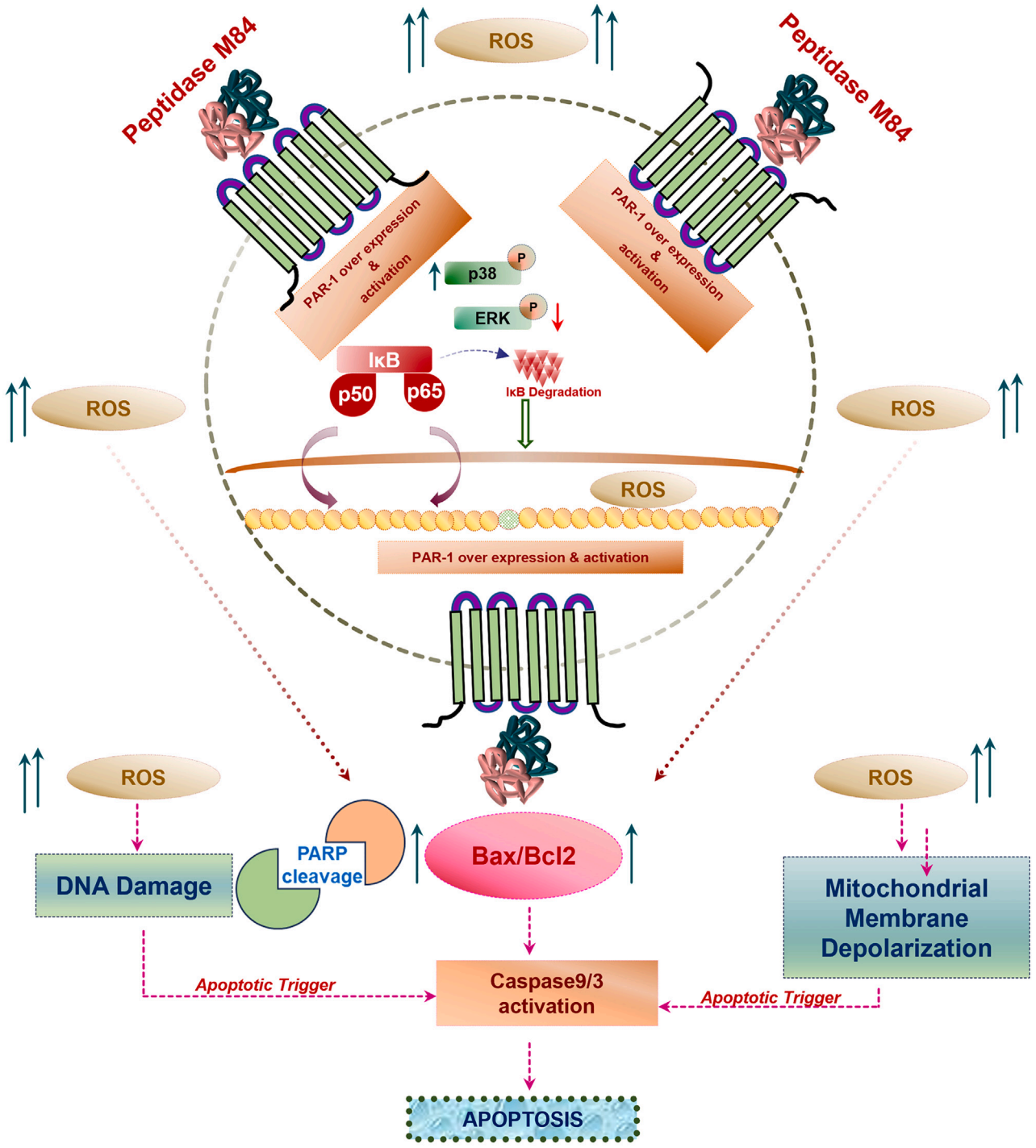

Figure 8. Schematic representation of Peptidase M84 induced apoptosis in ovarian cancer cells

Peptidase M84 induced activation and overexpression of PAR-1 thus enhancing cellular ROS and activation of NF-κB, p38 followed by downregulation of pERK1/2. ROS mediated DNA damage induced changes in mitochondrial membrane potential and triggered the release of mitochondrial cytochrome *c* which subsequently activated caspase 3 ultimately promoting Bax, Bcl2 mediated intrinsic pathway of apoptosis. Enhanced ROS level in malignant cells allows to meet the threshold level of cellular ROS that affect cell survival earlier than the normal healthy cells ultimately triggering apoptotic cell death.

in ovarian and breast adenocarcinoma cells along with xenograft models.[61,62] However, thrombin is found to mediate apoptosis in a dose-dependent way through modulation of PAR-1 in tumor cells.[33] Previously we reported that metallo-protease HAP from *V. cholerae* could cause overexpression of PAR-1 by inducing its cleavage.[37] Nevertheless, such a paradox is not limited only to PAR-1. Biomolecules like granulocyte/macrophage colony-stimulating factor, RAR-β2, E-cadherin, CD44, α/β-catenin, and CAV1 have also been reported to impart such contrasting functions in tumorigenesis.[41,63] In order to reveal the relationship between alteration in PAR-1 expression and apoptosis in the presence of Peptidase M84 in ovarian cancer cells, we performed gene knockdown, signaling inhibition, and immunoprecipitation studies. Our findings also demonstrated that Peptidase M84 could specifically bind and interact with PAR-1. Moreover, Peptidase M84 failed to induce apoptosis in PAR-1 silenced ovarian cancer cells. Furthermore, ML161, a PAR1-mediated Gq signaling inhibitor[64] also showed a significant decrease in apoptosis in Peptidase M84 treated cells. This suggests that Peptidase M84 caused PAR-1 activation through Gq signaling induction. Cumulative data strengthened the possible correlation regarding the role of PAR-1 in induction of apoptosis and established PAR-1 as a novel oncogenic target for Peptidase M84 mediated apoptosis in ovarian cancer cells. PAR1 has emerged as a promising hot spot target for chemotherapeutic drugs in recent years as well. PAR1 targeting drugs like vorapaxar and atropaxar have entered phases of clinical trials.[31]

Thrombin-mediated PAR-1 activation regulates major signaling pathways, such as p38 MAPK[47] and NF-κB.[48] Herein, inhibition studies using NF-κB and p38 inhibitors confirmed the involvement of NF-κB and MAPK in Peptidase M84-mediated apoptosis in PA-1 and SKOV3 cells. Pre-treatment with NF-κB, p38, and ROS inhibitors downregulated cellular apoptosis even after Peptidase M84 treatment compared to the absence of any prior inhibition. Interestingly, besides the upregulation of p38 phosphorylation, we also observed downregulation of *p*-ERK1/2 in these cells upon Peptidase M84 treatment. Blockade of AKT/ERK pathway and enhanced phosphorylation levels of p38, contributing majorly to apoptosis in response to different stimuli in cancer cells.[65] Furthermore, NF-κB regulates gene expression in cellular processes like cellular proliferation, stress responses, and apoptosis under different stimulations.[66] Besides, ROS can also regulate either activation or repression of NF-κB signaling depending on phase and context.[67,68] We noticed that the cellular ROS level was gradually increased with time by Peptidase M84 treatment in ovarian cancer cells. Peptidase M84 promoted PAR-1 dependent activation of p38 and NF-κB signaling which can augment the cellular ROS levels as well as inhibition of these signalings attenuated ROS levels in ovarian cancer cells. Phosphorylation of p38, a major component of MAPK pathway is linked with ROS generation and cell proliferation in the majority of the events.[49,69] However, when p-p38 levels cross the critical threshold in conjugation with the downregulation of ERK, cells get immensely stressed to meet death.[70] In addition, there was no significant expression of PAR-1 in IOSE cells. Therefore, the load of cellular ROS level was found to be lower in IOSE cells even after Peptidase M84 treatment as compared to cancer cells, as there was no effective alteration in PAR-1 activity or expression. Thus, Peptidase M84 failed to trigger the intrinsic apoptotic pathway in normal IOSE cells. In light of these findings, we established that PAR-1, NF-κB, p38, ERK1/2, and ROS regulate Peptidase M84-induced apoptosis by playing decisive roles in a collaborative manner in ovarian cancer cells (Figure 8).

Finally, to validate our findings *in vivo* we investigated the role of Peptidase M84 in a syngeneic mouse model. ID8 is a spontaneous murine ovarian adenocarcinoma cell line used to study ovarian tumor biology. This cell line is advantageous due to its efficacy in developing tumors in both solid and ascitic forms.[71,72] Herein, we report that Peptidase M84 treatment in ID8-mice resulted in inhibition of body weight increase due to less ascites formation. An increase in the survival rate of the ID8-bearing mice following Peptidase M84 treatment as compared to the tumor control group indicated that Peptidase M84 treatment affected the viability of cancer cells *in vivo*. However, Peptidase M84 pre-treated with EDTA was found to be ineffectual and did not show any kind of alterations. This indicated the antitumour activity of Peptidase M84 was linked to its proteolytic activity. In the ID8-bearing mice, the cellular ROS level was increased significantly after Peptidase M84 treatment. An increase in the Peptidase M84 induced oxidative stress corroborated with a rise in the levels of GSH, SOD, and catalase along with reduced LPO titers in the ID8-bearing mice receiving Peptidase M84 treatment as compared to the ID8 control mice. Moreover, the reduction in viable ID8 cell count in mouse peritoneum indicated that Peptidase M84 treatment decreased the survivability of tumor cells and strengthened the remedial effect of chemotherapy. The histopathological studies illustrated that the cellular architecture and morphology of the liver and kidney tissues of mice were not affected by Peptidase M84. Hence, it is significantly non-toxic for normal tissue of mice. However, Peptidase M84 treatment was capable of recovering the damaged tissue morphology in ID8-bearing mice. The increase in the levels of SGOT, SGPT, urea, and creatinine in the ID8 control group with respect to the Peptidase M84 treated group in regular intervals further validated our findings. No significant mortality or toxic symptoms were noticed in only Protease control group. Thus, our findings demonstrated a reduction in cancer cell proliferation via oxidative stress-mediated apoptosis without causing harm to normal healthy cells following Peptidase M84 treatment *in vivo*.

Limitations of the study

Unlike thrombin, the Peptidase M84 mediated exact PAR-1 cleavage site is in the process of identification which will be the major focus of our future study. Further investigations may be executed in other experimental models and clinical settings to enlist Peptidase M84 as an anti-cancer drug, which may widen the amplitude for a long-lasting targeted therapy for ovarian cancer. Thus, Peptidase M84 warrants further exploration as a new antitumour agent.

STAR★METHODS

Detailed methods are provided in the online version of this paper and include the following:

- KEY RESOURCES TABLE
- RESOURCE AVAILABILITY

SUPPLEMENTAL INFORMATION

Supplemental information can be found online at https://doi.org/10.1016/j.isci.2024.109828.

ACKNOWLEDGMENTS

This work was supported by the Indian Council of Medical Research adhoc project grant BMS/adhoc/56/2020-21 dt: 23.01.2021. Mr. Niraj Nag is thankful to the University Grants Commission, India for providing fellowship under the prestigious UGC-NET-JRF fellowship award (UGC-ref. no.: 757/CSIR-UGC-NET JUNE 2017).

We wish to express our gratefulness to Dr. Shanta Dutta (Director, ICMR-NICED) for providing us with the central research instrumentation facility of NICED. Mr. Biplab Roy (NICED) is acknowledged for helping us in the screening of environmental isolates. We sincerely thank Dr. Sib Sankar Roy (CSIR-IICB) for providing us with cell lines and Dr. Shruti Chatterjee (Nirma University) for providing us with all the bacterial isolates. We thankfully acknowledge Ms. Ritoja Shee (Manipal University Jaipur), Dr. Mainak Chakraborty (NICED), Mr. Prolay Halder (NICED), Ms. Suparna Chakraborty (NICED), Dr. Sutapa Mukherjee (CNCI), Mr. Arup Dutta Roy (Association of Chartered Certified Accountants, UK), and Dr. Atish Barua (Tufts University, USA) for their technical support and co-operation during the study.

AUTHOR CONTRIBUTIONS

N.N. conceptualized the study, investigated, performed experiments, wrote the original draft, reviewed, data curation, and analyzed and validated the data; T.R. performed experiments and reviewed; R.T. formal analysis and reviewed; A.G. performed experiments; R.D. formal

analysis of confocal imaging data; E.M. formal analysis and reviewed; S.S. formal analysis; A.P. flowcytometric data acquisition and formal analysis; P.P. provided resources; A.P. conceptualized the study, supervised the research work, funding acquisition, data curation, reviewed and approved the final manuscript.

Consent to publish: Not applicable.

DECLARATION OF INTERESTS

The authors declare no competing interests.

Received: October 5, 2023
Revised: January 2, 2024
Accepted: April 24, 2024
Published: April 26, 2024

REFERENCES

1. Ciucci, A., Buttarelli, M., Fagotti, A., Scambia, G., and Gallo, D. (2022). Preclinical models of epithelial ovarian cancer: practical considerations and challenges for a meaningful application. Cell. Mol. Life Sci. *79*, 364. https://doi.org/10.1007/s00018-022-04395-y.
2. Kurnit, K.C., Fleming, G.F., and Lengyel, E. (2021). Updates and New Options in Advanced Epithelial Ovarian Cancer Treatment. Obstet. Gynecol. *137*, 108–121. https://doi.org/10.1097/AOG.0000000000004173.
3. Moschetta, M., Boussios, S., Rassy, E., Samartzis, E.P., Funingana, G., and Uccello, M. (2020). Neoadjuvant treatment for newly diagnosed advanced ovarian cancer: where do we stand and where are we going? Ann. Transl. Med. *8*, 1710. https://doi.org/10.21037/atm-20-1683.
4. Huang, M., Lu, J.J., and Ding, J. (2021). Natural Products in Cancer Therapy: Past, Present and Future. Nat. Prod. Bioprospect. *11*, 5–13. https://doi.org/10.1007/s13659-020-00293-7.
5. Barua, A., Choudhury, P., Nag, N., Nath, A., Kundagrami, S., Pal, A., Panda, C.K., and Saha, P. (2022). Xanthone from Swertia chirata exerts chemotherapeutic potential against colon carcinoma. Curr. Sci. *122*, 47–55.
6. Mehta, J., Rayalam, S., and Wang, X. (2018). Cytoprotective Effects of Natural Compounds against Oxidative Stress. Antioxidants *7*, 147. https://doi.org/10.3390/antiox7100147.
7. Sahayasheela, V.J., Lankadasari, M.B., Dan, V.M., Dastager, S.G., Pandian, G.N., and Sugiyama, H. (2022). Artificial intelligence in microbial natural product drug discovery: current and emerging role. Nat. Prod. Rep. *39*, 2215–2230. https://doi.org/10.1039/d2np00035k.
8. Li, P., Li, X., Saravanan, R., Li, C.M., and Leong, S.S.J. (2012). Antimicrobial macromolecules: synthesis methods and future applications. RSC Adv. *2*, 4031–4044.
9. Ab Mutalib, N.S., Wong, S.H., Ser, H.L., Duangjai, A., Law, J.W.F., Ratnakomala, S., Tan, L.T.H., and Letchumanan, V. (2020). Bioprospecting of microbes for valuable compounds to mankind. Prog. Micobes. Mol. Biol. *3*.
10. Carswell, E.A., Old, L.J., Kassel, R.L., Green, S., Fiore, N., and Williamson, B. (1975). An endotoxin-induced serum factor that causes necrosis of tumors. Proc. Natl. Acad. Sci. USA *72*, 3666–3670. https://doi.org/10.1073/pnas.72.9.3666.
11. Trivanović, D., Pavelić, K., and Peršurić, Ž. (2021). Fighting Cancer with Bacteria and Their Toxins. Int. J. Mol. Sci. *22*, 12980. https://doi.org/10.3390/ijms222312980.
12. Xu, Y., Kersten, R.D., Nam, S.J., Lu, L., Al-Suwailem, A.M., Zheng, H., Fenical, W., Dorrestein, P.C., Moore, B.S., and Qian, P.Y. (2012). Bacterial biosynthesis and maturation of the didemnin anti-cancer agents. J. Am. Chem. Soc. *134*, 8625–8632. https://doi.org/10.1021/ja301735a.
13. Punj, V., Bhattacharyya, S., Saint-Dic, D., Vasu, C., Cunningham, E.A., Graves, J., Yamada, T., Constantinou, A.I., Christov, K., White, B., et al. (2004). Bacterial cupredoxin azurin as an inducer of apoptosis and regression in human breast cancer. Oncogene *23*, 2367–2378. https://doi.org/10.1038/sj.onc.1207376.
14. Nadeem, A., Aung, K.M., Ray, T., Alam, A., Persson, K., Pal, A., Uhlin, B.E., and Wai, S.N. (2021). Suppression of β-catenin signaling in colon carcinoma cells by a bacterial protein. Int. J. Cancer *149*, 442–459. https://doi.org/10.1002/ijc.33562.
15. Toh, E., Baryalai, P., Nadeem, A., Aung, K.M., Chen, S., Persson, K., Persson, J.L., Uhlin, B.E., and Wai, S.N. (2022). Bacterial protein MakA causes suppression of tumour cell proliferation via inhibition of PIP5K1α/Akt signalling. Cell Death Dis. *13*, 1024. https://doi.org/10.1038/s41419-022-05480-7.
16. Taggart, C.C., Greene, C.M., Smith, S.G., Levine, R.L., McCray, P.B., Jr., O'Neill, S., and McElvaney, N.G. (2003). Inactivation of human beta-defensins 2 and 3 by elastolytic cathepsins. J. Immunol. *171*, 931–937. https://doi.org/10.4049/jimmunol.171.2.931.
17. Moncada, D., Keller, K., and Chadee, K. (2003). Entamoeba histolytica cysteine proteinases disrupt the polymeric structure of colonic mucin and alter its protective function. Infect. Immun. *71*, 838–844. https://doi.org/10.1128/IAI.71.2.838-844.2003.
18. Denecker, G., Declercq, W., Geuijen, C.A., Boland, A., Benabdillah, R., van Gurp, M., Sory, M.P., Vandenabeele, P., and Cornelis, G.R. (2001). Yersinia enterocolitica YopP-induced apoptosis of macrophages involves the apoptotic signaling cascade upstream of bid. J. Biol. Chem. *276*, 19706–19714. https://doi.org/10.1074/jbc.M101573200.
19. Maeda, H., Matsumura, Y., and Molla, A. (1987). Antitumor activity of some bacterial proteases: eradication of solid tumors in mice by intratumor injection. Cancer Res. *47*, 563–566.
20. Maeda, H., Molla, A., Sakamoto, K., Murakami, A., and Matsumura, Y. (1989). Cytotoxicity of bacterial proteases in various tumor cells mediated through alpha 2-macroglobulin receptor. Cancer Res. *49*, 660–664.
21. Singh, N., Tapader, R., Chatterjee, S., Pal, A., and Pal, A. (2022). Subtilisin from Bacillus amyloliquefaciens induces apoptosis in breast cancer cells through ubiquitin-proteasome-mediated tubulin degradation. Int. J. Biol. Macromol. *220*, 852–865. https://doi.org/10.1016/j.ijbiomac.2022.08.086.
22. Pieters, R., Hunger, S.P., Boos, J., Rizzari, C., Silverman, L., Baruchel, A., Goekbuget, N., Schrappe, M., and Pui, C.H. (2011). L-asparaginase treatment in acute lymphoblastic leukemia: a focus on Erwinia asparaginase. Cancer *117*, 238–249. https://doi.org/10.1002/cncr.25489.
23. Alrumman, S.A., Mostafa, Y.S., Al-Izran, K.A., Alfaifi, M.Y., Taha, T.H., and Elbehairi, S.E. (2019). Production and Anticancer Activity of an L-Asparaginase from Bacillus licheniformis Isolated from the Red Sea, Saudi Arabia. Sci. Rep. *9*, 3756. https://doi.org/10.1038/s41598-019-40512-x.
24. Pereira, F.V., Ferreira-Guimarães, C.A., Paschoalin, T., Scutti, J.A.B., Melo, F.M., Silva, L.S., Melo, A.C.L., Silva, P., Tiago, M., Matsuo, A.L., et al. (2014). A natural bacterial-derived product, the metalloprotease arazyme, inhibits metastatic murine melanoma by inducing MMP-8 cross-reactive antibodies. PLoS One *9*, e96141. https://doi.org/10.1371/journal.pone.0096141.
25. Hayes, J.D., Dinkova-Kostova, A.T., and Tew, K.D. (2020). Oxidative Stress in Cancer. Cancer Cell *38*, 167–197. https://doi.org/10.1016/j.ccell.2020.06.001.
26. Perillo, B., Di Donato, M., Pezone, A., Di Zazzo, E., Giovannelli, P., Galasso, G., Castoria, G., and Migliaccio, A. (2020). ROS in cancer therapy: the bright side of the moon. Exp. Mol. Med. *52*, 192–203. https://doi.org/10.1038/s12276-020-0384-2.
27. Ray, T., Chakrabarti, M.K., and Pal, A. (2016). Hemagglutinin protease secreted by V. cholerae induced apoptosis in breast cancer cells by ROS mediated intrinsic pathway and regresses tumor growth in mice model. Apoptosis *21*, 143–154. https://doi.org/10.1007/s10495-015-1194-1.
28. Soh, U.J.K., Dores, M.R., Chen, B., and Trejo, J. (2010). Signal transduction by protease-activated receptors. Br. J. Pharmacol. *160*, 191–203. https://doi.org/10.1111/j.1476-5381.2010.00705.x.
29. Flynn, A.N., and Buret, A.G. (2004). Proteinase-activated receptor 1 (PAR-1) and

cell apoptosis. Apoptosis *9*, 729–737. https://doi.org/10.1023/B:APPT.0000045784.49886.96.

30. Sébert, M., Sola-Tapias, N., Mas, E., Barreau, F., and Ferrand, A. (2019). Protease-Activated Receptors in the Intestine: Focus on Inflammation and Cancer. Front. Endocrinol. *10*, 717. https://doi.org/10.3389/fendo.2019.00717.
31. Liu, X., Yu, J., Song, S., Yue, X., and Li, Q. (2017). Protease-activated receptor-1 (PAR-1): a promising molecular target for cancer. Oncotarget *8*, 107334–107345. https://doi.org/10.18632/oncotarget.21015.
32. Turk, B., Turk, D., and Turk, V. (2012). Protease signalling: the cutting edge. EMBO J. *31*, 1630–1643. https://doi.org/10.1038/emboj.2012.42.
33. Zain, J., Huang, Y.Q., Feng, X., Nierodzik, M.L., Li, J.J., and Karpatkin, S. (2000). Concentration-dependent dual effect of thrombin on impaired growth/apoptosis or mitogenesis in tumor cells. Blood *95*, 3133–3138.
34. Grisaru-Granovsky, S., Salah, Z., Maoz, M., Pruss, D., Beller, U., and Bar-Shavit, R. (2005). Differential expression of protease activated receptor 1 (Par1) and pY397FAK in benign and malignant human ovarian tissue samples. Int. J. Cancer *113*, 372–378. https://doi.org/10.1002/ijc.20607.
35. Chin, A.C., Vergnolle, N., MacNaughton, W.K., Wallace, J.L., Hollenberg, M.D., and Buret, A.G. (2003). Proteinase-activated receptor 1 activation induces epithelial apoptosis and increases intestinal permeability. Proc. Natl. Acad. Sci. USA *100*, 11104–11109. https://doi.org/10.1073/pnas.1831452100.
36. Mußbach, F., Henklein, P., Westermann, M., Settmacher, U., Böhmer, F.D., and Kaufmann, R. (2015). Proteinase-activated receptor 1- and 4-promoted migration of Hep3B hepatocellular carcinoma cells depends on ROS formation and RTK transactivation. J. Cancer Res. Clin. Oncol. *141*, 813–825. https://doi.org/10.1007/s00432-014-1863-4.
37. Ray, T., and Pal, A. (2016). PAR-1 mediated apoptosis of breast cancer cells by V. cholerae hemagglutinin protease. Apoptosis *21*, 609–620. https://doi.org/10.1007/s10495-016-1229-2.
38. Sheng, Y.N., Luo, Y.H., Liu, S.B., Xu, W.T., Zhang, Y., Zhang, T., Xue, H., Zuo, W.B., Li, Y.N., Wang, C.Y., and Jin, C.H. (2020). Zeaxanthin Induces Apoptosis via ROS-Regulated MAPK and AKT Signaling Pathway in Human Gastric Cancer Cells. OncoTargets Ther. *13*, 10995–11006. https://doi.org/10.2147/OTT.S272514.
39. Sabirova, A.R., Rudakova, N.L., Balaban, N.P., Ilyinskaya, O.N., Demidyuk, I.V., Kostrov, S.V., Rudenskaya, G.N., and Sharipova, M.R. (2010). A novel secreted metzincin metalloproteinase from Bacillus intermedius. FEBS Lett. *584*, 4419–4425. https://doi.org/10.1016/j.febslet.2010.09.049.
40. Gomes, M.S.R., Naves de Souza, D.L., Guimarães, D.O., Lopes, D.S., Mamede, C.C.N., Gimenes, S.N.C., Achê, D.C., Rodrigues, R.S., Yoneyama, K.A.G., Borges, M.H., et al. (2015). Biochemical and functional characterization of Bothropoidin: the first haemorrhagic metalloproteinase from Bothrops pauloensis snake venom. J. Biochem. *157*, 137–149. https://doi.org/10.1093/jb/mvu058.
41. Scholzen, T., and Gerdes, J. (2000). The Ki-67 protein: from the known and the unknown. J. Cell. Physiol. *182*, 311–322. https://doi.org/10.1002/(SICI)1097-4652(200003)182:3<311::AID-JCP1>3.0.CO;2-9.
42. Deb, M., Sengupta, D., Kar, S., Rath, S.K., Parbin, S., Shilpi, A., Roy, S., Das, G., and Patra, S.K. (2014). Elucidation of caveolin 1 both as a tumor suppressor and metastasis promoter in light of epigenetic modulators. Tumour Biol. *35*, 12031–12047. https://doi.org/10.1007/s13277-014-2502-z.
43. Higuchi, M., Honda, T., Proske, R.J., and Yeh, E.T. (1998). Regulation of reactive oxygen species-induced apoptosis and necrosis by caspase 3-like proteases. Oncogene *17*, 2753–2760. https://doi.org/10.1038/sj.onc.1202211.
44. von Harsdorf, R., Li, P.F., and Dietz, R. (1999). Signaling pathways in reactive oxygen species-induced cardiomyocyte apoptosis. Circulation *99*, 2934–2941. https://doi.org/10.1161/01.cir.99.22.2934.
45. Susin, S.A., Zamzami, N., Castedo, M., Daugas, E., Wang, H.G., Geley, S., Fassy, F., Reed, J.C., and Kroemer, G. (1997). The central executioner of apoptosis: multiple connections between protease activation and mitochondria in Fas/APO-1/CD95- and ceramide-induced apoptosis. J. Exp. Med. *186*, 25–37. https://doi.org/10.1084/jem.186.1.25.
46. Bossy-Wetzel, E., Newmeyer, D.D., and Green, D.R. (1998). Mitochondrial cytochrome c release in apoptosis occurs upstream of DEVD-specific caspase activation and independently of mitochondrial transmembrane depolarization. EMBO J. *17*, 37–49. https://doi.org/10.1093/emboj/17.1.37.
47. Marin, V., Farnarier, C., Grès, S., Kaplanski, S., Su, M.S., Dinarello, C.A., and Kaplanski, G. (2001). The p38 mitogen-activated protein kinase pathway plays a critical role in thrombin-induced endothelial chemokine production and leukocyte recruitment. Blood *98*, 667–673. https://doi.org/10.1182/blood.v98.3.667.
48. Rahman, A., True, A.L., Anwar, K.N., Ye, R.D., Voyno-Yasenetskaya, T.A., and Malik, A.B. (2002). Galpha(q) and Gbetagamma regulate PAR-1 signaling of thrombin-induced NF-kappaB activation and ICAM-1 transcription in endothelial cells. Circ. Res. *91*, 398–405. https://doi.org/10.1161/01.res.0000033520.95242.a2.
49. Tapader, R., Bose, D., Dutta, P., Das, S., and Pal, A. (2018). SslE (YghJ), a Cell-Associated and Secreted Lipoprotein of Neonatal Septicemic Escherichia coli, Induces Toll-Like Receptor 2-Dependent Macrophage Activation and Proinflammation through NF-κB and MAP Kinase Signaling. Infect. Immun. *86*, e00399-18. https://doi.org/10.1128/IAI.00399-18.
50. Shivaji, S., Chaturvedi, P., Suresh, K., Reddy, G.S.N., Dutt, C.B.S., Wainwright, M., Narlikar, J.V., and Bhargava, P.M. (2006). Bacillus aerius sp. nov., Bacillus aerophilus sp. nov., Bacillus stratosphericus sp. nov. and Bacillus altitudinis sp. nov., isolated from cryogenic tubes used for collecting air samples from high altitudes. Int. J. Syst. Evol. Microbiol. *56*, 1465–1473. https://doi.org/10.1099/ijs.0.64029-0.
51. Rao, M.B., Tanksale, A.M., Ghatge, M.S., and Deshpande, V.V. (1998). Molecular and biotechnological aspects of microbial proteases. Microbiol. Mol. Biol. Rev. *62*, 597–635. https://doi.org/10.1128/MMBR.62.3.597-635.1998.
52. Nguyen, T.T.H., Myrold, D.D., and Mueller, R.S. (2019). Distributions of Extracellular Peptidases Across Prokaryotic Genomes Reflect Phylogeny and Habitat. Front. Microbiol. *10*, 413. https://doi.org/10.3389/fmicb.2019.00413.
53. Asharaf, S., and Chakraborty, K. (2022). Seaweed-associated heterotrophic Bacillus altitudinis MTCC13046: a promising marine bacterium for use against human hepatocellular adenocarcinoma. Arch. Microbiol. *205*, 10. https://doi.org/10.1007/s00203-022-03346-2.
54. Zheng, L., Zhu, X., Yang, K., Zhu, M., Farooqi, A.A., Kang, D., Sun, M., Xu, Y., Lin, X., Feng, Y., et al. (2021). PBN11-8, a Cytotoxic Polypeptide Purified from Marine Bacillus, Suppresses Invasion and Migration of Human Hepatocellular Carcinoma Cells by Targeting Focal Adhesion Kinase Pathways. Polymers *13*, 166. https://doi.org/10.3390/polym13010166.
55. Yang, J., Liu, X., Bhalla, K., Kim, C.N., Ibrado, A.M., Cai, J., Peng, T.I., Jones, D.P., and Wang, X. (1997). Prevention of apoptosis by Bcl-2: release of cytochrome c from mitochondria blocked. Science *275*, 1129–1132. https://doi.org/10.1126/science.275.5303.1129.
56. Srinivas, U.S., Tan, B.W.Q., Vellayappan, B.A., and Jeyasekharan, A.D. (2019). ROS and the DNA damage response in cancer. Redox Biol. *25*, 101084. https://doi.org/10.1016/j.redox.2018.101084.
57. Goldstein, J.C., Waterhouse, N.J., Juin, P., Evan, G.I., and Green, D.R. (2000). The coordinate release of cytochrome c during apoptosis is rapid, complete and kinetically invariant. Nat. Cell Biol. *2*, 156–162. https://doi.org/10.1038/35004029.
58. Rath, S.K., Deb, M., Sengupta, D., Kari, V., Kar, S., Parbin, S., Pradhan, N., and Patra, S.K. (2016). Silencing of ZRF1 impedes survival of estrogen receptor positive MCF-7 cells and potentiates the effect of curcumin. Tumour Biol. *37*, 12535–12546. https://doi.org/10.1007/s13277-016-5114-y.
59. Kim, G., Ison, G., McKee, A.E., Zhang, H., Tang, S., Gwise, T., Sridhara, R., Lee, E., Tzou, A., Philip, R., et al. (2015). FDA Approval Summary: Olaparib Monotherapy in Patients with Deleterious Germline BRCA-Mutated Advanced Ovarian Cancer Treated with Three or More Lines of Chemotherapy. Clin. Cancer Res. *21*, 4257–4261. https://doi.org/10.1158/1078-0432.CCR-15-0887.
60. Lourbakos, A., Chinni, C., Thompson, P., Potempa, J., Travis, J., Mackie, E.J., and Pike, R.N. (1998). Cleavage and activation of proteinase-activated receptor-2 on human neutrophils by gingipain-R from Porphyromonas gingivalis. FEBS Lett. *435*, 45–48. https://doi.org/10.1016/s0014-5793(98)01036-9.
61. Agarwal, A., Covic, L., Sevigny, L.M., Kaneider, N.C., Lazarides, K., Azabdaftari, G., Sharifi, S., and Kuliopulos, A. (2008). Targeting a metalloprotease-PAR1 signaling system with cell-penetrating pepducins inhibits angiogenesis, ascites, and progression of ovarian cancer. Mol. Cancer Ther. *7*, 2746–2757. https://doi.org/10.1158/1535-7163.MCT-08-0177.
62. Boire, A., Covic, L., Agarwal, A., Jacques, S., Sherifi, S., and Kuliopulos, A. (2005). PAR1 is a matrix metalloprotease-1 receptor that promotes invasion and tumorigenesis of breast cancer cells. Cell *120*, 303–313. https://doi.org/10.1016/j.cell.2004.12.018.

63. Patra, S.K. (2008). Dissecting lipid raft facilitated cell signaling pathways in cancer. Biochim. Biophys. Acta *1785*, 182–206. https://doi.org/10.1016/j.bbcan.2007.11.002.
64. Gandhi, D.M., Rosas, R., Jr., Greve, E., Kentala, K., D-R Diby, N., Snyder, V.A., Stephans, A., Yeung, T.H.W., Subramaniam, S., DiMilo, E., et al. (2019). The parmodulin NRD-21 is an allosteric inhibitor of PAR1 Gq signaling with improved anti-inflammatory activity and stability. Bioorg. Med. Chem. *27*, 3788–3796. https://doi.org/10.1016/j.bmc.2019.06.043.
65. Yang, C., Luo, J., Luo, X., Jia, W., Fang, Z., Yi, S., and Li, L. (2020). Morusin exerts anti-cancer activity in renal cell carcinoma by disturbing MAPK signaling pathways. Ann. Transl. Med. *8*, 327. https://doi.org/10.21037/atm.2020.02.107.
66. Oeckinghaus, A., and Ghosh, S. (2009). The NF-kappaB family of transcription factors and its regulation. Cold Spring Harb. Perspect. Biol. *1*, a000034. https://doi.org/10.1101/cshperspect.a000034.
67. Lingappan, K. (2018). NF-κB in Oxidative Stress. Curr. Opin. Toxicol. *7*, 81–86. https://doi.org/10.1016/j.cotox.2017.11.002.
68. Nakajima, S., and Kitamura, M. (2013). Bidirectional regulation of NF-κB by reactive oxygen species: a role of unfolded protein response. Free Radic. Biol. Med. *65*, 162–174. https://doi.org/10.1016/j.freeradbiomed.2013.06.020.
69. Kulisz, A., Chen, N., Chandel, N.S., Shao, Z., and Schumacker, P.T. (2002). Mitochondrial ROS initiate phosphorylation of p38 MAP kinase during hypoxia in cardiomyocytes. Am. J. Physiol. Lung Cell Mol. Physiol. *282*, L1324–L1329. https://doi.org/10.1152/ajplung.00326.2001.
70. Berra, E., Diaz-Meco, M.T., and Moscat, J. (1998). The activation of p38 and apoptosis by the inhibition of Erk is antagonized by the phosphoinositide 3-kinase/Akt pathway. J. Biol. Chem. *273*, 10792–10797. https://doi.org/10.1074/jbc.273.17.10792.
71. Roby, K.F., Taylor, C.C., Sweetwood, J.P., Cheng, Y., Pace, J.L., Tawfik, O., Persons, D.L., Smith, P.G., and Terranova, P.F. (2000). Development of a syngeneic mouse model for events related to ovarian cancer. Carcinogenesis *21*, 585–591. https://doi.org/10.1093/carcin/21.4.585.
72. Janát-Amsbury, M.M., Yockman, J.W., Anderson, M.L., Kieback, D.G., and Kim, S.W. (2006). Comparison of ID8 MOSE and VEGF-modified ID8 cell lines in an immunocompetent animal model for human ovarian cancer. Anticancer Res. *26*, 2785–2789.
73. Kruk, P.A., Maines-Bandiera, S.L., and Auersperg, N. (1990). A simplified method to culture human ovarian surface epithelium. Lab. Invest. *63*, 132–136.
74. Ghosh, D., Pakhira, S., Ghosh, D.D., Roychoudhury, S., and Roy, S.S. (2023). Ets1 facilitates EMT/invasion through Drp1-mediated mitochondrial fragmentation in ovarian cancer. iScience *26*, 107537. https://doi.org/10.1016/j.isci.2023.107537.
75. Syngkon, A., Elluri, S., Koley, H., Rompikuntal, P.K., Saha, D.R., Chakrabarti, M.K., Bhadra, R.K., Wai, S.N., and Pal, A. (2010). Studies on a novel serine protease of a ΔhapAΔprtV Vibrio cholerae O1 strain and its role in hemorrhagic response in the rabbit ileal loop model. PLoS One *5*, e13122. https://doi.org/10.1371/journal.pone.0013122.
76. Tapader, R., Bose, D., Basu, P., Mondal, M., Mondal, A., Chatterjee, N.S., Dutta, P., Basu, S., Bhadra, R.K., and Pal, A. (2016). Role in proinflammatory response of YghJ, a secreted metalloprotease from neonatal septicemic Escherichia coli. Int. J. Med. Microbiol. *306*, 554–565. https://doi.org/10.1016/j.ijmm.2016.06.003.
77. Mondal, A., Tapader, R., Chatterjee, N.S., Ghosh, A., Sinha, R., Koley, H., Saha, D.R., Chakrabarti, M.K., Wai, S.N., and Pal, A. (2016). Cytotoxic and Inflammatory Responses Induced by Outer Membrane Vesicle-Associated Biologically Active Proteases from Vibrio cholerae. Infect. Immun. *84*, 1478–1490. https://doi.org/10.1128/IAI.01365-15.
78. Kar, S., Sengupta, D., Deb, M., Shilpi, A., Parbin, S., Rath, S.K., Pradhan, N., Rakshit, M., and Patra, S.K. (2014). Expression profiling of DNA methylation-mediated epigenetic gene-silencing factors in breast cancer. Clin. Epigenet. *6*, 20. https://doi.org/10.1186/1868-7083-6-20.
79. Chakraborty, M., and Bhaumik, M. (2020). Prenatal arsenic exposure interferes in postnatal immunocompetence despite an absence of ongoing arsenic exposure. J. Immunotoxicol. *17*, 135–143. https://doi.org/10.1080/1547691X.2020.1767238.
80. Naskar, D., Maiti, G., Chakraborty, A., Roy, A., Chattopadhyay, D., and Sen, M. (2014). Wnt5a-Rac1-NF-κB homeostatic circuitry sustains innate immune functions in macrophages. J. Immunol. *192*, 4386–4397. https://doi.org/10.4049/jimmunol.1302817.
81. Prasad, P., Ghosh, S., and Roy, S.S. (2021). Glutamine deficiency promotes stemness and chemoresistance in tumor cells through DRP1-induced mitochondrial fragmentation. Cell. Mol. Life Sci. *78*, 4821–4845. https://doi.org/10.1007/s00018-021-03818-6.
82. Singh, N.P., McCoy, M.T., Tice, R.R., and Schneider, E.L. (1988). A simple technique for quantitation of low levels of DNA damage in individual cells. Exp. Cell Res. *175*, 184–191. https://doi.org/10.1016/0014-4827(88)90265-0.
83. Das, R., Kamal, I.M., Das, S., Chakrabarti, S., and Chakrabarti, O. (2022). MITOL-mediated DRP1 ubiquitylation and degradation promotes mitochondrial hyperfusion in a CMT2A-linked MFN2 mutant. J. Cell Sci. *135*, jcs257808. https://doi.org/10.1242/jcs.257808.
84. Dimauro, I., Pearson, T., Caporossi, D., and Jackson, M.J. (2012). A simple protocol for the subcellular fractionation of skeletal muscle cells and tissue. BMC Res. Notes *5*, 513. https://doi.org/10.1186/1756-0500-5-513.
85. Li, J., Cui, J., Li, Z., Fu, X., Li, J., Li, H., Wang, S., and Zhang, M. (2020). ORP8 induces apoptosis by releasing cytochrome c from mitochondria in non-small cell lung cancer. Oncol. Rep. *43*, 1516–1524. https://doi.org/10.3892/or.2020.7517.
86. Sun, L., Xie, P., Wada, J., Kashihara, N., Liu, F.Y., Zhao, Y., Kumar, D., Chugh, S.S., Danesh, F.R., and Kanwar, Y.S. (2008). Rap1b GTPase ameliorates glucose-induced mitochondrial dysfunction. J. Am. Soc. Nephrol. *19*, 2293–2301. https://doi.org/10.1681/ASN.2008030336.
87. Barua, A., Choudhury, P., Maity, J.K., Mandal, S.B., Mandal, S., and Saha, P. (2019). Chemotherapeutic potential of novel non-toxic nucleoside analogues on EAC ascitic tumour cells. Free Radic. Res. *53*, 57–67. https://doi.org/10.1080/10715762.2018.1551999.
88. Dasgupta, S., Kar, K., Barua, A., Ghosh, D., Kabi, B., Dewan, K., and Chandra, A. (2022). A significantly non-toxic novel Cobalt(III) Schiff base complex induces apoptosis via G2-M cell cycle arrest in human breast cancer cell line MCF-7. Life Sci. *308*, 120963. https://doi.org/10.1016/j.lfs.2022.120963.
89. Barua, A., Choudhury, P., Mandal, S., Panda, C.K., and Saha, P. (2020). Therapeutic potential of xanthones from Swertia chirata in breast cancer cells. Indian J. Med. Res. *152*, 285–295. https://doi.org/10.4103/ijmr.IJMR_1153_18.

STAR★METHODS

KEY RESOURCES TABLE

REAGENT or RESOURCE	SOURCE	IDENTIFIER
Antibodies		
Anti-cleaved PARP antibody	Cell Signaling Technology	Cat# 5625; RRID:AB_10699459
Anti Bax antibody	Cell Signaling Technology	Cat# 5023; RRID:AB_10557411
Anti Bcl-2 antibody	Cell Signaling Technology	Cat# 15071; RRID:AB_2744528
Anti-caspase 8 antibody	Cell Signaling Technology	Cat# 9746; RRID:AB_2275120
Anti-Cytochrome c antibody	Cell Signaling Technology	Cat# 11940; RRID:AB_2637071
Anti-Histone H3 antibody	Cell Signaling Technology	Cat# 14269; RRID:AB_2756816
Anti-α-Tubulin antibody	Cell Signaling Technology	Cat# 3873; RRID:AB_1904178
Anti GAPDH antibody	Cell Signaling Technology	Cat# 97166; RRID:AB_2756824
Anti-Ki-67 antibody	Cell Signaling Technology	Cat# 9449; RRID:AB_2797703
Anti-cleaved caspase 9 antibody	Cell Signaling Technology	Cat# 7237; RRID:AB_10895832
Anti-p65 antibody	Cell Signaling Technology	Cat# 4764; RRID:AB_823578
Anti-p38 antibody	Cell Signaling Technology	Cat# 8690; RRID:AB_10999090
Anti-PAR-1 antibody	Millipore, Merck	Cat# MABF244; RRID: AB_2935797
Anti-ERK1/2 antibody	Santa Cruz Biotechnology	Cat# sc-514302; RRID: AB_2571739
Anti-phospho-ERK1/2	Santa Cruz Biotechnology	Cat# sc-136521; RRID: AB_10856869
Anti-phospho-p38 antibody	Santa Cruz Biotechnology	Cat# sc-166182; RRID: AB_2141746
Anti-p50 antibody	Santa Cruz Biotechnology	Cat# sc-8414; RRID: AB_628015
Anti-cleaved caspase 3 antibody	Abcam	Cat# ab13847; RRID: AB_443014
Anti-mouse IgG, HRP-linked Antibody	Cell Signaling Technology	Cat# 7076; RRID:AB_330924
Anti-rabbit IgG, HRP-linked Antibody	Cell Signaling Technology	Cat# 7074; RRID:AB_2099233
Anti-mouse IgG, AP-linked Antibody	Cell Signaling Technology	Cat# 7056; RRID:AB_330921
Anti-rabbit IgG, AP-linked Antibody	Cell Signaling Technology	Cat# 7054; RRID:AB_2099235
Anti-mouse IgG (H+L), F(ab')2 Fragment (Alexa Fluor® 488 Conjugate)	Cell Signaling Technology	Cat# 4408; RRID: AB_10694704
Anti-rabbit IgG (H+L), F(ab')2 Fragment (Alexa Fluor® 488 Conjugate)	Cell Signaling Technology	Cat# 4412; RRID: AB_1904025
Anti-rabbit IgG (H+L), F(ab')2 Fragment (Alexa Fluor® 555 Conjugate)	Cell Signaling Technology	Cat# 4413; RRID: AB_10694110
Anti-mouse IgG (H+L), F(ab')2 Fragment (Alexa Fluor® 555 Conjugate)	Cell Signaling Technology	Cat# 4409; RRID: AB_1904022
Veri Blot	Abcam	Cat# ab131366
Bacterial and virus strains		
Environmental bacterial isolates	salt farm of CSIR-CSMCRI, Bhavnagar (21° 47'50'' N, 72° 07'16'' E), Gujrat, India.	N/A
Chemicals		
JC-1 staining powder	Invitrogen™	Cat# T3168
2',7'-Dichlorodihydrofluorescein diacetate	Sigma	Cat# D6883
Mito tracker green FM	Invitrogen™	Cat# M7514
ML-161	Sigma	Cat# SML0418
SB203580	Sigma	Cat# 559389
MG132	Sigma	Cat# M7449

(*Continued on next page*)

Continued

REAGENT or RESOURCE	SOURCE	IDENTIFIER
DAPI	Sigma	Cat# D9542
Hoechst 33342	Invitrogen™	Cat# H21492
Lipofectamine™ 3000 transfection reagent	Invitrogen™	Cat# L3000001
Protein A agarose beads	Cell Signaling Technology	Cat# 9863S
Protein G agarose beads	Cell Signaling Technology	CST# 37478S
DEAE-52 matrix	Whatman	Cat# 4057050
Sephadex G-75 matrix	MP biomedical	Cat# 195589
DNA ladder	Invitrogen™	Cat# 15628050
Protein ladder	Abcam	Cat# ab116028
Protein ladder	G-bioscience	Cat# 786419
ECL substrate	Thermo scientific	Cat# 34580
BCIP/NBT substrate	Bio-rad	Cat# 1706432
Azocasein	Sigma	Cat# A2765
Ammonium sulphate	Sigma	Cat# A4915
Freund's complete adjuvant	Sigma	Cat# F5881
Freund's incomplete adjuvant	Sigma	Cat# F5506
GoTaq green master mix	Promega	Cat# M7122
SYBR green reagent	Eurogentec	Cat# UFRSMTBC101
MTT	Sigma	Cat# M5655
BCA assay kit	Thermo Scientific™	Cat# 23225
Annexin V and PI staining kit	BD	Cat# 556547
RNA isolation kit	Zymo research	Cat# R1057
Revertaid first strand cDNA synthesis kit	Thermo scientific	Cat# K1622
NE-PER™ Nuclear and Cytoplasmic Extraction kit	Thermo Scientific™	Cat#78833
Deposited data		
16s rRNA sequence of *Bacillus altitudinis* isolate GDL-186	This Paper	GenBank: OP738003.1
Whole genome sequence of *Bacillus altitudinis* isolate GDL-186	This Paper	GenBank : JAZHFY000000000.
Experimental models: Cell lines		
Human: PA-1	Gift from Dr. S.S.Roy, CSIR-IICB, Kolkata, India	ATCC, Cat# CRL-1572; RRID:CVCL_0479
Human: SKOV3	Gift from Dr. S.S.Roy, CSIR-IICB, Kolkata, India	ATCC, Cat# HTB-77; RRID:CVCL_0532
Human: IOSE 364	Gift from Dr. S.S.Roy, CSIR-IICB, Kolkata, India	RRID: CVCL_5540
Murine: ID8	Gift from Dr. S.S.Roy, CSIR-IICB, Kolkata, India	(MERCK Cat# SCC145; RRID: CVCL_IU14
Mouse peritoneal macrophage	Isolated in our lab	N/A
Experimental models: organisms/strains		
	India.	
C57BL/6 Female Mice	ICMR-NICED	N/A
New Zealand White Rabbit	ICMR-NICED	N/A
Oligonucleotides		
PAR-1 si-RNA	Eurogentec	N/A
Scrambled (SCR) siRNA	Santa Cruz Biotechnology	Cat#sc-37007
Primers for human PAR-1, PAR-2, PAR-3, PAR-4, GAPDH, Bacterial Peptidase M84, DNA gyrase B (Table S1)	Integrated DNA Technologies	N/A

(*Continued on next page*)

Continued

REAGENT or RESOURCE	SOURCE	IDENTIFIER
Software and algorithms		
ImageJ software	ImageJ	RRID: SCR_003070
BD FACS Aria II using 'Cell Quest' software	BD	RRID: SCR_014489
GelQuant	Thermo Fisher Scientific	N/A
Fiji	Image J	RRID: SCR_002285
Microsoft Office Excel 2021	Microsoft Windows	N/A
Adobe photoshop CS2	Adobe	N/A

RESOURCE AVAILABILITY

Lead contact

Information and requests for resources should be directed to and will be fulfilled by the lead contact, Dr. Amit Pal (pala.niced@gov.in/ palamit.app@gmail.com).

Materials availability

This study did not generate any new unique reagents.

Data and code availability

- Data: The data presented in this study are available in the article and supplemental information.
- Code: NCBI GenBank accession number of *Bacillus altitudinis* strain GDL-186 https://www.ncbi.nlm.nih.gov/nuccore/OP738003.1. The whole genome shotgun project of *Bacillus altitudinis* GDL 186 has been deposited at DDBJ/ENA/GenBank under the accession JAZHFY000000000. The version described in this paper is version JAZHFY010000000.
- Any additional information required to re-analyse the data reported in this paper is available from the lead contact upon request.
- The data presented in this study are available in the article and supplemental information. Any additional information required to re-analyse the data reported in this paper is available from the lead contact upon request.

EXPERIMENTAL MODEL AND STUDY PARTICIPANT DETAILS

Ethical approval for animal studies

All animal experiments were approved by the institutional animal ethics committee (IAEC), for animal care of National Institute of Cholera and Enteric Diseases (NICED), supplied with food pellets and autoclaved water *ad libitum*. The experimental design of the present study was approved by the Institutional Animal Ethics Committee (License No: PRO/168/Jan 2022), NICED, Kolkata, India.

Bacterial isolates and its growth conditions

A total of 200 bacterial isolates were isolated from salt farm of CSIR-CSMCRI, Bhavnagar (21° 47'50'' N, 72° 07'16'' E), Gujrat, India. All the isolates were stored in 25% glycerol at -80° C. Bacterial isolates were revived in nutrient broth (BD, USA; Cat# 234000) of pH 8.0 containing 2% NaCl (BD, USA; Cat# 234000). Initially, isolates were grown in 5.0 ml NB (primary culture) at 37° C in a shaker incubator till the OD_{600} reached 0.6. Secondary cultures were given in 1000 ml NB at a ratio of 1:100 and grown at 37° C in a shaker incubator for 18 h. The culture supernatant of the bacterial isolates was used for screening of protease.

Cell culture and treatments

Human ovarian cancer cells PA-1 (ATCC; Manassas, Virginia, United State; Cat# CRL-1572; RRID: CVCL_0479) and SKOV3 (ATCC; Manassas, Virginia, United State; Cat# HTB-77; RRID:CVCL_0532) were cultured (10-12 passage) and maintained in alpha-minimum essential medium (MEM-α) (Sigma; Cat# M0644) and RPMI-1640 (Gibco; Cat# 23400021) respectively with 10% FBS (Gibco; Cat# 10270106), 100 U/ml penicillin G and 100 μg/ml Streptomycin sulphate solution (Gibco, Cat # 15140122) at 37°C in presence of 5% CO_2 incubator. Human immortalised ovarian surface epithelial cells, IOSE (IOSE-364 from N. Auersperg and C. Salamanca, Vancouver, Canada, RRID: CVCL_5540) was maintained in MCDB-105 (Sigma Aldrich; Cat# M6395) and Medium-199 (Gibco; Cat# 31100035) in 1: 1 ratio and supplemented as stated earlier. Here, the low-passage cultures of human ovarian surface epithelium cells (isolated by scraping from human ovarian surface tissue) were immortalised by transfecting with SV40 large-T antigen viral particles.[73,74] Mouse ovarian carcinoma ID8 (MERCK Cat# SCC145; RRID: CVCL_IU14) cell line was cultured in DMEM high glucose medium (Gibco; Cat# 31600034) supplemented with 10% FBS, 100 U/ml penicillin G and 100 μg/ml Streptomycin sulphate and 1% AOF-ITS supplement (Merck; Cat# SCM 054) at 37°C in presence of 5% CO_2 incubator. All cell lines were supplied by

Dr. Sib Sankar Roy (CSIR-IICB, Kolkata) as a gift. Cell lines were tested for mycoplasma contamination and validated by short tandem repeat (STR) polymorphism analysis performed by the Life code genomic technologies.

Mice for animal model experiments

The mice that were used in this study were healthy adult female C57BL/6 mice of approximately 22–25 g of weight (6-8 weeks old), bred and maintained in an animal colony as per the principles and guidelines of the ethical committee for animal care of National Institute of Cholera and Enteric Diseases (NICED).

Rabbit for animal model experiments

Antiserum against Peptidase M84 was raised by immunizing an adult male New Zealand White rabbit (bred and maintained in an animal colony as per the principles and guidelines of the ethical committee for animal care of NICED.

METHOD DETAILS

Azocasein assay

Azocasein assay was performed to determine the protease activity of the bacterial isolates as described earlier (Syngkon et al., 2010).[75] Briefly, the overnight grown culture supernatants were mixed with 0.7% azocasein (prepared in 100 mM Tris-HCl; pH 8.0) (Sigma, Cat# A2765) followed by incubation at 37° C for 1 h. The reaction was stopped using 10% Tri Chloro Acetic Acid (Sigma; Cat# T6399) and kept at 4° C for 30 min. Precipitate was removed by centrifugation (12,000 rpm for 10 min). NaOH (500 mM) was added to the supernatant and absorbance was measured at 440 nm. Nutrient broth and purified haemagglutinin protease (HAP) from *Vibrio cholerae* C6709 were used as negative and positive controls respectively.

Purification and identification of protease

Peptidase M84 was purified from the culture supernatant of 'GDL-186'. Bacterial strain was grown in 1000 ml NB (containing 2% NaCl, pH 8.0) for 19 h at 37° C in a shaker incubator. After centrifugation at 12,000 rpm for 10 min at 4° C, the culture supernatant was salted out with 80% saturated ammonium sulphate (Sigma; Cat# A4915) and kept overnight (O/N) at 4° C. Protein pellet was collected by centrifugation at 14000 rpm at 4°C and the pellet was dissolved in 25 mM Tris-Cl buffer, pH 8.0. The protein solution was dialysed against the same buffer for 48 h at 4° C using dialysis membrane (Himedia; Cat# LA395-30MT). Dialysed protein solution was concentrated using speed-vac vacuum centrifugation and run on DEAE-52 ion-exchange column (2.5 X 20 cm) pre-equilibrated with 25 mM Tris-Cl buffer, pH 8.0. Flow through or non-binding fraction was collected, concentrated and checked for protease activity. Binding fractions were collected using increasing concentration of NaCl (0.1 M - 0.5 M) solution. The eluted fractions were pooled, dialysed, concentrated and examined for protease activity. Non-binding fraction showing protease activity, was further pooled, concentrated and loaded into Sephadex G-75 gel filtration column (1.5 X 30 cm) with 25 mM Tris-HCl buffer of pH 8.0. Fractions positive for protease activity were eluted, concentrated and analysed by SDS and Native-PAGE. The single band from Native-PAGE and two bands from SDS-PAGE were cut out from the gel and sent to C-CAMP, NCBS, Bangalore, India for identification by nano-LC-MS/MS-TOF. Peptide sequence generated from MS/MS spectra was searched in NCBI and Uniprot databases for homology alignment.

Determination of physico-chemical characteristics of the purified protease

Inhibition of the protease activity with different inhibitors was performed in order to determine the type of the purified protease and the culture supernatant of isolate GDL-186. PMSF (10 mM) (Sigma; Cat# P7626), EDTA (10 mM) (Sigma; Cat# E9884) and 1,10 phenanthroline (10 mM) (Sigma, Cat# 131377) were used in the inhibition study as described in our previous study (Tapader et al., 2016).[76] 100 mM stocks of PMSF and 1,10 phenanthroline were prepared in isopropanol and methanol respectively and 500 mM stock of EDTA was prepared in water. 5.0 μg of purified protease was pre-incubated at 37° C for 1 h with each inhibitor. The residual protease activity was measured by azocasein assay.

The optimum pH for protease activity was determined using buffers of different pH ranging from 4.0–11.0. 5.0 μg of purified protease was dialysed overnight against 25 mM acetate buffer (pH 4.0–5.0), 25 mM phosphate buffer (pH 6.0–7.0), 25 mM Tris-HCl (pH 8.0–9.0), 25 mM glycine-NaOH buffer (pH 10.0–11.0) and activity were determined with azocasein assay.

To determine the optimum temperature for activity, 5.0 μg of the purified protease was incubated over a wide range of temperatures: 4° C, 25° C, 37° C, 50° C, 60° C and 70° C for 1 h and the enzyme activity was determined by azocasein assay as already described.

Gelatine zymography was performed to determine the substrate specificity of the purified protease as per the protocol described earlier (Tapader et al., 2016).[41] For native zymography, samples were electrophoresed under non-reducing conditions without boiling using 7.5% Native-PAGE co-polymerised with 0.1% gelatin (Sigma; Cat# G2500). The gel was incubated after electrophoresis in renaturation buffer (2.5% Triton-X-100) for 1 h at room temperature (RT) with gentle shaking. The gel was then developed in development buffer containing 5 mM $CaCl_2$, 25 mM Tris-HCl (pH 8.0) for O/N at 37°C with gentle shaking. The gel was visualised after staining using Coomassie Brilliant Blue G-250 (Himedia; Cat# ML046) and subsequent destaining.

The effect of zinc ion (Zn^{2+}) or zinc dependency of the protease was also examined. The enzyme (5 μg) was preincubated with different concentrations of $ZnCl_2$ ranging from 0.5 mM to 15 mM at 37° C for 1 h. The azocaseinolytic activity was evaluated as described above.

16s-rRNA and whole genome sequencing

The protease positive bacterial isolate which showed significant apoptotic activity was identified by 16s rRNA sequencing. First, genomic DNA was isolated from O/N grown bacterial culture and run on 1.0% Agarose gel.16S rRNA gene was amplified by 27F 5′-AGAGTTT-GATCCTGGCTCAG-3′ and 1492R 5′-GGTTACCTTGTTACGACTT-3′ primers. The PCR reaction was as follows: 95° C for 10 min; 35 cycles of 95° C for 30 s, 55° C for 1 min, and 72° C for 1.5 min; and final extension at 72° C for 10 min. The PCR amplicon was purified to remove contaminants. Forward and reverse DNA sequencing reaction of PCR amplicon was carried out with forward primer and reverse primers using BDT v3.1 Cycle sequencing kit on ABI 3730xl Genetic Analyzer. The consensus sequence of 16S rRNA gene was generated from forward and reverse sequence data using aligner software. The 16S rRNA gene sequence was used to carry out BLAST with database of NCBI GenBank. Based on maximum identity score first ten sequences were selected and aligned using multiple alignment software program Clustal W. Distance matrix was generated and the phylogenetic tree was constructed using MEGA 7. The evolutionary history was inferred by using the Maximum Likelihood method based on the Kimura 2- parameter model. In addition to this, The DNA gyrase B gene sequence was used to carry out BLAST with database of NCBI GenBank. Based on maximum identity score first ten sequences were selected and aligned using multiple alignment software program Clustal W and NCBI. The evolutionary history was inferred by using the Neighbour joining method based on the Kimura 2- parameter model. Final confirmation of the isolate was validated by whole genome-based shotgun sequencing. Paired-end raw sequence reads were assessed for base quality and contamination by sequencing artefacts. Trimming of adapters and poor-quality sequences was performed for paired sequence reads with Trim Galore. Trimmed sequence reads were assembled into scaffolds with SPAdes. Taxonomic classification with Bracken and BLAST was used to identify closest genomic reference sequences. Sequences from draft genome assembly were mapped and ordered with RagTag. Annotation of assembled and ordered draft genome sequences was performed with Prokka. Genomic map plots were generated with Cgview from .gbk annotation file generatedby Prokka. Kraken2 and Bracken are used to align the filtered reads to prebuilt standard reference (archaea, bacteria, viral, plasmid, human, UniVec_Core).

Identification of the isolate based on biochemical, microbiological and physiological characteristics

Phenotypic characteristics of the isolate, including motility, cell morphology, Gram staining, catalase, and oxidase production, among others, were investigated according to standard protocols. The fermentation of substrate belonging to carbohydrates and derivatives was determined as per standard protocols.

Raising of antisera against purified Peptidase M84

Antiserum against Peptidase M84 was raised by immunizing a New Zealand White rabbit as described previously by Mondal et al., 2016.[77] Intramuscular injection was given with 100 μg of purified Peptidase M84 emulsified with an equal volume of Freund's complete adjuvant (Sigma, USA; Cat# F5881). This was followed by four booster injections with 100.0 μg of Peptidase M84 and incomplete adjuvant (Sigma, USA; Cat# F5506) at 7-day intervals. Blood samples were collected from rabbits on day 0 and 3rd day after the final injection and were allowed to clot O/N at RT. Sera were collected and centrifuged (1,000 rpm, 5 min), diluted in autoclaved glycerol (Sigma, USA) and stored at -80°C until use at a dilution of 1:800 unless otherwise mentioned.

PCR amplification to detect the gene encodes Peptidase M84 from *Bacillus altitudinis*

Genomic DNA was isolated from 1 ml of O/N bacterial culture using Promega Wizard genomic DNA purification kit (Cat# A1120) according to the manufacturer's protocol. 20 ng of genomic DNA was subjected to PCR amplification using GoTaq green master mix (Promega; Cat# M7122) in an automated thermal cycler (Bio-Rad, USA) to detect the presence of gene codes for Peptidase M84 using specific primers (mentioned in Table S1) under the following conditions: 10 min initial denaturation at 95°C followed by 35 cycles of 1 min denaturation at 95°C, 30 s, annealing at 55°C, followed by 1 min extension at 72°C and final 10 min extension at 72°C.

Cell viability and cell proliferation assay

The effect of Peptidase M84 on cellular viability and to determine the sub-lethal concentration of peptidase M84, MTT assay was done as per standard protocol (Kar et al., 2014).[78] About 1X10^5 live cells/well were seeded in a 96-well plate for viability assay. Trypan blue was used to determine cell viability. After 24 h of incubation, PA-1, SKOV3 and ID8 cells were treated with different concentrations of Peptidase M84 to determine the minimal inhibitory concentration (IC_{50}) value. After 24 h of protease treatment at different concentrations of 0.5 μg/ml – 5.0 μg/ml, MTT solution (0.8 mg/ml dissolved in serum free medium) was added to the cells and further incubated for 4 h in the dark at 37°C. The media containing MTT was removed and DMSO was added followed by incubation for 15 min in the dark. The absorbance was measured at 595 nm and mean of five replicates was taken to obtain IC_{50} value for subsequent experiments.

The effect of Peptidase M84 on cell viability was also studied by immunofluorescence of ki-67 nuclear antigen in PA-1 and SKOV3 cells. Peptidase M84 treated (with 2.0 μg/ml for 18 h) and untreated PA-1 and SKOV3 cells were fixed with 4 % paraformaldehyde for 10 min at RT. Cells were then permeabilised with 0.1 % Triton X-100 in 0.1% sodium citrate solution and blocked with 5% serum. Cells were incubated O/N with anti-ki-67 primary antibody (1:200) at 4°C in a moist chamber. Cells were washed with (phosphate buffer saline) PBS and then incubated with Alexa 488 conjugated secondary antibody. Nuclei were stained with DAPI for 10 min at 37°C. Cells were then washed twice with PBS, mounting was done with 10% glycerol. Images were captured using Zeiss (LSM 710) confocal microscope.

Flow cytometry analysis to study apoptosis

Flow cytometry was performed for screening of apoptotic activity of protease positive bacterial culture supernatants. Cellular apoptosis was detected by double staining, FITC conjugated annexinV/propidium iodide (PI) staining, as described in our previous studies (Ray et al., 2016).[27] Briefly, PA-1 cells (1×10^6) were seeded into 6 well tissue culture plates. Cells with 70% confluency were washed with PBS and starved in serum free media for 18 h. Cells were treated with filter sterilised protease positive bacterial supernatant for 18 h in complete medium. Untreated control cells were replaced with fresh media and incubated under similar conditions. After treatment, cells were harvested and flow cytometric analysis was done by using Annexin V and PI staining kit (BD, USA, Cat# 556547) as per the manufacturer's protocol. For protease inhibition studies bacterial culture supernatant was pre-incubated with both 10 mM EDTA and 10 mM PMSF before treatment.

Flow cytometry was also performed with the purified protease as described below. After treatment with purified Peptidase M84 at a concentration range between 1.0 μg/ml to 3.0 μg/ml for 18 h, PA-1, SKOV3, IOSE and ID8 cells were harvested by centrifugation and washed twice with PBS. Cells were re-suspended in 1X binding buffer (provided with BD annexin-V kit), stained with annexin V/PI and kept at RT for 15 mins. Cells were analysed by BD FACS Aria II using 'Cell Quest' software. For protease inhibition studies, Peptidase M84 was preincubated with either 10 mM EDTA or 10 mM PMSF before treatment.

Chromatin condensation assay

After treatment with 2.0 μg/ml of protease for 18 h, ovarian cancer cells were stained with Hoechst 33342 stain (2 μg/ml) and incubated for 10 min at 37°C, and images were taken under Zeiss confocal microscope. Condensed nucleus was counted against total number of nuclei in the field, and the percentage of apoptotic nuclei were calculated and plotted graphically.[42]

Isolation of peritoneal exudate macrophages (PEMΦ) and treatment

To assess the cytotoxic effects of purified protease on normal healthy cells of mice the peritoneal exudate macrophages (PEMΦ) were isolated from 6-8 weeks of old C57BL/6 female mice as described previously (Chakraborty and Bhaumik, 2020; Naskar et al., 2014).[79,80] Briefly, Naive C57BL/6 mice were injected intraperitoneally once with 3.0 ml of a 4% (w/v) starch (Sigma, USA) solution. After 48 h, PEMΦ were collected by peritoneal washing with chilled PBS followed by centrifugation of the exudate and resuspension of cell pellet in RPMI-1640 medium supplemented with 10% FBS (Gibco, USA), 100 U penicillin/ml, and 100 μg streptomycin/ml (Gibco, USA). Cells were then seeded into 6-well plates at $5X10^4$ cells/ml. The cells were then cultured for 48 h at 37°C in a humidified 5% CO_2 incubator to dampen any residual effects of the starch. Non-adherent cells were removed thereafter by gentle washing with serum-free medium. The remaining adherent cells were treated with 3.0 μg/ml of Peptidase M84 for 18 h. The untreated and treated cells were collected by gentle scraping for use in the FITC conjugated annexin V/ (PI) dual staining-based apoptosis detection assay by flow cytometry as per the protocol described earlier.

Detection of ROS by DCFDA staining

In-situ ROS level was measured by oxidation of 2′,7′- dichlorofluorescin diacetate (DCFDA) to highly fluorescent 2′,7′-dichlorofluorescin (DCF). Peptidase M84 treated (2.0 μg/ml) PA-1, SKOV3, IOSE cells and ID8 (3.0 μg/ml) cells for 6 h and 18 h with their respective untreated controls were incubated with DCFDA at a working concentration of 20 μM for 20 min at 37°C, washed with PBS and subsequently the cell pellet was resuspended in 500 μl of PBS and then subjected to flow cytometry and analysed by BD FACS Aria II using 'Cell Quest' software. At least three independent experiments were conducted to validate our results and the mean fluorescence intensity value of DCF was plotted for quantification.

Flow cytometry detection of JC-1 fluorescence

JC-1 dye (Invitrogen, USA) staining to detect changes in mitochondrial membrane potential in ovarian cancer cells was done according to the protocol described by Prasad et al., 2021.[81] Briefly, PA-1 and SKOV3 cells ($1X10^6$) were harvested by centrifugation (5 min at 500×g) after Peptidase M84 treatment (2.0 μg/ml for 6 h and 18 h). Cells were then resuspended in 500 μl of PBS. JC-1 (5,50,6,60-tetrachloro-1,10,3,30-tetraethylimidacarbocyanine iodide) was added to a final concentration of 10.0 μg/ml from a stock solution of 5.0 mg/ml and cells were incubated in dark at 37°C for 30 min. Cells were then washed once and again resuspended in 500 μl of PBS. Cells were analysed in a BD FACS Aria II flow cytometer (BD Bioscience, San Jose, CA, USA). The ratio of the median value of green and red fluorescence was plotted for quantification.

Comet assay

DNA damage (single strand breaks) was measured by alkaline comet assay (Singh et al., 1988).[82] Briefly, PA-1 and SKOV3 control and Peptidase M84 treated (2.0 μg/ml for 18 h) cells were suspended in 0.6% (w/v) low melting agarose. Subsequently, cells were layered over a frosted microscopic slide previously coated with a layer of 0.75% normal melting agarose. The slides were then immersed in a lysis buffer of pH 10.0 and left overnight at 4°C. Slides were transferred into a horizontal electrophoresis chamber containing an alkaline solution (300 mM NaOH, 1 mM Na_2EDTA; pH 13.0). Pre-soaking for 20 min was done in order to unwind DNA. Electrophoresis was then carried out for 20 min (300 mA, 20 V). Slides were washed thrice with neutralizing buffer (Tris Buffer 0.4 M, pH 7.5) followed by staining with ethidium bromide (final concentration 40.0 μg/ml). Slides were examined under Axio observer 7 Apotome.2; objective-EC Plan-Neofluar 40X / 0.75 NA fluorescence microscope and image analysis was done using comet assay software programme Komet 5.5. DNA damage was quantitated by tail moment measurement.

Western blotting (WB)

Western blot was done as described by Ray et al., 2016; Das et al., 2022.[27,83] Briefly, cultured cells were lysed with RIPA buffer and the concentration of protein samples was measured using BCA assay kit. Equal amount of protein was loaded onto SDS-PAGE for separation and then electrophoretically transferred to the PVDF membrane (Merck; Cat# IPVH00010). After transfer the membrane was blocked with 3% BSA (Sigma; Cat# A1470) in Tris-buffered-saline (TBS) and incubated overnight with primary antibody (1: 1000) against the protein of interest (as per requirement) at 4°C. The blot was washed with TBS-Twin 20 (TBST) buffer and incubated with HRP/AP-tagged secondary antibody for 2 h at RT. Proteins were either visualized by Bio-Rad gel documentation system using specific ECL substrate (Thermo scientific; Cat# 34580) for HRP tagged antibodies (Cell Signaling Technology Cat# 7076 and Cell Signaling Technology Cat# 7074) or using BCIP/NBT substrate (Bio-rad; Cat# 1706432) for AP tagged antibodies (Cell Signaling Technology Cat# 7056 and Cell Signaling Technology Cat# 7054). Quantification of western blots was performed using GelQuant (Thermo Fisher Scientific, USA) and ImageJ (NIH, Bethesda, MD) software. At least three independent experiments were performed to confirm the findings and band intensities were normalised to loading controls.

Immunocytochemistry and confocal imaging

Peptidase M84 treated (2.0 μg/ml for 18 h) and untreated PA-1 and SKOV3 cells were fixed with 4% paraformaldehyde for 10 min at RT. Cells were then permeabilized with 0.1 % Triton X-100 in 0.1% sodium citrate solution and blocked with 5% FBS. Cells were incubated O/N with primary antibody (1:200) against the protein of interest (as per requirement) at 4°C in a moist chamber. Cells were washed with PBS and incubated with either Alexa 488 (Cell Signaling Technology Cat# 4408 and Cell Signaling Technology Cat# 4412) or Alexa 555 conjugated secondary antibody (Cell Signaling Technology Cat# 4413 and Cell Signaling Technology Cat# 4409) for 2 h at RT. Nuclei were stained with either DAPI or Hoechst 33342 (working concentration 1.0 μg/ml) for 10 min at 37°C. Cells were washed twice and mounting was done with 10% glycerol. Images were captured using confocal microscope (Zeiss 710); objective-Plan-Apochromat 63X / 1.40 NA. c and all the other required analysis was done according to the procedure described by Das et al., 2022.[83]

Evaluation of intracellular cytochrome c by western blot and immunofluorescence

Subcellular fractionation to extract mitochondria free cytosol from PA-1 and SKOV3 cell lysates was performed. using the method described by Dimauro et al. 2012.[84] Briefly, $5x10^6$ cells were harvested after 18 h of protease treatment (2.0 μg/ml) by trypsinisation followed by the isolation of mitochondria free cytosolic fraction to assess the release of cytochrome c. Concentration of cytochrome c in cytosolic fraction was measured by western blot in protease treated and untreated cells. Cytosolic GAPDH (mitochondria free) was used as loading control.

To observe the intracellular cytochrome c distribution, co-localization-based immunofluorescence was used as described earlier (Li et al., 2020; Sun et al., 2008).[85,86] Briefly, PA-1 and SKOV3 cells were treated with Peptidase M84 for 18 h at a concentration of 2.0 μg/ml. Untreated and treated cells were incubated with Mito Tracker dye (Mito Tracker Green FM; Molecular Probes; Thermo Fisher Scientific) at a working concentration of 100 nm for 40 min in a 37°C incubator in dark. The slides were then fixed with 4% formaldehyde at RT for 15 min. The fixed slides were stained with anti-cytochrome c antibody (1:200) and kept O/N at 4°C in a moist chamber, followed by staining with Alexa 555 labelled secondary antibody (1:200) at RT for 2 h. Cells were stained with DAPI (1.0 μg/ml) for 10 min, washed twice and mounted with 10% glycerol in glass slides. Images were obtained using different excitation filters and merged. Co-localisation was quantified by calculating Pearson's co-efficient values.

RT-qPCR

RT-qPCR of PARs was done as described previously (Ray and Pal, 2016).[37] Total cellular RNA was isolated from untreated and Peptidase M84 treated (2.0 μg/ml for 18 h) PA-1 and SKOV3 cells (about 1X 10^6 cells for PA1 and $0.8X10^6$ cells for SKOV3) using RNA isolation kit (Zymo research; Cat# R1057). 2.0 μg of the total RNA was reverse transcribed using Revertaid first strand cDNA synthesis kit (Thermo scientific; Cat# K1622) to synthesize the cDNA first strand. Thereafter, the cDNA first strand was used in the subsequent amplification by Real-Time PCR with the primers described in Table S1. GAPDH was used as an internal control to normalize the results. Real-Time PCR was performed using SYBR green reagent (Eurogentec; Cat# UFRSMTBC101) in a total volume of 25 μl containing 10 pM of each primer (mentioned in Table S1), 12.5 μl of SYBR green reagent and 2.0 μl of cDNA. PCR reactions were carried out by using an ABI multicolour real time PCR detection system. The thermal cycling conditions used for Real Time PCR were: denaturation at 95°C for 30 s followed by 35 cycles of 1 min denaturation at 95°C, 30 s, annealing at 55°C, followed by 1 min extension at 72°C and final 10 min extension at 72°C.

Immunoprecipitation

For immunoprecipitation (IP), cells were lysed in immunoprecipitation buffer [50 mM Tris-HCl, pH 7.5, 150 mM NaCl, 0.1% Triton X-100, 1% IGEPAL and 1 mM PMSF], and it was performed under denaturing conditions as described previously by Ray and Pal, 2016.[37] Briefly, 2.0 μg/ml of Peptidase M84 was added to the PA-1 and SKOV3 cell medium and incubated for 30 min. The incubation media was removed after centrifugation and cells were fixed with 4% formaldehyde and the cell lysate was prepared using RIPA buffer. 500 μg of the total lysate was incubated with either PAR-1 antibody or antisera raised against Peptidase M84 for 5 h at 4°C in a rotating shaker at a speed of 10 rpm. The lysate along with antibody was allowed to bind with A/G agarose beads and incubated O/N at 4°C in a rotating shaker at a speed of 10 rpm. The lysates were centrifuged and washed twice with IP buffer to remove any non-specific bindings. Beads were boiled with SDS-protein loading dye for 10 min and subjected to electrophoresis. The proteins were transferred to a PVDF membrane and western blot was done with either

anti-Peptidase M84 antibody (1:3000) or anti-PAR-1 antibody (1:1000). Immunoblots (IB) were developed using Veri Blot (Abcam Cat# ab131366) as per the manufacturer's instruction to observe the interaction between Peptidase M84 and PAR-1.

Nuclear cytosolic fractionation

To detect the nuclear translocation of NFκB subunits, PA-1 and SKOV3 ($5X10^6$) cells were treated with 2.0 μg/ml of Peptidase M84 for 18 h. Extraction of nuclear and cytosolic fractions of untreated and Peptidase M84 treated cells were performed using NE-PER™ Nuclear and Cytoplasmic Extraction Reagents (Thermo Scientific™, USA, Cat#78833) according to manufacturer's protocol. The fractions were used for western blotting to determine nuclear translocation of p50 and p65. Here, α-tubulin and Histone H3 were used as cytosolic and nuclear loading controls respectively.

Treatments of cells and siRNA transfection

The cells were first starved for at least 18 h with an incomplete medium prior to respective treatments. Scrambled (SCR) siRNA (Cat#sc-37007, Santa Cruz Biotechnology) was used as control for knockdown studies. Lipofectamine 3000 was used as transfection reagent and transfection was performed according manufacturer's protocol. The transfection was done at 50–60% confluency and the transfection reagents were added in Opti-MEM (Gibco, USA; Cat# 31985062). medium and after 4 h of transfection the media was changed to respective media of treatment. PAR-1 si-RNA (CGGUCUGUUAUGUGUCUAUdTdT) was transfected for at least 48 hours for efficient knock down.

Flowcytometric analysis for apoptosis and ROS detection using inhibitors

Quantitative evaluation of apoptosis and ROS was performed using the flow cytometry methods as described previously by Ray and Pal, 2016.[37] PA-1 and SKOV3 cells ($1X10^6$ cells) were incubated with either 2.0 μg/ml of Peptidase M84 or pre-incubated for 1 h with 0.5 μM PAR1 inhibitor (ML161) or 3.0 μM of NFκB inhibitor (MG132), or 10.0 μM p38 inhibitor (SB203580) and then incubated with 2.0 μg /ml of Peptidase M84 for 18 h. Cells were washed with PBS and analysed to detect apoptosis by Annexin-V-FITC and PI dual staining based method. In-situ ROS was determined by DCFDA staining using FACS Aria II (Cell Quest software) as per the protocol described earlier.

Animal model

Survival kinetics and body weight changes were studied by implanting $5X10^6$ number of ID8 cells (0.2 ml) into the peritoneal cavity of C57BL/6 female mice and allowed to multiply.[71,72] The day of tumour implantation was assigned as day '0'. In the present study, the animals were randomised into six groups containing ten animals (n = 10) in each group. (i) **Group 1** normal set (non-tumour-bearing; untreated control); (ii) **Group 2** only tumour-bearing set (ID8 control); (iii) **Group 3** Peptidase M84-treated ID8 bearing set; where 3.0 μg /ml Peptidase M84 (12.0 μg / kg of body weight) was injected intraperitonially on the day after inoculation of ID8 cells and injected once in a week for seven successive weeks; (iv) **Group 4** Peptidase M84 pre-treated with 10 mM EDTA; tumour bearing set where Peptidase M84 was inhibited with 10 mM EDTA at 37°C for 1 h and then injected into the peritoneum cavity of ID8 treated mouse for seven successive weeks (v) **Group 5** Only Buffer treated set (vehicle control) where 100 μl of 1X PBS buffer was injected intraperitonially once in a week for seven successive weeks. (vi) **Group 6** only Peptidase M84 treated group (protease control).

The life span of each group of mice was evaluated by measuring the percentage of survival rate in each group at 10 days interval by using a formula:

(Number of live animals in a group/number of initial animals in that group) X100.

Collection of blood and serum samples

Blood samples from mice were collected as per the protocol reported previously (Barua et al., 2019).[87] Before euthanasia, all animals were fasted for 4 h then the blood samples were collected by cardiac puncture into microcentrifuge tubes and left to clot. The serum was separated by centrifugation at 2000 X g for 15 min and stored at -20°C until analysis.

Measurement of cellular ROS and liver and kidney toxicity in mice

Cellular ROS level was detected by biochemical analysis of different markers in serum samples of all groups of experimental mice as described above. Different biochemical parameters like lipid peroxidation (LPO), reduced glutathione (GSH), catalase (CAT) and superoxide dismutase (SOD) were measured in the serum of different groups of mice at day 0- and 45-days intervals after inoculation of cells using standard protocols as described earlier by Ray et al., 2016.[27]

Liver toxicity markers such as serum aspartate transaminase (AST), alanine aminotransferase (ALT) level and kidney toxicity markers such as urea and creatinine were analysed by automated clinical chemistry analyzer (AU400, Olympus, Japan) according to the manufacturer's protocol after 45 days of treatment.

Histology of liver and kidney tissue of mice

Histopathology and hematoxylin-eosin (HandE) staining of liver and kidney tissue was done as per protocol suggested by Dasgupta et al., 2022.[88] For the experimental purpose, euthanasia was done as per CPCSEA guidelines. The liver and kidney were harvested from all six

groups of mice mentioned earlier after 45 days of tumour implantation. The tissues were fixed in 10 % buffered formalin. The fixed tissue was paraffin embedded and serially sectioned at 4.0 μm, and stained with hematoxylin and eosin (H&E). Tissue Sections were viewed under 40X magnification of Zeiss Axiovert 40 C microscope.

In vivo evaluation of cell viability

The effects of 3.0 μg/ml of Peptidase M84 were compared against control groups, where mice were randomised in six different groups as mentioned earlier. After 45 days and 60 days of tumour inoculation, mice were sacrificed to collect total cells from the peritoneum and cells viability was checked by trypan blue exclusion method as described previously by Barua et al., 2020.[89]

Statistical analysis

All experiments were replicated at least thrice (n=3). All animal experimental groups contained either 10 or 6 animals. The experimental results were expressed as mean ± standard deviation. All statistical analysis was done by applying Student's t-test (unpaired two-tailed) and bar graphs were plotted using Microsoft Office Excel 2021. In all panels, ns (non-significant) $p>0.05$, *$p \leq 0.05$, **$p \leq 0.01$, and ***$p \leq 0.001$. In each panel, error bars were calculated based on results obtained from a minimum of three independent experiments.

Xanthone from *Swertia chirata* exerts chemotherapeutic potential against colon carcinoma

Atish Barua[1], Pritha Choudhury[1], Niraj Nag[2], Anirban Nath[3], Sabyasachi Kundagrami[3], Amit Pal[2], Chinmay Kumar Panda[4] and Prosenjit Saha[1,*]

[1]Department of Cancer Chemoprevention, Chittaranjan National Cancer Institute, 37, S.P. Mukherjee Road, Kolkata 700 026, India
[2]Division of Pathophysiology, National Institute of Cholera and Enteric Diseases, P-33, CIT Road, Scheme-XM, Beliaghata, Kolkata 700 010, India
[3]Department of Genetics and Plant Breeding, University of Calcutta, Kolkata 700 073, India
[4]Department of Oncogene Regulation, Chittaranjan National Cancer Institute, 37, S.P. Mukherjee Road, Kolkata 700 026, India

The present study examines whether 1,5,8-tri-hydroxy-3-methoxy xanthone (TMX) isolated from *Swertia chirata* could restrict colon cancer cells by downregulating proliferation and inducing apoptosis. The chemotherapeutic activity of TMX was evaluated in several colon cancer and normal cell lines using *in vitro* assays like MTT assay, cell-cycle analysis, caspase-3 activity assay, annexin V/PI staining, JC10 assay, intracellular reactive oxygen species (ROS) level determination by dicholorofluorescein di-acetate (DCFH-DA). The present study revealed that TMX from *S. chirata* could effectively inhibit proliferation of metastatic colon cancer cell lines. The chemotherapeutic potential of TMX against metastatic colon cancer cell lines was achieved by downregulating several critical regulatory genes enabling the suppression of the proliferative potential of colon cancer cells and driving them towards apoptosis in a ROS dependent manner. In addition, TMX showed chemosensitization potential in colon cancer cell lines.

Keywords: Apoptosis, chemosensitization, colon cancer, reactive oxygen species, *Swertia chirata*.

IN India, the annual incidence rate (AIR) for colon cancer in men is 4.4 per 100,000 and in women is 3.9 per 100,000. Colon cancer ranks eighth among men and ninth among women. Survival chances are 50% for every patient for five years. However, depending on the time of diagnosis and staging, it varies as follows: for stage 1 colon cancer, the survival chances are 90% for five years, stage 2 80–83%, stage 3 60% and stage 4 11% for five years[1]. In the developed countries, where modern diagnostic infrastructure is readily available, early diagnosis and treatment significantly increase a patient's chances of overall survival. However, since the cost of cancer treatment is unaffordable to most people in the developing countries, traditional medicine provides the much affordable alternative for the poor population[2]. Majority of the conventional medicines depend on natural products of plant origin and in the vast majority of cases, purified plant products have shown promising results. One of the main advantages of the drugs of plant origin is that since most of the products come from plants, they are non-toxic to normal cells[3]. Since the current treatments show toxic side effects by killing both normal, healthy, dividing cells and cancerous ones, plant extracts can shed new light on the treatment of colon cancer by lowering the side effects and increasing the efficacy of the chemotherapeutic drugs and decreasing their toxic side effects[4]. The major hurdle in establishing the small molecules of herbal origin as successful drug candidates is their low bioavailability.

In a recent study, a small molecule was proven to have bio-availability in *in vivo* studies and chemotherapeutic potential against cancer cells, while being non-toxic to normal cells[5]. *Swertia chirata* is one of the oldest known medicinal plants; it forms a reservoir for a large number of small, bioactive molecules possessing various therapeutic activities. Among the large number of small bioactive molecules, our laboratory had previously established 1,5,8-tri-hydroxy-3-methoxy xanthone (TMX) to have chemotherapeutic potential against metastatic breast and skin cancer while being non-toxic to normal cells, and also to be bio-available in normal Swiss albino mice[6,7]. We have also shown TMX to be more efficacious compared to other chemotherapeutic drugs[6,8]. Here we examine the efficacy of TMX against colon cancer cell lines and also evaluate its chemosensitizing potential by calculating the combination index along with a chemotherapeutic drug, 5 fluoro uracil (5FU).

Materials and methods

Plant material

The whole plant of *S. chirata* was obtained from a regional plant supplier from Kolkata, India, and validated by

*For correspondence. (e-mail: prosenjit_cnci@yahoo.co.in)

Dr S. R. Das (Central Research Institute (Ayurveda), Kolkata). The collected *S. chirata* specimen has been preserved in the Herbarium of the Central Research Institute (Ayurveda), Kolkata.

Isolation and purification of TMX from S. chirata

Extraction, purification and characterization of TMX from *S. chirata* were done at the National Research Institute for Ayurvedic Drug Development, Kolkata. The isolation process has been patented, the details of which are as follows: Indian Patent no. 191129, dated 26.03.2002. Mandal, S., Das, P. C., Das, A., Das, S. and Saha, P. (2002).

Cell line and cell culture conditions

Cell lines CaCo2, HCT-116, HT-29, SW480, SW837 and CCD-18Co were obtained from the National Centre for Cell Sciences, Pune, India. CCD-18Co and CaCo2 were maintained in Eagle's minimum essential medium, HCT-116 and HT-29 in McCoy's 5A medium, and SW837 in Leibovitz's L-15 medium with 10% foetal bovine serum, 2 mM glutamine, 100 U penicillin and 100 µg/ml streptomycin. Cells were grown at 37°C in a humidified CO_2 incubator with 5% CO_2. Refeeding with fresh growth medium and subculturing (using 0.05% trypsin–EDTA) of the cells was done as required[9].

Cytotoxicity analysis

Cytotoxic effects of TMX on CaCo2, HCT-116, HT-29, SW480, SW837 and CCD-18Co cells were assessed using the MTT assay according to the manufacturer's protocol (HiMedia, India). Briefly, the cells (6×10^4) were seeded into 96-well plates. After 24 h, they were treated with different concentrations of TMX (1–10 µM for cancer cells, and 1–100 µM for normal cells) and 5FU (1–10 µM for all the cells) for 48 h. Then cell viability test was performed and the dose–response curve was plotted[10].

Cell-cycle analysis

Cell-cycle analysis was done to evaluate the effect of TMX and 5FU on normal and cancerous colon cell lines. The pattern of cell-cycle phase distribution of all the cells was analysed using FACS (Calibur, Becton Dickinson, USA) assay with 50 µg/ml propidium iodide (PI) staining, and data were analysed utilizing cell Quest Pro Software[11].

Mitochondrial membrane potential by JC10 staining

JC10 assay was performed in normal and cancerous colon cell lines using JC10 kit from Abcam, according to the manufacturer's protocol. Data were obtained using 96-well plates and a plate reader (Cary Varian, Germany); fluorescence intensities were monitored at exitation/emission = 490/525 nm (cut-off at 515 nm) and 540/590 nm (cut-off at 570 nm) for ratio analysis[12].

Caspase-3 activity assay

Caspase-3 enzyme activity assay was performed to evaluate whether TMX was effectively induced in colon cancer cells. According to the manufacturer's protocol, the assay was performed with the caspase-3 colorimetric assay kit (Abcam kit no. ab39401) to detect the caspase-3 enzyme activity. Briefly, after 24 h of different treatments, the supernatant was removed and the cells were trypsinized. Then they were collected and centrifuged at 14,000 rpm for 5 min. Next, cell-lysis buffer which was supplied with the kit was added and the cells were retained on ice and centrifuged. Finally, protein concentration was calculated using Bradford assay[13].

Flowcytometric analysis of apoptosis

Validation of apoptosis was done by quantitating through dual staining of annexin V/PI staining. Cells were treated with IC-50 dosage of TMX, 5FU and a combination of TMX and 5FU. Cells were washed with PBS and incubated with PI and Annexin-V at 37°C for 15 min. Then they were analysed by FACS Aria II using Cell Quest software[14].

Evaluation of cellular damage by quantitating intracellular ROS generation

Cancer cells have higher ROS content than normal cells as they are much more metabolically active to facilitate cancer cell proliferation, survival and adaptation. Therefore, if ROS is further increased, it leads to the death of cancer cells through apoptosis[15]. The relative level of ROS was measured using DCFH-DA dye and quantitated using spectrofluorimetric (Cary Varian) analysis of both cancer and normal cells, following the method previously used in our laboratory[16].

Is apoptosis mediated by TMX was ROS-dependent

NAC (*N*-acetyl-L-cysteine) is commonly used to identify and test ROS inducers and to inhibit ROS. Previous studies revealed that NAC was able to scavenge intracellular ROS of cells at a concentration of 3 µM (ref. 17). So this dose was chosen in the present study along with the IC-50 dosage of TMX to validate whether TMX-induced apoptosis is ROS-dependent.

Evaluation of chemosensitization potential of TMX

The effect (synergistic, additive or antagonastic) TMX exerts in combination with chemotherapeutic drug 5FU is calculated by combination index (CI).

$$CI = (D)1/(D\chi)1 + (D)2/(D\chi)2,$$

where $(D\chi)1$ and $(D\chi)2$ are the concentration of each drug alone to exert χ% effect, while $(D)1$ and (D)2 are the concentration of the drugs in combination to elicit the same effect[18].

Quantitation of mRNA of different genes

RNA was isolated from both normal and cancer colon cells using Roche high-pure RNA isolation kit, according to the Roche life science kit no. 11828665001 protocol. cDNA synthesis was done and real-time analysis was performed using cDNA Synthesis Kit and FastStart Essential DNA Green Master (Roche Life Science) respectively, according to the manufacturer's protocol. All the data were normalized using GAPDH as an internal standard. The data were acquired in the light cycle (Roche). Table 1 provides the list of primers used for qRT-PCR.

Statistical analysis

Statistical analysis was performed to find any significance in the present study. A *t*-test was used for the analysis, where $P < 0.005$ was considered to be statistically significant. Data were represented as mean with standard deviation (SD) of at least three different experiments.

Results

Cellular cytotoxicity analysis upon treatment with TMX

The cytotoxic effect of TMX on colon cell lines, both normal and cancerous, was measured using MTT assay. This revealed that TMX exerted selective cytotoxicity, i.e. it was cytotoxic to cancer cells as evident by their low IC-50 values, such as 5 μM for CACO2, 3 μM for HCT116, 3.8 μM for HT29, 3.9 μM for SW480 and 3.5 μM for SW837, whereas it remained non-toxic to CCD-18Co cell line up to a concentration of 60 μM. This dose was much higher than the IC-50 dosage for cancerous cell lines. Therefore, for normal cell lines 60 μM and for cancer cells, their respective IC-50 dosages were taken as the dose of TMX for further downstream analysis. Here 5FU, a conventional chemotherapeutic drug, was used as the positive control. 5FU showed IC-50 which is comparable with that of TMX against colon cancer cell lines. But unlike TMX, 5FU showed toxicity to normal cell line CCD-18Co with IC-50 of 9 μM (Figure 1 *a* and *b*).

Cell-cycle analysis upon treatment with TMX

Cell-cycle analysis by FACS using PI staining was performed on both normal and cancer colon cell lines. This validated the results obtained in the MTT assay, which showed TMX effectively induced apoptosis to colon cancer cells as evidenced by 40% SUBG0 population in CACO2 cells, 45% SUBG0 population in HCT-116, 41% SUBG0 population in HT29, 47% SUBG0 population in SW480, 43% SUBG0 population in SW837, and which significantly decreased to 2% SUBG0 population in normal cell line CCD-18Co (Figure 1 *c* and *d*).

Effect of TMX treatment on intracellular ROS generation

TMX treatment significantly increased intracellular ROS generation in cancer cells, while no such modulation was observed in normal colon cells. The increased intracellular ROS upon TMX treatment in cancer cells indicated cellular cytotoxicity, which may drive the cells towards apoptosis (Figure 1 *e*).

Effect of TMX treatment on mitochondrial membrane potential

JC-10 is capable of selectively entering the mitochondria and reversibly changing its colour from green to orange as the membrane potential increases. This property is due to the reversible formation of JC-10 aggregates upon membrane polarization that causes shifts in emitted light from 520 nm (i.e. emission of JC-10 monomeric form) to 570 nm (i.e. emission of J-aggregate form). When excited at 490 nm, the colour of JC-10 changes reversibly from green to greenish-orange as the mitochondrial membrane

Table 1. List of primers used for qRT-PCR

PCNA	F.P. CTGCAGATGTACCCCTTGGT
	R.P. ACAACTGAAAGACAGGAAGATGGT
Cyclin D1	F.P. GTGCTGTCTGGGAAGATGTCC
	R.P. ACCCATTCTGGAATACCGGC
P21	F.P. GACATGTGCACGGAAGGACT
	R.P. GGGCAGGGTGACAAGAATGT
BCL2	F.P. CAGGCAATGGAAAAGGGCAA
	R.P. AGGTTAATGAGACCGGGGGA
BAX	F.P. TTGGTGATGTGAGTCTGGGC
	R.P. AACGCTTTGTCCAGAGGAGG
P53	F.P. CTTCTTTGGCTGGGGAGAGG
	R.P. CTTCTTTGGCTGGGGAGAGG

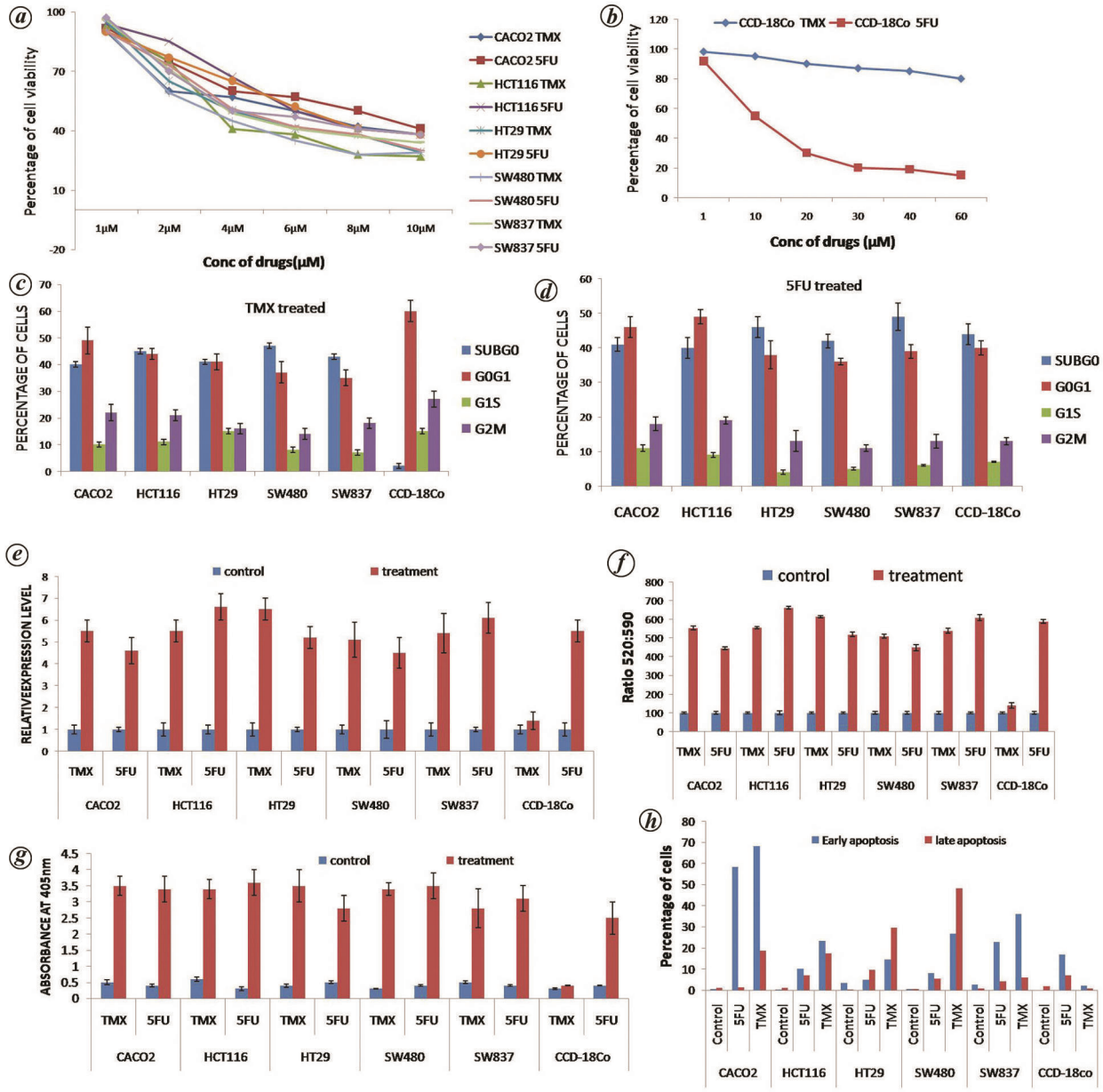

Figure 1. ***a***, Cellular viability assay using MTT analysis (cytotoxic effects) of different dosages of TMX and 5FU after 48 h of treatment against CACO2, HCT116, HT29, SW480 and SW837. Data are presented as mean ± SD. Each experiment was done in triplicate and repeated at least three times. ***b***, Cellular viability assay by MTT analysis (cytotoxic effects) of different dosages of TMX and 5FU after 48 h of treatment against normal colon CCD-18Co. Data are presented as mean ± SD. Each experiment was done in triplicate and repeated at least three times. ***c***, Cell-cycle phase distribution upon treatment with IC-50 dosage of TMX and 5FU against colon cancer cells determined by propidium iodide staining in FACS. Data are represented as ± S.D. *indicates a significant difference versus untreated control ($P < 0.005$). Each experiment was done in triplicate and repeated at least three times. ***d***, Cell-cycle phase distribution upon treatment with the highest non-toxic dosage of TMX and IC-50 dosage of 5FU against normal colon cells determined by propidium iodide staining in FACS. Data are represented as ± S.D. *indicates a significant difference versus untreated control ($P < 0.005$). Each experiment was done in triplicate and repeated at least three times. ***e***, Intracellular ROS generation determination in the CACO2, HCT116, HT29, SW480, SW837 and CCD-18Co cells by DCFH-DA staining after treatment with TMX at IC-50 dosage for cancer cell lines and the highest dosage of 60 μM for normal cell lines. Data were taken 48 h after TMX treatment. Each value shows mean ± S.D. *indicates a significant difference versus untreated control ($P < 0.005$). Each experiment was done in triplicate and repeated at least three times. ***f***, Mitochondrial membrane potential measured in the CACO2, HCT116, HT29, SW480, SW837 and CCD-18Co cells by JC1 staining after treatment with TMX at IC-50 dosage for cancer cell lines and the highest dosage of 60 μM for the normal cell line. Data were taken 48 h after TMX treatment. Each value shows mean ± S.D. *indicates a significant difference versus untreated control ($P < 0.005$). Each experiment was done in triplicate and repeated at least three times. ***g***, Activity of caspase-3 measured in the CACO2, HCT116, HT29, SW480, SW837 and CCD-18Co cells by caspase-3 activation assay after treatment with TMX at IC-50 dosage for cancer cell lines and the highest dosage of 60 μM for the normal cell line. Data were taken 48 h after TMX treatment. Each value shows the mean ± S.D. *indicates a significant difference versus untreated control ($P < 0.005$). Each experiment was done in triplicate and repeated at least three times. ***h***, Induction of apoptosis upon treatment with TMX analysed in colon cell lines by annexin V/PI staining. The respective IC-50 dosage was used for colon cancer cell lines and a high dose 60 μM was used for the normal colon cell line. Data were taken 48 h after TMX treatment. *indicates a significant difference versus untreated control ($P < 0.005$). Each experiment was done in triplicate and repeated at least three times.

becomes more polarized. Increased green fluorescence upon TMX treatment indicated a higher number of monomeric forms followed by a lower number of J-aggregates. An increase in the number of monomeric forms of JC-10 upon TMX treatment is indicative of apoptosis (Figure 1 *f*).

Effect of TMX treatment on caspase-3 activation assay

Caspase-3 is a critical indicator of apoptosis, as it is responsible for the proteolytic cleavage of many essential proteins. TMX treatment selectively induced apoptosis in cancer cells while eliciting no effect in normal colon cells, while 5FU indiscreetly induced apoptosis in normal and cancer cells (Figure 1 *g*).

Flowcytometric validation apoptosis induction upon treatment with TMX

The effect of TMX treatment on apoptosis induction in colon cell lines was studied by annexin V/PI staining in flowcytometry. As in previous experiments it was observed that TMX treatment could induce apoptosis much more efficiently than 5FU in all colon cancer cell lines. TMX treatment showed no apoptosis in normal colon cell line at a high dosage of 60 μM in contrast to 5FU which showed induction of apoptosis in normal cell line (Figure 1 *h*).

Validation of cellular cytotoxicity induced by TMX in cancer cells as ROS generated

Cellular cytotoxicity induced by TMX in cancer cells was significantly downregulated upon co-treatment of ROS scavenger NAC at a dosage of 3 μM (Figure 2 *a*). The data were validated by cell-cycle analysis, which showed a dramatic decrease in SUBG0 followed by an increase in G0G1 upon co-treatment with NAC. This signifies that upon treatment with ROS scavenger and TMX apoptosis induction, TMX is abrogated, thereby leading to the conclusion that apoptosis induction in colon cancer cells upon TMX treatment is ROS-dependent (Figure 2 *b*). The fact that co-treatment of NAC and TMX scavenged intracellular ROS was proved by staining with di-chlorofluorescein-diacetate (DCFH-DA), which showed a significant decrease in intracellular ROS in cancer cell lines, whereas no change in intracellular ROS was observed in a normal cell line (Figure 2 *c*). Furthermore, upon co-treatment with NAC, there was an increase in red fluorescence, i.e. formation of J-aggregates, which indicates healthy cells. This proves that co-treatment with NAC-restricted TMX induces apoptosis in cancer cells (Figure 2 *d*).

Molecular mechanism of induction of apoptosis by TMX against colon cancer cell lines

The molecular mechanism of apoptosis by TMX was studied by analysing the RNA expression of proliferation and apoptosis-related genes using qRT-PCR. Upon treating the colon cancer cells with TMX, PCNA which is a cell proliferation marker was significantly downregulated. PCNA interacts with P21, thereby sequestering P21. Upon severe downregulation of PCNA, it cannot sequester P21 which in turn transactivate P53, thus leading to apoptosis[19]. Here P53–P21-mediated apoptosis was seen in all the colon cancer cell lines upon TMX treatment, followed by downregulation of PCNA. Apoptosis was validated by downregulation of BCL2 and followed by upregulation of BAX. Cyclin D1 is a proliferation marker that is highly expressed in cancer cells, as demonstrated by heightened G0G1 in all cancer cells, and is significantly downregulated by TMX treatment (Figure 2 *e*).

Chemosensitization effect of TMX on treatment with 5FU in cancer cells

CaCo2 cell line separately showed IC-50 against TMX and 5FU at 6 and 8 μM respectively, but when given together, their joint IC-50 against the CaCo2 cell line decreased to 0.5 μM for TMX and 1 μM for 5FU. Therefore CI for TMX and 5FU for CaCO2 cells reduced to 0.2, which signifies a synergistic effect. Individually IC-50 for TMX for HCT-116, HT-29, SW 480 and SW 837 are 4 μM, 4 μM, 5 μM and 3 μM and the IC-50 for 5FU for same cell lines are 6 μM, 5 μM, 4 μM and 4 μM. When these drugs were given together their combined IC-50 for the respective cell lines such as HCT 116, HT29, SW480 and SW837 was 0.7 μM TMX and 1.2 μM 5FU, 0.5 μM TMX and 1 μM 5FU, 0.5 μM TMX and 1 μM 5FU, 1 μM TMX and 2 μM 5FU respectively. Therefore CI values for these two drugs for the cell lines were calculated according to the previously described formula and were found to be 0.375, 0.325, 0.35 and 0.833 respectively. Thus, in all the colon cancer cell lines, co-treatment with TMX and 5FU showed a synergistic effect. Thus TMX treatment sensitizes the cancer cells against treatment with 5FU (Figure 3 *a*). As in individual therapy, combining 5FU and TMX did not elicit any toxicity against the normal cell lines (Figure 3 *b*). The synergistic effect of TMX and 5FU co-treatment significantly increased intracellular ROS in cancer cells, while it did not elicit any effects on cancer cells. The level of ROS generation in cancer cells upon co-treatment with 5FU and TMX was much higher than when separately applied (Figure 3 *c*). Caspase-3 activation assay is one of the confirmatory assays for apoptosis. The combined effect of TMX and 5FU causes significant increased caspase-3 cleavage, which signifies apoptosis. The combined IC-50 group induced apoptosis at a much

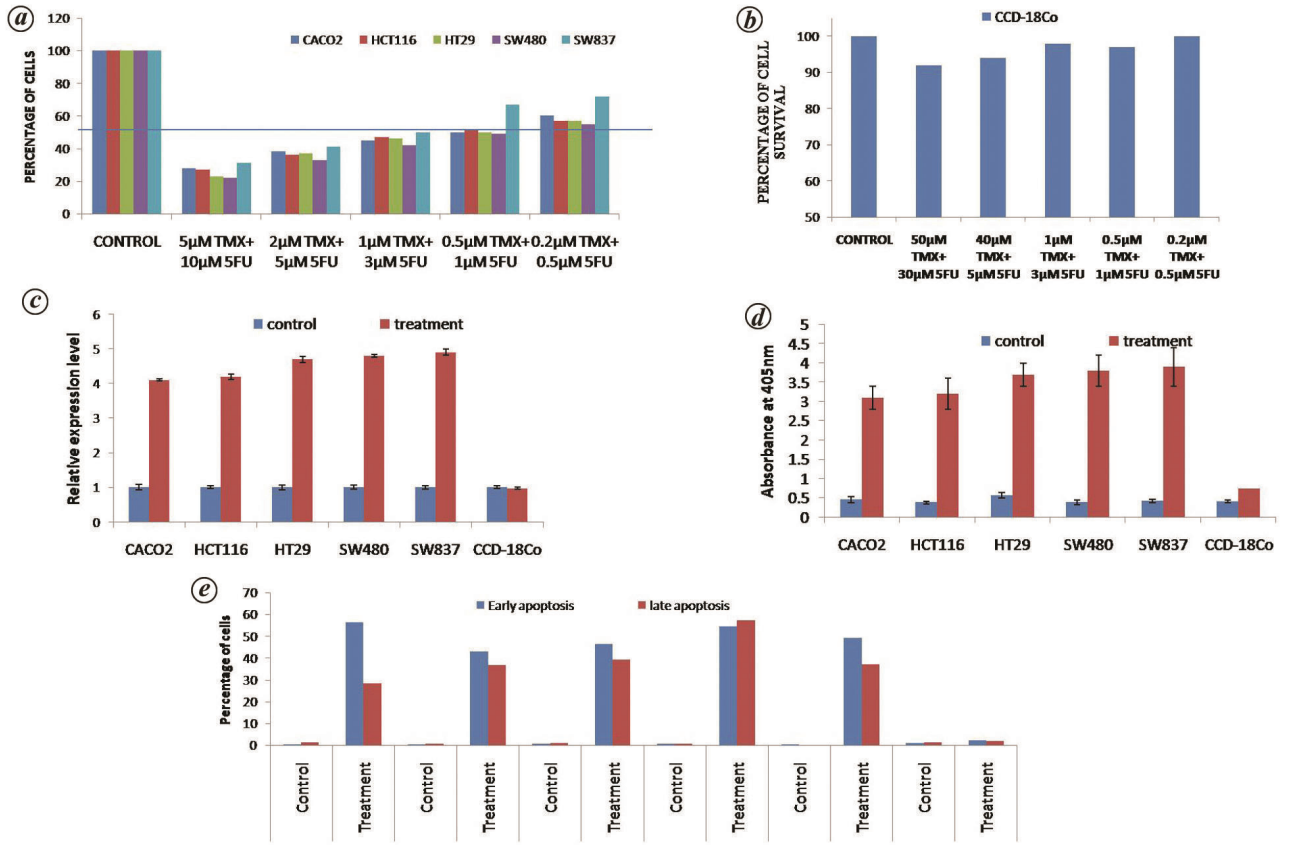

Figure 2. ***a***, Cellular viability assay by MTT analysis (cytotoxic effects) of TMX alone or co-treatment with ROS scavenger NAC measured after 48 h of treatment against CACO2, HCT116, HT29, SW480, SW837 and CCD-18Co cells. Data are presented as mean ± SD. Each experiment was done in triplicate and repeated at least three times. ***b***, Cell-cycle phase distribution upon treatment with IC-50 dosage of TMX and 3 μM NAC against both colon cancer and normal cells determined by propidium iodide staining in FACS. Data are represented as ± S.D. *indicates a significant difference versus untreated control ($P < 0.005$). Each experiment was done in triplicate and repeated at least three times. ***c***, Intracellular ROS generation determination in the CACO2, HCT116, HT29, SW480, SW837 and CCD-18Co cells by DCFH-DA staining after treatment with TMX at IC-50 dosage and 3 μM NAC for cancer cell lines and highest dosage of 60 μM for the normal cell line. Data were taken 48 h after TMX treatment. Each value shows mean ± S.D. *indicates a significant difference versus untreated control ($P < 0.005$). Each experiment was done in triplicate and repeated at least three times. ***d***, Mitochondrial membrane potential measured in the CACO2, HCT116, HT29, SW480, SW837 and CCD-18Co cells by JC1 staining after treatment with TMX at IC-50 and 3 μM NAC dosage for cancer cell lines and the highest dosage of 60 μM for the normal cell line. Data were taken 48 h after TMX treatment. Each value shows mean ± S.D. *indicates a significant difference versus untreated control ($P < 0.005$). Each experiment was done in triplicate and repeated at least three times. ***e***, RT-PCR analysis to determine the effects of TMX on PCNA, cyclin D1, P21, P53, BAX and BCL-2 mRNA levels. Data are normalized for each respective cell line taking GAPDH as the internal control. Data are represented as mean fold changes ± standard deviation. *Significant difference to control ($P < 0.005$). Each experiment was done in triplicate and repeated at least three times.

higher rate than their counterparts (Figure 3 *d*). This observation inferred from the caspase-3 activation assay was validated by annexin V/PI staining, which showed synergism between 5FU and TMX treatment, since significant increase in apoptosis of cancer cells at a lower dosage of IC-50 was observed followed by decrease in toxic effects of 5FU in cancer cells (Figure 3 *e*).

Discussion

A Chinese herbal medicine combined with 5FU, compared with 5FU alone, reduced the risk of death in different stages of colon cancer patients: stage I by 95%, stage II by 64%, stage III by 29% and stage IV by 75% (ref. 20). Thus natural cytotoxic products with proven therapeutic potential increase the efficacy of conventional chemotherapeutic drugs, and this type of combinatorial treatment enables overcoming the drawbacks of traditional chemotherapeutics[21]. Chemotherapeutic drugs work as an antimetabolite to avert cell proliferation; they work by down-regulating the enzyme thymidylate synthase blocking thymidine formation required for DNA synthesis. 5FU has a short half-life but very high diffusion potential, enabling it to impart systemic toxicity in the host body, which is one of the major drawbacks that overshadows its efficacy[22]. Natural products possess the dual role of cytoprotection to normal cells while being cytotoxic to cancer cells by increasing ROS and targeting several key molecules[23]. Most of the time, the molecules targeted by natural

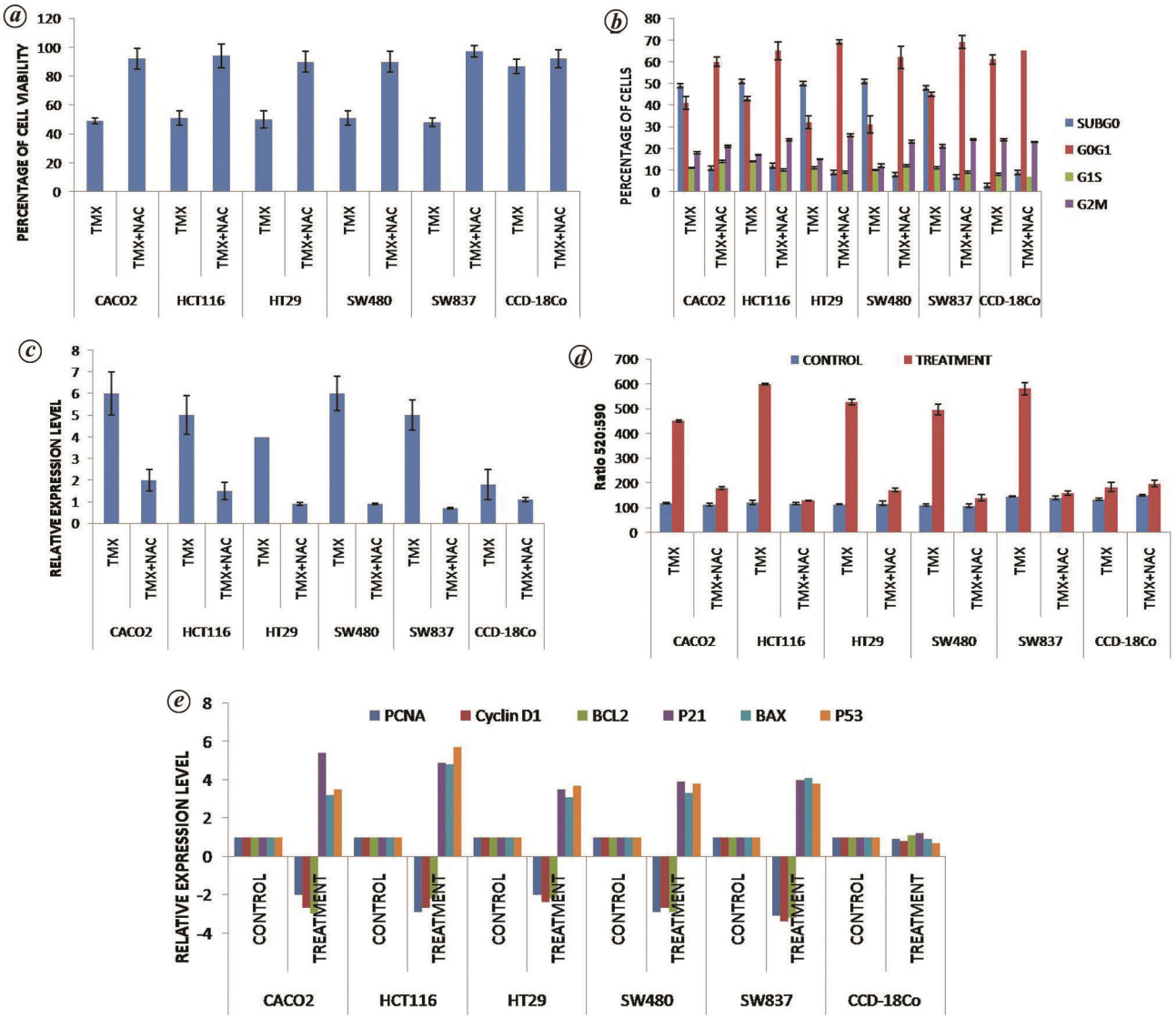

Figure 3. ***a***, Cellular viability assay by MTT analysis (cytotoxic effects) in combination with different doses of TMX and 5FU measured after 48 h of treatment against CACO2, HCT116, HT29, SW480 and SW837. Data are as mean ± SD. Each experiment was done in triplicate and repeated at least three times. ***b***, Cellular viability assay by MTT analysis (cytotoxic effects) in combination with different doses of TMX and 5FU measured after 48 h of treatment against CCD-18Co cells. Data are presented as mean ± SD. Each experiment was done in triplicate and repeated at least three times. ***c***, Intracellular ROS generation determination in the CACO2, HCT116, HT29, SW480, SW837 and CCD-18Co cells by DCFH-DA staining after treatment with a combination of TMX and 5FU at IC-50 dosage for cancer cell lines and the highest dosage of 50 µM TMX+ 30 µM 5FU for the normal cell line. Data were taken 48 h after TMX treatment. Each value shows mean ± S.D. *indicates a significant difference versus untreated control ($P < 0.005$). Each experiment was done in triplicate and repeated at least three times. ***d***, Activity of caspase-3 measured in the CACO2, HCT116, HT29, SW480, SW837, and CCD-18Co cells by caspase-3 activation assay after treatment with a combination IC-50 dosage of TMX and 5FU for cancer cell lines and the highest dosage of 50 µM TMX+ 30 µM 5FU for the normal cell line. Data were taken 48 h after TMX/5FU treatment. Each value shows the mean ± S.D. *indicates a significant difference versus untreated control ($P < 0.005$). Each experiment was done in triplicate and repeated at least three times. ***e***, Induction of apoptosis upon co-treatment of TMX and 5FU analysed in colon cell lines by annexin V/PI staining with a combination IC-50 dosage of TMX and 5FU for cancer cell lines and the highest dosage of 50 µM TMX+ 30 µM 5FU for the normal cell line. Data were taken 48 h after TMX/5FU treatment. Each value shows mean ± SD. *indicates a significant difference versus untreated control ($P < 0.005$). Each experiment was done in triplicate and repeated at least three times.

molecules impart chemoresistance against the conventional chemotherapeutic drugs. Therefore, several reports suggest that prophylactic use of natural products imparts protection against diseases and may increase usage of traditional chemotherapeutic drugs[24]. So a natural product with proven therapeutic efficacy that can combat the drawbacks and improve the effectiveness, i.e. exert synergistic action with the conventional chemotherapeutics, is the need of the hour. *S. chirata* is an ancient medicinal plant with proven multiferous uses. The main reason for its medicinal properties is the large reservoir of different groups of bioactive compounds. Among the group of bioactive compounds present in *S. chirata*, xanthones form an important group. Among the xanthones present, TMX

has been proven to be most bioactive with cytotoxic efficacy against breast and skin cancer cell lines while being non-toxic to normal cells[11]. In this study, TMX was able to exert its cytotoxic potential effectively on several cancer cell lines, while being non-toxic to normal colon cell lines. TMX showed comparable cytotoxic potential with the conventional chemotherapeutic drug 5FU. However, unlike 5FU, it was non-toxic to normal colon cells. This observation was validated by analysis related to the cell cycle, ROS generation and apoptosis. Here ten times (approximately) higher dosage of TMX than that which is cytotoxic to cancer cells was found to be non-toxic to normal colon cells. This observation was also validated by analysis related to the cell cycle, ROS and apoptosis. NAC is a free-radical scavenger that can be used to evaluate the effect of experimental drug-induced ROS generation on apoptosis. NAC pre-treatment is reported to effectively diminish cellular ROS and confirm the role of oxidative stress in drug treatment[25]. In the present study, NAC co-treatment abrogated TMX-induced apoptosis in all colon cancer cell lines; again, no effect on normal colon cell lines was seen with or without co-treatment of NAC and TMX. This observation was validated by analysis related to cell cycle, ROS and apoptosis. ROS upregulation can result in oxidative damage to mitochondrial and cellular proteins. In this study, ROS upregulation upon TMX treatment caused damage to the mitochondrial membrane proteins which in turn leads to the loss of mitochondrial membrane potential of cancer cells[26]. This observation was validated by JC-1 staining[27]. Molecular analysis showed that TMX restricts the colon cancer cell proliferation by downregulating proliferation marker PCNA which in turn upregulates P21, which transactivates tumour suppressor P53 which in turn drives the cell towards apoptosis. Upon establishing the efficacy of plant-derived small-molecule TMX, we examined whether it could increase the efficacy of conventional chemotherapeutic drug 5FU. For quantifying drug interactions between TMX and 5FU, and classifying the interactions of synergy, additivity or antagonism, CI was calculated[18]. Here it was found that for all the colon cancer cell lines, co-treatment of TMX and 5FU yielded a CI value that was less than that of 1, signifying synergism. Further validation of synergism was seen in a normal cell line which showed that upon co-treatment with TMX, cytotoxic effects of 5FU decreased significantly.

Conclusion

In conclusion, TMX from *S. chirata* successfully induced apoptosis in colon cancer cell lines while being non-toxic to the normal cell line. Further analysis revealed that this apoptosis induction was ROS-dependent, which was validated by co-treatment of ROS scavenger NAC with TMX. The chemotherapeutic potential of TMX was further validated by showing that it acts in synergism with 5FU by increasing its efficacy and decreasing its cytotoxic potential to normal cells.

Conflicts of interest: The authors declare that they have no conflict of interest.

1. Patil, P. S. *et al.*, Colorectal cancer in India: an audit from a tertiary center in a low prevalence area. *Indian J. Surg. Oncol.*, 2017, **8**, 484–490.
2. Brinkhaus, B. *et al.*, World Congress on Integrative Medicine & Health 2017: Part one. *BMC Complement. Altern. Med.*, 2017, **17**, 322.
3. Atanasov, A. G. *et al*., Discovery and resupply of pharmacologically active plant-derived natural products: a review. *Biotechnol. Adv.*, 2015, **33**, 1582–1614.
4. Cossarizza, A. *et al*., Guidelines for the use of flow cytometry and cell sorting in immunological studies (second edition). *Eur. J. Immunol.*, 2019, **49**, 1457–1973.
5. Atanasov, A. G., Zotchev, S. B., Dirsch, V. M. and Supuran, C. T., Natural products in drug discovery: advances and opportunities. *Nature Rev. Drug Discov.*, 2021, **20**, 200–216.
6. Barua, A., Choudhury, P., Mandal, S., Panda, C. K. and Saha, P., Therapeutic potential of xanthones from *Swertia chirata* in breast cancer cells. *Indian J. Med. Res.*, 2020, **152**, 285–295.
7. Barua, A., Choudhury, P., Mandal, S., Panda, C. K. and Saha, P., Anti-metastatic potential of a novel xanthone sourced by *Swertia chirata* against *in vivo* and *in vitro* breast adenocarcinoma frameworks. *Asian Pac. J. Cancer Prev.*, 2020, **21**, 2865–2875.
8. Barua, A., Choudhury, P., Panda, C. K. and Saha, P., Chemotherapeutic potential of novel xanthone sourced from *Swertia chirata* against skin carcinogenesis. *Asian J. Pharm. Clin. Res.*, 2020, **13**, 84–88.
9. Fang, C.-Y., Wu, C.-C., Fang, C.-L., Chen, W.-Y. and Chen, C.-L., Long-term growth comparison studies of FBS and FBS alternatives in six head and neck cell lines. *PLoS ONE*, 2017, **12**, e0178960.
10. Mohammadian, M., Feizollahzadeh, S., Mahmoudi, R., Toofani Milani, A., Rezapour-Firouzi, S. and Karimi Douna, B., Hsp90 inhibitor; NVP-AUY922 in combination with doxorubicin induces apoptosis and downregulates VEGF in MCF-7 breast cancer cell line. *Asian Pac. J. Cancer Prev.*, 2020, **21**, 1773–1778.
11. Barua, A., Choudhury, P., Maity, J. K., Mandal, S. B., Mandal, S. and Saha, P., Chemotherapeutic potential of novel non-toxic nucleoside analogues on EAC ascitic tumour cells. *Free Radic. Res.*, 2019, **53**, 57–67.
12. Park, J. W. *et al.*, 99mTc-MIBI uptake as a marker of mitochondrial membrane potential in cancer cells and effects of MDR1 and verapamil. *PLoS ONE*, 2020, **15**, e0228848.
13. Ernst, O. and Zor, T., Linearization of the Bradford protein assay. *J. Vis. Exp.*, 2010.
14. Ray, T., Kar, D., Pal, A., Mukherjee, S., Das, C. and Pal, A., Molecular targeting of breast and colon cancer cells by PAR1 mediated apoptosis through a novel pro-apoptotic peptide. *Apoptosis*, 2018, **23**, 679–694.
15. Zhang, Z., Guo, M., Zhao, S., Shao, J. and Zheng, S., ROS-JNK1/2-dependent activation of autophagy is required for the induction of anti-inflammatory effect of dihydroartemisinin in liver fibrosis. *Free Radic. Biol. Med.*, 2016, **101**, 272–283.
16. Yamamoto, T. *et al.*, Roles of catalase and hydrogen peroxide in green tea polyphenol-induced chemopreventive effects. *J. Pharmacol. Exp. Ther.*, 2004, **308**, 317–323.
17. Halasi, M., Wang, M., Chavan, T. S., Gaponenko, V., Hay, N. and Gartel, A. L., ROS inhibitor *N*-acetyl-l-cysteine antagonizes the activity of proteasome inhibitors. *Biochem. J.*, 2013, **454**, 201–208.

18. Huang, L., Jiang, Y. and Chen, Y., Predicting drug combination index and simulating the network-regulation dynamics by mathematical modeling of drug-targeted EGFR-ERK signaling pathway. *Sci. Rep.*, 2017, **7**, 40752.
19. Li, R., Hannon, G. J., Beach, D. and Stillman, B., Subcellular distribution of p21 and PCNA in normal and repair-deficient cells following DNA damage. *Curr. Biol.*, 1996, **6**, 189–199.
20. McCulloch, M. *et al*., Colon cancer survival with herbal medicine and vitamins combined with standard therapy in a whole-systems approach: ten-year follow-up data analyzed with marginal structural models and propensity score methods. *Integr. Cancer Ther.*, 2011, **10**, 240–259.
21. Senapati, S., Mahanta, A. K., Kumar, S. and Maiti, P., Controlled drug delivery vehicles for cancer treatment and their performance. *Signal Transduct. Target Ther.*, 2018, **3**, 7.
22. Zhang, N., Yin, Y., Xu, S.-J. and Chen, W.-S., 5-Fluorouracil: mechanisms of resistance and reversal strategies. *Molecules*, 2008, **13**, 1551–1569.
23. Zorov, D. B., Juhaszova, M. and Sollott, S. J., Mitochondrial reactive oxygen species (ROS) and ROS-induced ROS release. *Physiol. Rev.*, 2014, **94**, 909–950.
24. Greenwell, M. and Rahman, P. K. S. M., Medicinal plants: their use in anticancer treatment. *Int. J. Pharm. Sci. Res.*, 2015, **6**, 4103–4112.
25. Chang, H.-W. *et al.*, Withaferin A induces oxidative stress-mediated apoptosis and DNA damage in oral cancer cells. *Front. Physiol.*, 2017, **8**, 634.
26. Guo, C., Sun, L., Chen, X. and Zhang, D., Oxidative stress, mitochondrial damage and neurodegenerative diseases. *Neural Regen. Res.*, 2013, **8**, 2003–2014.
27. Tan, H.-Y., Wang, N., Li, S., Hong, M., Wang, X. and Feng, Y., The reactive oxygen species in macrophage polarization: reflecting its dual role in progression and treatment of human diseases. *Oxid. Med. Cell. Longev.*, 2016, e2795090.

ACKNOWLEDGEMENTS. We thank Dr Koustubh Panda, Department of Biotechnology (University of Calcutta, Kolkata) for encouragement; Dr Sukta Das, Cancer Foundation of India for support; Dr Jayanta Chakrabarti (Director Chittaranjan National Cancer Institute, Kolkata) for providing infrastructural support. No funding was received for this study. This study was performed at Chittaranjan National Cancer Institute, NICED Kolkata and University of Calcutta.

Received 13 August 2021; revised accepted 12 November 2021

doi: 10.18520/cs/v122/i1/47-55